Phenomenology of Neutrino Oscillations and Masses

A thesis submitted in partial fulfilment of

the requirements for the degree of

Doctor of Philosophy

by

Kaustav Chakraborty

(Roll No. 15330019)

Under the supervision of

Prof. Srubabati Goswami

Senior Professor

Theoretical Physics Division

Physical Research Laboratory, Ahmedabad, India.

DISCIPLINE OF PHYSICS

INDIAN INSTITUTE OF TECHNOLOGY GANDHINAGAR

2020

to

My Family

Declaration

I, Kaustav Chakraborty declare that this written submission represents my ideas in my own words and where others' ideas or words have been included, I have adequately cited and referenced the original sources. I also declare that I have adhered to all principles of academic honesty and integrity and have not misrepresented or fabricated or falsified any idea/data/fact/source in my submission. I understand that any violation of the above will be cause for disciplinary action by the Institute and can also evoke penal action from the sources which have thus not been properly cited or from whom proper permission has not been taken when needed.

Signature

Name: Kaustav Chakraborty

(Roll No: 15330019)

Date:

CERTIFICATE

It is certified that the work contained in the thesis titled **" Phenomenology of Neutrino Oscillations and Masses"** by Mr. Kaustav Chakraborty (Roll No. 15330019), has been carried out under my supervision and that this work has not been submitted elsewhere for a degree.

Prof. Srubabati Goswami
Theoretical Physics Division,
Physical Research Laboratory,
Ahmedabad, India.

(Thesis Supervisor)

Date:

Thesis Approval

The thesis entitled

Phenomenology of Neutrino Oscillations and Masses

by

Kaustav Chakraborty

(Roll No. 15330019)

is approved for the degree of

Doctor of Philosophy

Examiner	Examiner
Supervisor	Chairman

Date: ____________________

Place: ____________________

Acknowledgments

The work presented in this thesis would not have been possible without the help and support that I received from many people. I take this opportunity to extend my sincere gratitude and appreciation to all those who made this Ph.D thesis possible.

First and foremost, I would like to extend my sincere gratitude to my supervisor Prof. Srubabati Goswami for her guidance, encouragement and support without which this thesis could not have been realized. Her immense knowledge and expertise in the field along with the critical understanding of the subject encouraged me to develop an imperative attitude towards research. I am extremely grateful to her for her immense patience, dedication, continuous moral and academic support during my PhD. I could not have imagined a better mentor for guidance.

I would like to give my special thanks my doctoral committee members Prof. Partha Konar and Prof. Namit Mahajan for their insightful comments and motivations throughout my PhD tenure. I would also like to acknowledge Prof. Hiranmaya Mishra, Prof. Subhendra Mohanty, Prof. Saurabh Rindani, Prof. Jitesh Bhat, Prof. Raghavan Rangarajan, Prof. Dilip Angom, Prof. Bijaya Sahoo, Dr. Ketan Patel for their proficient lectures and Dr. Navinder Singh, Dr. Satyajit Seth for various discussions. I sincerely thank Prof. Anjan Joshipura, Prof. Amol Dighe, Prof. Kenneth Long for illuminating me with their immense knowledge of the subject. I would also like to thank Dr. Pomita Ghoshal for her diligence in explaining me the atmospheric neutrino code.

I would specially like to thank Dr. Goutam Samanta for many interesting discussions and numerous invitations which never allowed me to feel being away from home.

Additionally, I also acknowledge the Indo-French Centre for the Promotion of Advanced Research (IFCPAR/CEFIPRA) for awarding me the Raman-Charpak fellowship and the kind hospitality of The Hubert Curien Pluridisciplinary Institute (IPHC), Strasbourg, France where I could collaborate with Prof. Marcos Dracos, Dr. Eric Baussan and learn from them. A special thanks to Marie-Laure Schneider for kindly helping me through the visa process, arranging accommodations and all the logistics involved during the visit.

I also express my sincere gratitude to Monojit from whom I learned a lot during my initial days of my research. I sincerely thank my collaborators Biswajit, Deepthi, Newton, Chandan, Lakshmi, Dipyaman working with whom have been a learning experience. I also thank all the neutrino group fellows Vishnu, Ananya, Tanmay, Samiran, Supriya whose insight in the subject have always been very beneficial. I would like to give my regards to Loris, Julie, Leonidas for many enlightening discussions with special thanks to Luis for the memorable trips through the heart of Paris to the trek in *the midst Black forest.*

I am thankful to all the staff members of THEPH division, computer center, library, canteen, dispensary, administration of PRL for their constant assistance and support. I also thank the academic and administrative staff members of IIT Gandhinagar for helping with the registration procedures.

I would like to acknowledge Varun for the exciting trips we had across the foothills of Lonavala to the woods of Ranthambhore to the deserts of Jaisalmer. I also thank Ashish, my office mate, who has been kind enough to tolerate my discordant songs for the last four years. I would also like to thank Subir for never letting me forget the taste of delicious Bengali food. I express appreciation from the bottom of my heart to my batch-mates Shefali, Nidhi, Rahul, Archita, Aarthy, Balbeer, Akanksha, Ranadeep, Richa, Arvind, Shivangi, Harsh Raj, Harsh Oza, Naman for the glorious time we spent.

I thank each and every football and volleyball player with whom I have enjoyed every minute of the game which inspired me to be more competitive and focused. Especially I would like to mention Apurv, Manu, Bivin, Avdhesh, Ashim, Tanmoy Chattopadhyay, Jabir, Ali, Aathi, Madhusudhan, Aravind, Ankit, Soumya, Sandeep, Surendra, Abdur, Priyank, Hrushikesh, Sunil, Anirban, Abhay, Sabir, Naval, Sovan.

I am also grateful to everybody at the PRL for making my stay memorable. I am fortunate to have the company of Shweta, Priyanka, Amarendra, Lalit, Gaurav Tomar, Ujjal, Sudip, Nabyendu, Ila, Gaurav Jaiswal, Girish Kumar, Pankaj, Dipti, Deepak, Arun, Naveen, Abhishek, Tripurari, Gulab, Tanmoy Mondal, Abhaya, Lata, Ikshu, Sukanya, Surya, Ayon, Rukmani, Navpreet, Rupa, Chandan Hati, Kuldeep, Satish, Prahlad, Aman, Shoumik, Nijil, Bhavesh, Bharti, Anshika, Harish, Shivani, Sana, Deepika, Dayanand, Vishal, Sudipta, Pravin, Deepak. I would specially like to thank Arko for the encouragement and help he provided during the initial days of my research, also would like to mention Girish Chakravarty for inspiring me to stay fit and healthy.

I would most sincerely extend my gratitude towards my childhood physics teacher Mr. Subhendu Mazumdar for making me realize the beauty of physics. I would also like to acknowledge Dr. Satadal Bhattacharya whose excellent way of teaching was the first stepping stone towards research.

This year have been difficult for the whole world due to the Covid-19 pandemic. In this regard, I would like to thank all the doctors, nurses and essential workers who have shown extraordinary courage to fight this pandemic. Personally, I acknowledge the support provided by CISF unit posted at PRL Thaltej during this difficult time in keeping us safe and healthy.

I am totally indebted to my parents who have always been my greatest source of *encouragement and support throughout my life. I am also extremely grateful to my grandparents especially my grandfather who always believed in me. This thesis would not have been possible without their unconditional love, support and motivations.*

Kaustav

Abstract

Neutrinos are one of the most abundant subatomic particles in the universe second only to the photons. Yet, they are one of the most mysterious particles in the universe. This particle is emitted along with the electron in a nuclear β-decay thus making it a three body decay and explaining the continuous spectrum of the electron. In fact neutrino was postulated by Pauli in 1930 to explain this continuous spectrum. Neutrinos are spin half, neutral particles which interact only via weak interactions and are massless in the Standard Model. But, the discovery of neutrino oscillations has established that neutrinos have mass.

Neutrino oscillation physics is an established field of research that has been posing many challenges over the past few decades. Neutrinos are produced in certain flavor states, but, when the same neutrino is detected after a certain time the flavor state might be different, this phenomena is called neutrino oscillations. Three flavour neutrino oscillations is governed by three mixing angles, two mass squared differences and one complex CP phase. With the help of many phenomenal experiments much progress has been made in precisely determining the oscillation parameters θ_{12}, θ_{13}, $|\Delta m^2_{31}|$ and Δm^2_{21}. This leaves determination of neutrino mass hierarchy i.e. the sign of $|\Delta m^2_{31}|$, CP phase δ_{CP} and the octant of θ_{23} as the primary objectives of the on-going and the upcoming neutrino oscillation experiments. Oscillation experiments are sensitive to the mass-squared differences but the absolute mass scale of the light neutrinos are still unknown and there exists only an upper bound on the sum of absolute neutrino masses from cosmology. Although neutrino oscillations among the three neutrino flavors have been well established there are various studies to explore if there can be other beyond the standard model scenarios at a sub leading level and their detectability in current and future oscillation experiments. This includes the existence of a fourth sterile neutrino, non-standard interactions, neutrino decay, non-unitarity of neutrino mixing matrix, neutrino decoherence, CPT violations, Lorentz violations etc.

The primary objective of the thesis is to study the physics potential of current and future accelerator neutrino experiments to determine the unknown parameters. Neutrino oscillations experiments are sensitive to the probability of oscillations. However,

the determination of the parameters are challenging due to the presence of various parameter degeneracies. This can be resolved by exploring the synergies between various experiments. In particular we concentrate on the future experiments DUNE, T2HK/T2HKK, ESνSB and, perform a comprehensive and comparative analysis of the sensitivities of the current unknowns at these experiments.

The symmetry based approaches have been quite successful in predicting the inter-relations among these quantities and the structure of the leptonic mixing matrix. One such symmetry, called $\mu - \tau$ reflection symmetry leads to very successful predictions of mixing angles which are close to the present experimental values. The consideration of partial $\mu - \tau$ reflection symmetry leads to various correlations between the mixing angles and the CP phase. We study the possibility of studying these correlations in the future long baseline experiments like DUNE, T2HK/T2HKK.

We also investigate the predictions of the $\mu - \tau$ reflection symmetry in presence of a light sterile neutrino and find bounds on the unconstrained parameters. These predictions can be tested in neutrino oscillation experiments like DUNE as well as in neutrinoless double-beta decay experiments.

Additionally we also consider a future proposal nuSTORM proposed primarily for accurate determination of neutrino cross-sections. We study the possibility of exploring sterile neutrinos and non-unitarity of neutrino mixing matrix in the context of this proposal emphasizing on the inclusion on neutral current events in the analysis.

Keywords: Neutrino Physics, Neutrino Oscillation, PMNS matrix, Long-Baseline Neutrino Experiments, Flavour Symmetry, $\mu - \tau$ Symmetry, Leptonic CP Phase, Neutrinoless Double-beta Decay, Sterile Neutrino, Non-Unitarity.

Contents

List of Tables

List of Figures

Chapter 1

Introduction

1.1 Neutrinos through time

Neutrinos are one of the most abundant subatomic particles in the Universe second only to the photons. Yet, they are one of the most mysterious particles in the Universe. The idea of neutrino was conceived by Wolfgang Pauli in December 1930 to explain the continuous energy spectrum observed in beta decay. A β-decay is a process in which a nucleus emits an electron (the β particle) to transform into a nucleus with the atomic number increased by one, keeping the mass number same.

This was represented as,

$$X(A,Z) \rightarrow Y(A,Z+1) + e^{-}. \tag{1.1}$$

Since this is a a two body process, the conservation of energy and momentum requires the kinetic energy of the emitted β particle to be approximately constant. So, an electron with fixed kinetic energy given by $Q = M_{X(A,Z)} - M_{Y(A,Z+1)} - m_e$ should have been observed. But, a continuous energy spectrum with maximum kinetic energy Q was observed. It was believed that the missing kinetic energy could be because of loss of electrons which was ruled out by the a calorimetric β-decay experiment by Ellis and Wooster in 1927. This problem was addressed by Pauli through the “neutrino hypothesis”.

Pauli postulated that a neutral, spin $1/2$ particle with a very tiny mass was also emitted along with the electron in a β-decay, thus making it a three body decay and the energy was shared between the electron and this particle explaining the continuous spectrum of the process. He also believed that the postulated particle was a part of the nucleus along with protons and electrons and called it "neutron". Pauli believed that this particle carries away the remaining energy while avoiding direct detection in any experiments, thus making it a very weakly interacting particle. Pauli was also worried that nobody will be able to detect this particle experimentally. In 1932, James Chadwick discovered the neutron, a neutral particle with mass very close to the proton mass. However, as the "neutrino hypothesis" was successful in explaining the β decay spectrum it inspired Enrico Fermi to formulate the Fermi theory of β-decay in 1934. He also coined the term *neutrino* which means *little neutral one* in Italian. The β-decay was postulated to be,

$$n \to p + e^{-} + \bar{\nu}. \tag{1.2}$$

The properties of neutrinos makes it very difficult to detect this particle and it took around 23 years to directly detect the neutrinos. The first direct evidence of neutrino was observed in 1953 by Fredrick Reines and Clyde Cowan where they detected electron anti-neutrino produced in the Savannah River reactor [12, 13]. They were awarded the Nobel prize for their discovery in 1995. After the discovery of pion a question was raised whether the neutrino associated with the decay $\pi \to \mu\nu$ is the same as the neutrino associated with the beta decay. It was established by Leon M. Lederman, Melvin Schwartz and Jack Steinberger in 1962 [14] at the Brookheaven neutrino experiment, an accelerator based neutrino experiment that this neutrino has different properties than that of the electron neutrino. In this experiment they looked for signature of electrons in the final state however they observed only muons. This established that the neutrinos are different from ν_e. This experiment was the first accelerator based experiment which could produce collimated neutrino beams intense enough for detection. They received the Nobel prize in 1988 for the production of neutrino beam by this method and establishing the doublet structure of leptons with their discovery of muon neutrinos which was a stepping stone for the Standard Model. After the discovery of the tau particle at SLAC, the Stanford Linear Accelerator Center in 1978, it was predicted that a third type of neutrino should exist because tau decay presented similar energy and momentum spectra spectrum like β-decay. In 2002, the DONUT collaboration at Fermilab discovered the tau neutrino[15]. These experiments established the existence of three generations of neutrino.

1.2 Neutrinos in Standard Model

The elementary particles are the fundamental constituents of all the visible matter in the Universe. These particles can be grouped under a gauge symmetry group $SU(3)_c \times SU(2)_L \times U(1)_Y$, where c denotes the color quantum number and Y the hypercharge while L in the $SU(2)$ group signifies the left-handed of the fermions. The Pauli matrices are the generators of the $SU(2)$ group and the Gell-Mann matrices are the generators of $SU(3)$. The Standard Model (SM) is a local gauge invariant theory that describes the interactions between the elementary particles. It describes three fundamental forces namely, the electromagnetic interaction mediated by the photons, the weak interaction mediated by $W^{\pm}$ and Z bosons and the strong interaction which are mediated by eight gluons[16, 17, 18]. But, the Standard Model framework cannot account for the gravitational interaction.

The Standard Model has two types of fermions occurring in three generations. The SM is a chiral theory, the left handed fermions are $SU(2)$ doublet and right handed fermions are singlets. The fermions which are singlets under $SU(3)$ are leptons while fermions which are triplets under $SU(3)$ are quarks. The quarks are the building blocks of hadrons which can be further classified into mesons and baryons. Mesons are bound states of a quark anti-quark while baryons are composed of three quarks. The diagrammatic representation of the SM has been presented in the fig.1.1. The Fermionic representation of the SM and their charges can be summarized as follows:

$$Q_L(3,\ 2,\ \frac{1}{6}) \quad \sim \quad \begin{bmatrix} u_L \\ d_L \end{bmatrix}, \begin{bmatrix} c_L \\ s_L \end{bmatrix}, \begin{bmatrix} t_L \\ b_L \end{bmatrix} \quad ; \tag{1.3}$$

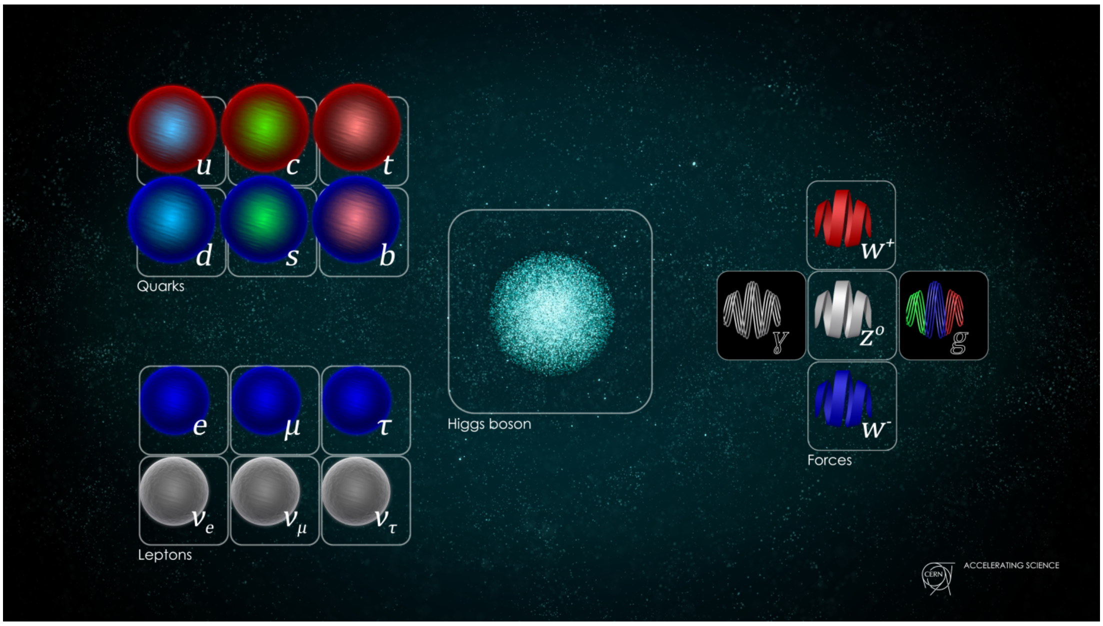

Figure 1.1: The pictograph description of the Standard Model of particle physics. Image from[7].

$$
\begin{aligned}
d_R(3,\ 1,\ -\frac{1}{3}) &\sim d_R, s_R, b_R\ ; && (1.4)\\
u_R(3,\ 1,\ \frac{2}{3}) &\sim u_R, c_R, t_R, && (1.5)\\
l_L(1,\ 2,\ -\frac{1}{2}) &\sim \begin{bmatrix}\nu_{eL}\\ e_L\end{bmatrix} \begin{bmatrix}\nu_{\mu L}\\ \mu_L\end{bmatrix} \begin{bmatrix}\nu_{\tau L}\\ \tau_L\end{bmatrix}\quad ; && (1.6)\\
e_R(1,\ 1,\ -1) &\sim e_R, \mu_R, \tau_R\quad . && (1.7)
\end{aligned}
$$

where the charges are colour charge, $SU(2)$ charge and hypercharge in this order. The particles described above are also accompanied by their respective antiparticles in the SM.

The $SU(2)$ symmetry of the Lagrangian is broken via spontaneous symmetry breaking to give masses to the gauge bosons, this process is called the Higgs mechanism. The scalar boson associated with the Higgs field is called the Higgs boson. The Higgs boson was eventually discovered by the CMS and ATLAS experiments at the Large Hadron Collider in 2012[19, 20]. The fermion mass is generated from the Higgs-lepton Yukawa term $y\bar{\psi}_L\psi_R < \phi >$, where y is the Yukawa coupling and the vacuum expectation value of the Higgs field is given by $< \phi >$.

The SM also has two accidental symmetries, the baryon number and three lepton number symmetries corresponding to each lepton flavour namely L_e, L_μ and L_τ symmetries. The baryon(lepton) numbers are assigned +1 if they are baryon(lepton) and -1 for anti-baryon(anti-lepton). In the SM the total baryon number is conserved while in case of the lepton numbers L_e, L_μ and L_τ numbers are individually conserved.

Neutrinos are still massless in the SM because of the absence any right handed neutrinos which prevents one from writing a mass term which renders the neutrinos massless in SM. The reason for the absence of right handed neutrinos is that weak interactions violate parity. The parity violation in weak interactions was conjectured by Lee and Yang in 1956 to solve the $\tau - \theta$ puzzle [21]. The parity violation was observed by Chien-Shiung Wu and collaborators in 1956 at an experiment conducted at the National Institute of Standards and Technology (NIST). The experiment observed the decay:

$$^{60}\text{Co} \rightarrow \ ^{60}\text{Ni} + e^- + \bar{\nu}_e.$$

Where, an external magnetic field was used to align the nuclear spins of ^{60}Co. The spin of the emitted electrons were always opposite to the electron momentum[22]. To conserve momentum, the anti-neutrino is always emitted in the direction of spin i.e. anti-neutrinos are right handed. This implies the absence of mirror image state which is left-handed antineutrinos. This correlation could only be explained by the absence right-handed neutrino which proved the violation of parity in weak interactions. In 1958, the experiment by Goldhaber and Sunyar [23] showed that antineutrinos have negative helicity.[1]

The leptons in SM are colour singlet so they do not participate in strong interactions, the charged leptons have electromagnetic interactions. Neutrinos are uncharged, they only interact via weak interactions. The weak interactions are mediated by the $W^\pm$ and Z bosons, the former results in charged current (CC) and the latter neutral current (NC) interactions. The Z boson decay at the LEP experiments established that only three light neutrino species could exist in the SM. In the SM the Z boson can have

[1] A particle has left helicity when the spin is aligned opposite to the direction of momentum while in right helicity the spin is aligned in the direction of momentum.

several decay modes like:

$$Z \rightarrow \nu_l + \bar{\nu}_l \quad \text{(invisible decay)} \tag{1.8}$$

$$Z \rightarrow l^+ + l^- \quad (l = e, \mu, \tau) \tag{1.9}$$

$$Z \rightarrow \text{hadrons} \tag{1.10}$$

The number of neutrino species was found from the branching ratios as[24]

$$R^0_{inv} = \frac{\Gamma(Z \rightarrow inv)}{\Gamma(Z \rightarrow l\bar{l})} = N_\nu \left(\frac{\Gamma(Z \rightarrow \nu_l \bar{\nu}_l)}{\Gamma(Z \rightarrow l\bar{l})} \right)_{SM} \tag{1.11}$$

Under the assumption that invisible Z decays are only to the neutrinos coupling according to SM expectations, the number of light neutrino generations, N_ν, can then be determined by comparison between the measured R^0_{inv} with the SM prediction. Which gives $N_\nu = 2.984 \pm 0.008$. However, these data cannot rule out the presence of heavy neutral leptons (including neutrinos) with mass $M_{hnl} > m_Z$ because of the BSM processes like:

$$Z \rightarrow \bar{\nu} N \tag{1.12}$$

$$Z \rightarrow \bar{N}_i N_j. \tag{1.13}$$

1.3 Neutrino Sources

Neutrinos are the second most abundant particle in the Universe with energy range of $10^{-6} - 10^{18}$ eV. Neutrinos can come from different natural and artificial sources. The fig.1.2 shows the flux of the neutrinos from these sources as a function of energy.

The sources of neutrinos are,

- **Relic Neutrinos:** The relic neutrinos which are decoupled from other particles in the early Universe. The processes of neutrino interactions were,

$$n + e^+ \rightleftharpoons p + \bar{\nu}_e, p + e^- \leftrightharpoons n + \nu_e, n \leftrightharpoons p + e^- + \bar{\nu}_e. \tag{1.14}$$

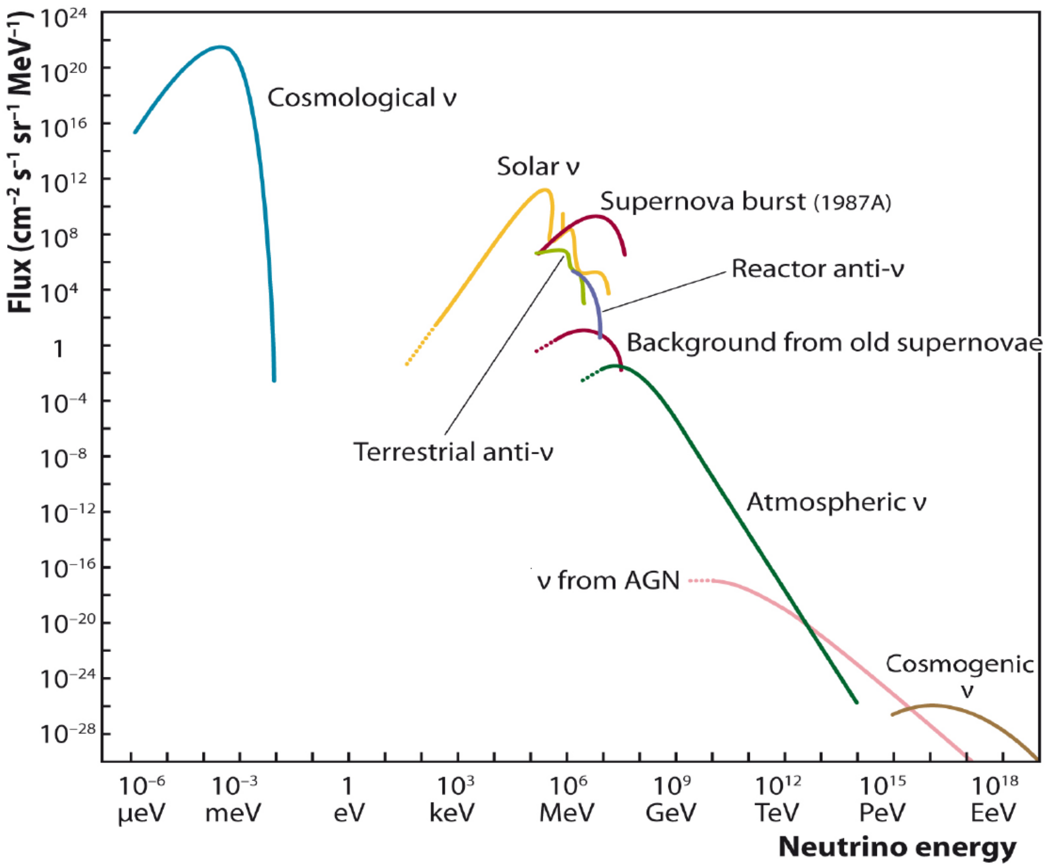

Figure 1.2: The neutrino flux as a function of neutrino energy [8].

As the Universe started expanding, the rate of expansion surpassed the rate of weak interaction and the neutrinos decoupled. These neutrinos have the smallest energies but highest flux and make up the Cosmic Neutrino Background (CνB).

- **Thermal Solar Neutrinos:** Neutrinos in keV range are produced in the Sun through thermal processes like plasmon decay, the Compton process, and electron bremsstrahlung. These are called thermal solar neutrinos. The energy range of these neutrinos lie between the relic neutrinos and solar neutrino not shown in the fig1.2.

- **Solar Neutrinos:** The solar neutrinos are one of the most abundant sources of neutrinos on Earth. These are produced in the core of the Sun by thermo-nuclear fusion reactions where protons are fused to produce α particles. Around 98% of the neutrinos in the sun are created in the pp chain process as

$$4p \rightarrow\ ^4He + 2e^+ + 2\nu_e \tag{1.15}$$

The rest is formed in the carbon-nitrogen-oxygen CNO cycle. Solar neutrinos were observed in several detectors on Earth and gave rise to the solar neutrino problem. We will discuss this in the next chapter.

- **Supernova Neutrinos:** The supernova neutrinos are emitted during a supernova explosion where a star collapses into a neutron star or a black hole. The neutrinos are formed by electron capture and "thermal" pair production so they are MeV energy neutrinos [25]. The neutrinos from the supernova SN1987A explosion in the Large-Magellanic-Cloud were observed by the Kamiokande detector [26] in Japan and IMB [27] in USA.

- **Geo Neutrinos :** The geo neutrinos originate when the radioactive nuclei (mainly ^{238}U, ^{232}Th) present in the Earth undergo β-decay to produce electron anti-neutrino ($\bar{\nu_e}$). The energy range varies from sub-MeV to a few MeV. Geoneutrinos have been detected by KamLAND [28] and Borexino [29] experiments.

- **Atmospheric Neutrinos:** The atmospheric neutrinos are produced when high energetic cosmic rays interact with the nuclei in the Earth's atmosphere via the following processes,

$$\pi^{\pm}(K^{\pm}) \rightarrow \mu^{\pm} + \nu_\mu(\bar{\nu_\mu}) \tag{1.16}$$

$$\mu^{\pm} \rightarrow e^{\pm} + \nu_e(\bar{\nu_e}) + \nu_\mu(\bar{\nu_\mu}) \tag{1.17}$$

The above decay chain suggests that the number of muon neutrinos is twice that of the electron neutrinos. Atmospheric neutrinos are produced in the energy range from a few MeV to hundreds of GeV. Atmospheric neutrinos were observed in several detectors and gave rise to the atmospheric neutrino anomaly which will be discussed in the next chapter.

- **Reactor Neutrinos:** Nuclear reactors which are a major source of electron anti-neutrinos produced from β-decay during nuclear fission reactions. The typical energy range of these neutrinos lie in the range 1.8 MeV to 8 MeV. In a nuclear reactor, nuclei like ^{235}U, ^{238}U, ^{239}Pu, ^{241}Pu are allowed to undergo fission in controlled conditions. The first neutrinos observed were from a nuclear reactor. In the next chapter we will discuss more about the reactor experiments.

- **Accelerator Neutrinos:** Accelerator neutrino beams are created from the decays of charged π and K mesons. These mesons have short lifetimes and are created when high energy proton beams are bombarded on thick nuclear targets. The production mechanisms are from the decay of π^+ and π^- given as follows:

$$\pi^+ \to \nu_\mu + \mu^+$$

$$\pi^- \to \bar{\nu}_\mu + \mu^-$$

  . Neutrinos from accelerator beams have been observed by several experiments which will be discussed in the next chapter.

- **Ultra High Energetic(UHE) Neutrinos:** The cosmological ultra high energy neutrinos generally originate from active galactic nuclei (AGN) [30] and gamma ray bursts (GRB) [31]. The neutrinos with energy greater than $10^{15}\mathrm{GeV}$ are considered as UHE neutrinos. The UHE neutrinos are produced when very high energetic protons interact with soft photons or matter. The sources containing protons are accelerated to very high energy via Fermi acceleration mechanism. These protons, when interact with matter, produce UHE neutrinos. The sources of UHE neutrinos are present at a very large distance from Earth and the oscillations average out. The flavour composition of such neutrinos are dependent on the source of the neutrinos and can vary from source to source. Many experiments like IceCube neutrino observatory [32], ANtarctic Impulsive Transient Antenna(ANITA) [33], Astronomy with a Neutrino Telescope and Abyss environmental RESearch (ANTARES) [34] are currently looking for the cosmological UHE neutrinos. All of the experiments have detected several UHE neutrino events.

1.4 Neutrino Oscillations

Neutrino oscillation is a quantum mechanical phenomena which was proposed by Bruno Pontecorvo in 1957 [35, 36] in analogy to the $K_0 \rightleftarrows \bar{K}_0$ oscillations in the quark sector. Pontecorvo was fascinated by the idea of $K_0 \rightleftarrows \bar{K}_0$ oscillations and raised the possibility of existence of other particles undergoing similar particle $\rightleftarrows$ anti-particle oscillations and he proposed a similar mechanism for neutrinos since at that time only one flavour of neutrino was known. In 1962 after the discovery of ν_μ, Maki, Nakagawa, Sakata first proposed the mixing between two kinds of neutrinos [37]. This idea was further expanded by Pontecorvo in 1967 [38] to describe neutrino oscillation. Neutrinos are produced in certain flavor states when the same neutrino is detected after a certain time, the flavor state might be a different. The phenomena by which a neutrino can change its flavour when it propagates is called neutrino oscillation. Neutrino oscillation requires the flavor eigenstates to be different from mass eigenstates and each flavor eigenstate is formed by the quantum superposition of the mass eigenstates which results in the mixing between the different neutrino flavors. The mass eigenstates and the flavour eigenstates are connected by the neutrino mixing matrix as follows:

$$|\nu_\alpha\rangle = \sum_i U^*_{\alpha i}|\nu_i\rangle, \tag{1.18}$$

where, $|\nu_\alpha\rangle$,$|\nu_i\rangle$ are the flavour and mass eigenstates respectively and U is the unitary mixing matrix also known as the Pontecorvo, Maki, Nakagawa, Sakata (PMNS) matrix. The sum runs over the number of mass eigenstates.

The neutrino mixing matrix for three generation oscillations is

$$U^* = \begin{pmatrix} c_{12}c_{13} & s_{12}c_{13} & s_{13}e^{-i\delta_{CP}} \\ -s_{12}c_{23} - c_{12}s_{23}s_{13}e^{i\delta_{CP}} & c_{12}c_{23} - s_{12}s_{23}s_{13}e^{i\delta_{CP}} & s_{23}c_{13} \\ s_{12}s_{23} - c_{12}c_{23}s_{13}e^{i\delta_{CP}} & -c_{12}s_{23} - s_{12}c_{23}s_{13}e^{i\delta_{CP}} & c_{23}c_{13} \end{pmatrix}, \tag{1.19}$$

where $c_{ij} = \cos\theta_{ij}$ and $s_{ij} = \sin\theta_{ij}$.

The probability that a neutrino of energy E produced in state α will be detected in a state β on propagation over a distance L in vacuum is given by:

$$\begin{aligned} P_{\alpha\beta} = \delta_{\alpha\beta} \quad &- \quad 4\sum_{i>j}^{3} \mathrm{Re}\big(U^*_{\alpha i}U_{\beta i}U_{\alpha j}U^*_{\beta j}\big)\sin^2\{\Delta m^2_{ij}L/4E\} \qquad (1.20) \\ &+ \quad 2\sum_{i>j}^{3} \mathrm{Im}\big(U^*_{\alpha i}U_{\beta i}U_{\alpha j}U^*_{\beta j}\big)\sin\{2\Delta m^2_{ij}L/4E\}, \end{aligned}$$

where $\Delta m^2_{ij} = m^2_i - m^2_j$. Some of the important features of the probability expressions are: neutrino oscillation is only sensitive to the mass-squared difference and not the absolute masses. The oscillatory character is present in $\sin^2\{\Delta m^2_{ij}L/4E\}$; the oscillation maxima is reached when $\Delta m^2_{ij}L/4E = n\pi/2$.

Neutrino oscillations have been observed in several experiments using solar, atmospheric, reactor and accelerator neutrinos. Together these experiments have established oscillation among three flavour of neutrinos on a firm footing.

The parameters governing the three generation neutrino oscillation phenomena are the three mixing angles (namely, solar mixing angle θ_{12}, atmospheric mixing angle θ_{23} and rector mixing angle θ_{13}), two mass-squared differences (namely, solar mass-squared difference $\Delta m^2_{sol} = m^2_2 - m^2_1$ and atmospheric mass-squared difference $\Delta m^2_{atm} = m^2_3 - m^2_1$) and Dirac CP phase δ. Among these, the unknown parameters at the present epoch are (a) the octant of θ_{23}, $i.e.$ whether $\theta_{23} < 45^\circ$ (Lower Octant, LO) or $\theta_{23} > 45^\circ$ (Higher Octant, HO), (b) sign of Δm^2_{atm}, $i.e.$ mass ordering of neutrinos where $\Delta m^2_{atm} > 0$ is called Normal Hierarchy (NH), $\Delta m^2_{atm} < 0$ is called Inverted Hierarchy (IH) as shown in fig.1.3 and (c) magnitude of Dirac CP phase δ.

The present best-fit values for the oscillations parameters are: $\theta_{12} = 33.82^\circ$, $\theta_{13} =$

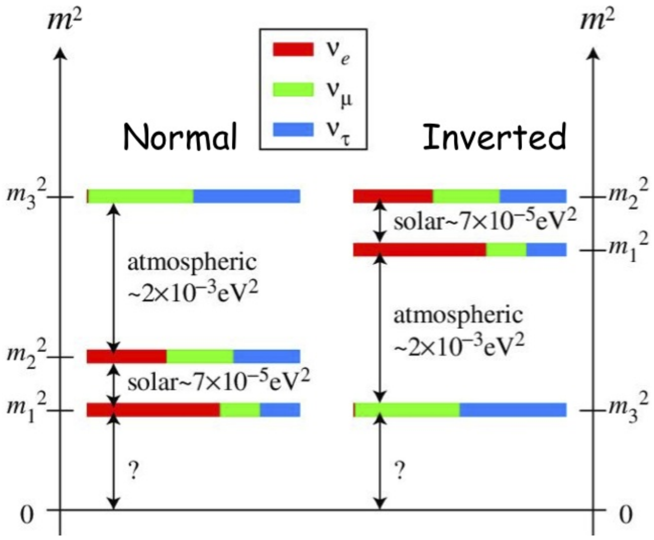

Figure 1.3: The two possible mass hierarchies. Image from: [9].

$8.61°$, $\theta_{23} = 48.3°$, $\Delta_{21} = 7.39 \times 10^{-5}$, $|\Delta_{31}| = 2.52 \times 10^{-3}$ and $\delta_{CP} = 222°$. Oscillation experiments are sensitive to the mass-squared differences but the absolute mass scale of the light neutrinos are still unknown and there exists only an upper bound on the sum of absolute neutrino masses $\sum_{i=1}^{3} m_i \leq 0.12$ eV [39], from cosmology.

A detailed description on the current status of neutrino oscillations parameters, mathematical formalism of the neutrino mixing and oscillation probabilities is discussed in the next chapter.

1.5 Neutrino mass and mixing

Observation of neutrinos oscillations has established that neutrinos have tiny mass which leads to the question on the mechanism of neutrino mass generation. In quantum field theory, generally a fermion mass term is a combination of a left handed fermion and a right handed fermion written as,

$$-\mathcal{L}_m^D = m_D(\bar{\nu_L} N_R + \bar{N_R}\nu_L), \tag{1.21}$$

where, N_R is a heavy right handed neutrino. Such a mass term where the left handed and the right handed fields are different is the Dirac mass term. Lepton number is conserved in a Dirac mass term. The SM do not have a right handed neutrino so a neutrino mass term cannot be written in SM. To generate the neutrino mass the SM can be extended to include a right handed neutrino. Such an approach requires the Yukawa coupling $\sim 10^{-12}$, the smallness of the coupling has no natural reason.

Since, neutrinos are neutral particles they can be anti-particle of itself and such a fermion is called a Majorana fermion. To write a Majorana mass term, the charged conjugated fields serve as the right handed counterparts. A Majorana mass can be expressed as:

$$\mathcal{L}_m^M = \frac{1}{2} m_L (\bar{\nu_L^C} \nu_L) + \frac{1}{2} M_R (\bar{N_R} N_R^C), \tag{1.22}$$

where, C denotes the charged conjugation operator. In a Majorana mass term, lepton number is violated by exactly by 2 units. Such a term cannot be included in the SM because $\bar{\nu_L^C} \nu_L$ has $Y = -2$ (hypercharge). Hence, to write a gauge invariant term a Higgs with and $Y = 2$ is needed which does not exist in the SM.

The most general neutrino mass can be written as,

$$\begin{aligned} -\mathcal{L} &= \mathcal{L}_m^D + \mathcal{L}_m^M && (1.23)\\ &= \bar{N_R} m_D \nu_L + \frac{1}{2} m_L (\bar{\nu_L^C} \nu_L) + \frac{1}{2} M_R (\bar{N_R} N_R^C) + \text{H.C.} && (1.24)\\ &= \frac{1}{2} \bar{N_R} m_D \nu_L + \frac{1}{2} \bar{\nu_L^C} m_D^T N_R^C + \frac{1}{2} m_L (\bar{\nu_L^C} \nu_L) + \frac{1}{2} M_R (\bar{N_R} N_R^C) + \text{H.C.} && (1.25)\\ &= \frac{1}{2} \bar{N_L^C} \mathcal{M} N_L + \text{H.C.}. && (1.26) \end{aligned}$$

where $N_L = (\nu_L, N_R^C)^T$ and

$$\mathcal{M} = \begin{bmatrix} m_L & m_D^T \\ m_D & M_R \end{bmatrix}. \tag{1.27}$$

In a special case when $m_L << m_D << M_R$ leads to the seesaw mechanism. The mass-matrix $\mathcal{M}$ can be block-diagonalized by a unitary matrix. After block diagonalization the light neutrino mass and the heavy neutrino mass can be obtained as,

$$M_{light} = m_\nu = m_L - m_D^T M_R^{-1} m_D. \tag{1.28}$$

$$M_{heavy} = M_R \tag{1.29}$$

For example, in type-I see-saw mechanism $m_L = 0$, so from eq. 1.28,

$$m_\nu = -m_D^T M_R^{-1} m_D. \tag{1.30}$$

We can see that for the the light neutrino mass m_ν to be light, M_R should be high, this is called the see-saw mechanism.

The origin of seesaw mechanism is from effective dimension-5 operator given by:

$$\mathcal{L}_5 = -\frac{1}{8}\frac{\kappa_{ji}}{M}(\bar{L_{Lj}^c}\epsilon\tau^a l_{Li})(H^T\epsilon\tau^a H) + h.c. \tag{1.31}$$

where, l, H denote SM leptons and Higgs doublet respectively and κ_{ij} is the effective coupling, $\tau^a/2$ represent $SU(2)$ generators and ϵ is the anti-symmetric $SU(2)$ tensor. This type of operator is obtained by integrating out intermediate heavy fields of mass scale M, which sets the energy scale of new physics

The Weinberg operator[40] can be generated in three ultraviolet completions: (i) Heavy right-handed neutrino is added to SM to generate the Type-I see-saw mechanism [41, 42, 43, 44], (ii) SM is extended by a scalar triplet in Type-II see-saw mechanism [45, 46, 47, 48] and (iii) a fermion triplet is added in Type-III see-saw mechanism [49]. The see-saw mechanism provides the most natural way to generate tiny neutrino masses [50].

In general the mass matrix is not diagonal in the flavour basis. Since it is a symmetric matrix it can be diagonalized using unitary transformation as given by:

$$m_\nu^{\text{diag}} = U_\nu^T m_\nu U_\nu. \tag{1.32}$$

In a basis where charged lepton mass matrix is diagonal $U_{PMNS} = U_\nu$. The Weinberg operator violates lepton number by two units implying neutrinos are Majorana particles. Whether the neutrino is a Dirac or Majorana particle has not yet been established experimentally. The experimental signature which can establish whether neutrino is a Majorana partilce is the neutrinoless double-beta decay ($0\nu\beta\beta$) [51, 52, 53, 54, 55].

The $0\nu\beta\beta$ is a nuclear transition under which a nuclei with atomic number Z transitions into a nuclei with atomic number $Z+2$ emitting two electrons and no neutrinos.

$$X(A,Z) \rightarrow Y(A,Z+2) + 2e^{-}. \tag{1.33}$$

This process violates lepton number by 2 units [56, 57]. The process is forbidden in the Standard Model. $0\nu\beta\beta$ is an extremely rare process which if observed will establish the Majorana nature of the neutrinos.

1.6 Beyond the standard three neutrino paradigm

Although neutrino oscillations among the three neutrino flavors have been well established there are various studies to explore if there can be other beyond the standard model scenarios at a sub leading level and their detectability in current and future oscillation experiments. This includes the existence of a fourth sterile neutrino, non-standard interactions, neutrino decay, non-unitarity of neutrino mixing matrix, neutrino decoherence, CPT violations, Lorentz violations etc.

The existence of sterile neutrinos gained importance due to the results from the Liquid Scintillator Neutrino Detector (LSND) experiment [58, 59] at the Los Alamos laboratory. LSND reported $\bar{\nu_\mu} \rightarrow \bar{\nu_e}$ oscillations with $\bar{\nu_\mu}$ with energy around 0 to 53 MeV produced by pion decay at rest detected at a distance of 31 m. This excess could be explained by the presence of oscillations with $\Delta m^2 \sim 1\text{eV}^2$ which raised the possibility of the existence of a fourth light neutrino. In view of the constraint from Z-decay this extra neutrino has to be sterile i.e. it will not have the standard weak interactions hence it is called the *sterile neutrino*.

This LSND [59] result was further tested by the MiniBoone experiment. The MiniBoone experiment was designed by Fermilab to specifically probe the Δm^2_{LSND} using booster neutrino beam in the energy range 200 MeV to 1250 MeV and a baseline of 541 m. The collaboration reported excess electron anti-neutrino events in the $\nu_\mu \rightarrow \nu_e$ and $\bar{\nu_\mu} \rightarrow \bar{\nu_e}$ channels to report similar excess in electron neutrino events [60, 61]. But, other appearance experiments like KARMEN, NOMAD, E776, ICARUS, OPERA have not shown any such evidence. The ν_e reactor experiments Bugey, Daya Bay have also given null result. However, after the recent results from DANSS [62] and NEOS [63] the reactor neutrino disappearance data favours sterile neutrino oscillations with $\Delta m^2_{41} \approx 1.3eV^2$. Which is again not supported by ν_μ disappearance experiments like CDHS, IceCube, MINOS/MINOS+, SK, DeepCore, MiniBooNE, NOνA [64].

The sterile neutrino hypothesis is further supported by the Gallium anomalies in GALLEX [65], SAGE [66] detectors where a deficiency of electron neutrinos were observed in experiments using ^{37}Ar and ^{51}Cr source respectively [67, 68, 69]. In addition, recalculation of the electron antineutrino spectra for ^{235}U, ^{239}Pu, ^{241}Pu and ^{238}U increased the fluxes of reactor antineutrino by 3% which created a shortage of the observed anti-neutrino events [70, 71, 72] known as the reactor antineutrino problem. This deficit cannot be explained by the standard three neutrino scenario and sterile neutrino hypothesis can be invoked to explain this.

In order to accommodate the eV^2 oscillation scale the simplest possibility is to add a sterile neutrino to the Standard Model. There are two possible ways this can be done (i) The 2+2 scenario in which the oscillation to sterile neutrino constitute the dominant solution either to solar or atmospheric neutrino anomaly and disfavoured from current data [73]. (ii) The 3+1 or 1+3 picture in which the sterile neutrino is separated by an eV^2 mass difference from the 3 active states [74]. 3+1 (1+3) corresponds to the 3 active states to be lighter (heavier). Cosmological constraints on sum of neutrino masses pose a serious challenge in accommodating an eV scale sterile neutrino scenario. To address these, scenarios like secret neutrino interactions [75] or lower reheating temperature [76, 77, 78] are proposed. The 1+3 picture is more disfavoured from cosmology since there are three heavier states. The 3+1 picture can provide an acceptable fit to the data [4, 79] albeit the tension between disappearance and appearance data. This tension is driven mainly by ν_μ disappearance data and the LSND appearance data [80] while the contribution from MiniBooNE appearance is subleading. The disappearance data which contribute to tension is from from CDHS and more recent experiments like IceCube, MINOS/MINOS+, SK, DeepCore, MiniBooNE, NOνA.

1.7 Thesis Overview

In this thesis we have studied the capability of the future long baseline experiments like DUNE, T2HK/T2HKK, ESSνSB to determine the unknown oscillation parameters. We have also studied the impact of partial $\mu - \tau$ flavour symmetry for neutrino mixing and the testability of the correlations predicted by this symmetry at DUNE and T2HK/T2HKK. We have also studied the impact of $\mu-\tau$ flavour symmetry in presence of light sterile neutrinos. Finally, we study sterile neutrinos and non-unitary mixing at a future short baseline experiment Neutrinos from STORed Muons (nuSTORM).

In chapter 2 we have discussed the derivation of the neutrino oscillation probabilities in vacuum as well as in presence of matter for two and three generations. Then we discuss the experimental evidence of neutrino oscillation in details followed by the current status of neutrino oscillation parameters. We analyze the parameter degeneracies affecting the unambiguous determination of the parameters. We also discuss salient features of the present and future accelerator neutrino experiments studied in this thesis.

In chapter 3 we examine the potential of the future experiments DUNE, T2HK/T2HKK, ESSνSB to determine the unknown oscillation parameters. We draw a thorough comparison of the sensitivities of these experiments. In particular, we do a comprehensive analysis of the octant discovery potential of all the set-ups by providing the underlying physics reasons explaining the differences in their sensitivities. Further, we give a detailed account of the underlying physics reasons which are causing differences in the octant sensitivity of these three experiments. Additionally, we also do a comparative analysis of the hierarchy and CP discovery.

The chapter 4 is dedicated to the study and consequences of partial $\mu-\tau$ symmetry in neutrino mixing matrix and its impact on the determination of the unknown neutrino oscillation parameters in a three neutrino framework. The partial $\mu - \tau$ symmetry predict interesting correlations connecting the oscillation parameters θ_{23} and δ_{CP}. We consider the testability of these relations at the DUNE and T2HK experiments.

Next we discuss implications of the $\mu - \tau$ symmetry in presence of a light sterile neutrinos in chapter 5. We discuss the various predictions in presence 3+1 neutrino mixing which provides additional constraints involving the three generation as well as sterile neutrino parameters. We study the experimental consequences at DUNE. Finally we explore the impact of $\mu-\tau$ symmetry for 3+1 neutrino mixing for neutrinoless double-β decay.

In chapter 6 we shift our focus to the proposed nuSTORM experiment. This plans to use neutrinos from muon decay with the primary aim to measure the neutrino-nucleon cross-sections with unprecedented precision. We consider possibility of probing beyond Standard Model physics at nuSTORM. The two scenarios that we consider are sterile neutrinos and non-unitarity of neutrino mixing matrix. We stress on the use of neutral current events.

Finally our work is summarized in chapter 7.

Chapter 2

Neutrino Oscillations

In this chapter we discuss the derivation of the probability of neutrino oscillations. As discussed in chapter 1 if the neutrinos have mass then flavour eigenstates and mass eigenstates are not the same but are connected by a mixing matrix. We start with the discussions on the neutrino mixing matrix and the parameters required to describe the neutrino mixing matrix. We present the derivation of the neutrino oscillations probability in vacuum in section 2.1 and in the presence of matter in section 2.2. Neutrino oscillation has been observed in many experiments and the oscillation parameters have been measured with considerable precision. The section 2.3 is dedicated to the past and present neutrino experiments which were crucial in determining the currently known parameters. We also discuss the current status of the oscillation parameters in section 2.4. The determination of the yet determined oscillation parameters face challenges due to degeneracies which will be discussed in the next section 2.5. In the final section 2.6 of the chapter we describe the present and future running neutrino oscillation experiments which have been studied in the thesis.

2.1 Neutrino Oscillations in Vacuum

2.1.1 Two generation propagation

For simplicity let us begin with the two generation case, let us take the first two neutrino generations $|\nu_e\rangle$ and $|\nu_\mu\rangle$ which will require two mass eigenstates $|\nu_1\rangle$ and $|\nu_2\rangle$. The

PMNS matrix for 2 generations can be parametrized with only one angle (θ). [1] The relationship between the flavor eigenstates and mass eigenstates can be written as:

$$\begin{pmatrix} \nu_e \\ \nu_\mu \end{pmatrix} = \begin{pmatrix} \cos\theta & \sin\theta \\ -\sin\theta & \cos\theta \end{pmatrix} \begin{pmatrix} \nu_1 \\ \nu_2 \end{pmatrix}. \tag{2.1}$$

The time evolution of the flavor eigenstates is given as:

$$|\nu_e\rangle = \cos\theta e^{-iE_1 t}|\nu_1\rangle + \sin\theta e^{-iE_2 t}|\nu_2\rangle \tag{2.2}$$

$$|\nu_\mu\rangle = -\sin\theta e^{-iE_1 t}|\nu_1\rangle + \cos\theta e^{-iE_2 t}|\nu_2\rangle \tag{2.3}$$

where, E_1 and E_2 are the energy eigenvalues of the free particle Hamiltonian of the mass eigenstates $|\nu_1\rangle$ and $|\nu_2\rangle$ respectively and can be expressed as,

$$E_i^2 = p_i^2 + m_i^2 \tag{2.4}$$

where, p_i^2 and m_i^2 are the momentum and mass of the mass eigenstate ν_i respectively.

In the case where $p_i >> m_i$, the above equation can be approximated as,

$$E_i \approx p_i + \frac{m_i^2}{2p}. \tag{2.5}$$

We proceed further considering a plane wave approximation [81] where all the states have been assumed to have same momentum

$$p \approx p_i >> \frac{m_i^2}{2p}. \tag{2.6}$$

[2]With the above approximation and utilizing the orthogonality of the mass eigenstates the survival probability of electron neutrino can be expressed as,

$$P_{ee} = |\langle\nu_e|\nu_e(t)\rangle|^2 \tag{2.7}$$

$$= (\cos^2\theta e^{-iE_1 t} + \sin^2\theta e^{-iE_2 t})(\cos^2\theta e^{iE_1 t} + \sin^2\theta e^{iE_2 t}) \tag{2.8}$$

[1] A discussion on parametrization of the PMNS matrix have been presented in the appendix A.

[2] A more realistic approach is the wave packet treatment of neutrino oscillations [82].

$$= \quad 1 - \sin^2 2\theta \sin^2\{(E_2 - E_1)t/2\}. \tag{2.9}$$

Also, in the relativistic limit $p \approx E$ and $t \approx L$ (for $c = 1$ and $\hbar = 1$) and we obtain

$$P_{ee} \quad = \quad 1 - \sin^2 2\theta \sin^2\{\Delta m^2_{21} L/4E\} \tag{2.10}$$

$$= \quad 1 - \sin^2 2\theta \sin^2\{1.27 \Delta m^2_{21} L/E\}, \tag{2.11}$$

where, $\Delta m^2_{21} = m^2_2 - m^2_1$ is in eV^2, L is in km and E is in GeV. Since, this is a two flavor approach the transition probability $\nu_e \to \nu_\mu$ obtained from Eq. 2.11 is,

$$P_{e\mu} \quad = \quad 1 - P_{ee} \tag{2.12}$$

$$= \quad \sin^2 2\theta \sin^2\{1.27 \Delta m^2_{21} L/E\}. \tag{2.13}$$

We can also arrive at the same result by Hamiltonian approach. In the mass basis the Schrödinger equation is written as

$$i\frac{\partial \nu_i}{\partial t} \quad = \quad H_M \nu_i, \tag{2.14}$$

Now, taking two generations

$$H_M = \begin{pmatrix} E_1 & 0 \\ 0 & E_2 \end{pmatrix}. \tag{2.15}$$

Using Eq. 2.5 one gets

$$H_M = EI + \frac{1}{2E}\begin{pmatrix} m^2_1 & 0 \\ 0 & m^2_2 \end{pmatrix}, \tag{2.16}$$

Any diagonal matrix just results in an overall phase which do not contribute to oscillation probabilities and one can write the propagation equations as,

$$i\frac{\partial}{\partial t}\begin{pmatrix} \nu_e \\ \nu_\mu \end{pmatrix} \quad = \quad H_F \begin{pmatrix} \nu_e \\ \nu_\mu \end{pmatrix}, \tag{2.17}$$

where, H_F is the Hamiltonian in the flavor basis which can be written as

$$H_F = U^\dagger \begin{pmatrix} m_1^2/2E & 0 \\ 0 & m_2^2/2E \end{pmatrix} U. \tag{2.18}$$

$$H_F = \frac{1}{4E} \begin{pmatrix} -\Delta m_{21}^2 \cos 2\theta & \Delta m_{21}^2 \sin 2\theta \\ \Delta m_{21}^2 \sin 2\theta & \Delta m_{21}^2 \cos 2\theta \end{pmatrix}, \tag{2.19}$$

The propagation equation now becomes

$$i\frac{\partial \nu_e}{\partial t} = -\frac{\Delta m_{21}^2 \cos 2\theta}{4E}\nu_e + \frac{\Delta m_{21}^2 \sin 2\theta}{4E}\nu_\mu, \tag{2.20}$$

$$i\frac{\partial \nu_\mu}{\partial t} = \frac{\Delta m_{21}^2 \sin 2\theta}{4E}\nu_e + \frac{\Delta m_{21}^2 \cos 2\theta}{4E}\nu_\mu. \tag{2.21}$$

The equations form a pair of coupled different equations. Such a pair of coupled differential equations as in eq. 2.20,2.21 has solutions of the from,

$$\nu_e(t) = A_1 e^{-i\omega t} + A_2 e^{i\omega t}, \tag{2.22}$$

$$\nu_\mu(t) = B_1 e^{-i\omega t} + B_2 e^{i\omega t}, \tag{2.23}$$

where, $|\nu_e(t)|^2 + |\nu_\mu(t)|^2 = 1$ due to unitarity and $\omega^2 = \left(\frac{\Delta m_{21}^2}{4E}\right)^2$. Let us take the case where we produce ν_e and then study the time evolution. This will provide us with the following initial conditions, at $t = 0$, $\nu_e(0) = 1$ and $\nu_\mu(0) = 0$. Which gives,

$$A_1 = \sin^2\theta,\ A_2 = \cos^2\theta,\ B_1 = \sin\theta\cos\theta,\ B_2 = -\sin\theta\cos\theta. \tag{2.24}$$

The transition probability $\nu_e \to \nu_\mu$ becomes,

$$P_{e\mu} = |\nu_\mu(t)|^2 = \sin^2 2\theta \sin^2\{1.27\Delta m_{21}^2 L/E\}. \tag{2.25}$$

In the eq. 2.25 $\sin^2 2\theta$ denotes the amplitude of oscillations while the oscillatory term is $\sin^2\{1.27\Delta m_{21}^2 L/E\}$. The above probability equation can also be written in terms of the oscillation wavelength(λ_{osc}) as,

$$P_{e\mu} = |\nu_\mu(t)|^2 = \sin^2 2\theta \sin^2\{\pi L/\lambda_{osc}\}. \tag{2.26}$$

from which the λ_{osc} can be calculated to be,

$$\lambda_{osc} = 2.47 \frac{E}{\text{GeV}} \frac{\text{eV}^2}{\Delta m^2_{21}} \text{ km}. \tag{2.27}$$

The condition $\lambda_{osc} = 2L$, represents the first oscillation maxima, i.e. the oscillatory term $\sin^2 2\theta \sin^2\{\pi L/\lambda_{osc}\} = 1$. When $\lambda_{osc} >> L$, $\sin^2 2\theta \sin^2\{\pi L/\lambda_{osc}\} \to 0$, which means that the oscillation has not yet developed. For $\lambda_{osc} << L$, $\sin^2 2\theta \sin^2\{\pi L/\lambda_{osc}\} \to 1/2$, rapid oscillations occur so, the oscillations average out.

2.1.2 Generalized N generation propagation

We derive the generalized N generation oscillation probability in vacuum. $N \times N$ dimensional unitary matrix requires $N(N-1)/2$ mixing angles and $(N-1)(N-2)/2$ phases. Similar to the two generations case the relationship between the flavour and mass eigenstates can be written as [3],

$$|\nu_\alpha\rangle = \sum_{i=1}^{N} U^*_{\alpha i} |\nu_i\rangle. \tag{2.28}$$

Then the oscillation probability $P_{\alpha\beta}$ which signifies the oscillation probability from initial state $|\nu_\alpha\rangle$ to final state $|\nu_\beta\rangle$ is $|\langle\nu_\alpha|\nu_\beta\rangle|^2$. This can be calculated as,

$$P_{\alpha\beta} = |\langle\nu_\beta|\nu_\alpha\rangle(t)|^2 . \tag{2.29}$$

Using the orthogonality of mass states we obtain,

$$P_{\alpha\beta} = \left| \sum_{i=1}^{N} U^*_{\alpha i} U_{\beta i} e^{-iE_i t} \right|^2 \tag{2.30}$$

[3] The fields in the leptonic charged current weak interaction Lagrangian transform as U and states transform as U^*

$$
\begin{aligned}
&= \sum_{i=1}^{N}\sum_{j=1}^{N}(U^*_{\alpha i}U_{\beta i}e^{-iE_it})(U_{\alpha j}U^*_{\beta j}e^{iE_jt}) && (2.31)\\
&= \sum_{i=j}|U_{\alpha i}|^2|U_{\beta i}|^2 + \sum_{i\neq j}U^*_{\alpha i}U^*_{\beta j}U_{\alpha j}U_{\beta i}e^{-i(E_i-E_j)t}. && (2.32)
\end{aligned}
$$

We know that,

$$
\left|\sum_i U^*_{\alpha i}U_{\beta i}\right|^2 = \sum_i |U_{\alpha i}|^2|U_{\beta i}|^2 + \sum_{i\neq j}U^*_{\alpha i}U^*_{\beta j}U_{\alpha j}U_{\beta i}, \tag{2.33}
$$

utilizing the above relationship in Eq. 2.32 we obtain,

$$
\begin{aligned}
P_{\alpha\beta} = &\left|\sum_i U^*_{\alpha i}U_{\beta i}\right|^2 - \sum_{i\neq j}U^*_{\alpha i}U^*_{\beta j}U_{\alpha j}U_{\beta i} && (2.34)\\
&+ \sum_{i\neq j}U^*_{\alpha i}U^*_{\beta j}U_{\alpha j}U_{\beta i}e^{-i(E_i-E_j)t}.
\end{aligned}
$$

Using the unitary property of the mixing matrix, the probability can be expressed as

$$
\begin{aligned}
P_{\alpha\beta} = \; &\delta_{\alpha\beta} - 2\sum_{i>j}\mathrm{Re}\big(U^*_{\alpha i}U^*_{\beta j}U_{\alpha j}U_{\beta i}\big) && (2.35)\\
&+ 2\sum_{i>j}\mathrm{Re}\big(U^*_{\alpha i}U^*_{\beta j}U_{\alpha j}U_{\beta i}\big)\cos(E_i-E_j)t\\
&+ 2\sum_{i>j}\mathrm{Im}\big(U^*_{\alpha i}U^*_{\beta j}U_{\alpha j}U_{\beta i}\big)\sin(E_i-E_j)t.
\end{aligned}
$$

Using the plane wave approximation eq. 2.5,2.6 the oscillation probability can be expressed as

$$
\begin{aligned}
P_{\alpha\beta} = \; &\delta_{\alpha\beta} - 4\sum_{i>j}\mathrm{Re}\big(U^*_{\alpha i}U^*_{\beta j}U_{\alpha j}U_{\beta i}\big)\sin^2\{\Delta m^2_{ij}L/4E\} && (2.36)\\
&+ 2\sum_{i>j}\mathrm{Im}\big(U^*_{\alpha i}U^*_{\beta j}U_{\alpha j}U_{\beta i}\big)\sin\{2\Delta m^2_{ij}L/4E\},
\end{aligned}
$$

where $\Delta m^2_{ij} = m^2_i - m^2_j$.

2.2 Neutrino oscillations in matter

Neutrinos interact with the electrons, protons and neutrons present in matter via coherent charged current and neutral current scattering, this leads to an effective potential which is encountered by the neutrino. The oscillations probability in matter is modified due to the effective potential.

2.2.1 Effective potential for neutrino propagation in matter

Neutrinos interact with matter through coherent forward elastic charge current scattering and neutral current scattering. Matter is composed of electrons, protons and neutrons so, only ν_e takes part in charged current scattering while all flavours of neutrinos take part in neutral current scattering with electrons, protons and neutrons. The neutral current interaction affects all the neutrino flavours identically and hence, NC interaction will add an overall phase which is irrelevant for the oscillation probability. On the other hand CC interaction only affects ν_e hence it will be significant for the oscillation probabilities. The Hamiltonian for the CC interaction is given by,

$$H_{\text{eff}} = \frac{G_F}{\sqrt{2}} \left[\bar{e}\gamma_\mu(1-\gamma_5)\nu_e\right]\left[\bar{\nu}_e\gamma^\mu(1-\gamma_5)e\right], \tag{2.37}$$

where G_F is the Fermi constant. By performing Fierz transformation we get,

$$H_{\text{eff}} = \frac{G_F}{\sqrt{2}} \left[\bar{e}\gamma_\mu(1-\gamma_5)e\right]\left[\bar{\nu}_e\gamma^\mu(1-\gamma_5)\nu_e\right]. \tag{2.38}$$

The interaction potential is obtained by the averaging the effective Hamiltonian over the electron background i.e.,

$$\overline{H}_{\text{eff}} = \frac{G_F}{\sqrt{2}} \langle\bar{e}\gamma_\mu(1-\gamma_5)e\rangle\left[\bar{\nu}_e\gamma^\mu(1-\gamma_5)\nu_e\right]. \tag{2.39}$$

In the non-relativistic limit from the explicit forms of Dirac spinors it can be shown that [83, 84],

$$\langle\bar{e}\gamma_\mu\gamma_5 e\rangle \quad \sim \quad \text{spin}, \tag{2.40}$$

$$\langle \bar{e}\gamma_i e\rangle \sim \text{velocity}, \tag{2.41}$$

$$\langle \bar{e}\gamma_0 e\rangle = N_e, \tag{2.42}$$

here, N_e represents the number density of electrons of the medium. The velocity and the average spin of electrons vanishes in the rest frame of unpolarized electrons and only surviving term is N_e term so, we obtain,

$$\begin{aligned} \overline{H}_{\text{eff}} &= \sqrt{2}G_F N_e \bar{\nu}_{eL}\gamma^0\nu_{eL} && (2.43)\\ &= v_{CC}\bar{\nu}_{eL}\gamma^0\nu_{eL} && (2.44)\\ &= v_{CC}j_\nu. \end{aligned}$$

where $\nu_{eL} = \dfrac{1-\gamma_5}{2}\nu_e$, $j_\nu = \bar{\nu}_{eL}\gamma^0\nu_{eL}$ and v_{CC} is the interaction potential given by

$$v_{CC} = \sqrt{2}G_F N_e. \tag{2.45}$$

To calculate the effective potential for anti-neutrinos the charge conjugate field ν^C_{eL} needs to be considered:

$$\begin{aligned} j^C_\nu &= \bar{\nu}^C_{eL}\gamma^0\nu^C_{eL} && (2.46)\\ &= -\nu^T_{eL}C^{-1}\gamma^0 C\bar{\nu}^T_{eL}, && (2.47) \end{aligned}$$

where C is the charge conjugation operator. We have used the fact that,

$$\nu^C_{eL} = C\bar{\nu}^T_{eL}, \tag{2.48}$$

$$\bar{\nu}^C_{eL} = -\nu^T_{eL}C^{-1}. \tag{2.49}$$

Using the property

$$C^{-1}\gamma^0 C = (-\gamma^0)^T, \tag{2.50}$$

we obtain,

$$j_\nu^C = \nu_{eL}^T(\gamma^0)^T\bar{\nu}_{eL}^T \tag{2.51}$$

$$= -\bar{\nu}_{eL}\gamma^0\nu_{eL}, \tag{2.52}$$

and the effective Hamiltonian for antineutrinos can be expressed as,

$$\overline{H}_{\text{eff}} = -\sqrt{2}G_F N_e \bar{\nu}_{eL}\gamma^0\nu_{eL}, \tag{2.53}$$

which gives,

$$\bar{v}_{CC} = -\sqrt{2}G_F N_e. \tag{2.54}$$

2.2.2 Neutrino propagation in matter : Two flavour case

The time evolution equation in the presence of matter is given by,

$$i\frac{\partial}{\partial t}\begin{pmatrix}\nu_e \\ \nu_\mu\end{pmatrix} = H_{eff}^{\text{matt}}\begin{pmatrix}\nu_e \\ \nu_\mu\end{pmatrix}, \tag{2.55}$$

with

$$H_{eff}^{\text{matt}} = \begin{pmatrix} -\frac{\Delta m_{21}^2}{4E}\cos 2\theta + \frac{A}{2E} & \frac{\Delta m_{21}^2}{4E}\sin 2\theta \\ \frac{\Delta m_{21}^2}{4E}\sin 2\theta & \frac{\Delta m_{21}^2}{4E}\cos 2\theta \end{pmatrix}. \tag{2.56}$$

where,

$$A = 2Ev_{cc} = 2\sqrt{2}G_F N_e E = 7.6\times 10^{-5}\left[\frac{\rho}{\text{gm/cc}}\right]\left[\frac{E}{\text{GeV}}\right]\text{eV}^2. \tag{2.57}$$

where, ρ signifies the matter density of the medium in gm/cc. Any matrix proportional to identity matrix does not alter the oscillation probabilities hence we subtract $\frac{A}{4E}$ from the diagonal elements, the and eq. 2.56 simplifies to,

$$H_{eff}^{\text{matt}} = \frac{1}{4E}\begin{pmatrix} A - \Delta m_{21}^2 \cos 2\theta & \Delta m_{21}^2 \sin 2\theta \\ \Delta m_{21}^2 \sin 2\theta & -A + \Delta m_{21}^2 \cos 2\theta \end{pmatrix}. \tag{2.58}$$

The energy eigenvalues are obtained as,

$$E_1 = \frac{1}{4E}\left[A + \sqrt{(-A + \Delta m_{21}^2 \cos 2\theta)^2 + (\Delta m_{21}^2 \sin 2\theta)^2}\right]. \tag{2.59}$$

$$E_2 = \frac{1}{4E}\left[A - \sqrt{(-A + \Delta m_{21}^2 \cos 2\theta)^2 + (\Delta m_{21}^2 \sin 2\theta)^2}\right]. \tag{2.60}$$

By using the plane wave approximation as discussed earlier $E_2 - E_1 = (m_2^2 - m_1^2)/2E$, and the modified mass squared difference in presence of matter becomes,

$$\Delta_M m_{21}^2 = \sqrt{(-A + \Delta m_{21}^2 \cos 2\theta)^2 + (\Delta m_{21}^2 \sin 2\theta)^2}. \tag{2.61}$$

Denoting the diagonalizing matrix as U_M, the Hamiltonian in matter mass basis and flavour basis are related as,

$$H_M^{\text{matt}} = U_M^\dagger H_{eff}^{\text{matt}} U_M \tag{2.62}$$

where the mixing matrix will be composed of the modified mixing angles in matter as,

$$\begin{pmatrix} \cos\theta_M & \sin\theta_M \\ -\sin\theta_M & \cos\theta_M \end{pmatrix} \tag{2.63}$$

The modified mixing angle are given by,

$$\tan 2\theta_M = \frac{\Delta m_{21}^2 \sin 2\theta}{-A + \Delta m_{21}^2 \cos 2\theta}. \tag{2.64}$$

For constant matter density the probability can be written as,

$$P_{e\mu} = \sin^2 2\theta_M \sin^2(1.27\Delta_M m_{21}^2 L/E). \tag{2.65}$$

The MSW effect

From eq. 2.64 it can be understood that, under the condition,

$$\Delta m^2_{21} \cos 2\theta \quad = \quad A \tag{2.66}$$

$\tan 2\theta_M \to \infty$, which leads to $\theta_M = \dfrac{\pi}{4}$ and $\sin 2\theta_M \to 1$ so the oscillation amplitude is maximum. The maximum flavor conversion of a neutrino flavor into another due to matter effect is called the Mikheyev-Smirnov-Wolfenstein (MSW) resonance[85, 86]. The resonance condition in eq. 2.66 in case of neutrinos and antineutrinos are,

- Case 1: Neutrinos, $A > 0$ and this condition is only possible if
  1. $\Delta m^2_{21} > 0$ and $\theta < \dfrac{\pi}{4}$ or,
  2. $\Delta m^2_{21} < 0$ and $\theta > \dfrac{\pi}{4}$.
- Case 2: Antineutrinos, $A < 0$, the condition modifies to,
  1. $\Delta m^2_{21} > 0$ and $\theta > \dfrac{\pi}{4}$ or,
  2. $\Delta m^2_{21} < 0$ and $\theta < \dfrac{\pi}{4}$.

2.2.3 Neutrino propagation in matter : Three flavor case

In this case the analytical expansions of the probabilities are not straightforward. Therefore, it is required to use certain approximations to obtain the probabilities to study the nature of the neutrino oscillations in various experiments depending of the baseline and neutrino energy. Two approximations have been used widely, (i) The one mass scale dominance (OMSD) [87] approximation which uses the fact that $\Delta m^2_{21} << \Delta m^2_{31}$ and is applicable for $\dfrac{\Delta m^2_{21} L}{E} << 1$. (ii) The $\alpha - s_{13}$ approximation, which is series expansion in terms of the parameters α ($\alpha = \dfrac{\Delta m^2_{21}}{\Delta m^2_{31}} << 1$) and s_{13} ($\sin\theta_{13} << 1$). This approximation is valid for the long baseline experiments ($L \sim 100 - 1000$ km) where, the oscillation is governed by the Δm^2_{31} mass-squared difference. For the experimental setups considered in this thesis the $\alpha - s_{13}$ approximation can provide the analytical probabilities. This is discussed in the next part in detail.

Series Expansion (α-s_{13} approximation)

In this method the probabilities are expanded about the smallest parameters α and s_{13} [88]. The effective Hamiltonian can be written as

$$H_{eff}^{\text{matt}} = U \begin{pmatrix} 0 & 0 & 0 \\ 0 & \Delta m_{21}^2/2E & 0 \\ 0 & 0 & \Delta m_{31}^2/2E \end{pmatrix} U^{\dagger} + \begin{pmatrix} \sqrt{2}G_F N_e & 0 & 0 \\ 0 & 0 & 0 \\ 0 & 0 & 0 \end{pmatrix}. \tag{2.67}$$

The Hamiltonian can be rewritten as

$$H_{eff}^{\text{matt}} = \frac{\Delta m_{31}^2}{2E}\left[U\text{diag}(0,\alpha,1)U^{\dagger} + \text{diag}(\hat{A},0,0)\right], \tag{2.68}$$

where $\hat{A} = A/\Delta m_{31}^2$, $A = 2\sqrt{2}G_F N_e E$, $\alpha = \dfrac{\Delta m_{21}^2}{\Delta m_{31}^2}$.
One can further write,

$$H_{eff}^{\text{matt}} = \frac{\Delta m_{31}^2}{2E} R_{23} U_{\delta} \tilde{H} U_{\delta}^{\dagger} R_{23}^T, \tag{2.69}$$

in terms of $\tilde{H}$ which is defined by separating the CP violating phases and the rotation matrix R_{23}. This can be performed because $U_{\delta} = \text{diag}(1, 1, e^{i\delta_{CP}})$ and R_{23} commute with the matter potential matrix (diag$(\hat{A}, 0, 0)$). Next we define $H_{eff}^{\prime\text{matt}}$ in terms of $\tilde{H}$ as,

$$\begin{aligned} H_{eff}^{\prime\text{matt}} &= \frac{\Delta m_{31}^2}{2E}\tilde{H} && (2.70) \\ &= \frac{\Delta m_{31}^2}{2E}\left[R_{13}R_{12}\text{diag}(0,\alpha,1)R_{12}^T R_{13}^T + \text{diag}(\hat{A},0,0)\right] && (2.71) \\ &= \frac{\Delta m_{31}^2}{2E}\begin{pmatrix} s_{12}^2 c_{13}^2\alpha + s_{13}^2 + \hat{A} & \alpha c_{12}c_{13}s_{12} & s_{13}c_{13}(1-\alpha s_{12}^2) \\ s_{12}c_{12}c_{13}\alpha & \alpha c_{12}^2 & -\alpha c_{12}s_{12}s_{13} \\ s_{13}c_{13}(1-\alpha s_{12}^2) & -s_{12}c_{12}s_{13}\alpha & \alpha s_{12}^2 s_{13}^2 + c_{13}^2 \end{pmatrix} && (2.72) \end{aligned}$$

$\tilde{H}$ in the above equation can be written in the form because U_{δ} commutes with R_{12} and diag$(0, \alpha, 1)$. The eigenstates and eigenvalues are calculated by perturbative diagonalization of the Hamiltonian to second order in α and s_{13}

$$\tilde{H} = \tilde{H}^{(0)} + \tilde{H}^{(1)} + \tilde{H}^{(2)}, \tag{2.73}$$

where

$$\tilde{H}^{(0)} = \text{diag}(\hat{A}, 0, 1) = \text{diag}(\lambda_1^{(0)}, \lambda_2^{(0)}, \lambda_3^{(0)}), \tag{2.74}$$

$$\tilde{H}^{(1)} = \begin{pmatrix} \alpha s_{12}^2 & \alpha s_{12} c_{12} & s_{13} \\ \alpha s_{12} c_{12} & \alpha c_{12}^2 & 0 \\ s_{13} & 0 & 0 \end{pmatrix}, \tag{2.75}$$

$$\tilde{H}^{(2)} = \begin{pmatrix} s_{13}^2 & 0 & -\alpha s_{13} s_{12}^2 \\ 0 & 0 & -\alpha s_{13} s_{12} c_{12} \\ -\alpha s_{13} s_{12}^2 & -\alpha s_{13} s_{12} c_{12} & -s_{13}^2 \end{pmatrix}. \tag{2.76}$$

The eigenvalues and the eigenvectors are written as

$$\lambda_i = \lambda_i^{(0)} + \lambda_i^{(1)} + \lambda_i^{(2)}, \tag{2.77}$$

$$v_i = v_i^{(0)} + v_i^{(1)} + v_i^{(2)}. \tag{2.78}$$

As $\tilde{H}^{(0)}$ is diagonal,

$$v_i^{(0)} = e_i, \tag{2.79}$$

i.e.,

$$v_1^{(0)} = \begin{pmatrix} 1 \\ 0 \\ 0 \end{pmatrix}, \quad v_2^{(0)} = \begin{pmatrix} 0 \\ 1 \\ 0 \end{pmatrix}, \quad v_3^{(0)} = \begin{pmatrix} 0 \\ 0 \\ 1 \end{pmatrix}. \tag{2.80}$$

The corrections to the eigenvalues and eigenvectors for first and second order are given as,

$$\lambda_i^{(1)} = \tilde{H}_{ii}^{(1)} = \langle v_i^{(0)} | \tilde{H}^{(1)} | v_i^{(0)} \rangle, \tag{2.81}$$

$$\lambda_i^{(2)} = \tilde{H}_{ii}^{(2)} + \sum_{j \neq i} \frac{(\tilde{H}_{ij}^{(1)})^2}{\lambda_i^{(0)} - \lambda_j^{(0)}}, \tag{2.82}$$

$$v_i^{(1)} = \sum_{j \neq i} \frac{\tilde{H}_{ij}^{(1)}}{\lambda_i^{(0)} - \lambda_j^{(0)}} e_j, \tag{2.83}$$

$$v_i^{(2)} = \sum_{j \neq i} \frac{1}{\lambda_i^{(0)} - \lambda_j^{(0)}} \big[\tilde{H}_{ij}^{(2)} + (\tilde{H}^{(1)} v_i^{(1)})_j - \lambda_i^{(1)} (v_i^{(1)})_j\big] e_j. \tag{2.84}$$

As, $E_i = \dfrac{\Delta m_{31}^2}{2E} \lambda_i$. The energy eigenvalues are

$$E_1 = \frac{\Delta m_{31}^2}{2E} \big(\hat{A} + \alpha s_{12}^2 + s_{13}^2 \frac{\hat{A}}{\hat{A}-1} + \alpha^2 \frac{\sin^2 2\theta_{12}}{4\hat{A}}\big), \tag{2.85}$$

$$E_2 = \frac{\Delta m_{31}^2}{2E} \big(\alpha c_{12}^2 - \alpha^2 \frac{\sin^2 2\theta_{12}}{4\hat{A}}\big), \tag{2.86}$$

$$E_3 = \frac{\Delta m_{31}^2}{2E} \big(1 - s_{13}^2 \frac{\hat{A}}{\hat{A}-1}\big), \tag{2.87}$$

the eigenvectors are

$$v_1 = \begin{pmatrix} 1 \\ \dfrac{\alpha \sin 2\theta_{12}}{2\hat{A}} + \dfrac{\alpha^2 \sin 4\theta_{12}}{4\hat{A}^2} \\ \dfrac{s_{13}}{\hat{A}-1} - \dfrac{\hat{A}\alpha s_{13} s_{12}^2}{(\hat{A}-1)^2} \end{pmatrix}, \tag{2.88}$$

$$v_2 = \begin{pmatrix} -\frac{\alpha\sin 2\theta_{12}}{2\hat{A}} - \frac{\alpha^2\sin 4\theta_{12}}{4\hat{A}^2} \\ 1 \\ \frac{\alpha s_{13}\sin 2\theta_{12}(\hat{A}+1)}{2\hat{A}} \end{pmatrix},$$

$$\text{and} \quad v_3 = \begin{pmatrix} -\frac{s_{13}}{\hat{A}-1} + \frac{\hat{A}\alpha s_{13}s_{12}^2}{(\hat{A}-1)^2} \\ \frac{\hat{A}\alpha s_{13}\sin 2\theta_{12}}{2(\hat{A}-1)} \\ 1 \end{pmatrix}.$$

The modified mixing matrix in matter is:

$$U_M = R_{23}U_\delta W, \tag{2.89}$$

with $W = (v_1, v_2, v_3)$. For instance the probabilities $P_{\mu e}$ and $P_{\mu\mu}$ can be expressed as,

$$\begin{aligned} P_{\mu e} &= 4s_{13}^2 s_{23}^2 \frac{\sin^2(\hat{A}-1)\Delta}{(\hat{A}-1)^2} \qquad (2.90) \\ &+ 2\alpha s_{13}\sin 2\theta_{12}\sin 2\theta_{23}\cos(\Delta+\delta_{CP})\frac{\sin\hat{A}\Delta}{\hat{A}}\frac{\sin(\hat{A}-1)\Delta}{\hat{A}-1} \\ &+ \alpha^2\sin^2 2\theta_{12}c_{23}^2\frac{\sin^2\hat{A}\Delta}{\hat{A}^2}, \\ P_{\mu\mu} &= 1-\sin^2 2\theta_{23}\sin^2\Delta + \text{higher order terms}, \qquad (2.91) \end{aligned}$$

where, $\Delta = \Delta m_{31}^2/4E$. The above probabilities are probed in the experiments to observe neutrino oscillations which we will discuss in the next section.

2.3 Observation of neutrino oscillations

The Solar Neutrino Problem

In the 1964 Raymond Davis Jr. and John Bachall designed an experiment to test whether the fusion of hydrogen to helium was the source of energy generated in the Sun. If indeed the energy of the Sun was due to the above process the neutrinos should also be emitted from the Sun simultaneously. The experiment used 100,000 gallon of C_2Cl_4 to detect the neutrinos. The experiment was based on the process:

$$\nu_e + {}^{37}Cl \rightarrow {}^{37}Ar + e^-, \tag{2.92}$$

and is only sensitive to the electron neutrinos. The tank was kept at the Homestake mine in USA at depth of 1478 m.The counting was done by the radioactive decay of the chemically extracted Argon. These type of experiments are called radiochemical experiment.

John Bahcall calculated the interaction rate of the neutrinos at the experiment. But, when the result was announced in 1968 the number of neutrinos detected was around 1/3rd of the number predicted. This discrepancy is called the “solar neutrino problem”.

The “solar neutrino problem” was further confirmed by real time detectors like Kamiokande [89] a water Čerenkov detector. The detector used neutrino electron scattering to detect the neutrinos. Kamiokande verified the source of the neutrinos to be the Sun. Later many Gallium based experiments which were sensitive to the pp neutrinos like GALLEX [90], SAGE [66] and GNO [91] also observed this discrepancy in the solar neutrino flux. Later the upgraded version the Kamiokande detector the Super-kamiokande confirmed the same deficit with better statistics [92].

The solution of this problem became a challenge and various attempts were made to solve this problem which includes some model independent solutions [93, 94, 95, 96, 97], some soulutions also suggested the solar model to be incorrect [98, 99, 100]. Neutrino oscillations was also one of the proposed solutions to the problem.

The “solar neutrino problem” finally found a conclusive solution when SNO (Sudbury neutrino observatory) a heavy water based experiment declared their result [101, 102]. SNO could detect both CC and NC interactions hence, they could observe the CC interaction by electron neutrinos and NC events from all the three flavors of neutrinos. An important diagnostic for this experiment was the CC/NC ratio. If from sun only solar electron neutrinos are coming then this ratio should be 1. However if they get converted to other flavours then this ratio should be less than 1 since all flavours can take part in NC interactions. Since, the experiment found the CC/NC ratio to be

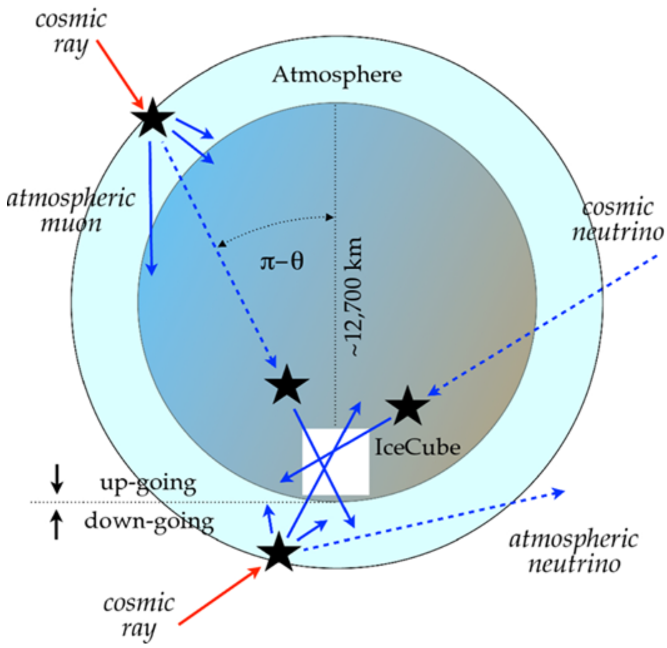

Figure 2.1: The figure describes the zenith angle dependence of the oscillation length. The neutrinos created in the atmosphere just above the detector are the downward going neutrinos which only travels through the atmosphere without encountering any Earth's matter. While the neutrinos created diametrically opposite travels the entire Earth before being detected at the detector are the upward going neutrinos. Image from [10].

around 1/3, it confirmed the presence of other neutrinos in the flux of solar ν_es. These results confirmed the fact that neutrinos oscillate when propagating from Sun to the Earth. SNO also measured the total ^8B flux and confirmed the Standard Solar Model predictions.

Atmospheric Neutrino Anomaly

The Kolar Gold Mine experiment [103] was the first to observe the atmospheric neutrinos. At the same time a gold mine in South Africa [104] also detected the same. Over the time many experiments were set up like Kamiokande [105] a water Čerenkov detector, IMB(Irvine-Michigan-Brookhaven detector) [106, 107] and Sudan2 [108] an iron calorimeter detector. These experiments measured the double ratio R to minimize the uncertainties in the absolute flux. The ratio R is given by:

$$R = \frac{(N_\mu/N_e)_{\text{obs}}}{(N_\mu/N_e)_{\text{MC}}} \tag{2.93}$$

where, MC denotes the expectations from monte-carlo simulation. The double ratio R was measured to be much much less than one. This discrepancy came to be known as the "Atmospheric Neutrino Anomaly" which could be explained by $\nu_\mu \to \nu_e$ and $\nu_\mu \to \nu_\tau$ oscillations. However, the experiments like Frejus [109, 110] and Nusex [111] did not observe this discrepancy. The "Atmospheric Neutrino Anomaly" was resolved when Super-Kamiokande [112], an upgraded version of the Kamiokande detector with a higher fiducial volume observed the zenith angle dependence of the neutrino flux. The atmospheric neutrino flux in multi-GeV range is predicted to be spherically symmetric. SK experiments observed a zenith angle dependence in multi-GeV atmospheric neutrino flux. This is explained by the fact that the oscillation length of the neutrinos is much larger than the height of the atmosphere so the downward going neutrinos are observed with the same ratio of flux as produced. But, the upward going neutrinos travels through the diameter of the earth so they undergo oscillations as described in the fig. 2.1.

Reactor Neutrino Experiments

Reactor neutrino are produced through β-decay during nuclear fission giving $\bar{\nu}_e$. The reactor neutrino experiments searches for the disappearance of $\bar{\nu}_e$ through inverse beta decay. Over the time several reactor neutrino oscillation experiments like ILL-Grenoble [113], Rovno [114], Savannah River [115], Gosgen [116], Krasnoyarsk [117], BUGEY [118] were unsuccessful in detecting neutrino oscillations at a distance <100 m from the reactor. Later, experiments like CHOOZ [119, 120] and Palo Verde [121, 122] unsuccessfully searched for evidence of neutrino oscillations through reactor neutrinos at a distance of 1 km. CHOOZ and Palo Varde were sensitive to θ_{13} and hence the angle θ_{13} came to be known as the reactor mixing angle. These experiments provided a bound on the mixing angle θ_{13} because of non-observance of oscillation.

KamLAND [123] was the first experiment to observe neutrino oscillation via reactor anti-neutrinos. The oscillations observed by KamLAND was very important because they could observe the oscillation due to the solar neutrino mass squared difference using a source on Earth. The baseline of KamLAND was 180 km which is ideal to probe the mass-squared difference of the order of $\sim 10^{-5}\mathrm{eV}^2$.

The reactor neutrino experiments like Double-CHOOZ [124], RENO [125] and Daya Bay [126] with baselines of the order of a few kilometers have been able to observe the oscillations due to the atmospheric mass-squared difference $\sim 10^{-3}\mathrm{eV}^2$. These experiments were pioneer in establishing the non-zero θ_{13}.

Accelerator Neutrino Experiments

Accelerator neutrino experiments are a powerful tool to study neutrino oscillations because the neutrino are artificially produced and their energies and fluxes are well known. The neutrino beam with the desired energy can be produced by the accelerator depending on the goal of the experiment.

Accelerator neutrinos beams are created from the decays of charged π and K mesons.These mesons are created when high energy proton beams are bombarded in thick nuclear targets. spectrum. As a result of the collisions numerous pions and kaons are formed. The energy of the proton beam projected can be varied which provide a precise handle to create the desired neutrino energy. These pions can be allowed to decay by two methods which are decay at rest (DAR) and decay in flight (DIF). In the DAR method the π^+ are brought to rest and then they decay via

$$\pi^+ \to \nu_\mu + \mu^+$$

$$\mu^+ \to \nu_e + e^+ + \bar{\nu}_\mu$$

while the π^- are absorbed. The ν_μ thus generated from the π^+ decay is monoenergetic with an energy of 29.8 MeV because it is a two body decay. The successive three body decay of the μ^+ which also decays at rest produces the ν_e and $\bar{\nu}_\mu$ with continuous energies upto 52.8 MeV.

In DIF the particles are passed through a decay tunnel after directing them through magnetic horns which sorts the charged particles according to their charges. The branching ratio of muon-neutrino is high because the production of electron-neutrino is helicity suppressed. For example the decay of π^+ and π^- are as follows:

$$\pi^+ \to \nu_\mu + \mu^+(\mu^+ \to \nu_e + e^+ + \bar{\nu}_\mu)$$

$$\pi^- \to \bar{\nu}_\mu + \mu^-(\mu^- \to \bar{\nu}_e + e^- + \nu_\mu).$$

The neutrinos from DIF can have energy from few tens of MeV to a few GeV. So, neutrinos from DIF can be utilized to design experiments over a range of energies.

In last few decades several accelerator neutrino experiments were able to observe neutrino oscillations. Past long baseline experiments like MINOS [127], K2K [128] have been successful in observing neutrino oscillations using neutrinos beam produced by decay in flight (DIF) mechanism. Both the experiments have neutrino beams of energy $\sim$ GeV and baselines of several hundred kilometers. The K2K experiments studied the $\nu_\mu \to \nu_\mu$ disappearance channel while MINOS looked at both $\nu_\mu \to \nu_\mu$ disappearance and $\nu_\mu \to \nu_e$ appearance channels. Both experiment confirmed oscillations driven by atmospheric mass-squared difference of 10^{-3}eV^2.

The ongoing long baseline experiments Tokai to Kamioka (T2K) [129, 130, 131] in Japan and NuMI Off-axis ν_e Appearance (NOνA) experiment [132, 133, 134] at Fermilab are also currently taking data and have observed neutrino oscillation in both the appearance and disappearance channels in both neutrino and anti-neutrino modes.

The accelerator neutrino experiments like LSND [59] and MiniBooNE [60, 61, 135] are also responsible for some unsolved anomalies in the neutrino data. The LSND experiment utilized DAR neutrinos in the neutrino mode to study the $\nu_\mu \to \nu_e$ channel and DIF neutrinos on the anti-neutrino mode for the $\bar{\nu}_\mu \to \bar{\nu}_e$. MiniBooNE experiment was designed to test the LSND anomaly. This has same L/E as LSND but the energy and baseline length are different. MiniBooNE has confirmed the LSND anomaly with both neutrino as well as anti-neutrinos.

2.4 Current Status of Neutrino Oscillation Parameters

Over the years there has been excellent progress by several neutrino oscillations experiments to determine the three generation neutrino oscillation parameters with remarkable precision. The three neutrino oscillation is governed by two mass-squared differences (Δm^2_{21}, Δm^2_{31}), three mixing angles (θ_{12}, θ_{13}, θ_{23}) and one CP violating phase (δ_{CP}). The parameters θ_{12} and Δm^2_{21} were measured by the data from solar neutrino experiments and KamLAND reactor experiment [136]. The mixing angle θ_{13} has been well measured by the reactor experiments Daya-Bay [126], RENO [137] and Double-CHOOZ [124]. The atmospheric neutrino experiments and MINOS [138] measured θ_{23} and $|\Delta m^2_{31}|$, these parameters are currently being probed by T2K [139] and NOνA [140]. The current best-fit values are presented in the tab. 2.1.

The current unknowns in the neutrino oscillations scenario are as follows:

1. **Mass Hierarchy:** It refers to the sign of the parameter Δm^2_{31} which has the following two possibilities as shown in fig. 1.3:

   - Normal Hierarchy (NH):

   $$m_3 >> m_2 > m_1$$

   $$\Delta m^2_{21} > 0, \quad \Delta m^2_{31} > 0$$

   - Inverted Hierarchy (IH):

   $$m_2 > m_1 >> m_3$$

   $$\Delta m^2_{21} > 0, \quad \Delta m^2_{31} < 0$$

   The sign of Δm^2_{21} was determined from solar matter effects while the magnitude is determined by the KamLAND data. The atmospheric neutrino and accelerator experiments measured the value $|\Delta m^2_{31}|$ quite precisely but determination the sign of Δm^2_{31} requires large matter effect as well as high statistics from the experiments. The current global analysis prefers NH . However, the recent NOνA data weakens this claim [141]. Future experiments such as atmospheric neutrino experiment proposed at the India based Neutrino Observatory (ICAL@INO) [142], e Precision IceCube Next Generation Upgrade (PINGU) at the IceCube Neutrino Observatory [143], Deep Underground Neutrino Experiment (DUNE) [144, 145], Tokai to Hyper-Kamiokande (T2HK/T2HKK) [146], Jiangmen Underground Neutrino Observatory (JUNO) [147] have good hierarchy sensitivity so are expected to determine this unknown.

2. **Octant of θ_{23}:** It is still unknown whether $\theta_{23} < 45^\circ$ or $\theta_{23} > 45^\circ$. If $\theta_{23} < 45^\circ$ then θ_{23} is said to lie in the lower octant (LO) and $\theta_{23} > 45^\circ$ is called the higher octant (HO). Although the 3σ allowed values range over both the octants, there are strong hints from T2K and NOνA data which suggests that θ_{23} lies in the higher octant.

3. **The CP phase :** The value of the CP violation phase δ_{CP} is still unknown. If the value of the CP phase is zero or 180° , CP is conserved in the leptonic sector. Any other value of δ_{CP} violates CP, with maximum CP violation at $\delta_{CP} = \pm 90^\circ$. The current T2K data suggests that CP is violated also strongly disfavours $\delta_{CP} = 90^\circ$ irrespective of hierarchy. The present NOνA data also prefers CP violation, but $\delta_{CP} = -90^\circ$ is disfavoured for NH and $\delta_{CP} = 90^\circ$ is disfavoured for IH. The global analysis reject $\delta_{CP} = 90^\circ$ at greater than 3σ confidence level [11, 148]. The second oscillation maxima of the $\nu_\mu \rightarrow \nu_e$ has good CP sensitivity. Future experiments like T2HKK and ESSνSB [149] which are proposed to study neutrino oscillations at the second oscillation maxima are expected to measure δ_{CP} precisely.

2.5 Challenges in measurements of oscillation parameters

The neutrino oscillation experiments measure the neutrino event rate at the detector which is proportional to the oscillation probability. The challenges to measure the

Parameter	Present Best-fit	Current 3σ Range
$\frac{\Delta m^2_{21}}{10^{-5}\ \text{eV}^2}$	$7.39^{+0.21}_{-0.20}$	$6.79 \to 8.01$
$\theta_{12}(^\circ)$	$33.82^{+0.78}_{-0.76}$	$31.61 \to 36.27$
$\frac{\lvert\Delta m^2_{31}\rvert}{10^{-3}\ \text{eV}^2}$	$+2.528^{+0.029}_{-0.031}$	$+2.436 \to +2.618$
$\frac{\lvert\Delta m^2_{32}\rvert}{10^{-3}\ \text{eV}^2}$	$-2.510^{+0.030}_{-0.031}$	$-2.601 \to -2.419$
$\theta_{23}(^\circ)$	$48.6^{+1.0}_{-1.4}$	$41.1 \to 51.3$
$\theta_{13}(^\circ)$	$8.60^{+0.13}_{-0.13}$	$8.22 \to 9.02$
$\delta_{CP}(^\circ)$	221^{+39}_{-28} (NH) 282^{+23}_{-25} (IH)	$144 \to 357$ (NH) $205 \to 348$ (IH)

Table 2.1: The best-fit values and 3σ ranges of neutrino oscillation parameters from global analysis by the Nu-fit group [1, 2].

neutrino oscillation parameters arises when more than one set of neutrino oscillations parameters result in the same oscillations probabilities. This is known as the parameter degeneracies. The degeneracies can be written as

$$P_{\alpha\beta}(x_1, x_2, ...) = P_{\alpha\beta}(y_1, y_2, ...). \tag{2.94}$$

The various degeneracies affecting $P_{\mu\mu}$ and $P_{\mu e}$ are,

- The $(\theta_{13}, \delta_{CP})$ degeneracy - This degeneracy in the $P_{\mu e}$ channel is defined by $P_{\mu e}(\theta_{13}, \delta_{CP}) = P_{\mu e}(\theta'_{13}, \delta'_{CP})$ [150]. With precise knowledge of θ_{13} this degeneracy is resolved.

- Hierarchy-δ_{CP} degeneracy - This degeneracy refers to the degeneracy in the $P_{\mu e}$ channel where $P_{\mu e}(\mathrm{NH}, \delta_{\mathrm{CP}}) = \mathrm{P}_{\mu e}(\mathrm{IH}, \delta'_{\mathrm{CP}})$ [151].

- Intrinsic hierarchy and octant degeneracies - The survival probability of $P_{\mu\mu}$ in eq. 2.91 gives rise to the intrincis degeneracies in this channel and can be expressed as [152],

$$P_{\mu\mu}(\theta_{23}) = P_{\mu\mu}(\pi/2 - \theta_{23}) \tag{2.95}$$

But, for non-zero θ_{13} the degeneracy is modifies as [153],

$$P_{\mu\mu}(\theta_{\mu\mu}) = P_{\mu\mu}(\pi/2 - \theta_{\mu\mu}) \tag{2.96}$$

where, $\sin^2 2\theta_{\mu\mu} = 4\cos^2\theta_{13}\sin^2\theta_{23}(1 - \cos^2\theta_{13}\sin^2\theta_{23})$.

The expression for $P_{\mu\mu}$ from eq. 2.91 depends on $\sin^2 2\theta_{23}$ which is responsible for the intrinsic octant degeneracy. The intrinsic hierarchy degeneracy occurs due to the dependence of $P_{\mu\mu}$ on $\sin^2\Delta$ which can be written as [154],

$$P_{\mu\mu}(\Delta m^2_{\mu\mu}) = P_{\mu\mu}(-\Delta m^2_{\mu\mu}) \tag{2.97}$$

where, $\Delta m^2_{\mu\mu} = \sin^2\theta_{12}\Delta m^2_{31} + \cos^2\theta_{12}\Delta m^2_{32} + \cos\delta_{CP}\sin 2\theta_{12}\sin\theta_{13}\Delta m^2_{21}$. If Δm^2_{21} is zero, this manifests in the form

$$P_{\mu\mu}(\Delta m^2_{31}) = P_{\mu\mu}(-\Delta m^2_{31}) \tag{2.98}$$

- Octant-δ_{CP} degeneracy - This degeneracy occurs in the $P_{\mu e}$ channel where $P_{\mu e}(\mathrm{LO}, \delta_{\mathrm{CP}}) = \mathrm{P}_{\mu\mathrm{e}}(\mathrm{HO}, \delta'_{\mathrm{CP}})$ [155].

The hierarchy-δ_{CP} degeneracy and octant-δ_{CP} degeneracy can be combined as a generalized hierarchy-octant-δ_{CP} degeneracy [156] given by:

$$P_{\mu e}(\Delta m^2_{31}, \theta_{23}, \delta_{CP}) = P_{\mu e}(-\Delta m^2_{31}, \theta'_{23}, \delta'_{CP}). \tag{2.99}$$

In the next section we describe the hierarchy-δ_{CP} degeneracy, octant-δ_{CP} degeneracy in details.

2.5.1 The Hierarchy-δ_{CP} Degeneracy

The hierarchy-δ_{CP} degeneracy affects the $P_{\mu e}$ channel from eq. 2.91,

$$P_{\mu e}(\Delta m^2_{31}(\mathrm{NH}), \delta_{CP}) = P_{\mu e}(-\Delta m^2_{31}(\mathrm{IH}), \delta'_{CP}). \tag{2.100}$$

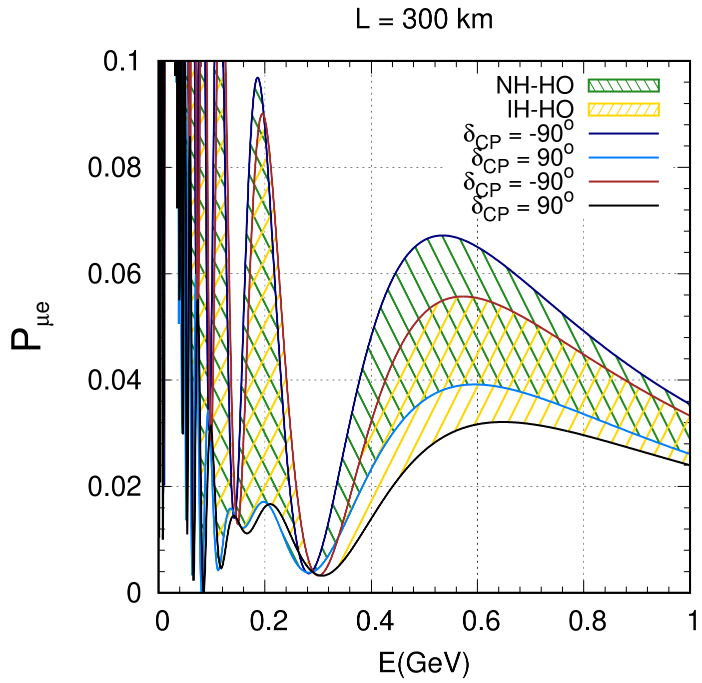

Figure 2.2: $P_{\mu e}$ vs E for L = 300 km and octant fixed at higher octant. The green band represent NH and the yellow band IH.

The fig. 2.2 illustrates the $P_{\mu e}$ vs E for the baseline of 300 km in the case of neutrinos. The green shaded region represents normal hierarchy and yellow shaded inverted hierarchy. The width of the bands are due to the variation in the δ_{CP} values from $-180°$ to $180°$. The NH probability band is encapsulated within the δ_{CP} values of $-90°$ and $90°$. The reason being that, at the oscillation maxima $\Delta = \pi/2$ so the maximum and minimum of the probability bands are obtained at $\delta_{CP} = \mp 90°$ which implies $\cos(\Delta + \delta_{CP}) = \pm 1$. The overlapping region between the green and yellow bands is the degenerate region where the same value of $P_{\mu e}$ is satisfied for opposite hierarchies and different values of δ_{CP}.

The degeneracy appears due to the second term of the $P_{\mu e}$ expression eq. 2.91 where we can see that $\cos(\Delta + \delta_{CP})$ is same as $\cos(-\Delta - \delta_{CP})$. So, with opposite hierarchies and different δ_{CP} gives the same solutions.

2.5.2 The Octant-δ_{CP} Degeneracy

This degeneracy occurs in the $P_{\mu e}$ channel

$$P_{\mu e}(\mathrm{LO}, \delta_{CP}) = P_{\mu e}(\mathrm{HO}, \delta'_{CP}). \tag{2.101}$$

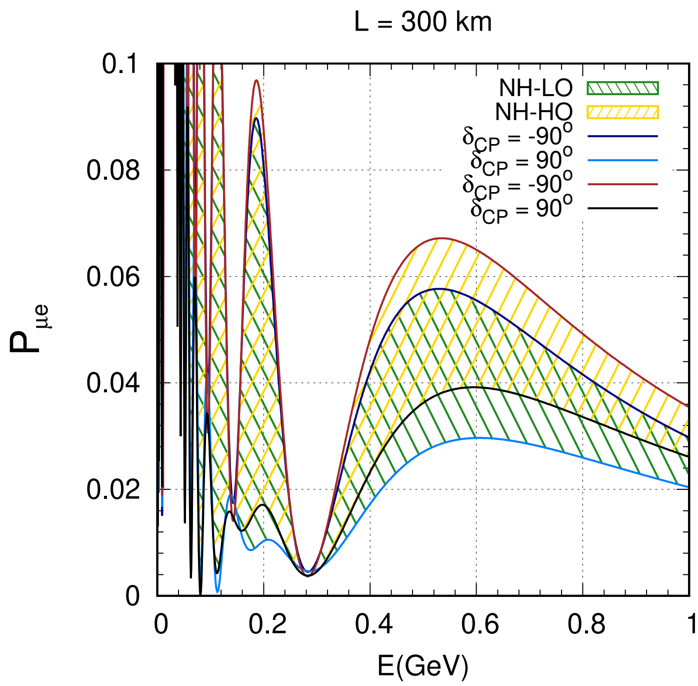

Figure 2.3: $P_{\mu e}$ vs E for L = 300 km, hierarchy fixed at normal hierarchy. The green band represent LO and the yellow band HO.

The fig. 2.3 presents the $P_{\mu e}$ vs E for L = 300 km with fixed hierarchy. The green shaded region represents the lower octant region while the yellow shaded higher octant. The δ_{CP} values from $-180°$ to $180°$ is responsible for the spread in the band. From the eq. 2.91 we can see that the $\sin^2\theta_{23}$ term is responsible for the probabilities of HO to be higher than that of LO. The overlapping region between the green and the yellow shaded region in the figure is the degenerate region where $P_{\mu e}$ has the same values for different octants and δ_{CP} values. This is the octant-δ_{CP} degeneracy.

A discussion on resolution of these degeneracies in long baseline experiments has been discussed in details in the next chapter.

2.6 Accelerator Neutrino Based Long-Baseline Experiments

In this section we discuss in detail the set up fro accelerator neutrino experiments. In accelerator neutrino experiment neutrinos are produced from particle accelerator. The neutrino from the source is then passed through a near detector where the neutrino flux is estimated. The neutrino is then allowed to oscillate followed by the detection of the neutrinos at the far detector. The far detector configuration can be of two types namely on-axis and off-axis. As the name itself suggests that on-axis location of the detector are such that it coincides with the neutrino beam axis. The off-axis detectors are located at a small angle from the beam axis, the advantage of an off-axis beam is the monochromaticity of the flux [157]. The currently running experiments T2K and NOνA employ off-axis configurations to suppress the ν_e background.

Off-axis beam

The pion decay is a two body process, it decays into a muon and a neutrino.

$$\pi^{+(-)} \rightarrow \mu^{+(-)} + \nu_\mu(\bar{\nu_\mu}) \tag{2.102}$$

In the rest frame of the pion the neutrino is mono energetic and isotropic. In such a frame the four momentum of the pion is given by $\pi(m_\pi, 0, 0, 0)$. Therefore,

$$m_\pi = E'_\mu + E'_\nu \tag{2.103}$$

where, prime represents the center of mass frame. The four momenta of the muon and the neutrino in the CM frame is given by:

$$\mu(E'_\mu, \vec{p}) \tag{2.104}$$

$$\nu(E'_\nu, -\vec{p}) \tag{2.105}$$

Since, m_ν is very small we have neglected it so $E'_\nu = p$.
As, we know that

$$\pi = \mu + \nu \tag{2.106}$$

we can write

$$m_\pi^2 = m_\mu^2 + 2(\pi \cdot \nu) \tag{2.107}$$

$$\Rightarrow p = E'_\nu = \frac{m_\pi^2 - m_\mu^2}{2m_\pi} \tag{2.108}$$

Since, the neutrino decays in flight in the lab frame the neutrino is no longer mono energetic or isotropic. We can characterize the neutrino beam relative to the angle of the emitted neutrino. Let us consider a neutrino emitted at an angle θ from the beam axis in the lab frame and θ' in the pion rest frame. The neutrino four momentum in pion rest frame with the z-axis as the beam axis will be

$$\nu(E'_\nu, E'_\nu \sin\theta', 0, E'_\nu \cos\theta') \tag{2.109}$$

To transform this to the lab frame a Lorentz boost $\gamma = \frac{E_\pi}{m_\pi}$ is required.
The neutrino four momentum in the lab frame is:

$$\nu(\gamma E'_\nu(1 + \beta\cos\theta'), E'_\nu \sin\theta', 0, \gamma E'_\nu(\beta + \cos\theta')) \tag{2.110}$$

where, $\beta = \sqrt{1 - \frac{1}{\gamma^2}} \approx 1 - \frac{1}{2\gamma^2}$.

The neutrino four momentum represented in the lab coordinates is,

$$\nu = (E_\nu, E_\nu \sin\theta, 0, E_\nu \cos\theta) \tag{2.111}$$

Therefore, from Eq. 2.110 and 2.111 we obtain

$$\tan\theta = \frac{E'_\nu \sin\theta'}{\gamma E'_\nu(\beta + \cos\theta')} . \tag{2.112}$$

If $E_\nu \gg m_\pi$, then $E_\pi \gg m_\pi$ also, so $\gamma \gg 1$ and $\beta \approx 1$. This results in,

$$\tan\theta \approx \frac{E'_\nu \sin\theta'}{\gamma E'_\nu (1+\cos\theta')} \approx \frac{E'_\nu \sin\theta'}{E_\nu}, \tag{2.113}$$

E_ν can be written as,

$$E_\nu \approx \frac{E'_\nu \sin\theta'}{\tan\theta}. \tag{2.114}$$

The change in E_ν with respect to θ' is given as,

$$\frac{dE\nu}{d\theta'} = \frac{E'_\nu \cos\theta'}{\tan\theta} \tag{2.115}$$

$$= \frac{m_\pi^2 - m_\mu^2}{2m_\pi} \frac{\cos\theta'}{\tan\theta}. \tag{2.116}$$

Therefore, the change in E_ν with respect to θ' is inversely proportional to the off-axis angle.

2.6.1 Present and Future long baseline experiments

2.6.1.1 T2K

The T2K (Tokai to Kamioka) [158] is long-baseline neutrino oscillations experiment based on muon-neutrino produced at J-PARC (Japan Proton Accelerator Research Complex). The J-PARC main ring accelerator produces 30 GeV protons which is incident on a graphite target and pions and kaons are produced. These pions and kaons are focused into a 90 m long decay volume through three electromagnetic horns to produce a relatively pure neutrino beam. The knowledge of the neutrino beam flux is essential to the precise determination of neutrino oscillation parameters. This is accomplished by the near detector complex, which consists of INGRID an on-axis detector for monitoring the direction of the beam and ND280 an off-axis detector at $2.5°$ from the beam axis to study the neutrino spectrum. The INGRID detector is an iron-scintillator detector consisting of 14 modules while the ND280 is a multi component detector.

The neutrinos are then detected at the far detector located at Kamioka 295 km away. The far detector is the Super-Kamiokande detector which is a water Čerenkov detector.

The neutrinos undergo charge current interaction in the detector which produces a charged lepton, these charged leptons produce Čerenkov light when they propagate through the detector. The Čerenkov light is produced in the shape of a cone which when reaches the photo multiplier tubes forms a ring. The radiations from muons forms a sharp ring and from electrons produces a fuzzy ring due to bremsstrahlungg in case of electrons owing to its low mass. The baseline of T2K is 295 km and the peak neutrino energy is 0.6 GeV. T2K is designed to determine the parameters Δm^2_{31}, θ_{23} and δ_{CP}.

2.6.1.2 NOνA

The NuMI Off-axis ν_e Appearance (NOνA) [132] experiment at Fermilab is an ongoing experiment. The neutrino beam is generated by the NuMI beamline at Fermilab which delivers beam power of 700 kW. The accelerator has the capacity to bombard 6×10^{20} protons on target. Graphite is used as the target material to generate mesons which are then allowed to decay in the decay tunnel to produce the neutrino beam.

The NOνA experiment utilizes two detectors, the near detector is 1 km from the source while the far detector is 810 km away located near Ash River, Minnesota. The two detectors are of identical properties and are located at an angle of 14.7 mrad from the beam axis. The detectors are liquid scintillator detectors made of active tracking calorimeters comprising of polyvinylchloride (PVC) cells filled with mineral oil and 5% pseudocumene. The scintillation light produced in a cell is detected at an avalanche photo-diode. The NOνA experiment is also an off-axis experiment with the peak energy of the flux near the first oscillation maximum. The goal for the NOνA experiment is the determination of the parameters Δm^2_{31}, θ_{23} and δ_{CP}.

2.6.1.3 DUNE

The Deep Underground Neutrino Experiment (DUNE) [144] is a future long baseline neutrino oscillations experiment. DUNE beam will be driven by the Long-Baseline Neutrino Facility (LBNF) at Fermilab. The LBNF will generate intense neutrino beam from protons with beam power of 1.2 MW which will be upgradeable to 2.4 MW. The beam is expected to have protons on target $1.1 \times 10^{21} - 1.89 \times 10^{21}$. The protons will be bombarded on NuMI style graphite target to produce mesons which will be guided into a 195 m decay tunnel by two magnetic horns. The neutrino spectrum thus obtained will have a peak energy around 2 GeV.

The DUNE near detector will be placed at the LBNF at a distance of 575 m from the source. The near detector will be a Liquid Argon Time Projection Chamber (LArTPC) along with fine-grained magnetic spectrometer. The far detector will be located at Sanford Underground Research Facility (SURF) in Lead, South Dakota, 1300 km from the neutrino source on the beam axis. As, this is an on-axis experiment the neutrino spectrum will be a broad band spectrum. The far detector is planned to consist of four identical LArTPC detectors. Each detector will have dimensions 14.0 m (W) $\times$ 14.1 m (H) $\times$ 62.0 m (L) and fiducial volume 10 kt. The neutrinos interacting with the Argon in the TPC will produce charged particles. These charged particles will ionize the Argon atoms producing electrons. The electrons thus produced will be directed by an electric filed and collected by the wires present at the wall of the detector modules. The DUNE design report has categorized LArTPC into Single Phase (SP) and Dual Phase (DP) technologies. In the former the charged particles are drifted horizontally and collected at the wires present in the liquid itself while the latter drifts them vertically towards the gas present above the liquid. Both the technologies are currently being studied with the prototypes proto-DUNE and the final design will be decided based on the results.

2.6.1.4 T2HK and T2HKK

The Tokai to Hyper-Kamiokande (T2HK) and Tokai to Hyper-Kamiokande extension to Korea (T2HKK) [146] are the two proposals of the same experiment. The neutrino source will be same J-PARC neutrino source used in the T2K experiment with some upgrades expected to be completed by the T2HK & T2HKK starts operating. The beam power of the current J-PARC is around 470 kW which is expected to reach above 1.3 MW by 2025.

The near detector complex ND280 currently has two detectors INGRID an iron-scintillator detector and ND280 a multi-component detector. The ND280 is planned to be upgraded before the T2HK experiment starts running. Additionally, a Čerenkov intermediate detector to measure the neutrino cross section is also planned at $\sim 1-2$ km from the source. The detector is designed to have the capability to measure the neutrino cross sections for various off-axis configurations from $1.0^\circ - 4.0^\circ$. This intermediate detector is expected to reduce the systematics uncertainties as the intermediate and far detectors will have same target nuclei material.

The Hyper-Kamiokande (HK) is the upgraded version of the Super-Kamiokande detector. HK will have two identical water Čerenkov detectors of 187 kt each. The first detector will be placed at Tochibora mine near Kamioka in Japan located at 295 km from the source and 8 km from the Super-K, but have the same off-axis angle of 2.5° from the beam line. As the peak neutrino energy is around 0.5 GeV, this baseline corresponds to the first oscillation maxima. The T2HK proposal will have both the detectors placed at the same location, the total fiducial volume of the detector is 374 kt under this proposal. For the same energy the baseline for second oscillation maxima comes around 1100 km. The T2HKK is a very broad proposal under which both the first and second oscillation maxima can be simultaneously studied by placing the second detector at Korea which offers the baselines from 1000 km to 1300 km at an angle of $1.0^\circ - 3^\circ$ from the beam axis and various sites have been identified for the same.

2.6.1.5 ESSνSB

The European Spallation Source Neutrino Super Beam (ESSνSB) [159] project is an under construction project at Lund, Sweden. European Spallation Source [160] when completed in 2025 will become the world's most powerful neutron source. The proton linac can deliver protons of 5 MW on average which can be raised upto 10 MW and provides 2.7×10^{23} protons on target per year. Along with neutrons, the ESS will also produce neutrino super beam with very high intensity. The neutrino beam thus produced will have a mean energy around 0.35 to 0.4 GeV. Such high intensity neutrino beam enables the ESSνSB experiment to explore the second oscillation maximum physics. The advantage of a second oscillation physics is the sensitivity of the experiment to the Dirac CP phase. A near detector is proposed to estimate the flux of the neutrino beam. The possibility of the near detector to be a water Čerenkov detector is under consideration and the possibilities of other detector technologies are also being explored. The near detector can also be helpful in studying the neutrino nucleon cross section.

The neutrinos will then be detected in a far detector located at the 1200 m deep Gerpenberg mine, 540 km from the neutrino source. There are also various alternative proposals for the experiment, one is the Zinkgruvan mine at a distance of 360 km from the source. Another interesting proposal is to place half the detector in Zinkgruvan and the other half in Garpenberg. Since, the goal of the experiment is the study of CP violation in the neutrino sector the 540 km baseline has been given more emphasis.

The far detector proposed is the MEgaton Mass PHYSics (MEMPHYS) [161] detector. The MEMPHYS detector is a 500 kt water Čerenkov detector whose latest design comprises of two modules. Each module is designed to have 120000 8” or 10” photo-multipliers (PMTs) which provides 30% optical coverage.

The future long baseline experiments are expected to play a very important role in determining the unknowns of neutrino physics. In the next chapter we present a comprehensive analysis of the potentials of the various detectors, stand alone and in conjunction with other detectors.

Chapter 3

Neutrino Oscillations at Hyper-Kamiokande, DUNE and ESSνSB

3.1 Introduction

This chapter is dedicated to the sensitivity study of presently running and the future accelerator based neutrino oscillation experiments of to determine the current unknown parameters $i.e.$ neutrino mass hierarchy (the sign of Δm^2_{31}), CP phase δ_{CP} and the octant of θ_{23}. We study the physics potential of the future accelerator based experiments DUNE, T2HK/T2HKK and ESSνSB to determine these unknown parameters assuming their full projected run time. We also explore the importance of synergy between the future experiments along with their synergies with currently running experiments T2K and NOνA for their full projected run time.

The accelerator neutrino experiments can probe the survival probability $P_{\mu\mu}$ and the appearance probability $P_{\mu e}$. The latter is sometimes referred to as the "golden channel" because this channel is sensitive to all the three current unknowns of the neutrino oscillations paradigm as described in the previous chapter. However, both channels suffer from parameter degeneracies. This gives rise to multiple solutions and make the accurate accurate determination of the parameters difficult. Most of these parameter degeneracies can be surpassed by the future experimental proposals like T2HK [162] / T2HKK [146], DUNE [144] and ESSνSB [163, 149] thereby clinching the issue of hierarchy, octant and δ_{CP}.

Our main focus is to do a comparative study of the potentials of the major upcoming facilities HK, DUNE and ESSνSB to determine the δ_{CP} phase, mass-hierarchy and the octant of θ_{23} in their individual capacity. In particular, since the octant sensitivity of the T2HKK set up has not been studied in detail earlier, we stress on this aspect and explore the underlying physics reasons which can explain the octant sensitivity of the various set ups. This discussion brings out the differences in the behaviour of the probabilities at the first and second oscillation maxima and the impact on the discovery potential of the various unknowns.

In addition, we also estimate the optimal exposures/run times of these setups to achieve 5σ sensitivity in octant and hierarchy determination and 5σ sensitivity to CP discovery potential for 60% values of the CP phase δ_{CP}. In view of the fact that by the time these experiments are operative, the current experiments T2K [131] and NOνA [140] will already have their results, we also present the optimal exposures including the information from T2K and NOνA experiments for their full projected run time. Furthermore since the time scales of the future projects HK, ESSνSB and DUNE are similar, we present a combined study of the mass hierarchy and CP sensitivity of T2HK+ESSνSB and DUNE+ESSνSB to explore the effect of enhanced statistics and possible synergies between these projects. Note that such studies for T2HK + DUNE and T2HKK+DUNE have already been performed [164]. Apart from the above we have also examined the effect of varying the neutrino and antineutrino proportions in the Hyper-K experiments. Note that the T2HK & T2HKK experiments have proposed a runtime ratio of $1\nu : 3\bar{\nu}$ in order to ensure that the initial number of neutrino and antineutrino events are approximately of the same order. In this regard, we considered two alternative runtime ratios $3\nu : 1\bar{\nu}$ & $1\nu : 1\bar{\nu}$ and thoroughly examined if these runtime ratios would give better sensitivity for the determination of mass hierarchy, octant of θ_{23} and the Dirac phase δ_{CP}.

There have been several studies on the capabilities of DUNE [165, 166, 167, 168, 169, 170], T2HK [162, 171, 172] and ESSνSB [173] for the determination of the three major unknowns mentioned above. The T2HKK proposal studied the hierarchy and δ_{CP} sensitivity of the set up with respect to three off-axis angles $1.5^{\circ}, 2^{\circ}, 2.5^{\circ}$ [146]. With the inception of this proposal, the physics possibilities of T2HKK regarding determination of hierarchy, octant and δ_{CP} have been studied in ref. [174, 175, 176, 164]. In ref. [174], the mass hierarchy and CP sensitivity of DUNE, T2HK, DUNE+T2HK were studied in detail. These also elaborated on the optimization of alternative designs for DUNE and the T2HKK proposal. In ref.[175, 177] a hybrid setup in which the antineutrino run of T2HK is substituted by antineutrinos coming from muon decay at rest (μ-DAR) has been studied for determination of hierarchy, octant and δ_{CP}. The author of ref. [164] has studied the sensitivity of T2HK, T2HKK and DUNE to determine mass hierarchy and to measure the CP phase δ_{CP} and also made a comparative analysis of DUNE+T2HK and DUNE+T2HKK. In ref. [176] the role of systematic uncertainties in the determination of hierarchy, octant and δ_{CP} in the three set ups were studied. However octant sensitivity of T2HKK and a detailed comparative study of the three setups have not been presented in any of these references. The proposal in ref.[149] studied the optimization of the set up with respect to discovery of δ_{CP} and the advocated configuration consisted of a neutrino beam with a peak energy of $\sim$ 0.2 GeV and baseline of 540 km. In ref.[178], in addition to δ_{CP}, the precision of atmospheric parameters including octant resolution capabilities were also studied.

The outline of the chapter is as follows. In section 3.2 we present the relevant probabilities and discuss the degeneracies that are faced by the different experiments in terms of probabilities. The following section (sec.3.4) contains the results on octant, hierarchy and CP discovery potentials of the three proposed experiments.

T2HK & T2HKK experiments have proposed a runtime ratio of $1\nu : 3\bar{\nu}$ in order to ensure that the initial number of neutrino and antineutrino events are approximately of the same order. In this regard, we considered two alternative runtime ratios $3\nu : 1\bar{\nu}$ & $1\nu : 1\bar{\nu}$ and thoroughly examined which of these runtime ratios would give maximum sensitivity for the determination of mass hierarchy, octant of θ_{23} and the Dirac phase δ_{CP}. So, we wanted to verify the significance of this runtime ratio and compare them with other runtime ratios of $1\nu : 1\bar{\nu}$ & $3\nu : 1\bar{\nu}$. Hereby we vary the neutrino-antineutrino proportion for T2HK and T2HKK and check if other best neutrino to antineutrino run time ratio for T2HK & T2HKK in order to maximize the sensitivity of these two experiments to determine neutrino mass hierarchy, octant of θ_{23} and the Dirac CP phase δ_{CP}. In the sec.3.5 we study the effect of varying the proportion of neutrino and antineutrino run times in the T2HK and T2HKK experiment to explore if this can cause any discernible effect as opposed to the proposed runtime ratio.

In section 3.6 we obtain the optimal exposures required by various setups to achieve 5σ octant and hierarchy sensitivity. We also present the exposure needed to achieve 5σ sensitivity to discovery of CP violation for 60% values of δ_{CP}. Additionally, we obtain how much the exposures can be reduced if the information from T2K and NOνA are included. The next section (sec-3.7) includes a study of the combined sensitivity of mass hierarchy and CP of ESSνSB with DUNE and T2HK.

We make our concluding remarks in the final section.

3.2 Probability discussions

Neutrino oscillation experiments measure the event rates which in turn depend on the probabilities. The probability most relevant for determination of the three unknowns in the long baseline experiments is the appearance probability $P_{\mu e}$ (eq. 2.91).

Figure 3.1 shows the behaviour of the probabilities as a function of energy for the baselines 295 km, 1100 km, 1300 km and 540 km. These plots are done for a fixed value of $\delta_{CP} = -90^\circ$. The bands correspond to variation over the octant of θ_{23} in the range $39^\circ - 42^\circ$ for LO and $48^\circ - 51^\circ$ for HO. The figure shows that for NH the bands are wider for T2HK and DUNE baselines as compared to the T2HKK and ESSνSB baselines. This indicates that the variation of the probability over θ_{23} is more for T2HK and DUNE than at 1100 km baseline and ESSνSB facility. For IH, the bands over θ_{23} for T2HK(E $\sim$ 0.6 GeV) are wider but the bands at 1100 km (E $\sim$ 0.6 GeV), DUNE (E $\sim$ 2 GeV) and ESSνSB (E $\sim$ 0.24 GeV) baselines are narrower, considering the peak energy of the flux for the above experimental setups given in brackets.

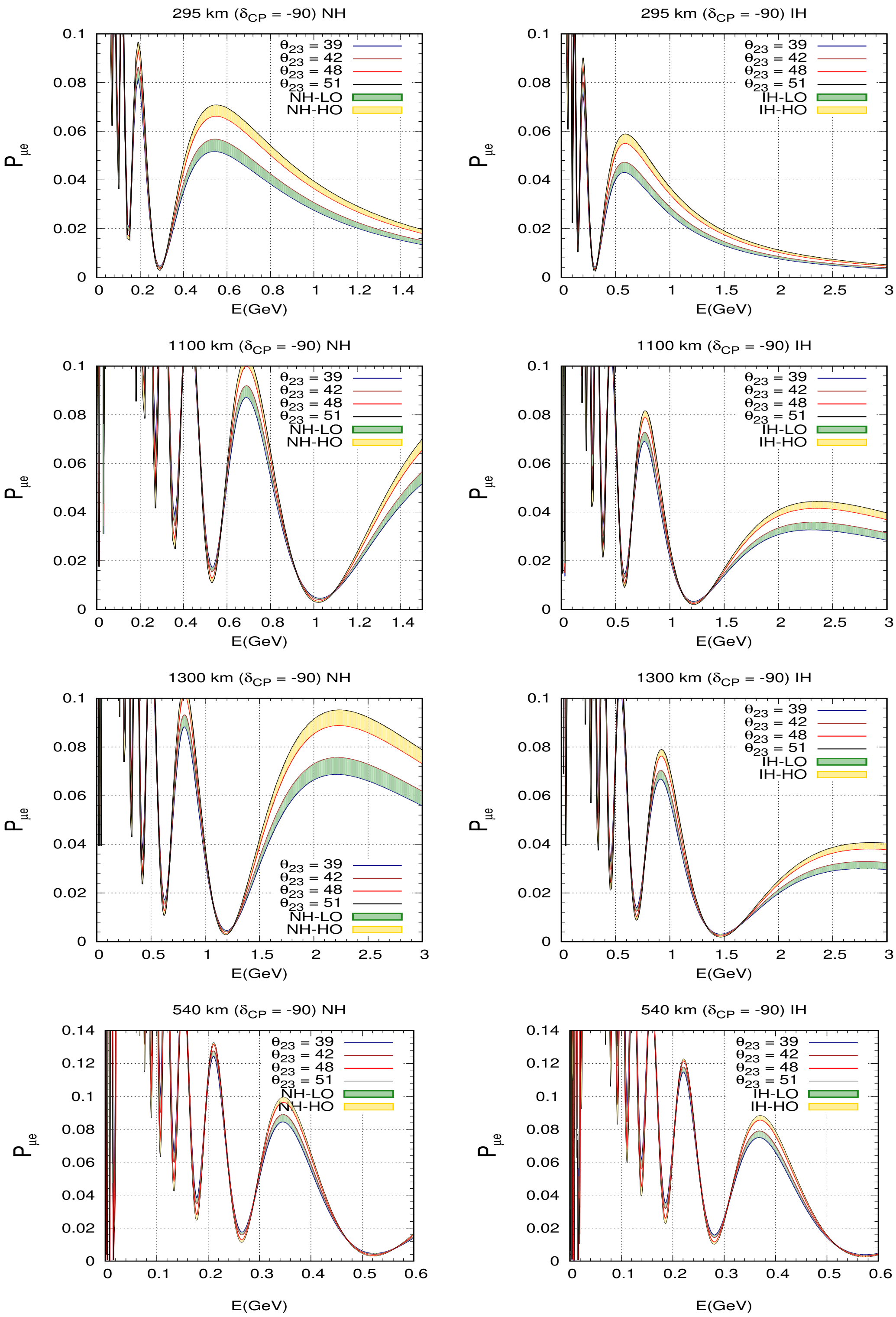

Figure 3.1: Appearance probabilities $P_{\mu e}$ vs Energy for 295 km, 1100 km, 1300 km and 540 km. The left panel is for NH and right panel for IH. The bands are due to variation over θ_{23}. Here δ_{CP} and θ_{23} are in degrees.

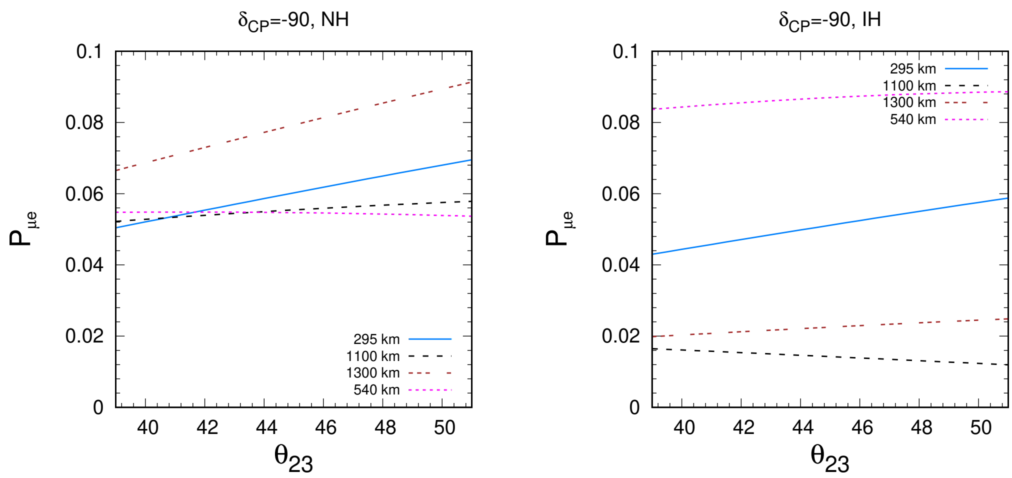

Figure 3.2: Appearance probabilities : $P_{\mu e}$vs θ_{23} for NH and IH. δ_{CP} and θ_{23} are in degrees.

In order to elucidate this further we plot $P_{\mu e}$ as a function of θ_{23} for different baselines of T2K & T2HK (295 km, 0.6 GeV), T2HKK (1100 km, 0.6 GeV), DUNE (1300 km, 2 GeV) and ESSνSB (540 km, 240 MeV) in fig. (3.2), by fixing the corresponding energies at the values in the parentheses where the respective flux peaks. Note that, the second oscillation maxima for ESSνSB occurs at 0.35 GeV and 0.24 GeV corresponds to the third oscillation maxima, both have been consideredin the numerical analysis. A thorough numerical and analytical study of ESSνSB have been performed in [179]. It is to be noted that 0.6 GeV corresponds to the first oscillation maxima for T2HK baseline while it is close to the second oscillation maxima for the T2HKK baseline. The left (right) plot corresponds to $P_{\mu e}$ vs θ_{23} assuming normal (inverted) hierarchy. It can be seen that the lines corresponding to the baselines of 295 km (blue-solid), 1300 km (brown-dash-dotted) have positive slopes both for NH and IH. However, the curves for 1100 km (black-dashed) and 540 km (pink-dotted) are much flatter with a small positive slope for NH and negative for IH.

With a view to understand this behaviour of the probability with θ_{23} at different baselines we write the probability expression given in eq.(3.1) in the following form [180]

$$P_{\mu e} = (\beta_1 - \beta_3)\sin^2\theta_{23} + \beta_2 \sin 2\theta_{23}\cos(\Delta + \delta_{CP}) + \beta_3 \tag{3.1}$$

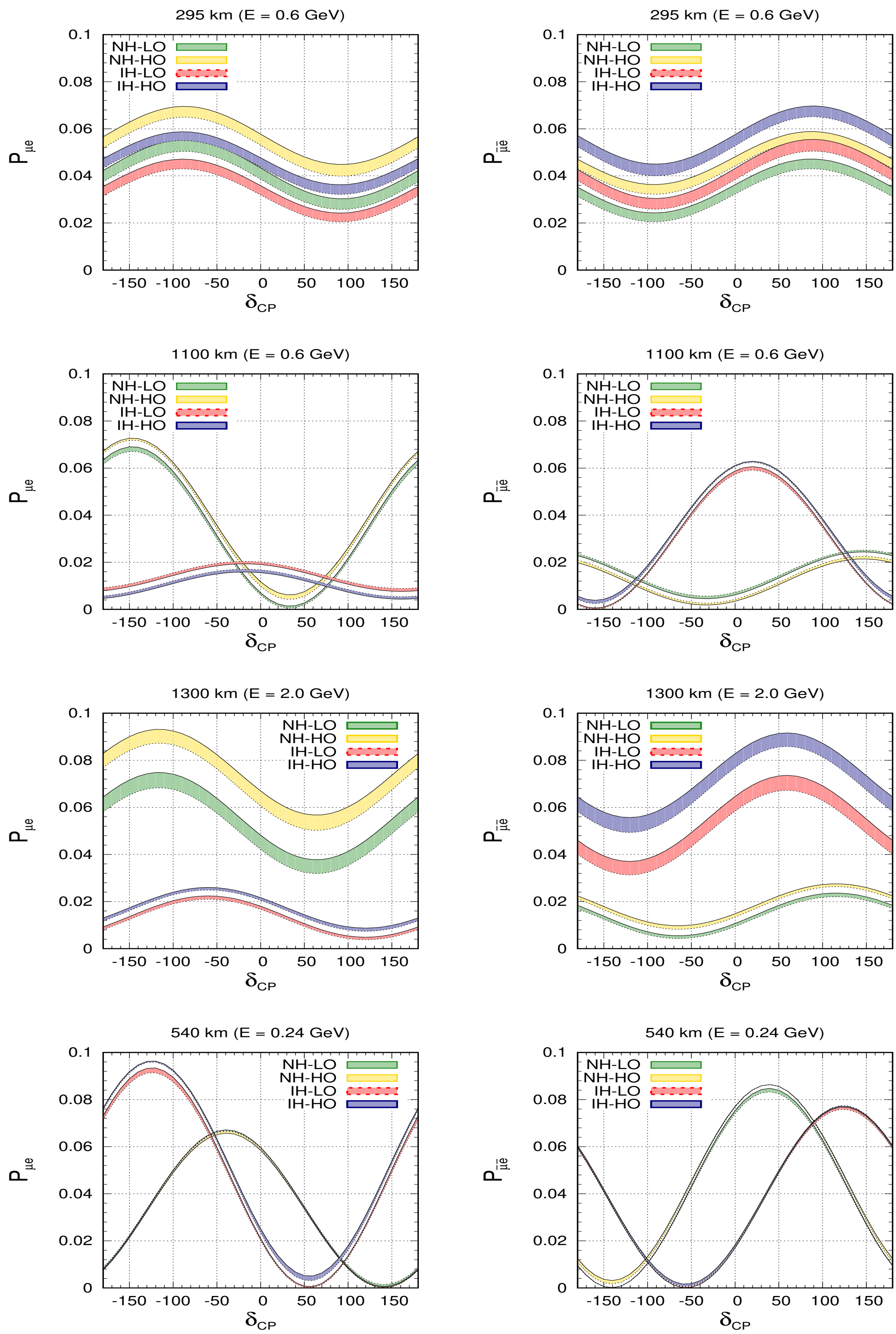

Figure 3.3: Appearance probabilities vs δ_{CP} (degrees) for 295 km,1100 km, 1300 km and 540 km. The left panel is for neutrinos while the right panel is for antineutrinos. Each panel contains plots for both NH and IH. The band represents variation over θ_{23}.

where,

$$\begin{aligned}
\beta_1 &= \sin^2 2\theta_{13}\frac{\sin^2\Delta(1-\hat{A})}{(1-\hat{A})^2}, \\
\beta_2 &= \alpha\cos\theta_{13}\sin 2\theta_{12}\sin 2\theta_{13}\frac{\sin\Delta\hat{A}}{\hat{A}}\frac{\sin\Delta(1-\hat{A})}{1-\hat{A}}, \\
\beta_3 &= \alpha^2\sin^2 2\theta_{12}\cos^2\theta_{13}\frac{\sin^2\Delta\hat{A}}{\hat{A}^2}
\end{aligned} \tag{3.2}$$

The θ_{23} dependence is seen to come from the first term of eq.(3.1), varying linearly with θ_{23} with a slope given by $(\beta_1 - \beta_3)$. Note that over the range of θ_{23} spanning $39^\circ - 51^\circ$, $\sin 2\theta_{23}$ stays close to 1 and so the second term of eq.(3.1) does not affect the behaviour of $P_{\mu e}$ vs θ_{23}. The β_is for the three different baselines are tabulated in table 3.1 for both the hierarchies.

The first column corresponds to the L/E ratios of different setups. For the baselines 295 km and 1100 km the peak energies being the same, the main difference between the β_is enumerated in table 3.1 is due to the L/E ratio which is much higher for the 1100 km baseline. Between the 1300 km and 295 km baselines the L/E ratio is approximately the same order and the β_is are different due to the different energies. The higher energy implies a higher value for the matter potential $\hat{A}$ for the 1300 km baseline entailing $(1-\hat{A})$ to be smaller and hence β_1 larger. This can be seen from the second column of table 3.1. Whereas for 1100 km and 1300 km baselines the energies as well as the different L/E ratios attribute to the difference in the β_i factors. For the ESS experiment with 540 km baseline, both the peak energy as well as the 0.9 baselines are different from that of T2HK and DUNE leading to differences in the L/E ratios. Whereas the L/E ratios for ESS and the Korean baseline in the T2HKK proposal are of the same order though the peak energies and baselines are different. This causes the difference in β_i values. 0.9 From the third column of table 3.1 it can be seen that the β_3 values of 1300 km and 295 km are smaller than β_1 and β_2 for both NH and IH. Thus the probabilities of these two experiments are expected to rise as $\sim \sin^2\theta_{23}$ with slope given by $\approx \beta_1$. This can be seen from the brown (dash-dotted) and the blue (solid) lines respectively. 0.9 Comparing these two cases for NH it can be seen that since β_1 is higher for the 1300 km baseline the variation with θ_{23} is more in this case, than that of 295 km. For IH, on the other hand, β_1 is much smaller for the 1300 km baseline (for the neutrinos) when compared to 295 km baseline due to the suppression caused by matter effect. Hence the variation of $P_{\mu e}$ with θ_{23} is much less for 1300 km when compared to 295 km as can be seen from right panel of fig. 3.2. For the 1100 km baseline and NH β_3 term is comparable to β_1 term which makes the θ_{23} variation much flatter. For IH, β_1 is less than β_3 and the probability decr0.9eases with θ_{23}. These patterns can be seen from the black (dashed) lines in the fig. 3.2. In the case of 540 km baseline, for NH, β_3 is almost the same as β_1 and the probability shows only a slight variation with θ_{23} as can been seen from the pink (dotted) line in the fig. 3.2. For IH, β_1 is greater than β_3 and the probability increases with θ_{23} as can be seen from the fig. 3.2.

	L/E (km/GeV)	β_1		β_2		β_3	
		NH	IH	NH	IH	NH	IH
295 km	~ 490	0.094	0.077	0.013	-0.011	0.002	0.002
1100 km	~ 1800	0.045	0.002	-0.032	0.007	0.023	0.023
1300 km	~ 650	0.122	0.028	0.018	-0.009	0.003	0.003
540 km	~ 2250	0.036	0.059	0.036	-0.046	0.037	0.037

Table 3.1: β_1, β_2 & β_3 values for 295 km, 1100 km, 1300 km and 540 km baselines.

Figure 3.3 shows the probabilities as a function of δ_{CP} for the baselines 295 km, 1100 km, 1300 km and 540 km for both neutrinos and antineutrinos. Each figure has four probability bands green, yellow, red and blue corresponding to NH-LO, NH-HO, IH-LO, IH-HO respectively. The bands are obtained due to the variation in θ_{23} in the range $39^\circ - 42^\circ$ in LO and $48^\circ - 51^\circ$ in HO [1]. These kind of plots are helpful in understanding the various degeneracies at a probability level for values of θ_{23} not very n0.9ear to maximal mixing. An overlap between the bands for different values of δ_{CP} (as can be seen by drawing a horizontal line through the bands) would indicate a degenerate solution with a wrong δ_{CP} value, whereas, intersection between the bands would signify a degenerate solution even with the same value of δ_{CP} [156]. For instance from the left hand plot in the first row one can see that NH-LO (green band) is degenerate

[1] This range suffices since in any case the position of the minima is determined by the disappearance channel to be near $\approx (90^\circ - \theta_{23})$

with IH-HO (blue band) in the range $-180^\circ < \delta_{CP} < 0$ (lower-half plane, LHP) for the 295 km baseline. This gives rise to the wrong hierarchy(WH) – wrong octant (W0.9O) solutions. On the other hand NH-HO (yellow band) in the LHP and IH-LO (red band) in the range $0 < \delta_{CP} < 180^\circ$ (upper-half plane, UHP) are devoid of any degeneracy for the neutrinos. For the antineutrinos, as can be seen from the right panel of the first row NH-LO (green band) in LHP and IH-HO (blue band) in UHP are non-degenerate. Thus the octant degeneracy is seen to be opposite for neutrinos and antineutrinos and hence combined neutrino and antineutrino run is expected to resolve wrong octant solutions. Again, considering $\delta_{CP} \sim 90^\circ$ in UHP, NH-HO (yellow0.9 band) in UHP is degenerate with IH-HO (blue-band) around $\delta_{CP} \sim 0$. This corresponds to wrong hierarchy-right octant solution. This kind of degeneracy also exists for antineutrinos and hence inclusion of antineutrino run cannot resolve the wrong hierarchy-right octant solutions. Similar conclusions are true for the DUNE baseline as can be seen from the figures in the bottom row. However, because of enhanced matter effects DUNE has much better hierarchy sensitivity and therefore the difference between NH and IH bands are much more for this case and wrong hierarchy solutions are not seen in the probability plots. However, for e.g. the wrong octant solutions between NH-HO (yellow band) and $\delta_{CP} \sim 90^\circ$ and NH-LO (green band) and $\delta_{CP} \sim 0$ is visible from the neutrino probability presented in the left-panel of the bottom row for DUNE baseline. But for antineutrinos this degeneracy is not present.

For the 1100 km baseline, since the peak coincides with the second oscillation maxima and the L/E is different the degeneracy pattern is somewhat different. In this case, as can be seen from the first plot in the second row, for neutrinos the NH probability can have hierarchy degeneracy only in the range -30° to 90° excepting the range $10^\circ < \delta_{CP} < 60^\circ$ for LO (green band) for which there is no degeneracy. For IH, on the other hand there is degeneracy over the entire range of δ_{CP}. Similarly the plot in the right panel of the 2nd row exhibits that for NH there is hierarchy degeneracy over the whole range. While for IH the hierarchy degeneracy occurs in the range -180° to -120° and 130° to 180° barring the small range $-170^0.9\circ < \delta_{CP} < -150^\circ$ for LO. From these discussions it is clear that for true NH, neutrino run is better for hierarchy sensitivity whereas for true IH, antineutrinos are more useful.

In the case of ESSνSB project, the left plot of the last row shows that, for neutrinos the NH probability has hierarchy degeneracy for all values of δ_{CP} and the IH probability has the hierarchy degeneracy in the range $-60^\circ < \delta_{CP} < 180^\circ$. However, in the case of antineutrinos the range of δ_{CP} with no hierarchy degeneracy is $0^\circ < \delta_{CP} < 75^\circ$ for NH probabilities whereas the IH probabilities suffer from the hierarchy degeneracy for the whole range of δ_{CP}. Thus, if the true hierarchy is NH, then the antineutrino run gives better hierarchy sensitivity while for true IH neutrino run gives better sensitivity.

For octant degeneracy if we check the NH plot in the left panel then (the green and yellow bands) we see that over most of the δ_{CP} range a horizontal line drawn through0.9 these bands intersect the probabilities at δ_{CP} values belonging to different half planes giving rise to right-hierarchy – wrong octant – wrong δ_{CP} solutions. Over the range of δ_{CP} for which hierarchy degeneracy occurs there can also be wrong-hierarchy – wrong octant solutions in the same half plane of δ_{CP}. For IH also, over almost full CP range octant degeneracy is seen from the probability curves. Similar conclusions can be drawn from the antineutrino probabilities. Similarly for the antineutrinos NH-LO (green band) has a higher probability than NH-HO (yellow band). We can also see that the the curves for LO and HO are much closer for the 1100 baseline. In addition, the widths of the octant bands are very small which is reflective of the fact that the variation in the probability with octant is much less as we have seen earlier. Thus the octant sensitivity is expected to be less for this baseline and energy combination. From the eq.(3.1), we can write the difference of the probabilities for two different θ_{23} values as,

$$P_{\mu e}(\theta_{23}) - P_{\mu e}(\theta'_{23}) \approx (\beta_1 - \beta_3)(\sin^2\theta_{23} - \sin^2\theta'_{23}) \tag{3.3}$$

Note that the β_2 term is not included since it $\sin 2\theta_{23} \sim 1$ over the range in which θ_{23} is varied. Because of this the difference is independent of δ_{CP}. This implies the width of the θ_{23} band is expected to be the same for all values of δ_{CP} which can be seen from the figure 3.3. Inserting the values of β_1 and β_3 from table 3.1 and putting θ_{23} as 39° and θ_{23} as 42° we find that the width of the LO band as 0.006 (DUNE), 0.005 (T2HK), 0.002 (T2HKK) and 0.00005 (ESSνSB). This is agreement with what is observed in the plots.

3.3 Simulation Details

For performing the numerical simulation we have used the package General Long Baseline Experiment Simulator (GLoBES) [181, 182]. In our statistical analysis the total χ^2 can be decomposed into two parts as shown below

$$\chi^2_{\rm tot} = \min_{\xi,\omega}\{\chi^2_{\rm stat}(\omega,\xi) + \chi^2_{\rm pull}(\xi)\} \tag{3.4}$$

where ω denotes oscillation parameters, $\chi^2_{\rm stat}$ is the poissonian χ^2 function and the effect of systematic uncertainties has been incorporated through Pull method in terms of pull variables (ξ). In our analysis four different "pull" variables are considered – signal normalization error, background normalization error, energy calibration error on signal & background (tilt). Here $\chi^2_{\rm pull}$ is a penalty term given by $\chi^2_{\rm pulls} = \sum_{r=1}^{r=4} \xi_r^2$ which accounts for these four systematics errors . The poissonian $\chi^2_{\rm stat}$ is given by

$$\chi^2_{\rm stat}(\omega,\xi) = 2\sum_i\{\tilde{N}_i^{\rm test} - \tilde{N}_i^{\rm true} + \tilde{N}_i^{\rm true}\ln\frac{\tilde{N}_i^{\rm true}}{\tilde{N}_i^{\rm test}}\}. \tag{3.5}$$

Here $\tilde{N}_i^{\rm test}$ denotes the number of events predicted by the theoretical model over a range of oscillation parameters ω in the i^{th} bin and is given by

$$0.9\tilde{N}_i^{\rm test}(\omega,\xi) = \sum_{k=s,b} N_i{}^k(\omega)[1 + c_i^{(k)norm}\xi^{(k)norm} + c_i^{(k)tilt}\xi^{(k)tilt}\frac{E_i - \bar{E}}{E_{max} - E_{min}}] \tag{3.6}$$

where, $k = s(b)$ denotes signal(background), $c_i^{norm}(c_i{}^{tilt})$ denotes the change in number of events by the variation of the "pull" variable $\xi^{norm}(\xi^{tilt})$. In the above equation E_i is the mean reconstructed energy of the i^{th} bin, E_{min} and E_{max} are the maximum and minimum energy in the entire energy range and $\bar{E} = (E_{max} + E_{min})/2$ is the mean energy over this range. The systematic errors on the signal and background normalizations are shown in table(3.2). $\tilde{N}_i^{\text{true}}$ in eq. (3.5) corresponds to the sum of simulated signal and background events $\tilde{N}_i^{\text{true}} = N_i^s + N_i^b$.

0.9 The statistical χ^2 for each experiment is calculated using the signal and background event rates that are simulated according to the details provided by the respective experimental collaborations. The experimental details for T2HK & T2HKK have been obtained from the reference [146] where the systematic study is based on both near detector and far detector analysis. Inclusion of the near detector reduces the systematic uncertainties. For signal events we consider ν_e ($\bar{\nu_e}$) appearance channel events0.9 and ν_μ ($\bar{\nu_\mu}$) disappearance channel events in the neutrino (anti-neutrino) mode. The background events for the appearance channel0.9 come from intrinsic beam background, neutral current (NC) background, wrong-sign signal error and mis-identified muon events. The background for the disappearance channel is due to wrong sign muons and NC background. The systematic uncertainties on signals and backgrounds originate from the measurement of interaction cross section, energy scale uncertainty for reconstructed events, matter density profile, near to far extrapolation, far detector modelling etc. In this analysis we have considered an overall normalization error, that takes into account all the aforementioned sources of systematic uncertainty, as obtained in the reference [146]. For the overall background normalization uncertainty a slightly conservative error of 5% is taken. We have also considered 10% signal and background tilt errors as prescribed in reference [146]. The events for ESSνSB experiments are simulated based on [149]. ESSνSB proposes to use a MEMPHYS type detector [161, 183] which is also a water $\hat{\text{C}}$herenkov detector. ESSνSB experiment will also use a near detector to reduce the systematic uncertainties to less than 5%. But the analysis for ESSνSB near detector has not yet been performed. Therefore the ESSνSB collaboration (ref.[149]) considered a uniform 5% signal normalization error and 10% background normalization error for all the channels. However, the normalization errors are expected to decrease once the near detector analysis is performed. We have considered the signal and background normalization errors for ESSνSB the same as that of T2HK because the detectors for T2HK & ESSνSB are both water $\hat{\text{C}}$herenkov detectors. DUNE simulation in our work is based on reference [144]. Detailed study of

Channel	T2HK(295 km)	T2HK(1100 km)	DUNE	ESSνSB
ν_e appearance	3.2%(5%)	3.8%(5%)	2.5%(10%)	3.2%(5%)
$\nu_{\bar{e}}$ appearance	3.9%(5%)	4.1%(5%)	2.5%(10%)	3.9%(5%)
ν_μ disappearance	3.6%(5%)	3.8%(5%)	7.5%(15%)	3.6%(5%)
$\nu_{\bar{\mu}}$ disappearance	3.6%(5%)	3.8%(5%)	7.5%(15%)	3.6%(5%)

Table 3.2: The signal(background) normalization uncertainties of the experiments in percentage for various channels.

systematics uncertainties of DUNE is an ongoing project. The signal normalization uncertainties are due to flux, cross section, energy scale and fiducial volume uncertainties. The background channels in the appearance events for both neutrino and anti-neutrino modes are due to intrinsic beam background, particle misidentification, neutral current background, tau neutrino/antineutrino appearance background and wrong sign background. The disappearance backgrounds for neutrino(antineutrino) modes are due to neutrino(antineutrino) neutral current, antineutrino(neutrino)neutral current, antineutrino(neutrino) charged current. The normalization errors used for signal and background in DUNE experiment are given in 3rd column of table(3.2). The background normalization errors are higher with respect to the signal normalization errors due to the uncertainties in the tau neutrino/antineutrino CC background which cannot be constrained by near detector measurements. Besides the signal normalization error in table(3.2), the energy uncertainty in terms of signal and background "tilt" error of 2.5% for all channels has been taken into account as described in [144].

We have marginalized over the test parameters. The true values of the parameters

Oscillation parameters	True value	Test value
$\sin^2 2\theta_{13}$	0.085	0.07 – 0.1
$\sin^2\theta_{12}$	0.304	–
θ_{23}	42°(LO), 48°(HO)	$39° - 51°$
Δm^2_{21}	7.40 $\times 10^{-5} eV^2$	–
Δm^2_{31}	2.50 $\times 10^{-3} eV^2$	(2.35 – 2.65) $\times 10^{-3} eV^2$
δ_{CP}	$-180°$ to $+180°$	$-180°$ to $+180°$

Table 3.3: True values and marginalization ranges of neutrino oscillation parameters used in our numerical analysis.

and the marginalization ranges of the other parameters are as given in Table 4.1.

3.4 CP, Hierarchy and octant discovery potentials of HK, DUNE and ESSνSB experiments

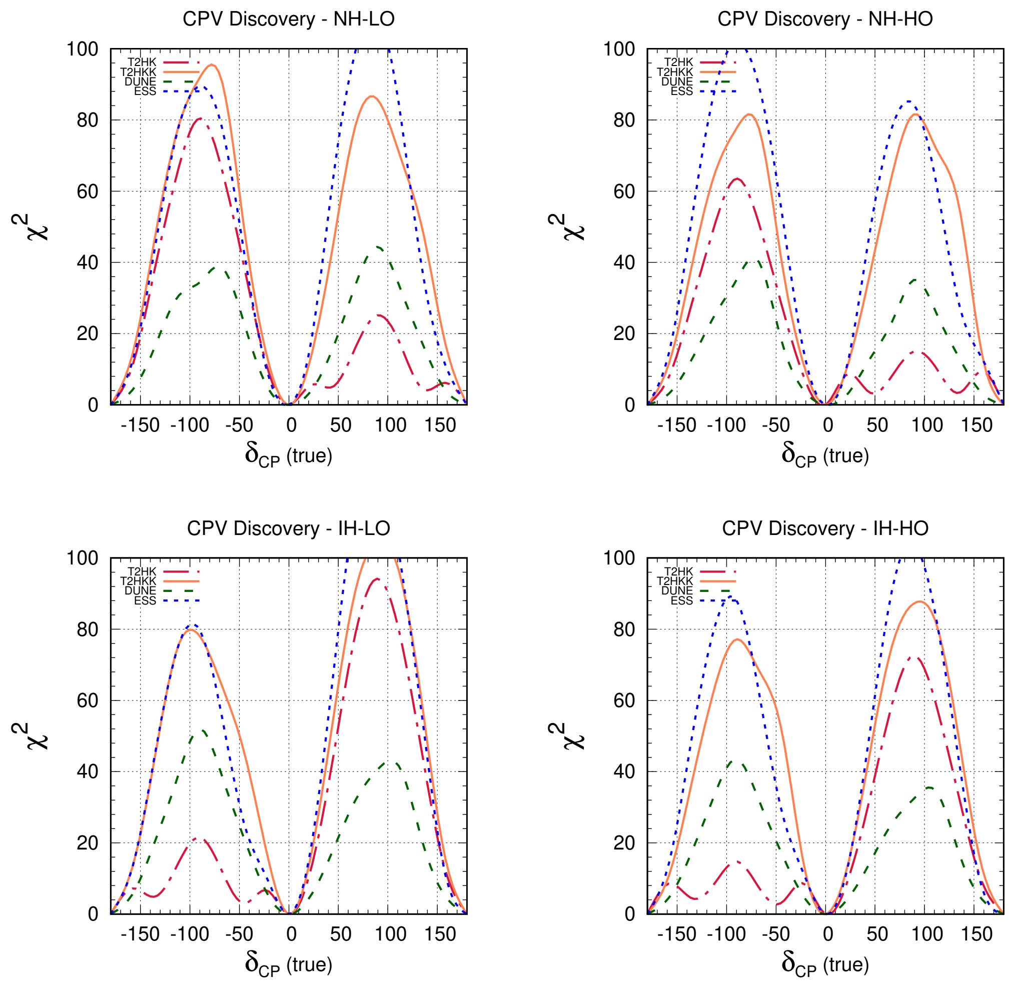

Figure 3.4: CP sensitivity in T2HK, T2HKK, DUNE and ESSνSB with all hierarchy-octant configurations, first(second) row represent NH(IH) and first(second) columns represent LO(HO).

In this section, we present a comprehensive analysis of the CP, hierarchy and octant discovery sensitivity of the experiments T2HK, T2HKK, DUNE and ESSνSB with their proposed configurations. The total protons on target (POT) for T2HK is 27×10^{21},

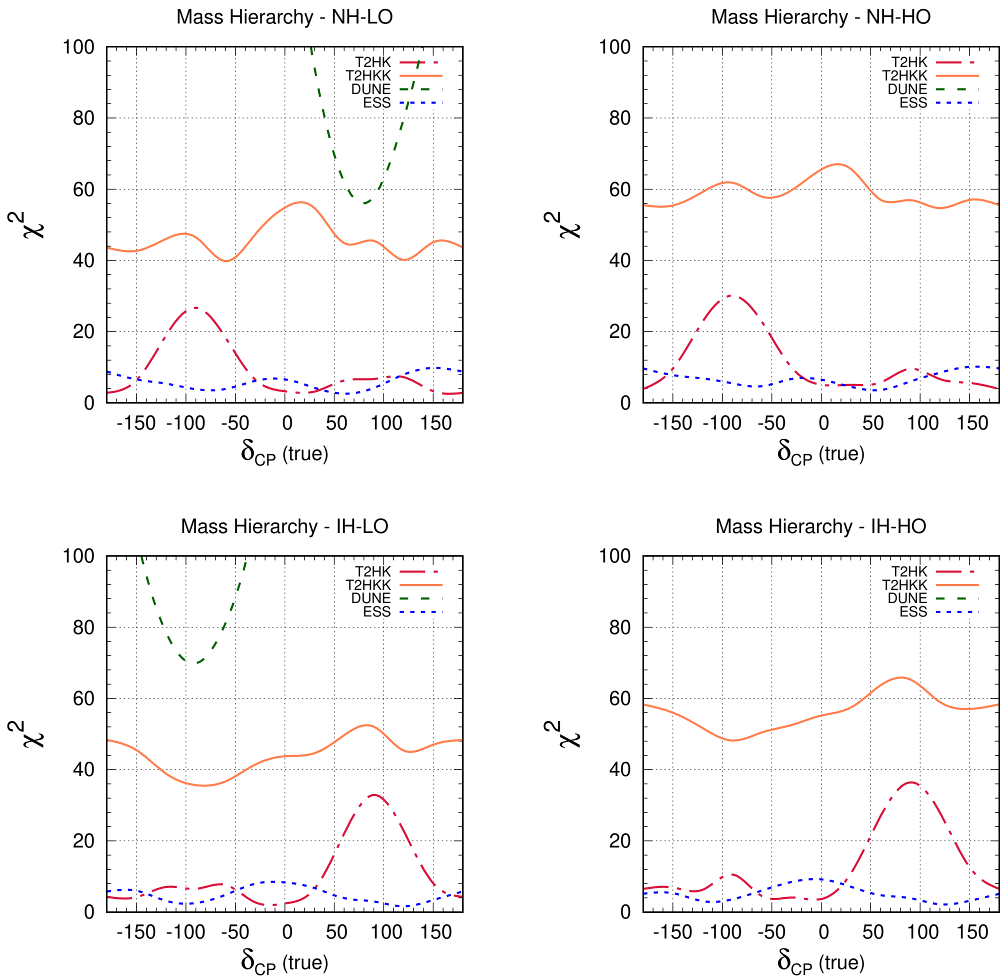

Figure 3.5: Mass hierarchy sensitivity in T2HK, T2HKK, DUNE and ESSνSB with all hierarchy-octant configurations, first(second) row represent NH(IH) and first(second) columns represent LO(HO)

DUNE is 10×10^{21} and ESSνSB is 27×10^{21} over the time of ten years for all the experiments.

We present the results for four true hierarchy-octant combinations – NH-LO, NH-HO, IH-LO & NH-HO. The true value of θ_{23} for LO is considered as 42° while for HO it is taken as 48° throughout our analysis unless otherwise mentioned. All the figures in this section show the performances of T2HK, T2HKK, DUNE and ESSνSB where their corresponding sensitivities are plotted in red, orange, green and blue colors respectively.

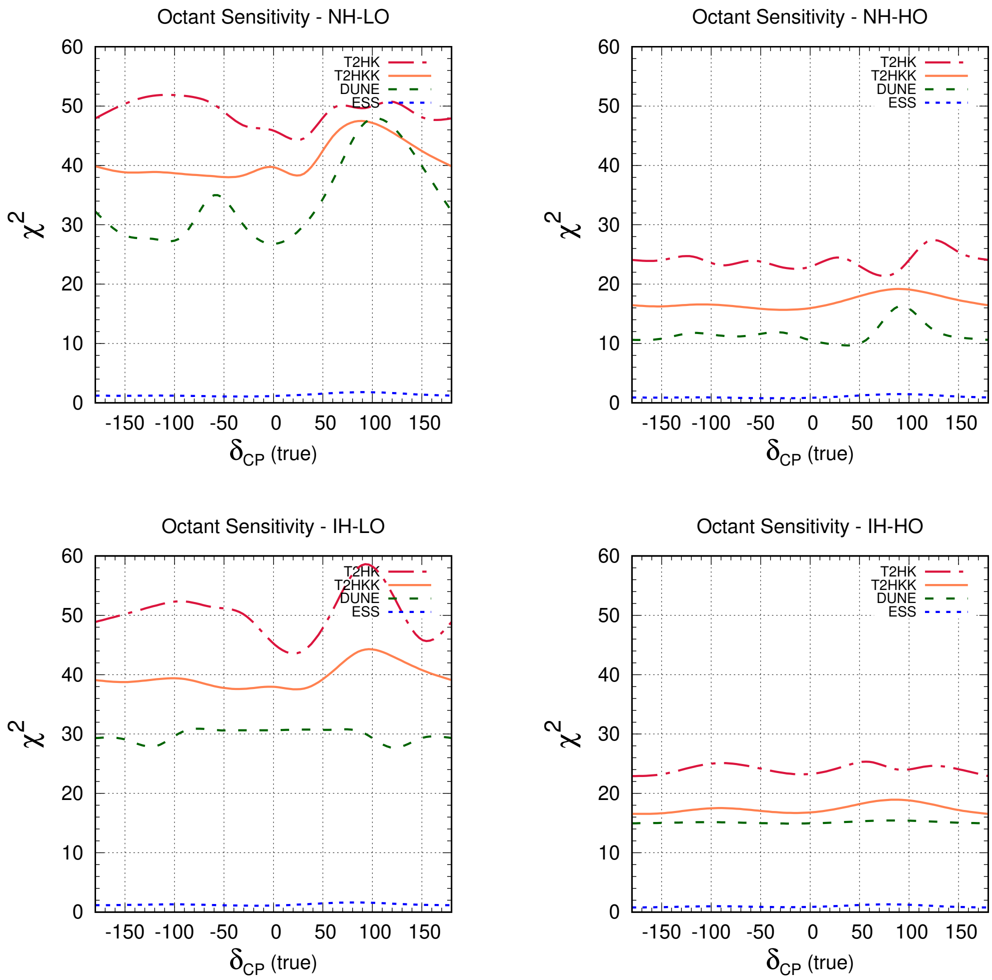

Figure 3.6: Octant sensitivity in T2HK, T2HKK, DUNE and ESSνSB with all hierarchy-octant configurations, first(second) row represent NH(IH) and first(second) columns represent LO(HO)

3.4.1 CP Sensitivity

Calculation of CP discovery sensitivity is performed by simulating the data for all true δ_{CP} values and comparing these with CP conserving values $\delta_{CP} = -180°,\ 0°\ \&\ 180°$. Marginalization is done over θ_{13}, θ_{23}, $|\Delta m^2_{31}|$ and hierarchy. The CP discovery potential of the experiments under consideration is shown in figure 3.4. The maximum CP discovery sensitivity can be achieved for $\delta_{CP} = \pm 90°$. For T2HK the CP discovery potential is seen to be less in one of the half-planes of δ_{CP}. This is due to the presence of wrong hierarchy solutions. In general T2HKK has a better CP sensitivity because at the second oscillation maxima the CP effect is larger and can compensate for the loss in flux due to a higher baseline [146]. In ref. [146] it was shown that the difference in the CP asymmetry between CP conserving and CP violating values is more for the 1100 km baseline. At the χ^2 level this gets reflected in the tension between the neutrino and the antineutrino contribution to the χ^2. For the T2HK experiment at 295 km the oscillation peak and the flux peak coincide and the probability for $\delta_{CP} = 0$ and $\pm180°$ are equidistant from the probability at $\pm90°$. However for the 1100 km baseline as can be seen from the probability plot for either NH or IH as the true hierarchy, for neutrinos $\delta_{CP} = -90°$ is closer to $\pm180°$ while for antineutrinos $\delta_{CP} = 0$ is closer to $\delta_{CP} = -90°$. This creates a tension between the neutrino and the antineutrino χ^2 which gives a better sensitivity to T2HKK as one of its baselines is at 1100 km. For DUNE, the wrong hierarchy solutions get resolved and hence the sensitivities do not suffer a drop in one half plane of δ_{CP} as in T2HK. In this case also, the neutrino and antineutrino tension can enhance the overall χ^2 for CP violation [170]. However, since the statistics of DUNE is lower compared to T2HKK and T2HK it has a lower CP discovery sensitivity. The ESSνSB probability has a sharp variation with respect to δ_{CP} which makes it promising to study the CP discovery sensitivity. The CP violation discovery potential of ESSνSB can be seen from the blue solid line and one can note that it is comparable to that of T2HKK (orange).

3.4.2 Mass Hierarchy Sensitivity

Mass hierarchy sensitivity is calculated by assuming a true hierarchy in the data and testing it by fixing the opposite hierarchy in theory. Marginalization is done over θ_{13}, θ_{23}, $|\Delta m^2_{31}|$ and δ_{CP}. The figure 3.5 demonstrates the mass hierarchy sensitivity of the proposed experiments. It is seen that for T2HK the hierarchy sensitivity is much reduced in the UHP for NH and in the LHP for the IH. This is due to the presence of hierarchy degeneracies between NH-LO and IH-LO (green and red band) as can be seen from fig. 3.3. Similarly for IH, the unfavourable zone for hierarchy determination is the LHP. Note that the WH-WO solutions are removed because of combined neutrino antineutrino run. For T2HKK the hierarchy 0.9 sensitivity is much higher. In this case the detectors are at two different baselines hence oscillation effects at both baselines will contribute. From the mass hierarchy plots fig. 3.5 we can conclude that there had been a significant increment in the overall mass hierarchy sensitivity over the previous case of both detectors being at 295 km baseline. In particular the degeneracy faced by the T2HK setup in the unfavourable region of δ_{CP} can be resolved by moving one detector to Korea. This is because for the Korean detector the behavior of the probability near second oscillation maxima shows that the degeneracy for neutrinos (NH) and for antineutrinos (IH) occur only over a small range of δ_{CP} values as discussed in the earlier section.

For DUNE because of matter effect the hierarchy degeneracy is lifted. DUNE has very high hierarchy sensitivity and for HO the $\Delta\chi^2$ value is > 100.

We note that ESSνSB has comparable hierarchy sensitivity to that of T2HK in UHP of NH and LHP of IH. This low hierarchy sensitivity can be ascribed to the hierarchy-δ_{CP} degeneracy for most of the values of δ_{CP} corresponding to both neutrinos and antineutrinos as can be seen from the fig. 3.3.

3.4.3 Octant Sensitivity

To resolve the octant ambiguity of θ_{23} is one of the important goals of current and up-coming LBL experiments. The figure 3.6 shows the ability of the various configurations to exclude the wrong octant of θ_{23} plotted as a function of true δ_{CP}. Octant sensitivity is calculated by assuming a true octant in data and considering the opposite octant as test in the theory. Marginalization is done over θ_{13}, θ_{23}(over the range of opposite octant), $|\Delta m^2_{31}|$, hierarchy and δ_{CP}.

For a true LO greater than 5σ sensitivity is obtained for all the experiments excepting ESSνSB . 0.9 For true HO, only T2HK experiment can attain 5σ octant sensitivity. In general, the best octant sensitivity is achieved by the proposed T2HK experiment for all the cases. The octant sensitivity for T2HKK experiment is less as compared to T2HK, since as is evident from the probability discussions the octant sensitivity gets reduced for the 1100 km baseline. We also find that the octant sensitivity for ESSνSB is also low because of the presence of octant degeneracy.

We find that the sensitivity is higher for a true lower octant for all the experiments.

There are two reasons for this. Firstly for non-zero θ_{13} the χ^2 vs θ_{23} curve is not symmetric about 45°. The two degenerate solutions in opposite octants are approximately related by $\theta_{23}^{LO} = 91.5^\circ - \theta_{23}^{HO}$ [184]. This implies that for a true θ_{23} of 42° the degenerate minima will be at 49.5° while for a true $\theta_{23} = 48^\circ$ it will be at 43.5°. The octant sensitivity of DUNE is seen to be slightly less as compared to T2HK and T2HKK in most of the parameter range. This can be attributed to the lesser detector volume of DUNE. The underlying physics issues behind octant sensitivity of DUNE has been discussed in detail in [170].

3.5 Neutrino and antineutrino run optimization in T2HK & T2HKK

In this section we are presenting a study for the neutrino antineutrino run time optimization. The proposed total runtime for the T2HK and T2HKK experiment is 10 years, which will consists of 2.5 years ν run and 7.5 years $\bar{\nu}$ run. This 1ν : $3\bar{\nu}$ runtime ratio was chosen to keep the number of neutrino events comparable to that of the antineutrino events. In this section, we explore the possibilities of acquiring better sensitivities by considering 3ν : $1\bar{\nu}$ and 1ν : $1\bar{\nu}$ as alternative runtime ratios.

3.5.1 Analysis of Mass hierarchy sensitivity

Fig. (3.7) and fig. (3.8) represent the mass hierarchy sensitivities of T2HK, T2HKK. In each plot three different run time ratios of 2.5ν + $7.5\bar{\nu}$, 7.5ν + $2.5\bar{\nu}$, 5ν + $5\bar{\nu}$ are shown by blue, magenta and green curves respectively. From all the plots of fig.3.7 corresponding to the true configurations – NH-LO, NH-HO, IH-LO and IH-HO we find that for T2HK all the three runtime ratios give hierarchy sensitivity in the same ballpark. The combinations $7.5+2.5$ and $5+5$ fare slightly better because of enhanced statistics except for the UHP of true IH-HO where $7.5 + 2.5$ is slightly lower than the other two cases. This is because in the UHP for IH-HO the neutrino probability is impaired by WH-WO and RH-WO degeneracies unlike that in antineutrinos. Thus, the wrong octant solutions can be removed by considering more antineutrino runs as can be

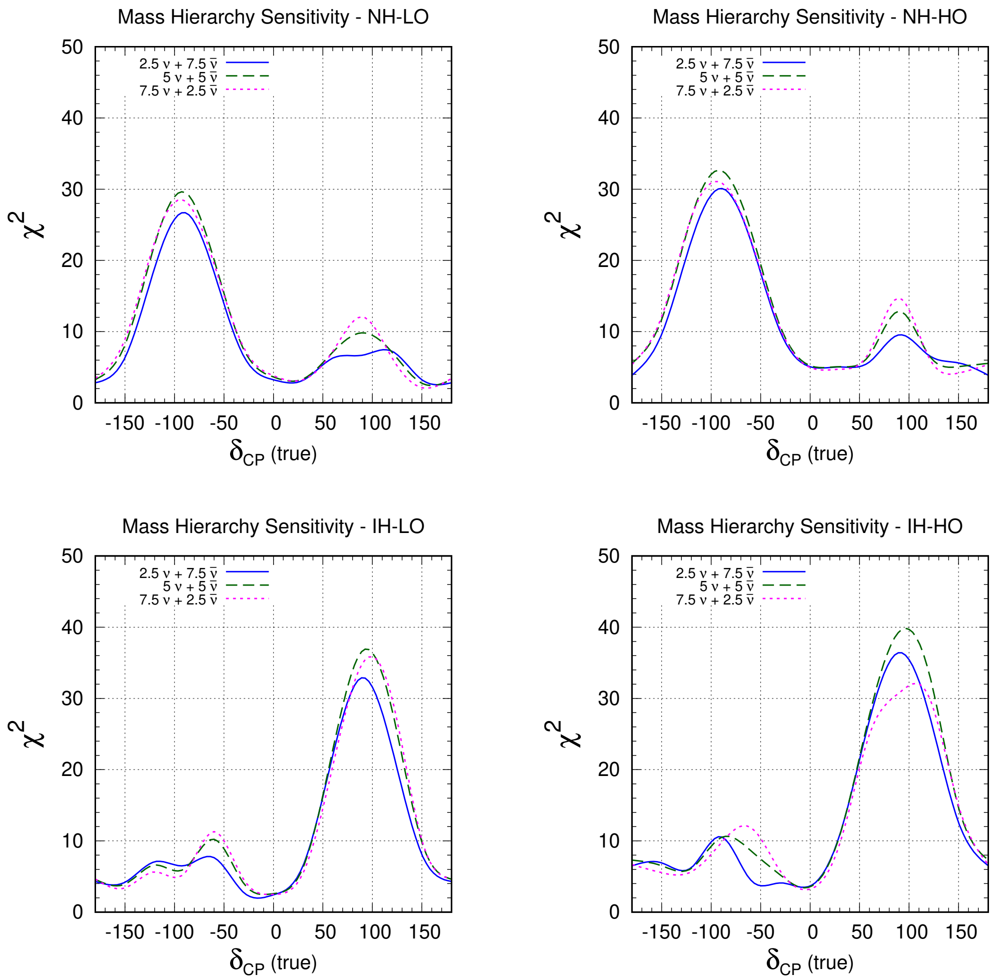

Figure 3.7: Mass hierarchy χ^2 vs δ_{CP} plots for T2HK (true NH first row and true IH second row). The labels signify the ν+$\bar{\nu}$ runs.

seen from the UHP of true IH-HO configuration in the fig. 3.7 where the proposed 2.5ν + 7.5$\bar{\nu}$ gives better sensitivity than 7.5ν + 2.5$\bar{\nu}$. However for T2HKK from fig. (3.8) we see that 7.5ν + 2.5$\bar{\nu}$ and 5ν + 5$\bar{\nu}$ give better sensitivity when compared to the proposed ratio of 2.5ν + 7.5$\bar{\nu}$ for some values of δ_{CP}. If we compare the best two cases we infer that for 7.5ν + 2.5$\bar{\nu}$ the significance is quite high with respect to the significance of 2.5ν + 7.5$\bar{\nu}$ both in upper and lower half plane, except the region with $-20^\circ < \delta_{CP} < 40^\circ$ where 2.5ν + 7.5$\bar{\nu}$ gives better hierarchy sensitivity. The greater hierarchy sensitivity in T2HKK can be understood from fig. 3.3 which depicts the oscillation probabilities. For 1100 km baseline in the region with $\delta_{CP} < -20^\circ$ and $\delta_{CP} > 40^\circ$ the neutrino appearance probabilities are not degenerate w.r.t. hierarchy, hence sensitivity

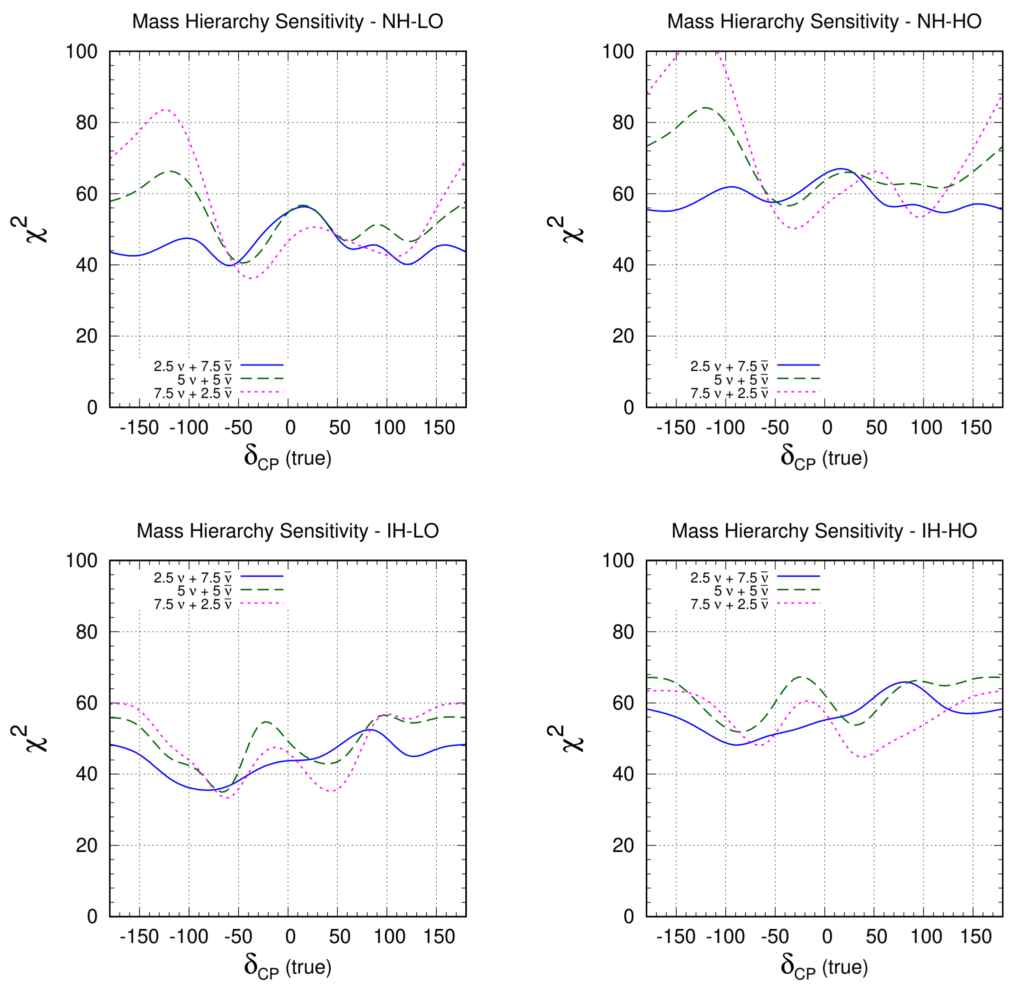

Figure 3.8: Mass hierarchy χ^2 vs δ_{CP} plots for T2HKK (true NH first row and true IH second row). The labels signify the ν+$\bar{\nu}$ runs.

in this region is governed by neutrino appearance, in the region $-20^\circ < \delta_{CP} < 40^\circ$ the sensitivity is governed by antineutrino appearance because in this region neutrino appearance probability is degenerate but antineutrino appearance is non-degenerate. Considering both baselines the IH sensitivity behaves differently because of the non-degenerate behaviour of the probabilities at 1100 km baseline. Similar to NH we obtain better sensitivities at the regions $\delta_{CP} < -20^\circ$ and $\delta_{CP} > 40^\circ$ for 7.5ν + 2.5$\bar{\nu}$ and $-20^\circ < \delta_{CP} < 40^\circ$ for 2.5ν + 7.5$\bar{\nu}$. We can conclude from this discussions that in the regions of maximum CP violation 5ν+5$\bar{\nu}$ give somewhat better sensitivity for T2HKK experiment.

3.5.2 Analysis of Octant sensitivity

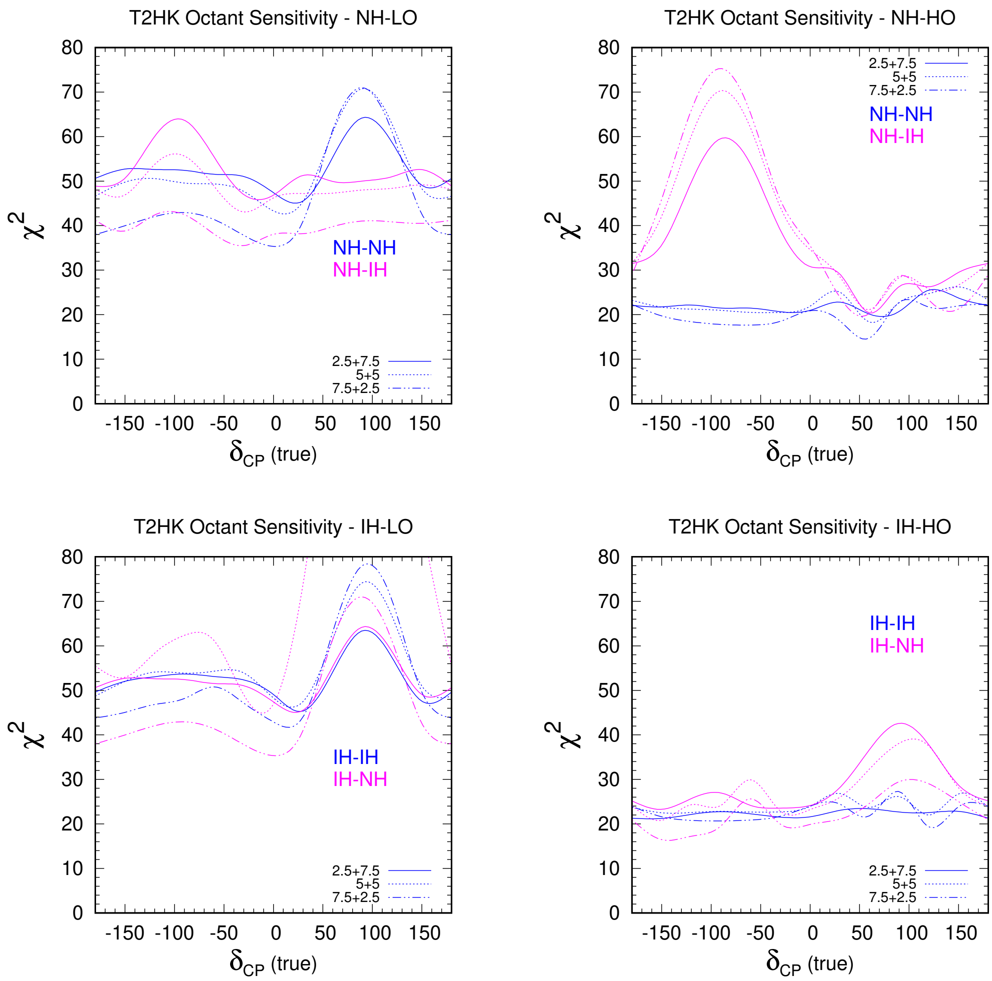

Figure 3.9: Octant sensitivity χ^2 vs δ_{CP} plots for T2HK (true NH first row and true IH second row). The labels signify the ν+$\bar{\nu}$ runs.

Since the octant degeneracies involving neutrinos and antineutrinos behave in an opposite way there are interesting interplay of run time ratios for octant sensitivity This issue has been delved in detail in [170] for DUNE. However for DUNE the WH solutions are largely absent and therefore one had to deal with only right hierarchy-wrong octant solutions. But for T2HK hierarchy degeneracy is also present and so one encounters wrong octant solutions for both right and wrong hierarchy, which further complicates the issue.

Fig. 3.9 and fig. 3.11 show the octant sensitivity of T2HK and T2HKK experiments for various true values of δ_{CP} with respect to different true hierarchy–octant combinations. In each plot we show the octant sensitivity corresponding to three different run time ratios of 2.5ν + 7.5$\bar{\nu}$, 5ν + 5$\bar{\nu}$ and 7.5ν + 2.5$\bar{\nu}$ shown by solid, dotted and dash-dotted curves respectively. The blue curves correspond to right hierarchy whereas magenta curves correspond to wrong hierarchy. Marginalization over hierarchy would chose the lower values of χ^2 in each case.

In the top left panel of fig. 3.9 where true hierarchy–octant configuration is NH-LO ($\theta_{23}(true) = 42°$) it can be seen that the higher sensitivity for all values of δ_{CP} is obtained from the proposed run-time ratio of 2.5ν + 7.5$\bar{\nu}$ for the right hierarchy in the LHP of δ_{CP} and over the whole range of δ_{CP} for the wrong hierarchy. If hierarchy is known to be NH then in the upper half plane 5+5 or 7.5+2.5 gives better results. This can be understood by relating to the corresponding probabilities shown in the top panel of fig. 3.3. In the LHP of the top right panel of fig. 3.3, we can see that the NH-LO(green) band for antineutrinos do not suffer from octant degeneracies for both right and wrong hierarchy (the yellow and blue bands). Thus more antineutrinos help to have a higher octant sensitivity in both the cases. In the UHP for wrong hierarchy (the magenta curves) the antineutrino run helps in removing the WH-WO solutions occurring with the same CP. However since neutrinos do not suffer from any degeneracy between NH-LO and NH-HO in the UHP, 7.5+2.5 or 5+5 gives better results.

For IH-LO, in the LHP neutrino has octant degeneracy for wrong as well as right hierarchy for wrong δ_{CP} as can be seen by comparing the red band with the yellow and the blue bands respectively in fig. 3.3. But antineutrino probabilities do not have any octant degeneracy. Thus the plan with more neutrinos is worse than that with equal or more antineutrinos. On the other hand in the UHP neutrino probability does not suffer from octant degeneracy as can be seen from the red band in the left panel of fig. 3.3 while the antineutrino probabilities have octant degeneracies. Thus for both right and wrong hierarchy the run with greater proportion of neutrinos is better. For wrong hierarchy 5+5 fares much better as in the LHP.

For NH-HO in the LHP we see that the WH-WO solutions give a much higher χ^2 and a run plan with more neutrinos perform better. This can be easily understood by

	$\theta_{23}(test)$ (total minima)	$\theta_{23}(test)$ (disapp minima)	App(ν)	App($\bar{\nu}$)	Disapp(ν)+ Dispp($\bar{\nu}$)	Total
10+0	43.5	43.3	13.94	0	0.6	14.54
7.5+2.5	43.6	43.2	12.79	9.63	1.83	24.25
5+5	43.7	43.2	11.44	13.66	3.08	28.17
2.5+7.5	43.8	43.2	9.37	15.67	3.99	29.03
0+10	44	43.1	0	15.79	5.17	20.96

Table 3.4: Contributions of χ^2 from appearance and disappearance channels for true NH-HO and $\delta_{CP} = -90°$.

comparing the yellow band and the red band from which it can be observed that there is no such degeneracy in the neutrino mode. However for the antineutrino probability WH-WO-Rδ_{CP} degeneracies can be observed. The NH-LO band (green) corresponding to the RH-WO solution is closer to the NH-HO band and thus the χ^2 for the RH case is lower. In this case also neutrino probabilities do not show any degeneracy. However, it is seen that even then the $2.5+7.5$ and $5+5$ give slightly better sensitivity even though antineutrinos have degeneracy for this case. In order to understand this in table 3.4 we display the contribution of the different components to χ^2. We ignore a constant prior term in this table. From the table we can see that for 10+0 i.e only neutrino run the contribution from the antineutrinos to the appearance channel χ^2 is zero. As we decrease the neutrino component and increase the antineutrino component the appearance channel contribution from the neutrinos get reduced whereas the antineutrino contribution is enhanced. Since neutrinos do not have any degeneracy for NH-HO whereas antineutrinos possess degeneracies with wrong CP the minima for neutrino and antineutrino do not come in the same position. The overall minima is controlled by the neutrinos because of more statistics. But since this point is not the minima for the antineutrinos they give a large octant sensitive contribution. Thus the tension between neutrinos and antineutrinos help in raising the χ^2 for the cases of mixed runs in spite of degeneracies in the antineutrino channel. There is another interesting feature which can be noticed in this table which is that the disappearance channels also contribute towards octant sensitivity. This is contrary to our expectations because the leading term in this channel goes as $1-\sin^2 2\theta_{23}\sin^2 \Delta m^2_{31}L/4E$ and does not have any octant sensitivity.

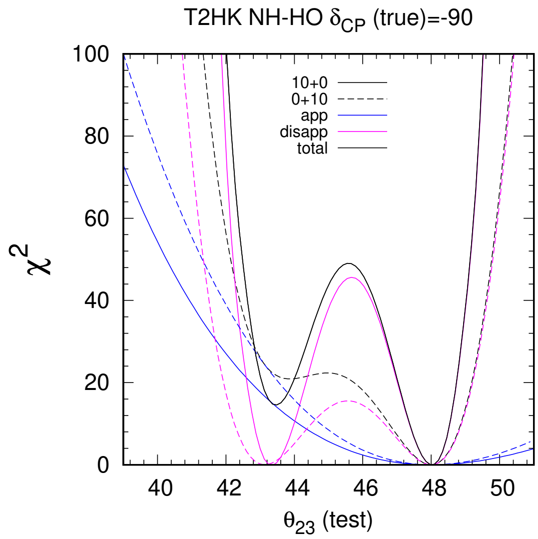

Figure 3.10: Octant sensitivity χ^2 vs test θ_{23} (degrees) plots for T2HK.

To understand this behaviour in fig. 3.10 we plot the disappearance and appearance χ^2 for neutrinos and antineutrinos separately as a function of test θ_{23}. True θ_{23} is taken as 48°. It is seen from the figure and the table that the the global minima does not come at the disappearance minima but the appearance χ^2 being a very steeply rising quantity tends to shift the global minima towards higher values of θ_{23}. This shift is more as the antineutrino component is increased since the antineutrino χ^2 for appearance channel is steeper as compared to the neutrino χ^2. Since the global minima is not the disappearance minima there is finite octant sensitive contribution from the disappearance channel as well.

For IH-HO (blue band) in fig. 3.3 there is WH-WO degeneracy with NH-LO (green band) at same CP value in the LHP for neutrinos. Antineutrinos on the other hand have degeneracy with both IH-LO (red band) and NH-LO (green band). However, still the runs with $2.5 + 7.5$ give similar results with $5 + 5$ and $7.5 + 2.5$. This can again be attributed to the tensions between neutrinos and antineutrinos as described for NH-HO. For the UHP IH-HO has degeneracy (both WH-WO and RH-WO, green and red bands respectively) for neutrinos. On the other hand for antineutrinos there is no degeneracy. Therefore $7.5 + 2.5$ give better sensitivities for the WH solutions. Note that for the

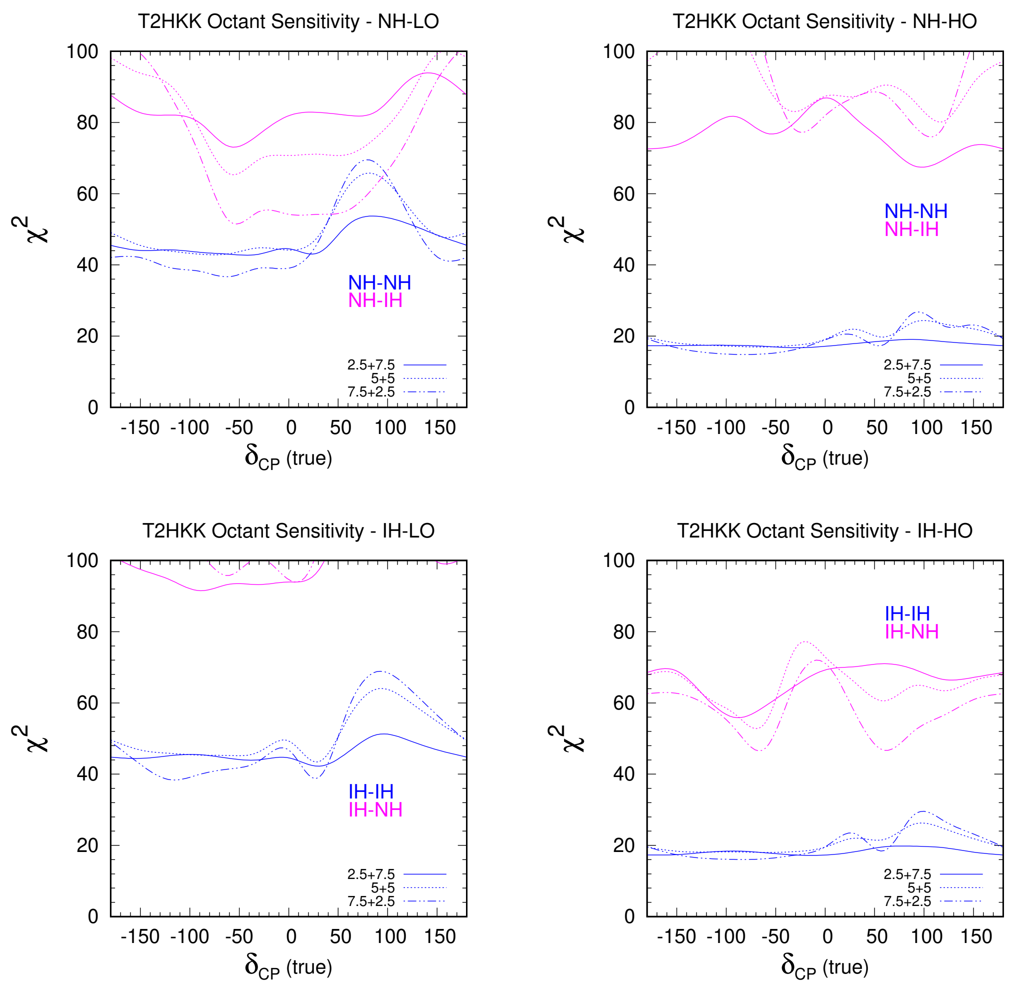

Figure 3.11: Octant sensitivity χ^2 vs δ_{CP} plots for T2HKK (true NH first row and true IH second row). The labels signify the ν+$\bar{\nu}$ runs.

WH solutions for neutrinos the degeneracy is at right CP value and hence neutrino and antineutrino minima both occur for right CP. On the other hand for the right hierarchy solutions the neutrino minima occurs in the LHP while the antineutrino minima occurs in the UHP. This the tensions between neutrino and antineutrino occur here also and all the three runtime proportions give similar results.

Fig. 3.11 shows the octant sensitivity χ^2 vs true δ_{CP} of T2HKK with NH-LO, NH-HO, IH-LO, IH-HO as true hierarchy–octant configurations, where each plot shows right hierarchy (blue) and wrong hierarchy (magenta) curves for three different run time ratios 2.5ν + 7.5$\bar{\nu}$ (solid), 5ν + 5$\bar{\nu}$ (dotted) and 7.5ν + 2.5$\bar{\nu}$ (dot-dashed). Note that we will get the solutions with lower χ^2 if we marginalize over the hierarchy.

Owing to its longer baseline of 1100 km we have shown in fig. 3.8 that T2HKK has high hierarchy sensitivity when compared to its counter-proposal T2HK. Thus the wrong hierarchy-octant solutions do not occur here. As a result it can be understood from fig. 3.11 that the wrong hierarchy solutions NH-IH (magenta) curves have comparatively higher χ^2 in all the four cases and they will get removed once the hierarchy is marginalized.

In section 3.2 we have given a detailed account of how the octant sensitivity at 1100 km baseline is very low because of the degeneracies. However, since T2HKK is a hybrid setup with one detector placed at 295 km and another at 1100 km, the probabilities at both baselines govern the physics of this experiment. Thus, one can attribute the considerably large octant sensitivity arising in fig. 3.11 to be mainly coming from the 295 km baseline. Note that these can be only right hierarchy solutions as the wrong ones get removed at 1100 km.

For instance, in the top left panel of the figure where we assume NH-LO as the true configuration, the proposed run time of $2.5\nu + 7.5\bar{\nu}$ (solid) or $5\nu + 5\bar{\nu}$ (dotted) give a better solution than $7.5\nu + 2.5\bar{\nu}$ in the LHP. This behaviour is the same for the right hierarchy solutions, shown by blue curves when true combination is NH-LO as can be seen from the top left panel of fig. 3.9. Similarly in the UHP $7.5\nu + 2.5\bar{\nu}$ or $5\nu + 5\bar{\nu}$ is better run, as neutrinos corresponding to NH-NH do not suffer from any degeneracy as seen from fig. 3.3.

To sum it up, for all true hierarchy-octant combinations, the conclusions corresponding to NH-NH solutions (blue curves) of fig. 3.11 follow the physics at 295 km baseline i.e. T2HK and can be understood from the detailed description of the NH-NH solutions (blue curves) of fig. 3.9 presented before.

3.5.3 Analysis of CP discovery potential

Fig. 3.12 shows the CP violation sensitivity of T2HK for different true hierarchy-octant combinations of NH-LO, NH-HO, IH-LO, IH-HO. Each plot shows the sensitivity corresponding to the run time ratios of $2.5\nu + 7.5\bar{\nu}$ (blue-solid), $5\nu + 5\bar{\nu}$ (magenta-dotted) and $7.5\nu + 2.5\bar{\nu}$ (green-dash-dotted). The figures show that in all cases the

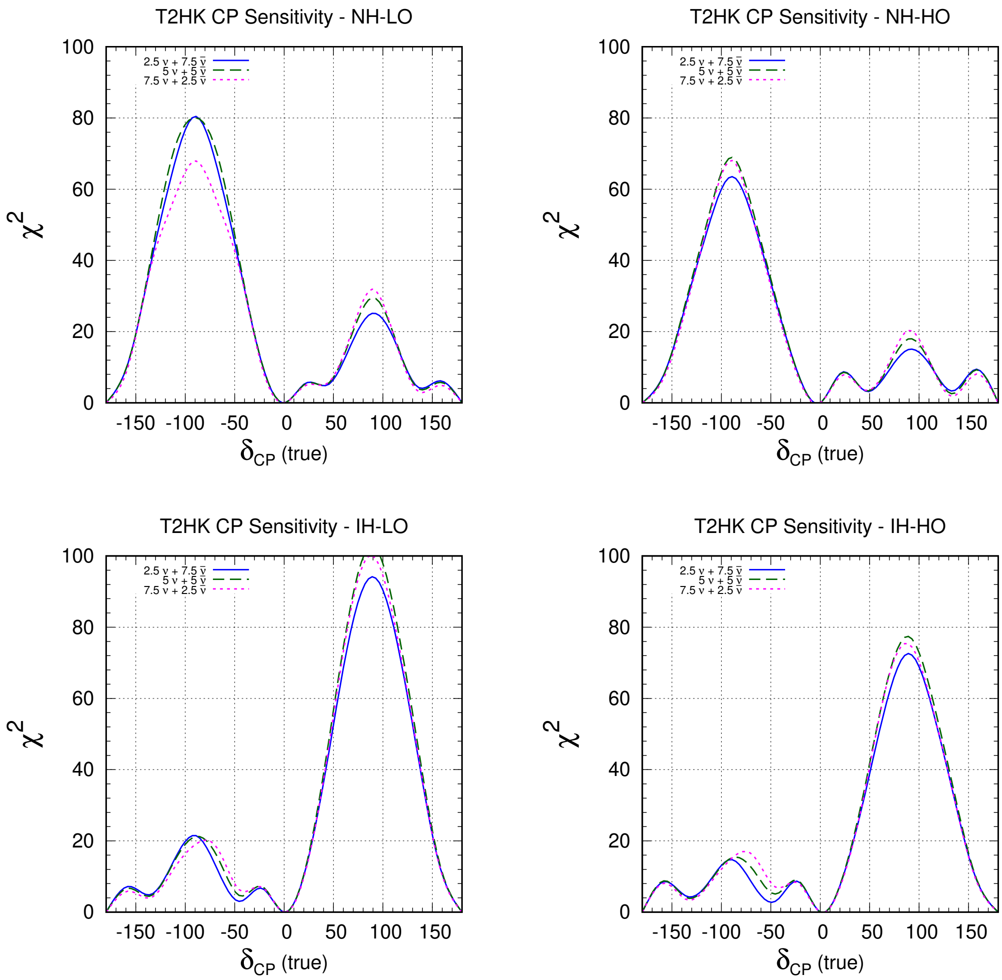

Figure 3.12: CP discovery potential χ^2 vs δ_{CP} plots for T2HK (true NH first row and true IH second row). The labels signify the ν+$\bar{\nu}$ runs.

CP discovery potential is much less in one of the half-planes. This can be attributed to the presence of wrong hierarchy solutions as can be seen in fig 3.8. However, we checked that the minima always occurs with the right octant. It is known that the role of antineutrinos for T2HK baseline and energy is to remove the wrong octant solutions [185]. Therefore, more neutrinos will help because of enhanced statistics. This can be seen from the plots in fig. 3.12 which show that the 1:1 or 3:1 ratios give slightly better results excepting true NH-LO. For this case, as can be observed from the left plot in the top panel, around the maximal δ_{CP} in the LHP, the sensitivity of 5ν + $5\bar{\nu}$ gives almost the same result as the proposed 2.5ν + $7.5\bar{\nu}$. However, the sensitivity of 7.5ν + $2.5\bar{\nu}$ i.e. for more neutrino run, is lower. This is because as seen from fig. 3.3

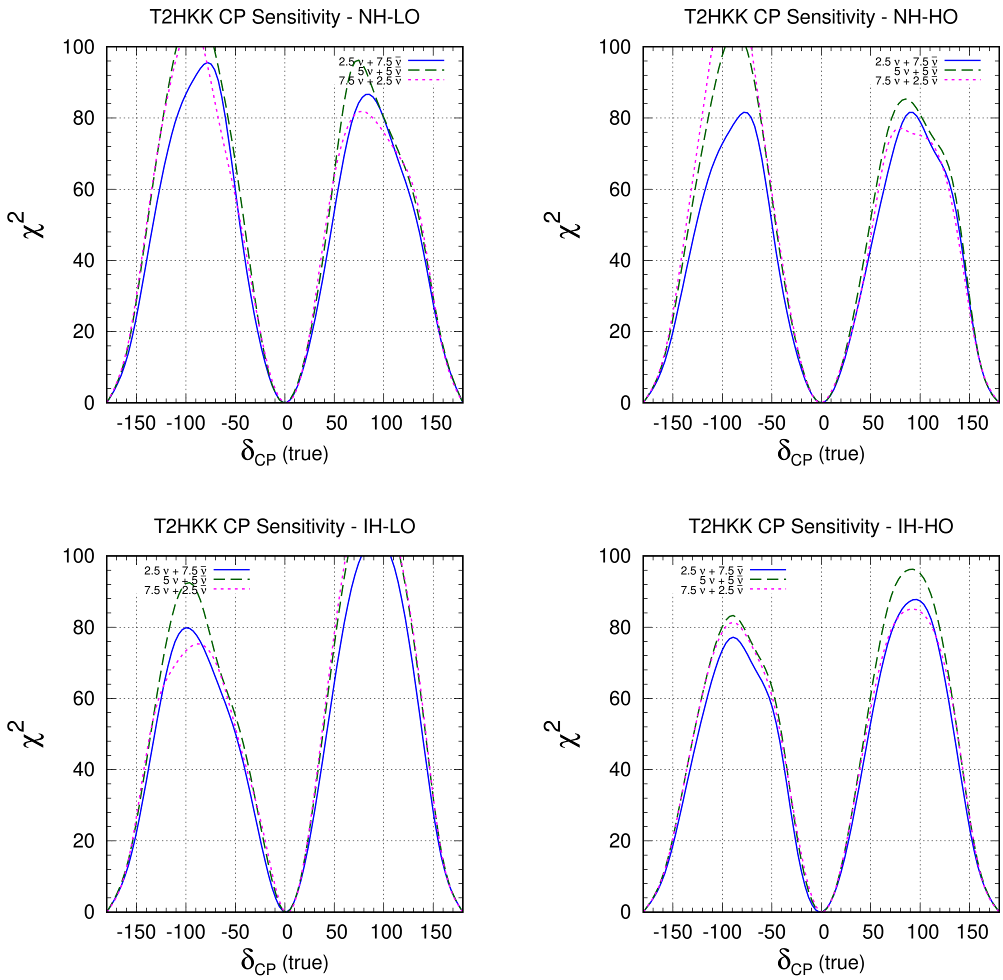

Figure 3.13: CP discovery potential χ^2 vs δ_{CP} plots for T2HKK (true NH first row and true IH second row). The labels signify the ν+$\bar{\nu}$ runs.

NH-LO is degenerate with NH-HO at $\delta_{CP} = 0, \pm 180$ and IH-HO for right δ_{CP}. But, in the case of antineutrinos NH-LO has degeneracy only with IH-LO at right δ_{CP}. As a result more antineutrinos are helping the sensitivity.

Fig. 3.13 displays the CP discovery potential of T2HKK. One major difference between the sensitivity of T2HK (in fig. 3.12 and T2HKK is that the UHP of true NH and the LHP of the true IH no longer suffer from degeneracy coming from the wrong hierarchy solutions as these get removed at the 1100 km baseline. On the other hand the wrong octant solutions are addressed by the 295 km baseline as seen earlier. Overall CP discovery potential of 5ν + 5$\bar{\nu}$ is comparatively better than the proposed run of 2.5ν + 7.5$\bar{\nu}$ years in all the four cases.

3.6 Optimal Exposures

In the earlier section we have delineated the sensitivities of the different experiments and compared the performances using the proposed plans. These being very high statistics experiments in some cases very high sensitivity is seen to be achieved. In this section we present the exposure required by each experiment to achieve 5σ sensitivity for 60% values of δ_{CP}. We also present the optimum exposure that is needed by each experiment to attain 5σ significance for hierarchy and octant sensitivity. We furnish our results for two representative hierarchy-octant configurations NH-LO(blue) and IH-HO(red). Stand alone experiments (experiment + T2K + NOνA) are depicted by solid(dashed) lines. The total POT for T2K is 8×10^{21} and the runtime considered is 4 years neutrino and 4 years antineutrino mode. While, in case of NOνA the total POT is 7.3×10^{20} with a runtime of 4 years neutrino and 4 years antineutrino mode. For true LO and HO we have taken representative values of θ_{23} as 42° and 48°.

In fig.3.14 we display the fraction of δ_{CP}(true) values for which the experiments can observe CP violation with minimum 5σ significance. For calculating the fraction of δ_{CP} values we compare the true δ_{CP} values against the CP conserving test δ_{CP} values of 0° and $\pm 180^\circ$. The fraction of δ_{CP} for more than 5σ CP discovery significance is the ratio of true δ_{CP} values for which the CP significance is more than 5σ to the total number of δ_{CP} values. We have also marginalized over θ_{13}, θ_{23}, Δm^2_{31} and hierarchy in test. The fig. 3.14 contains three plots for experiments T2HKK(leftmost), DUNE(middle) and ESSνSB (rightmost). Each plot has two sets of lines, solid and dashed, solid line represents the sensitivity of the stand alone experiment whereas the dashed line represents the experiment added with T2K+NOνA . In each plot true NH-LO(IH-HO) is depicted by blue(red) curve. We see that 60% coverage in δ_{CP}(true) values is obtained by an exposure of 1100 kt-yr and 1200 kt-yr of T2HKK (each detector) for NH-LO and IH-HO respectively. The minimum exposure remains approximately same even after addition of T2K+NOνA data. However for DUNE 60% coverage in δ_{CP}(true) is never reached but addition of T2K+NOνA increases the CP fraction. If we rather consider 40% coverage in δ_{CP}(true) for DUNE(DUNE+T2K+NOνA) we see that the exposure is 320 kt-yr(200 kt-yr) considering true NH-LO and 400 kt-yr for IH-HO only if

T2K+NOνA is added with DUNE . Lastly, ESSνSB (ESSνSB +T2K+NOνA) experiment requires an exposure of 4500 kt-yr(3500 kt-yr) to reach minimum 5σ sensitivity for 60% values of δ_{CP} for NH-LO and 5000 kt-yr(4000 kt-yr) for IH-HO. The above numbers correspond to approximately 6 years(6.5 years) of running of T2HKK and 9 years(10 years) of running of ESSνSB with their proposed volumes for NH-LO(IH-HO).

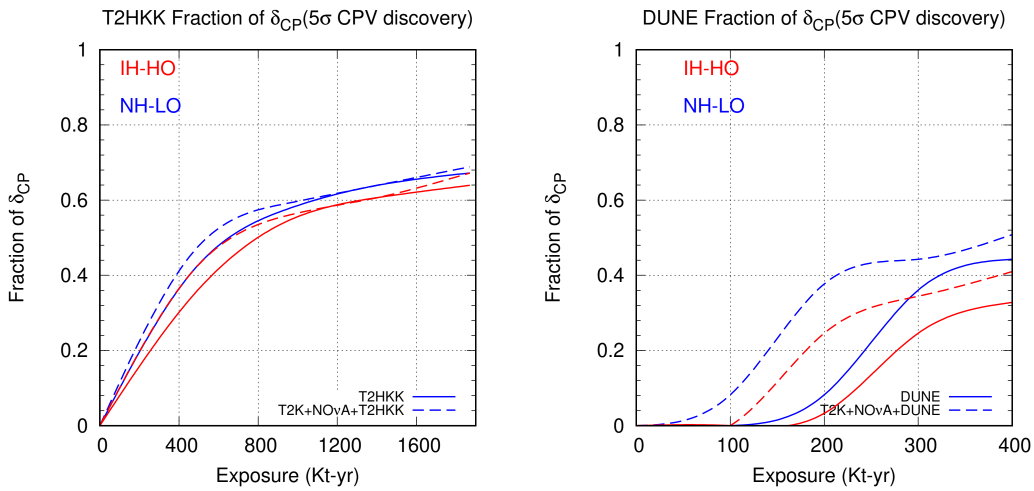

Figure 3.14: Fraction of δ_{CP} in T2HKK, DUNE and ESSνSB versus exposure for 5σ CPV sensitivity.

In fig. 3.15 we plot two sets of mass hierarchy χ^2 vs exposure in kt-yr for T2HKK and DUNE in the left and the right panels respectively. The blue (red) solid lines correspond to the sensitivity of true NH-LO (IH-HO) configuration of only the concerned experiment. The dashed lines represent the same when added with $3\nu + 3\bar{\nu}$ NOνA and $4\nu + 4\bar{\nu}$ T2K runs. We marginalized over true δ_{CP} in the range $[-180°, 180°]$.

From the left panel in fig. 3.15 we observe that considering only T2HKK the optimal exposure for 5σ hierarchy sensitivity is $\sim$ 1080 kt-yr for NH-LO and 680 kt-yr for IH-HO. This corresponds to volume of one detector. Therefore the total exposure for two detectors is 2160 kt-yr for NH-LO and 1360 kt-yr for IH-HO. For the fiducial volume of 187 kt for a single detector in true NH-LO configuration, this corresponds to $\approx$ 6 years run time *i.e.* 1.5 years in neutrino and 4.5 years in antineutrino mode. The more optimistic case would be with true IH-HO where it requires only 3.6 years (0.9ν+2.7$\bar{\nu}$) of run time. After adding T2K and NOνA information this exposure for each detector is reduced to 840 kt-yr for true NH-LO and 430 kt-yr for true IH-HO which for the proposed detector volume correspond to 4.5 years and 2.3 years of run time respectively. Performing the similar analysis for DUNE we see that, a minimum 5σ significance can be obtained for 140 kt-yr in true NH-LO. This corresponds to a run time of 3.5 years (split equally in neutrinos and antineutrinos) for 40 kt detector volume. Adding the information from T2K and NOνA reduces it to 70 kt-yr corresponding to just 1.75 years run time for DUNE. For the case where IH-HO is the true combination 5σ significance can be obtained with an exposure of 125 kt-yr, which reduces to 60 kt-yr once the data from T2K and NOνA is added. In the first line of table 3.5 we summarize the exposures for the different setups for 5σ hierarchy sensitivity for the favourable case of true IH-HO.

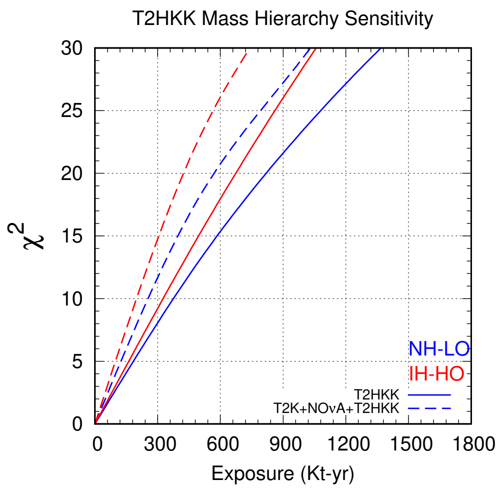

Figure 3.15: Mass hierarchy Sensitivity in T2HKK and DUNE versus exposure for true NH-LO with $\theta_{23} = 42°$

Similarly we also find out the optimum exposure for 5σ octant sensitivity. Since the octant sensitivity of T2HKK is poorer as compared to T2HK, as seen in the earlier section 3.4.3, we present the minimal optimal exposure required for T2HK to resolve the octant of θ_{23} with 5σ sensitivity assuming true NH-LO and IH-HO.

We observe that overall 5σ significance can be obtained by the T2HK experiment for an exposure of 2500 kt-yr for one detector which corresponds to approximately 13.4 years of run time in IH-HO as can be seen from the red solid line in fig. 3.16. Including the information from T2K and NOνA the exposure reduces to 2100 kt-yr corresponding to a run time of 11 years approximately. The second panel represents the octant sensitivity for DUNE. In this case, for true IH-HO (red curves) it can be seen that the exposure for 5σ octant sensitivity is 800 kt-yr which with the proposed volume of 40 kt corresponds to a runtime of 20 years. On adding T2K and NOνA information the optimal exposure is 680 kt-yr which corresponds to 17 years runtime. This is not surprising as we have seen in the previous section that DUNE doesn't reach 5σ octant sensitivity in 10 years for IH-HO with its proposed volume. However, from the blue lines of fig. 3.16, we can see that the true hierarchy–octant configuration NH-LO gives 5σ sensitivity for comparatively less exposure for both the experiments. We list the exposures required for this optimistic case in table 3.5. The number of operative years needed for T2HK to attain 5σ octant sensitivity is 3.8 yr in its individual capacity and 2.7 yrs when the data from T2K and NOνA experiments is added. However, DUNE requires 10 years of data taking to resolve octant of θ_{23} which reduces to 7.5 years when the T2K and NOνA results are taken into account.

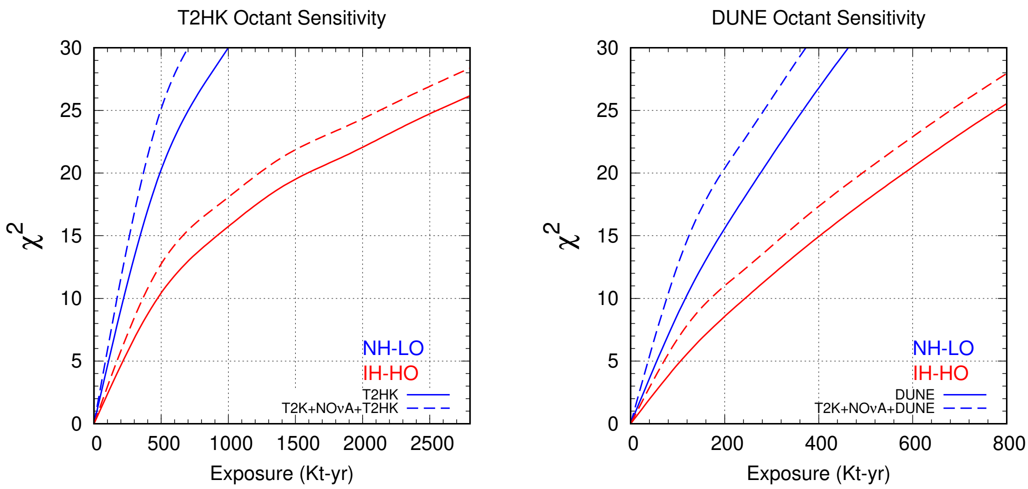

Figure 3.16: Octant Sensitivity in T2HK and DUNE versus exposure for true NH-LO

3.7 Combined Sensitivity of ESSνSB with T2HK, DUNE

In this section we study the CP discovery and mass hierarchy sensitivities for different combinations of the experiments. In this section we obtain the joint CP discovery and

Sensitivity	T2HKK	T2HK	DUNE	ESSνSB
Hierarchy($\chi^2 = 25$)(NH-LO)	1100(750)	–	150(100)	–
Hierarchy($\chi^2 = 25$)(IH-HO)	680(430)	–	140(70)	–
Octant($\chi^2 = 25$) (NH-LO)	–	700(500)	400(300)	–
Octant($\chi^2 = 25$) (IH-HO)	–	2500(2000)	600(500)	–
CP(60% at $\chi^2 = 25$, NH-LO)	1100(1100)	–	–	4500(3500)
CP(60% at $\chi^2 = 25$, IH-HO)	1200(1200)	–	–	5000(4000)

Table 3.5: Minimum exposures required for hierarchy, octant and CP in units of kt-yr for the various experiments and the quantities in brackets represent the minimum exposure required for the same on adding the contributions from T2K+NOνA .

mass hierarchy sensitivities of ESSνSB experiment with T2HK and DUNE. From fig. 3.17 we can see that stand alone ESSνSB (blue curve) can provide 60% δ_{CP} coverage after 9 years(10 years) of run for NH-LO(IH-HO). But, once we start adding the data from T2HK & DUNE with ESSνSB an enormous amount of increase in sensitivity is observed. ESSνSB + DUNE (green dashed curve) can resolve the CP in 4 years(5 years) run while ESSνSB + T2HK (red dotted curve)can do the same in just 3 years run. This increase can be accounted for due to the increase in statistics.

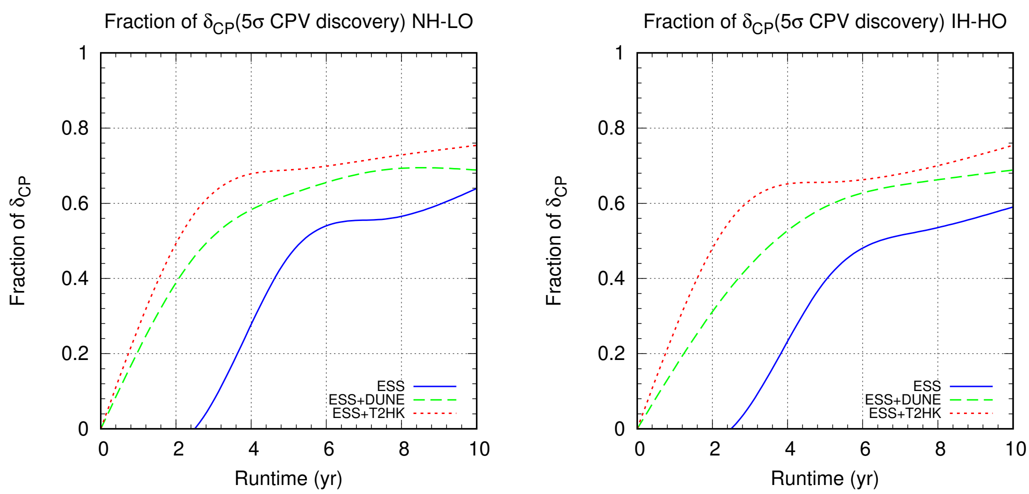

Figure 3.17: Fraction of δ_{CP} in ESSνSB , ESSνSB +DUNE and ESSνSB +T2HK versus simultaneous runtime for 5σ CPV sensitivity. The blue, green and red lines represent ESSνSB , ESSνSB +DUNE and ESSνSB +T2HK respectively. The figure left(right) is for true NH-LO(IH-HO).

The combined mass hierarchy sensitivities can be analyzed from fig.3.18. We see that the mass hierarchy sensitivity for DUNE was already very high, adding ESSνSB

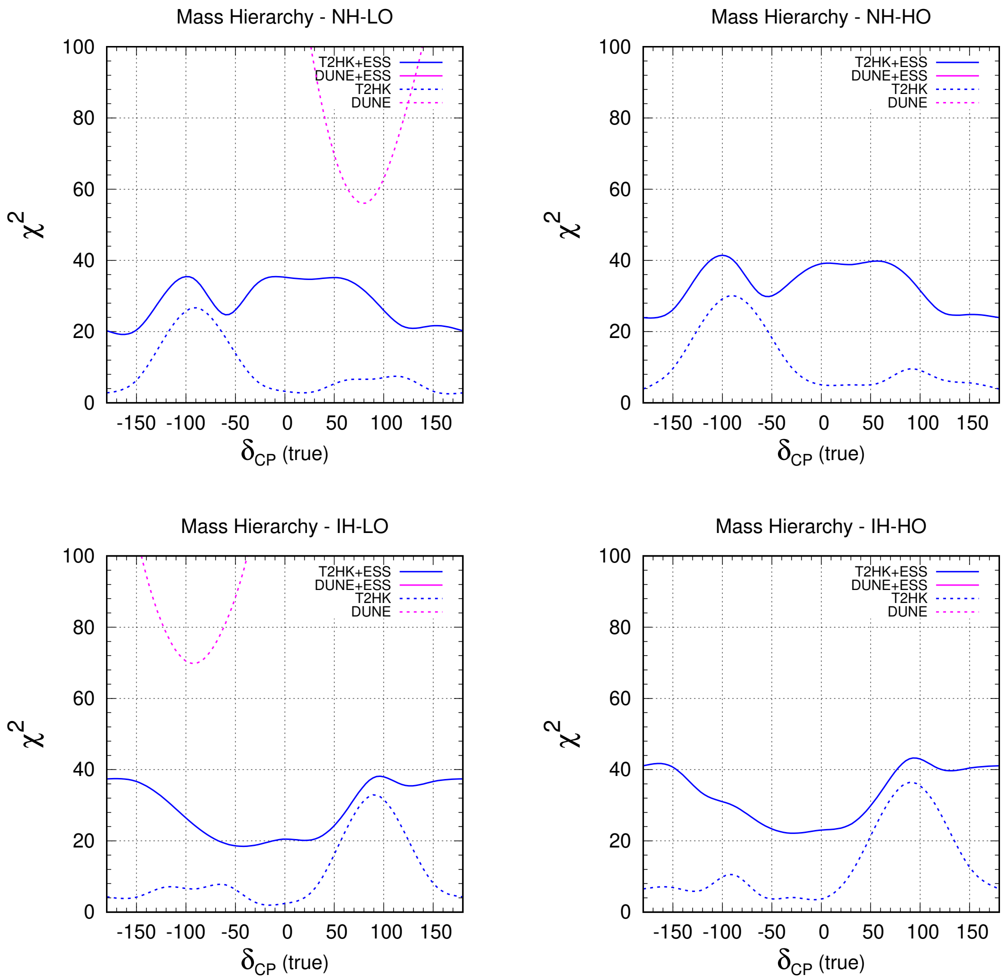

Figure 3.18: Mass hierarchy sensitivity for T2HK, DUNE and T2HK & DUNE in combination with ESSνSB with all hierarchy-octant configurations, first(second) row represent NH(IH) and first(second) columns represent LO(HO). The solid(dashed) lines represent the considered experiment(considered experiment + ESSνSB). The blue(magenta) lines represent T2HK(DUNE).

with DUNE ensured a minimum 10σ sensitivity for all hierarchy-octant combinations. When we consider the cases for T2HK mass hierarchy sensitivity we observe that the sensitivities of T2HK mass hierarchy are high in favourable half-planes and are very low in unfavourable half planes due to hierarchy-δ_{CP} degeneracies. Addition of ESSνSB with T2HK helps in resolving the hierarchy by breaking the hierarchy-δ_{CP} degeneracies. For instance let us consider the cases of true NH i.e NH-LO & NH-HO, in both the cases hierarchy degeneracy plagued the upper half plane in δ_{CP} range, but inclusion of ESSνSB helped to resolve the degeneracy. This can be explained from the last row second column of fig.3.3, the case for ESSνSB antineutrino. Here we observe that in the range $-10^\circ < \delta_{CP} < 60^\circ$ there is no hierarchy degeneracy for true NH hence the mass hierarchy significance is enhanced in this range which was earlier very low. Similar explanation also holds for IH in the range $-180^\circ < \delta_{CP} < -60^\circ$, considering the neutrino probability for ESSνSB in the fig.3.3. Due to the stated reasons the mass hierarchy sensitivities for T2HK+ESSνSB is minimum $\sim 4.4\sigma$ for entire δ_{CP} range.

3.8 Conclusions

In this chapter, we perform a comprehensive analysis of underlying physics issues related to the hierarchy, octant and CP discovery sensitivities of the proposed high statistics experiments T2HK, T2HKK, DUNE and ESSνSB . In particular we present a detailed discussion on the octant sensitivities bringing out the salient features of the relevant probabilities near the second oscillation maxima.

Our study shows that with their proposed fiducial volume and run time, T2HKK and DUNE experiments can achieve very high hierarchy sensitivity. The T2HK experiment on the other hand cannot resolve hierarchy-δ_{CP} degeneracy in the range $-180^\circ < \delta_{CP} < 0$ for IH and $0 < \delta_{CP} < 180^\circ$ for NH. Hence in these unfavourable regions the hierarchy sensitivity can reach maximum 3σ. In the favourable half-plane of δ_{CP} more than 5σ sensitivity is possible for T2HK. ESS can give comparable hierarchy sensitivity to T2HK for unfavourable values of δ_{CP}. However, in the favourable δ_{CP} range, sensitivity of T2HK is much higher. Highest hierarchy sensitivity can be achieved by DUNE. On the other hand T2HK has the highest octant sensitivity among all the three experiments. T2HKK and DUNE have comparable octant sensitivity. Octant sensitivity of ESSνSB is very low for the configuration that we have considered. The CP discovery potential on the other hand is best for ESSνSB . T2HKK can give comparable CP sensitivity as that of ESSνSB in some regions of parameter space. T2HK gives comparable sensitivity to T2HKK for favourable values of δ_{CP}. However for unfavourable δ_{CP} values due to wrong hierarchy-wrong CP solutions the CP discovery potential suffers. DUNE does not have hierarchy degeneracy. But the sensitivity to CP discovery potential is lower because of lower volume as compared to the other experiments.

Additionally, we also compute the optimal exposure for 5σ hierarchy and octant sensitivity of all the experiments both stand-alone and in conjunction with T2K and NOνA results. The sensitivity study is done for two representative configurations assuming true NH-LO ($\theta_{23} = 42°$) and IH-HO ($\theta_{23} = 48°$). For hierarchy sensitivity better result is obtained for IH-HO. We find that for the cases NH-LO(IH-HO) DUNE can attain 5σ sensitivity in approximately 4 years(3.5 years) (equal neutrino and antineutrino run) and with T2K and NOνA information it is just 2.5 years(2 years) with a 40 kt volume. T2HKK with the proposed volume can achieve this in 6 years(4 years) for T2HKK alone and 4 years(2.5 years) for T2HKK + T2K + NOνA . Optimum exposure required to obtain 5σ octant sensitivity is found to be less when we assumed true NH-LO. For octant sensitivity T2HK can deliver the result in 4 years(13 years) and with T2K and NOνA the same can be achieved within 3 years(11 years) for true NH-LO(IH-HO). On the other hand, T2HKK and DUNE would need more than 10 years of exposure to attain this goal for all hierarchy octant combinations. We also present the time for which 5σ CP violation discovery sensitivity can be reached for 60% fraction of δ_{CP} values for both NH-LO and IH-HO. This is found to be 6 years(6.5 years) for T2HKK for true NH-LO(IH-HO) which remains approximately the same after adding T2K + NOνA . For ESSνSB the time is 9 years(10 years) for true NH-LO(IH-HO), adding T2K + NOνA reduces the time to 7 years(8 years) .

Another new feature of our study is to obtain the combined sensitivities of T2HK and DUNE with ESSνSB and we observed that although the primary motivation for ESSνSB experiment is CP discovery, still ESSνSB can be very helpful in mass hierarchy sensitivity if combined with T2HK. This is because the hierarchy degeneracies for T2HK and ESSνSB occur at different δ_{CP} values.

From the detailed analysis of our results we can conclude that DUNE, T2HK & T2HKK experiments are very high precision experiments and are expected to be very successful in the determination of the unknowns of neutrino oscillation regime. If the data from the ongoing experiments like T2K and NOνA are combined with the future experiments then the fiducial volumes of the detectors required for the experiments can be reduced hence can reduce the cost of the future experiments. We also conclude that the best configuration for the T2HK & T2HKK experiment is if we have one detector at 295km and the other at 1100km 1.5° off-axis, although the proposed runtime for neutrino and antineutrino mode for the experiment is 2.5ν + 7.5$\bar{\nu}$ but from our analysis we observe that 7.5ν + 2.5$\bar{\nu}$ run time configuration is better than the proposed runtime configuration. Since DUNE is also a proposed experiment so on adding DUNE with T2HKK run with runtime configuration of 7.5ν + 2.5$\bar{\nu}$ will be able to solve all the three unknowns of neutrino oscillation physics with high precision. We see that adding DUNE with T2HKK improves the statistics and can resolve the neutrino oscillations regime at 5σ confidence level.

Chapter 4

Exploring Partial μ-τ Reflection Symmetry at DUNE and Hyper-Kamiokande

4.1 Introduction

In the last chapter we have discussed the potential of determining the unknown oscillation parameters in future proposed experiments. The study was model independent. However, flavour symmetry models can predict interesting correlations between various neutrino oscillations parameters which can assist in determining the present unknowns. In this chapter we discuss the implications of neutrino oscillation is the presence of partial μ-τ reflection symmetry. The symmetry based approaches have been quite successful in predicting the interrelations among these quantities and the structure of the leptonic mixing matrix as discussed in Refs. [186, 187, 188, 189, 190] and the references therein. General approaches along this line assume some individual residual symmetries of the leptonic mass matrices which could arise from the breaking of some bigger symmetry of the leptonic interactions. One such symmetry, called μ-τ reflection symmetry, originally discussed by Harrison and Scott in Ref. [191] leads to very successful predictions of mixing angles which are close to the present experimental knowledge. This symmetry may be stated as equality of moduli of the leptonic mixing matrix U:

$$|U_{\mu i}| = |U_{\tau i}| \ , \tag{4.1}$$

for all the columns $i = 1, 2, 3$. Both the origin and consequences of this relation have been discussed in [192, 193, 194, 195, 196, 197, 198, 199, 200, 201, 202, 203, 204, 205, 206, 207].

Using the standard PDG [208] parameterization of the matrix U

$$\begin{aligned} U &= U(\theta_{23})U(\theta_{13}, \delta_{CP})U(\theta_{12}) \\ &= \begin{bmatrix} c_{12}c_{13} & s_{12}c_{13} & s_{13}e^{-i\delta_{CP}} \\ -s_{12}c_{23} - c_{12}s_{23}s_{13}e^{i\delta_{CP}} & c_{12}c_{23} - s_{12}s_{23}s_{13}e^{i\delta_{CP}} & s_{23}c_{13} \\ s_{12}s_{23} - c_{12}c_{23}s_{13}e^{i\delta_{CP}} & -c_{12}s_{23} - s_{12}c_{23}s_{13}e^{i\delta_{CP}} & c_{23}c_{13} \end{bmatrix} \end{aligned} \tag{4.2}$$

one finds two well-known predictions

$$\theta_{23} = \frac{\pi}{4} \ , \quad s_{13} \cos \delta_{CP} = 0 \ . \tag{4.3}$$

Eq. (4.3) suggests maximal θ_{23}, which is allowed within 1σ by the global fits to neutrino observables [209, 210, 11]. Additionally, it allows a nonzero θ_{13} unlike the simple μ-τ symmetry which predicts vanishing θ_{13} [211, 212, 213, 214, 215, 216], see recent review [217] and references therein. Here, for $\theta_{13} \neq 0$, one gets $\delta_{CP} = \pm\frac{\pi}{2}$ using eq. (4.3). Both these predictions are in accord with the global fit of all neutrino data. However a sizeable range is still allowed at 3σ. Note that the best fit value of θ_{23} in the global fit deviates from the maximal value for either mass hierarchy. Such deviations can be regarded as a signal for the departure from the μ-τ reflection symmetry. A theoretically well-motivated possibility is to assume a 'partial μ-τ' reflection symmetry [218] and assume that eq. (4.1) holds only for a single column[1] of U. Assuming that it holds for the third column, one gets maximal θ_{23} and δ_{CP} remains unrestricted. These correlations are found from eq. (4.2) in respective cases $i = 1$ and $i = 2$ to be

[1] If it holds for any two columns then by unitarity, it holds for the third as well.

$$\cos\delta_{CP} = \frac{(c_{23}^2 - s_{23}^2)(c_{12}^2 s_{13}^2 - s_{12}^2)}{4c_{12}s_{12}c_{23}s_{23}s_{13}}, \quad (|U_{\mu 1}| = |U_{\tau 1}|) \quad , \quad C_1\ , \tag{4.4}$$

$$\cos\delta_{CP} = \frac{(c_{23}^2 - s_{23}^2)(c_{12}^2 - s_{12}^2 s_{13}^2)}{4c_{12}s_{12}c_{23}s_{23}s_{13}}, \quad (|U_{\mu 2}| = |U_{\tau 2}|) \quad , \quad C_2\ . \tag{4.5}$$

These equations correlate the sign of $\cos\delta_{CP}$ to the octant of θ_{23}. θ_{23} in the first (second) octant leads to a negative (positive) value of $\cos\delta_{CP}$ in case of eq. (4.4). It predicts exactly opposite behaviour for eq. (4.5). The exact quadrant of δ is still not fixed by these equations but it can also be determined from symmetry considerations[205]. These correlations were also obtained in [219, 220] in the context of Z_2 and $\overline{Z_2}$ symmetries [2]. Henceforth, we refer to these correlations as C_1 and C_2 respectively. The above equations also indirectly lead to information on the neutrino mass hierarchy since the best fit values of θ_{23} lie in the first (second) octant in case of the normal (inverted) hierarchy according to the latest global fits reported in [210, 11, 209]. Thus precise verification of the above equations is of considerable importance and the long baseline experiments can provide a way for such study. Similar study has been performed in the context of the NOνA and T2K experiments in [222, 223, 224].

In this chapter, we consider the testability of these relations at the forthcoming long baseline experiments Deep Under-ground Neutrino Experiment (DUNE) and Hyper-Kamiokande (HK). These potential high-statistics experiments will overcome the parameter degeneracies faced by the current experiments and lead us in to an era of precision measurements of the oscillation parameters [144, 225, 226, 227, 167, 166, 228, 169, 170, 229]. Because of this, these experiments are ideal to test the parameter correlations like the ones given in the eqs. (4.4, 4.5). In the following, we obtain the allowed parameter range in the δ_{CP} - $\sin^2\theta_{23}$ plane by fitting the symmetry relations embodied in the eqs. (4.4, 4.5) to the simulated DUNE and HK data. We also discuss whether the correlations C_1(eq. (4.4)) and C_2(eq. (4.5)) can be distinguished at DUNE and HK. Recent studies on testing various models from future experiments can be found for instance in [230, 231, 232, 233, 234, 235, 236, 237, 238].

[2] See, the review article [221] for references on other similar sum rules and their testability.

We begin by first discussing the origin of partial μ-τ reflection symmetry, after which in Section 4.2 we elaborate on the robustness of the resulting predictions in a large class of models based on flavour symmetry. We give a brief overview of the experiments and simulation details in Section 4.3. In Section 4.3.1, we perform a phenomenological analysis of the testability of the above symmetries in DUNE and HK. We use the extra correlations predicted by the symmetry in fitting the simulated data of these experiments and obtain the allowed areas in the $\delta_{CP} - \sin^2\theta_{23}$ plane. In subsection 4.3.3, we discuss the possibility of differentiating between the two symmetries – C_1 and C_2. We draw our conclusions in Section 4.4.

4.2 Partial μ-τ Reflection Symmetry and Discrete Flavour Symmetries

We briefly review here the general approach based on flavour symmetry to emphasize that partial μ-τ reflection symmetry is a generic prediction of almost all such schemes barring few exceptions. Basic approaches assume groups G_ν and G_l as the residual symmetries of the neutrino mass matrix M_ν and the charged lepton mass matrix $M_l M_l^\dagger$ respectively. Both these groups are assumed to arise from the breaking of some unitary discrete group G_f. The $U_{\rm PMNS}$ matrix U gets fixed upto the neutrino Majorana phases if it is further assumed that $G_\nu = Z_2 \times Z_2$ and $G_l = Z_n, n \geq 3$. In addition, if we demand that all the predicted mixing angles are non-zero, then the following unique form is predicted for almost all the discrete groups G_f [239, 240]

$$U \equiv U_{\rm gen}(\theta_n) = \frac{1}{\sqrt{3}} \begin{pmatrix} \sqrt{2}\cos\theta_n & 1 & \sqrt{2}\sin\theta_n \\ \sqrt{2}\cos(\theta_n - \frac{2\pi}{3}) & 1 & \sqrt{2}\sin(\theta_n - \frac{2\pi}{3}) \\ \sqrt{2}\cos(\theta_n - \frac{4\pi}{3}) & 1 & \sqrt{2}\sin(\theta_n - \frac{4\pi}{3}) \end{pmatrix}, \tag{4.6}$$

where $\theta_n \equiv \dfrac{\pi a}{n}$ is a discrete angle with $a = 0, 1, 2....\dfrac{n}{2}$. We have not shown here the unphysical phases which can be absorbed in defining charged lepton fields and unpredicted Majorana phases. All the discrete subgroups of $SU(3)$ with three dimensional irreducible representation are classified as class C or D and five exceptional groups [241]. Eq. (4.6) follows in all the type D groups taken as G_f. Type C groups lead instead to democratic mixing which shows full μ-τ reflection symmetry but predict large reactor angle. Eq. (4.6) arises even if G_f is chosen as a discrete subgroup of $U(3)$ having the same textures as class D groups [240].

Eq. (4.6) displays partial μ-τ reflection symmetry for the second column for all the values of $\theta_n \neq 0, \frac{\pi}{2}$. In the latter case, one gets total μ-τ reflection symmetry but at the same time one of the mixing angles is predicted to be zero and one would need to break the assumed residual symmetries to get the correct mixing angles. More importantly, eq. (4.6) being essentially a real matrix also predicts trivial Dirac CP phase $\delta_{CP} = 0$ or π. Eq. (4.5) in this case implies a correlation among angles. Non-zero CP phase and partial μ-τ symmetry in other columns can arise in an alternative but less predictive approach in which the residual symmetry of the neutrino mass matrix is taken as Z_2 instead of $Z_2 \times Z_2$. In this case, one can obtain the following mixing matrix U with a proper choice of residual symmetries

$$U = U_{\text{gen}}(0)U_{ij} \ , \tag{4.7}$$

where U_{ij} denotes a unitary rotation either in the ij^{th} plane corresponding to partial symmetry in the $k^{th}(i \neq j \neq k)$ column . Examples of the required residual symmetries are discussed in [186, 187, 188, 189, 190] and minimal example of this occurs with $G_f = S_4$.

The partial μ-τ symmetries obtained this way also lead to additional restrictions

$$c_{12}^2 c_{13}^2 = \frac{2}{3} \tag{4.8}$$

and

$$s_{12}^2 c_{13}^2 = \frac{1}{3} \ , \tag{4.9}$$

where eq. (4.8) and eq. (4.9) follow from the partial symmetries of the first and third columns respectively. These predictions arise here from the requirement that G_ν and G_l are embedded in DSG of $SU(3)$ and need not arise in a more general approach.

It is then possible to obtain specific symmetries [219, 220] in which solar angle is a function of a continuous parameter.

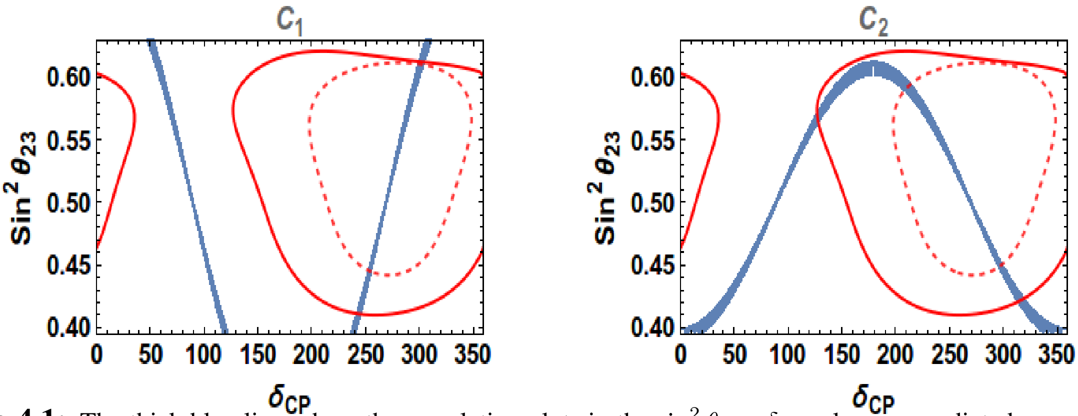

Figure 4.1: The thick blue lines show the correlation plots in the $\sin^2\theta_{23}$ - δ_{CP} plane as predicted by the symmetry relations. The left (right) panel correspond to Eq. (4.4) (Eq. (4.5)). The solid(dashed) red curves represent the 3σ allowed parameter space as obtained by the global analysis of data by the Nu-fit collaboration [11, 3] considering hierarchy to be NH(IH) respectively.

Fig. 4.1, shows the correlation plots (thick blue lines) between $\sin^2\theta_{23}$ and δ_{CP} as given by eqs. (4.4, 4.5). Here, the red solid(dashed) contours represent the 3σ allowed region for NH(IH) as obtained from the global-fit data by the Nu-fit collaboration [3]. Eqs. (4.4, 4.5) give two values of CP phase (namely, δ_{CP} and $360^\circ - \delta_{CP}$) for each value of θ_{23} except for $\delta_{CP} \equiv 180^\circ$. The width of the blue lines is due to the uncertainty of the angles θ_{12} and θ_{13} subject to the conditions given in eq. (4.8) and eq. (4.9) corresponding to eq. (4.4) and eq. (4.5) respectively. It is seen that the correlation between $\sin^2\theta_{23}$ and δ_{CP} is opposite in the class of symmetries that give eq. (4.4) vis-a-vis those that give eq. (4.5). The parameters, $\sin^2\theta_{23}$ and δ_{CP} are correlated between $0^\circ - 180^\circ$ and anti-correlated between $180^\circ - 360^\circ$ for eq. (4.4). The opposite is true for eq. (4.5). We also notice here that eq. (4.5) rules out regions around CP conserving (i.e. $0^\circ, 180^\circ, 360^\circ$) values. Additionally we observe that, at 3σ some of the allowed regions of $\sin^2\theta_{23}$ and δ_{CP} as predicted by the symmetries are disfavoured by the current global-fit data. From the global-fit data we observe that the region $39^\circ < \delta_{CP} < 125^\circ$ is completely ruled out at 3σ for NH and the region $\delta_{CP} < 195^\circ$ for IH. The symmetry predictions can further constrain the values of δ_{CP} presently allowed by the global data.

In the next section, we study how far the allowed areas in $\delta_{CP} - \sin^2\theta_{23}$ plane can be restricted if the simulated experimental data confronts the symmetry predictions.

4.3 Phenomenological Analysis

In this section, we perform a phenomenological analysis exploring the possibility of probing the correlations C_1 and C_2 at DUNE, T2HK and T2HKK. This is discussed in terms of correlation plots in $\sin^2\theta_{23} - \delta_{CP}$ plane. We also discuss the possibility of distinguishing between the two models at these experiments.

4.3.1 Details of Analysis

We have simulated DUNE, T2HK and T2HKK using the GLoBES package [181, 182] along with the required auxiliary files [242, 243].

We perform a χ^2 test with χ^2 defined as,

$$\chi^2_{\rm tot} = \min_{\xi,\omega}\{\chi^2_{\rm stat}(\omega,\xi) + \chi^2_{\rm pull}(\xi) + \chi^2_{prior}\}. \tag{4.10}$$

$\chi^2_{\rm stat}$ is the statistical χ^2 whereas χ^2_{pull} signifies the systematic uncertainties which are included using the method of pulls with ξ denoting the pull variable [244, 245, 246]. Here, ω represents the oscillation parameters : $\{\sin^2\theta_{23}, \sin^2\theta_{12}, \delta_{CP}, \Delta m^2_{21}, \Delta m^2_{31}\}$. χ^2_{prior} captures the knowledge of the oscillation parameters from other experiments and is defined as,

$$\chi^2_{prior}(p) = \frac{(p_0 - p)^2}{\sigma_0^2}\ , \tag{4.11}$$

p denotes the parameter for which a prior is added and p_0 and σ_0 correspond to its best fit value and 1σ error, respectively. In our analysis we have considered the effect of prior on the parameters θ_{13} and θ_{12}. We assume Poisson distribution to calculate the statistical χ^2_{stat},

$$\chi^2_{stat} = \sum_i 2(N_i^{test} - N_i^{true} - N_i^{true}\log\frac{N_i^{test}}{N_i^{true}})\ . \tag{4.12}$$

Here, 'i' refers to the number of bins and N_i^{test}, N_i^{true} are the total number of events due to test and true set of oscillation parameters respectively. N_i^{test} is defines as follows, including the effect of systematics

$$N_i^{(\mathrm{k})\mathrm{test}}(\omega,\xi) = \sum_{k=s,b} N_i^{(k)}(\omega)[1 + c_i^{(k)norm}\xi^{(k)norm} + c_i^{(k)tilt}\xi^{(k)tilt}\frac{E_i - \bar{E}}{E_{max} - E_{min}}] \tag{4.13}$$

where $k = s(b)$ represent the signal(background) events. $c_i^{norm}(c_i^{tilt})$ corresponds to the change in the number of events due to the pull variable $\xi^{norm}(\xi^{tilt})$. In the above equation E_i denotes the mean reconstructed energy of the i^{th} bin with E_{min} and E_{max} representing the maximum and minimum energy in the entire energy range and $\bar{E} = (E_{max} + E_{min})/2$ is the mean energy over this range. The systematic uncertainties (normalization errors) and efficiencies corresponding to signals and backgrounds of DUNE and HK are taken from [144, 146]. For DUNE the signal normalization uncertainties on ν_e/$\bar{\nu}_e$ and ν_μ/$\bar{\nu}_\mu$ are considered to be 2% and 5% respectively. While a range of 5% to 20% background uncertainty along with the correlations among their sources have also been included. On the other hand, for T2HK the signal normalization error on $\nu_e(\bar{\nu}_e)$ and $\nu_\mu(\bar{\nu}_\mu)$ are considered to be 3.2% (3.9%) and 3.6%(3.6%) respectively. In the case of T2HKK, 3.8% (4.1%) and 3.8% (3.8%) are taken as the signal normalization errors on $\nu_e(\bar{\nu}_e)$ and $\nu_\mu(\bar{\nu}_\mu)$ respectively. The background normalization uncertainties range from 3.8% to 5%. N_i^{true} in eq. (6.5) is obtained by adding the the simulated signal and background events i.e. $N_i^{\mathrm{true}} = N_i^s + N_i^b$.

In Table 4.1, we list the values for the neutrino oscillation parameters that we have used in our numerical simulation. These values are consistent with the results obtained from global-fit of world neutrino data [210, 11, 209].

4.3.2 Testing the $\sin^2\theta_{23} - \delta_{CP}$ correlation predicted by the symmetries at DUNE, T2HK and T2HKK

The numerical analysis is performed as follows.

- The data corresponding to each experiment is generated by considering the true values of the oscillation parameters given in table 4.1. Note that the true values

Osc. param.	True Values	Test Values
$\sin^2\theta_{13}$	0.0219	0.0197 – 0.0244
$\sin^2\theta_{12}$	0.306	0.272 – 0.346
θ_{23}	$39^\circ - 51^\circ$	$39^\circ - 51^\circ$
$\Delta m^2_{21}(\mathrm{eV}^2)$	7.50 $\times 10^{-5}$	Fixed
$\Delta m^2_{31}(\mathrm{eV}^2)$	2.50 $\times 10^{-3}$	(2.35 – 2.65) $\times 10^{-3}$
δ_{CP}	$(0\text{-}360)^\circ$	Symmetry predictions

Table 4.1: Values of Oscillation parameters that are considered in this study unless otherwise mentioned. We vary the true values of θ_{23} in the whole allowed range and marginalization for each $\theta_{23}^{\rm true}$ is done over the full allowed range of θ_{23}. See text for more details.

of θ_{23} and δ_{CP} are spanned over the range $(39-51)^\circ$ and $(0^\circ-360^\circ)$, respectively.

- In the theoretical fit, we calculate the test events by marginalizing over the parameters $\sin^2\theta_{13}$, $|\Delta m^2_{31}|$, $\sin^2\theta_{23}$ and $\sin^2\theta_{12}$ in the test plane using the ranges presented in table 4.1.

- The test values of δ_{CP} used are as predicted by the symmetries specified in eq. (4.4) for C_1 and eq. (4.5) in C_2.

- In addition we impose the conditions given in eq. (4.8) for the symmetry relation C_1 and eq. (4.9) for symmetry relation C_2 in the test. Note that given the current range of $\sin^2\theta_{13}$ these relations restrict the value of $\sin^2\theta_{12}$ to $0.316 < \sin^2\theta_{12} < 0.319$ for C_1 and $\sin^2\theta_{12}$ to $0.34 < \sin^2\theta_{12} < 0.342$ for C_2. These values of $\sin^2\theta_{12}$ are within the current 3σ allowed range. Note that these ranges exclude the current best-fit value of $\sin^2\theta_{12}$. Precise measurement of θ_{12} for instance in the reactor neutrino experiment JUNO [247] can provide a stringent test of these scenarios.

- We have not added any prior in this analysis. We have checked that the prior on θ_{13} does not play any role when the constraints represented by eq. (4.8) and eq. (4.9) are applied. In addition, since the best-fit θ_{12} is excluded already by the constraints, the imposition of θ_{12} prior will disfavour the scenarios.

- We minimize the χ^2 and plot the regions in the $\sin^2\theta_{23}(true) - \delta_{CP}(true)$ plane for which $\chi^2 \leq \chi^2_{min} + \Delta\chi^2$ where $\Delta\chi^2$ values used correspond to 1, 2 and 3 σ which are 2.34, 6.18 and 11.83 respectively.

The resultant plots are shown in fig. (4.2) for true hierarchy as NH and fig. (4.3) for true hierarchy as IH. We assume hierarchy to be known and do not marginalize over hierarchy [3]. The blue, grey and the yellow bands in the figs. (4.2, 4.3) represent 1σ, 2σ, 3σ regions in the $\sin^2\theta_{23} - \delta_{CP}$ plane, respectively. The red contours show the 3σ allowed area obtained by the Nu-fit collaboration [11, 3]. These plots show the extent to which these three experiments can test the correlations between the two yet undetermined variables $\sin^2\theta_{23}$ and δ_{CP} in conjunction with the symmetry predictions. The topmost panel corresponds to DUNE - 40 kT detector whereas the middle and the lowest panels correspond to T2HK and T2HKK experiments respectively. The left plots in all the rows are for testing C_1 whereas the right plots are for testing C_2.

The figures show that, because of the correlations predicted by symmetries, certain combinations of the true θ_{23} and δ_{CP} values get excluded by DUNE, T2HK and T2HKK. Owing to their high sensitivity to determine CP violation, T2HK and T2HKK constrain the range of δ_{CP} better than that of DUNE. This can be seen from the figures (see figs. (4.2, 4.3) which show that, as we go from top to bottom the contours gets thinner w.r.t. δ_{CP}. For instance for the C_1 correlation, the CP conserving values $0°$ and $360°$ get excluded at 3σ for both the octants by all the three experiments as can be seen from the plots in the left panels. However, for the C_2, these values are allowed at 3σ for all the three experiments. Whereas, $\delta_{CP} = 0°$ and $360°$ are excluded by DUNE and HK experiments at 1σ and 2σ respectively. Again one can see from the right panels that for C_2, $\delta_{CP} = 180°$ is allowed for $\sin^2\theta_{23} > 0.55$ (i.e. higher octant) by DUNE but gets barely excluded at 2σ by T2HK and T2HKK experiments. The correlations predicted by the symmetry considerations being independent of hierarchy, the allowed regions are not very different for NH and IH. But the region of parameter space allowed by current data for IH is more constrained and the symmetry predictions restrict it further as can be seen from fig. (4.3). Some of the parameter space allowed by the current data can also be disfavored by incorporating the correlations due to symmetry relations.

In section 4.2, it was discussed that the additional restrictions, eq. (4.8) and eq. (4.9),

[3]We verified that the effect of marginalizing over the hierarchy is very less. Hence to save the computation time we have presented the plots by assuming that the hierarchy is known.

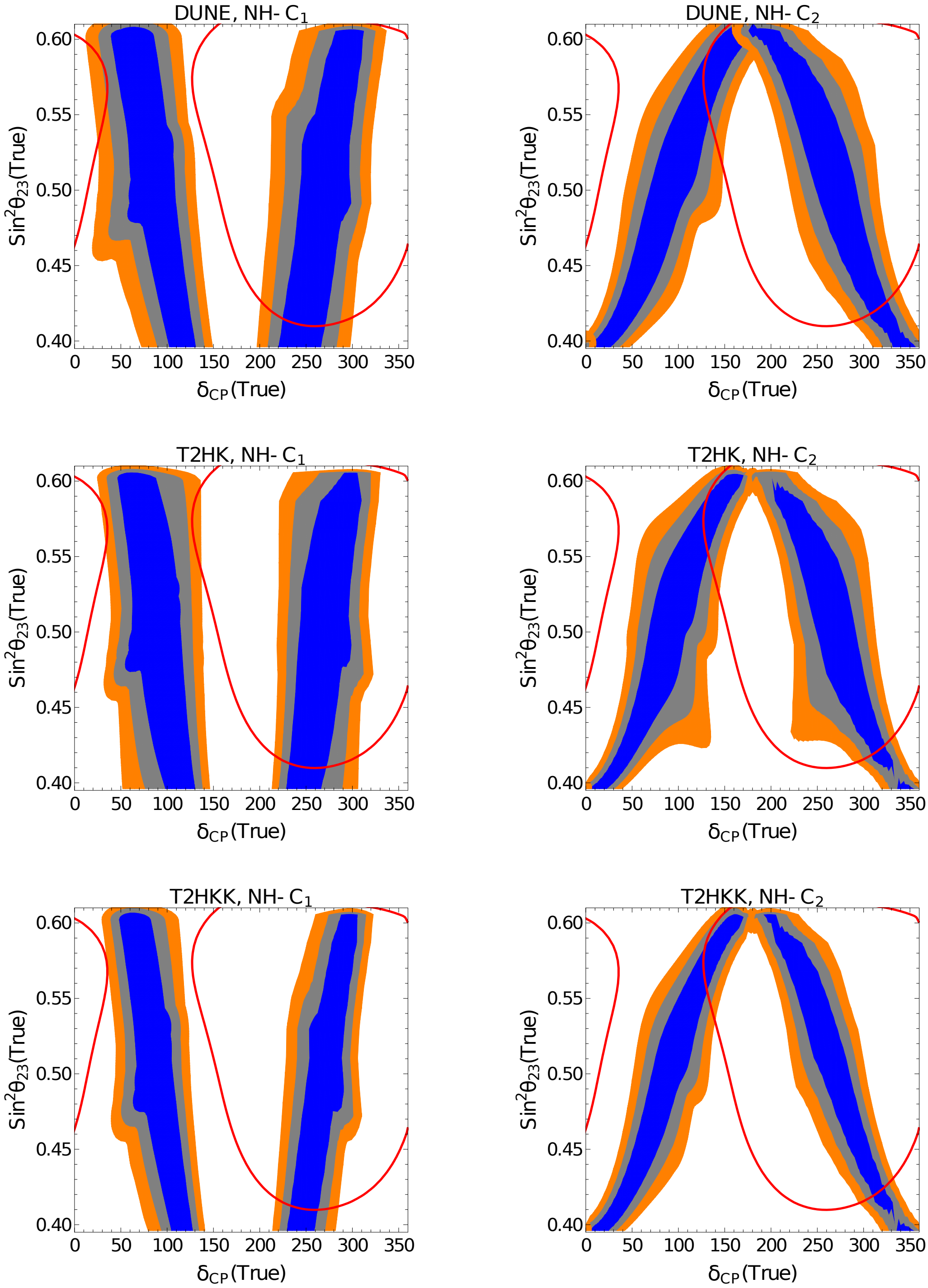

Figure 4.2: Contour plots in the true: $\sin^2\theta_{23}$(true) - δ_{CP}(true) plane for DUNE, T2HK, T2HKK. The left(right) panel represents the prediction from the symmetry relation $C_1(C_2)$ which corresponds to the eq. (4.4) ((eq. 4.5)). The hierarchy is fixed as NH. The red contour in each panel represents the 3σ allowed area from the global analysis of neutrino oscillation data as obtained by the Nu-fit collaboration [11, 3] for Normal Hierarchy. The blue, gray and yellow shaded contours correspond to 1σ, 2σ, 3σ respectively.

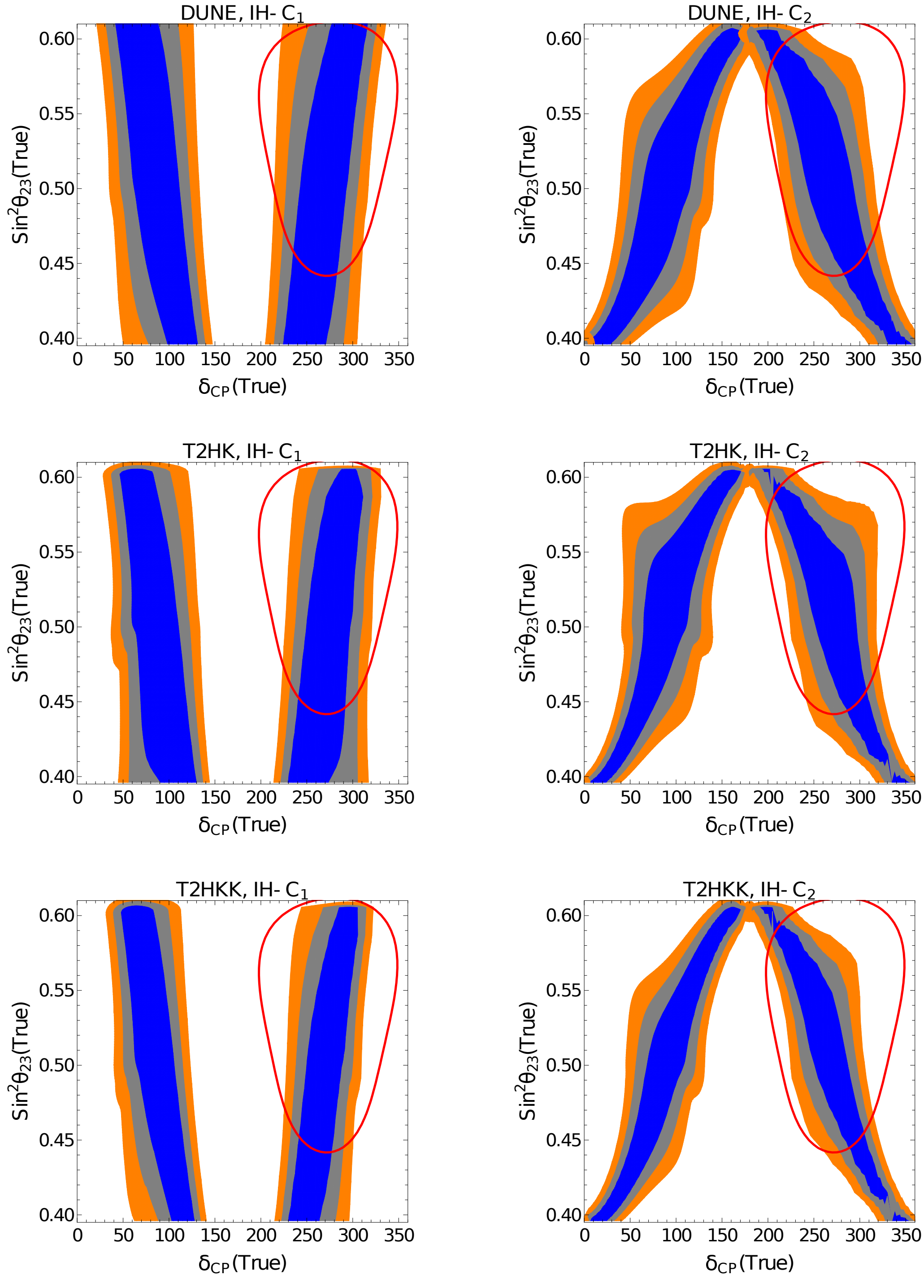

Figure 4.3: Same as fig. (4.2) but for Inverted Hierarchy.

are obtained when the partial $\mu - \tau$ symmetry is derived in the specific approach discussed. However, possibilities exist where partial $\mu - \tau$ symmetry can be generated without the additional restrictions. In this context, we analyzed the changes in the allowed areas when the additional restrictions are not imposed. This is done only for

DUNE which captures the essential trend of the impact of not imposing the extra constraints. This is shown in fig. (4.4). We have studied this for the representative case of the symmetry relation C_2. The procedure for generating the plots is the same as outlined earlier excepting the inclusion of priors. While the earlier plots were generated without any prior, for these cases, we have studied the following scenarios:

1. No prior on θ_{13} and θ_{12}.

2. Prior on θ_{13} and θ_{12}.

3. Prior on θ_{12} and no prior θ_{13}.

4. Prior on θ_{13} and no prior θ_{12}.

The first plot of top row is without any prior on the parameters θ_{12} and θ_{13} and no additional constraints imposed. We find that the allowed area increases in size as compared to the cases where the extra constraints embodied in eq. (4.8) and eq. (4.9) are not imposed. The second plot of top row is without imposing these additional restrictions, but including prior on θ_{12} and θ_{13}. In this case the allowed regions are more restricted and certain combinations of θ_{23} and δ_{CP} get disfavoured. We proceed further to show the impact of prior considering a single mixing angle at a time in the second row. In the first plot of the bottom row, we show the effect of including prior on θ_{12} but no prior on θ_{13}. In this case the shape of the allowed regions are same but they reduce in size. The effect of certain combination of θ_{23} and δ_{CP} values getting disfavoured are seen more at the 1σ level. Similarly, the second plot of the bottom row shows the effect of θ_{13} prior. In this case also, the allowed regions reduce in size as compared to the case where no priors are included (first panel of top row).

4.3.3 Differentiating between the C_1 and C_2 symmetries

In this subsection, we explore the possibility of differentiation between the symmetries C_1 and C_2. This is presented in fig. (4.5) where we plot $\Delta\chi^2$ vs true θ_{23}. To find χ^2_{stat} (as defined in eq. (6.5)), true events are calculated by varying the true values of θ_{23} in the range $(39^\circ - 51^\circ)$. For each true θ_{23}, true values of $\sin^2\theta_{13}$ and $\sin^2\theta_{12}$

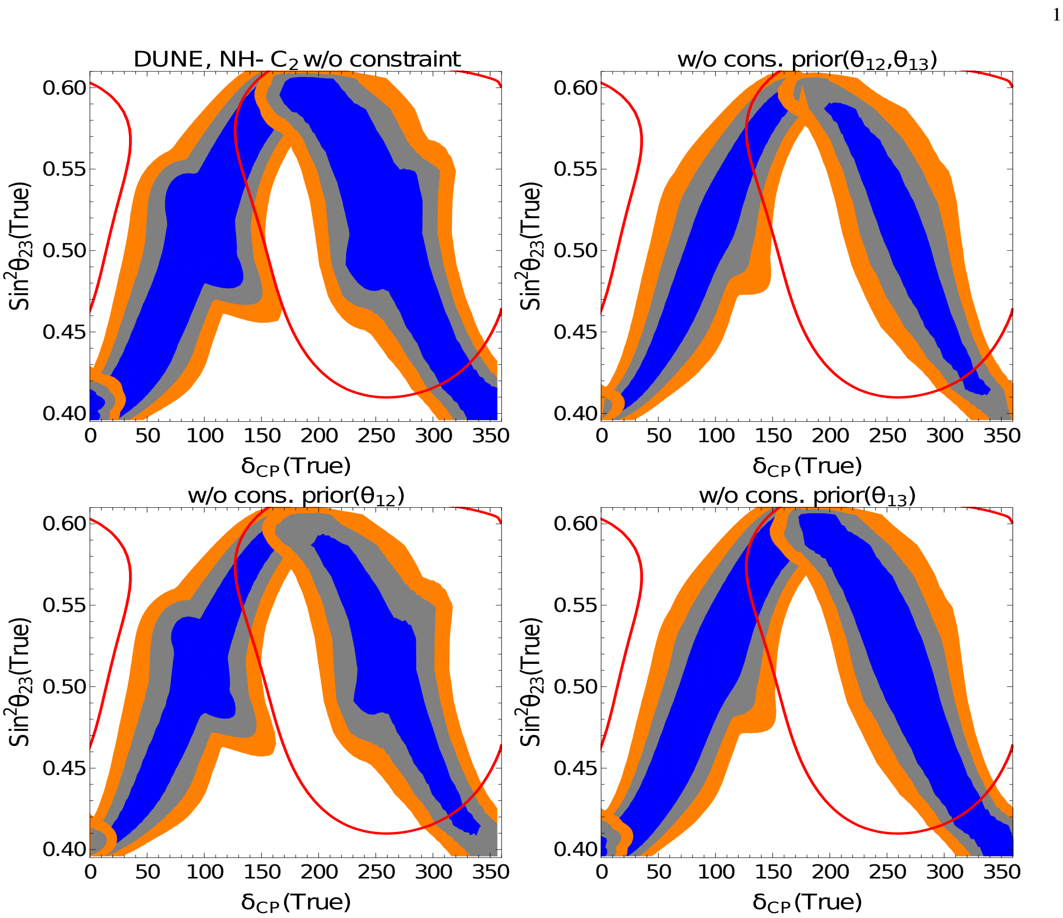

Figure 4.4: Contour plots in the true: $\sin^2\theta_{23}$(true) - δ_{CP}(true) plane for DUNE assuming the symmetry relation C_2 in the test. The additional constraints, eq. (4.9), has not been applied in generating this plot. The first panel represents the plot without including any prior. The second panel in the first row shows the effect of prior on θ_{12} and θ_{13}. The first plot in the second row shows the effect of inclusion of θ_{12} prior whereas the second plant shows the effect of inclusion of θ_{13} prior. The hierarchy is fixed as NH. The red contour in each panel represents the 3σ allowed area of the Nu-fit collaboration.

are allowed to vary in their 3σ range such that the condition as given in eq. (4.8) is satisfied. Using these true values of the angles the true δ_{CP} values are calculated using the correlation C_1. This leads to two sets of true events corresponding to δ_{CP} and $(360^\circ - \delta_{CP})$, respectively. The remaining oscillation parameters are kept fixed at their best-fit values as shown in table 4.1. In the theoretical fit, to calculate test events, we marginalize over $\sin^2\theta_{13}$, $|\Delta m^2_{31}|$, $\sin^2\theta_{23}$ in the range given in table 4.1 and test δ_{CP} values are calculated using the C_2. In addition we impose the condition as given in eq. (4.9) connecting test $\sin^2\theta_{23}$ and $\sin^2\theta_{13}$ and compute the χ^2. For each choice of true $\sin^2\theta_{23}$, the χ^2 is marginalized over true $\sin^2\theta_{13}$ and $\sin^2\theta_{12}$ and the minimum

χ^2 for each true $\sin^2\theta_{23}$ is taken as the value of χ^2. This process is done for both δ_{CP} and $360 - \delta_{CP}$ separately. We have performed the analysis considering the true hierarchy as NH. We have checked that if we assume IH as the true hierarchy we obtain similar results. The three panels from left to right represent DUNE, T2HK and T2HKK respectively. The solid blue curves in the plots are for predicted range $\delta_{CP} \in (0^\circ < \delta_{CP} < 180^\circ)$ and the dashed blue curves in the plots are for complementary range $360^\circ - \delta_{CP} \in (180^\circ < \delta_{CP} < 360^\circ)$ as predicted by the correlations. The brown solid line shows the 3σ C.L. We observe from the figure that at maximal θ_{23} both the correlations are indistinguishable by all the three experiments as is expected from the eqs. (4.4, 4.5).

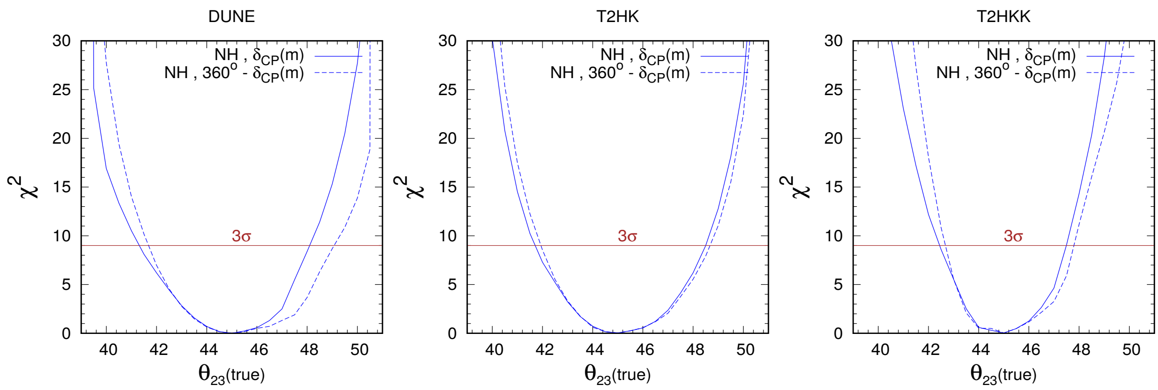

Figure 4.5: The sensitivity of the DUNE, T2HK & T2HKK experiments to differentiate between C_1 and C_2 correlations for known normal hierarchy.

Range of δ_{CP}	DUNE		T2HK		T2HKK	
$0^\circ \leq \delta_{CP} \leq 180^\circ$	$\theta_{23} \leq 41.5^\circ$	$\theta_{23} \geq 48^\circ$	$\theta_{23} \leq 41.8^\circ$	$\theta_{23} \geq 48.5^\circ$	$\theta_{23} \leq 42.6^\circ$	$\theta_{23} \geq 47.5^\circ$
$180^\circ \leq \delta_{CP} \leq 360^\circ$	$\theta_{23} \leq 41.8^\circ$	$\theta_{23} \geq 49^\circ$	$\theta_{23} \leq 42^\circ$	$\theta_{23} \geq 48.7^\circ$	$\theta_{23} \leq 42.8^\circ$	$\theta_{23} \geq 47.7^\circ$

Table 4.2: The limits of θ_{23} in degrees below and above which the correlations C_1 and C_2 can be differentiated at 3σ C.L. for two different ranges of δ_{CP}.

The capability of the experiments to differentiate between the two correlations increases as we move away from maximal value. The range of θ_{23} for which the three experiments can differentiate between the correlations at 3σ is given in table 4.2. The lower limits signify the values of θ_{23} below which the correlations can be differentiated at 3σ and the upper limits is for the values above which the same can be achieved.

4.4 Conclusion

We study here partial $\mu-\tau$ reflection symmetry of the leptonic mixing matrix, U, which can arise from discrete flavor symmetry. Specific assumptions which lead to this symmetry were reviewed here. This symmetry implies $|U_{\mu i}| = |U_{\tau i}|$ $(i = 1, 2, 3)$ for a single column of the leptonic mixing matrix U. If this is true for the third column of U then it leads to maximal value of the atmospheric mixing angle and the CP phase δ_{CP} takes the values $\pm\frac{\pi}{2}$. However, if this is true for the first or the second column then one obtains definite correlations among θ_{23} and δ_{CP}. We call these scenarios C_1 (equality for the first column) and C_2 (equality of the second column). We find that almost all the discrete subgroups of SU(3), except a few exceptional cases, having three dimensional irreducible representations display the form of partial $\mu-\tau$ symmetry. We study the correlations among θ_{23} and δ_{CP} in the two scenarios. Each scenario gives two values of δ_{CP} for a given θ_{23} – one belonging to $0° < \delta_{CP} < 180°$ and the other belonging to $180° < \delta_{CP} < 360°$. The models also give specific correlations between θ_{23} and δ_{CP} and these are opposite for C_1 and C_2. We study how the allowed areas in the $\sin^2\theta_{23} - \delta_{CP}$ plane obtained by the global analysis of neutrino oscillation data from the Nu-Fit collaboration compare with the predictions from the symmetries.

We also expound the testability of these symmetries considering next generation accelerator based experiments, DUNE and Hyper-Kamiokande. This is illustrated in terms of plots in the $\sin^2\theta_{23}$ (true) - δ_{CP}(true) plane obtained by fitting the simulated experimental data with the symmetry predictions for δ_{CP}. The values of θ_{23} are found to be more constrained for the CP conserving values namely $\delta_{CP} = 0°, 180°, 360°$. For the C_2 correlation, the θ_{23} is found to be in the higher octant for $\delta_{CP} = 180°$ and in the lower octant for $\delta_{CP} = 0°$ and $360°$. For the correlation C_1, values of δ_{CP} around all the three CP conserving values $\delta_{CP} = 0°$, $180°$ and $360°$ are seen to be disfavored. Finally, we illustrate the capability of DUNE and Hyper-Kamiokande to distinguish between the predictions of the two correlations. We observe that both the experiments can better differentiate between these two as one moves away from the maximal θ_{23} value.

In conclusion, the future experiments provide testing grounds for various symmetry relations, specially those connecting θ_{23} and δ_{CP}.

Chapter 5

Partial μ-τ Reflection Symmetry with 3+1 neutrino mixing

In the previous chapter we considered the μ-τ reflection symmetry in context of three neutrino mixing. In this chapter we study the implications of partial μ-τ symmetry for 3+1 neutrino mixing assuming the presence of a light sterile neutrino with a goal to understand the various correlation which arises when partial μ-τ symmetry is applied in presence of a light sterile neutrino.

In the context of $3 + 1$ neutrino mixing exact μ-τ permutation symmetry would still give θ_{13} to be zero. Studies have been accomplished in the literature examining the possible role of active-sterile mixing in generating a breaking of this symmetry starting from a μ-τ symmetric 3×3 neutrino mass matrix [248, 249, 250, 251, 204, 252, 253]. In this chapter we concentrate on the ramifications of μ-τ reflection symmetry for the 4×4 neutrino mass matrix in presence of one sterile neutrino. We study the consequences of total as well as partial μ-τ reflection symmetry in the 3+1 framework and obtain predictions and correlations between different parameters. We also formulate the 4×4 neutrino mass matrix which can give rise to such a μ-τ reflection symmetry. Further we study the experimental consequences of μ-τ reflection symmetry at the future long baseline neutrino oscillations experiment DUNE. In addition we discuss the implications of μ-τ reflection symmetry for Majorana phases and neutrinoless double β decay.

The chapter is organized as follows. In Section 5.1 we first construct the generic structure of the 4×4 mass matrix which can give rise to μ-τ reflection symmetry for sterile neutrinos. In the next section, we find the correlation among the active and sterile mixing angles and Dirac CP phases. In Section 5.3 we study the experimental implications of such μ-τ reflection symmetry for DUNE experiment and also calculate the effective neutrino mass which can be probed through neutrinoless double β decay experiments. Then finally in Section 5.4 we summarize the findings.

5.1 μ-τ reflection symmetry for 3+1 neutrino mixing

Guided by the atmospheric neutrino data, the μ-τ reflection symmetry was first proposed for 3-generation neutrino mixing back in 2002 [191, 192]. Under such symmetry the elements of lepton mixing matrix satisfy :

$$|U_{\mu i}| = |U_{\tau i}| \quad \text{where} \quad i = 1, 2, 3. \tag{5.1}$$

This indicates that the moduli of μ and τ flavor elements of the 3×3 neutrino mixing matrix are equal. With these constraints, the neutrino mixing matrix can be parameterised as [191, 192]

$$U_0 = \begin{pmatrix} u_1 & u_2 & u_3 \\ v_1 & v_2 & v_3 \\ v_1^* & v_2^* & v_3^* \end{pmatrix}, \tag{5.2}$$

where the entries in the first row, u_i's are real (and non-negative)[1]. v_i satisfy the orthogonality condition $2\mathrm{Re}(v_j v_k^*) = \delta_{jk} - u_k u_k$ [217]. In [192], it was argued that the mass matrix leading to the mixing matrix given in Eq. 5.2 can be written as

$$\mathcal{M}_0 = \begin{pmatrix} a & d & d^* \\ d & c & b \\ d^* & b & c^* \end{pmatrix}, \tag{5.3}$$

[1] Various implications of Majorana phases under such symmetry can be found in [254].

where a, b are real and d, c are complex parameters. As a consequence of the symmetry given in Eq. 5.1-5.3, we obtain the predictions for maximal $\theta_{23} = 45^\circ$ and $\delta = 90^\circ$ or 270° in the basis where the charged leptons are considered to be diagonal. This scheme however still leaves room for nonzero θ_{13}. Several attempts were made in this direction to explain correct mixing (for three active neutrinos) with μ-τ reflection symmetry and to study their origin and consequences in various scenarios [202, 207, 255, 256, 257, 258, 259, 201, 200, 260, 197, 261, 262, 263, 264, 265, 266].

Although, μ-τ reflection symmetry is well studied for three active neutrinos, it lacks a comprehensive study considering sterile neutrinos. Now such a mixing scheme can easily be extended for a $3+1$ scenario incorporating sterile neutrinos. Under such circumstances, the 4×4 neutrino mixing matrix can be parameterised as

$$U = \begin{pmatrix} u_1 & u_2 & u_3 & u_4 \\ v_1 & v_2 & v_3 & v_4 \\ v_1^* & v_2^* & v_3^* & v_4^* \\ w_1 & w_2 & w_3 & w_4 \end{pmatrix}, \tag{5.4}$$

where u_i, w_i are real but v_i are complex. Within this extended scenario, the mass matrix can now be written as

$$\mathcal{M} = \begin{pmatrix} a & d & d^* & e \\ d & c & b & f \\ d^* & b & c^* & f^* \\ e & f & f^* & g \end{pmatrix}, \tag{5.5}$$

where a, b, e, g are real and d, c, f are complex parameters. Such a complex symmetric mass matrix can be obtained from the Lagrangian

$$\mathcal{L}_{\text{mass}} = \frac{1}{2} \nu_L^T C^{-1} \mathcal{M}_\nu \nu_L + \text{H.C.} \tag{5.6}$$

with $U^T \mathcal{M}_\nu U = \hat{m} \equiv \text{diag}\,(m_1, m_2, m_3, m_4)$, where m_j's are the real positive mass eigenvalues. Here the matrix $\mathcal{M}$ is characterized by the transformation

$$S\mathcal{M}_\nu S = \mathcal{M}_\nu^* \quad \text{with} \quad S = \begin{pmatrix} 1 & 0 & 0 & 0 \\ 0 & 0 & 1 & 0 \\ 0 & 1 & 0 & 0 \\ 0 & 0 & 0 & 1 \end{pmatrix}, . \tag{5.7}$$

and respects the mixing matrix given in Eq. 5.4. To verify this compatibility between the neutrino mixing and mass matrix let us first write mixing matrix as $U = (c_1, c_2, c_3, c_4)$ with column vectors c_j. Then using the diagonalization relation $U^T \mathcal{M}_\nu U = \text{diag}\,(m_1, m_2, m_3, m_4)$ one can write

$$\mathcal{M}_\nu c_j = m_j c_j^* \,. \tag{5.8}$$

Now, using Eq. 5.7, we find

$$\mathcal{M}_\nu \left(S c_j^*\right) = m_j \left(S c_j^*\right)^* . \tag{5.9}$$

Following the above equation, one can therefore find another diagonalizing matrix, $U' = SU^*$. Now it can be shown that if both U and U' satisfy the diagonalization relation $U^T \mathcal{M}_\nu U = \text{diag}\,(m_1, m_2, m_3, m_4)$ with non-degenerate mass eigenvalues, then there exists a diagonal unitary matrix X such that

$$SU^* = UX \,, \tag{5.10}$$

here X_{jj} is an arbitrary phase factor for $m_j = 0$ and $X = \pm 1$ for $m_j \neq 0$. Therefore the constraint obtained in Eq. 5.10 leads to [2]

$$|U_{\mu i}| = |U_{\tau i}| \quad \text{where} \quad i = 1, 2, 3, 4. \tag{5.11}$$

The above equation can also be verified in an alternate way. Let us first define an

[2] Following the same approach for 3ν in [192].

Hermitian matrix as,

$$H = \mathcal{M}_\nu^* \mathcal{M}_\nu \tag{5.12}$$

considering the form of $\mathcal{M}_\nu$ given in Eq. 5.5 one can easily find

$$H_{\mu\mu} = H_{\tau\tau} \quad \text{and} \quad H_{e\mu} = H_{e\tau}^*, \quad H_{s\mu} = H_{s\tau}^* \, . \tag{5.13}$$

Now, one can write the diagonalization relation in this case as : $H_{\alpha\beta} = U_{\alpha i} \hat{m}_{ij}^2 U_{j\beta}^\dagger$. Hence using Eq (5.13) we get

$$\sum_{i=1}^{4} \hat{m}_{ii}^2 |U_{\mu i}|^2 = \sum_{i=1}^{4} \hat{m}_{ii}^2 |U_{\tau i}|^2 \tag{5.14}$$

which follows only if masses are degenerate or $|U_{\mu i}| = |U_{\tau i}|$ [192]. Therefore, it is now clear to us that the mass matrix given in Eq. 5.5 actually leads to a mixing matrix of the form in Eq. 5.4. In the following section we discuss the consequences of this μ-τ reflection symmetry involving the active and sterile mixing angles and phases in details.

It is important to note that the mixing matrix given in Eq. 5.2 should correspond to the standard neutrino mixing matrix U_{PMNS} for three generation case. Now, depending upon the choice of the arbitrary phase factor X given in Eq. 5.10 the Majorana phases can be fixed in the context of μ-τ reflection symmetry. With the choice of $X_{ii} = 1$ or -1 the Majorana phases are fixed at $0°$ or $90°$ [217, 201]. Such fixed values of phases can have implication for neutrinoless double beta decay which will be discussed later.

5.2 Constraining 3+1 neutrino mixing with μ-τ reflection symmetry

For 3+1 neutrino mixing scenario the neutrino mixing matrix U can be written in terms of a 4×4 unitary matrix. A 4×4 unitary matrix can be parametrized by 6 mixing angles and 10 phases. Such a matrix can be written in terms of rotation matrices and phase matrices as

$$U = P'(\phi_1, \phi_2, \phi_3, \phi_4) R_{34} U_{\delta 24} R_{24} U_{\delta 24}^{\dagger} U_{\delta 14} R_{14} U_{\delta 14}^{\dagger} R_{23} U_{\delta 13} R_{13} U_{\delta 13}^{\dagger} R_{12} P(\alpha, \beta, \gamma). \tag{5.15}$$

In the above matrix among the 10 phases, 3 phases are Dirac phases which cannot be separated from U, which are represented by the matrices $U_{\delta ij}$ composed of Dirac phases δ_{ij}. The phases ϕ_1, ϕ_2 , ϕ_3 can be absorbed by redefining the charge lepton fields. The phase ϕ_4 is unobservable because it appears with the field ν_4 which do not have any charge current interaction. The phases in the phase matrix P consists of three Majorana phases α, β and γ. The matrix P can be defined by $P = \mathrm{diag}\{1, \mathrm{e}^{\mathrm{i}\alpha}, \mathrm{e}^{\mathrm{i}\beta}, \mathrm{e}^{\mathrm{i}\gamma}\}$ additionally the matrix P can also be defined as $P = \mathrm{diag}\{1, \mathrm{e}^{\mathrm{i}\alpha}, \mathrm{e}^{\mathrm{i}(\beta+\delta_{13})}, \mathrm{e}^{\mathrm{i}(\gamma+\delta_{14})}\}$ by including the Dirac phases δ_{13} and δ_{14} from the matrices $U_{\delta 14}^{\dagger}$ and $U_{\delta 13}^{\dagger}$.

The 4×4 unitary matrix can be parameterized by three active neutrino mixing angles $\theta_{13}, \theta_{12}, \theta_{23}$ and three more angles originating from active-sterile mixing, namely, θ_{14}, θ_{24} and θ_{34}. It will also contain three Dirac CP violating phases, such as, δ, δ_{14} and δ_{24}. Hence this 4×4 unitary PMNS matrix U can be given by

$$U = R_{34} \tilde{R}_{24} \tilde{R}_{14} R_{23} \tilde{R}_{13} R_{12}, \tag{5.16}$$

where the rotation matrices R and $\tilde{R}$'s can be written as

$$R_{34} = \begin{pmatrix} 1 & 0 & 0 & 0 \\ 0 & 1 & 0 & 0 \\ 0 & 0 & c_{34} & s_{34} \\ 0 & 0 & -s_{34} & c_{34} \end{pmatrix}, \quad \tilde{R}_{24} = \begin{pmatrix} 1 & 0 & 0 & 0 \\ 0 & c_{24} & 0 & s_{24} e^{-i\delta_{24}} \\ 0 & 0 & 1 & 0 \\ 0 & -s_{24} e^{i\delta_{24}} & 0 & c_{24} \end{pmatrix},$$

$$\tilde{R}_{14} = \begin{pmatrix} c_{14} & 0 & 0 & s_{14} e^{-i\delta_{14}} \\ 0 & 1 & 0 & 0 \\ 0 & 0 & 1 & 0 \\ -s_{14} e^{-i\delta_{14}} & 0 & 0 & c_{14} \end{pmatrix}, \quad R_{23} = \begin{pmatrix} 1 & 0 & 0 & 0 \\ 0 & c_{23} & s_{23} & 0 \\ 0 & -s_{23} & c_{23} & 0 \\ 0 & 0 & 0 & 1 \end{pmatrix},$$

$$\tilde{R}_{13} = \begin{pmatrix} c_{13} & 0 & s_{13}e^{-i\delta} & 0 \\ 0 & 1 & 0 & 0 \\ -s_{13}e^{i\delta} & 0 & c_{13} & 0 \\ 0 & 0 & 0 & 1 \end{pmatrix}, \quad R_{12} = \begin{pmatrix} c_{12} & s_{12} & 0 & 0 \\ -s_{12} & c_{12} & 0 & 0 \\ 0 & 0 & 1 & 0 \\ 0 & 0 & 0 & 1 \end{pmatrix}. \tag{5.17}$$

Along with the parameterization defined in Eq. 6.12, there also exists a diagonal phase matrix, $P = \mathrm{diag}(1, \mathrm{e}^{\mathrm{i}\alpha}, \mathrm{e}^{\mathrm{i}(\beta+\delta)}, \mathrm{e}^{\mathrm{i}(\gamma+\delta_{14})})$, where α, β and γ are the Majorana phases. The PMNS matrix with the Majorana phases takes the form as

$$U = R_{34}\tilde{R}_{24}\tilde{R}_{14}R_{23}\tilde{R}_{13}R_{12}P, \tag{5.18}$$

Note that, the correspondence of the mixing matrix in Eq. 5.4 along with the diagonal phase matrix P in Eq. 5.18 implies that the Majorana phases are zero or $\pm\frac{\pi}{2}$ as described in the previous section. This means that the Majorana phases takes the values of 0 or $\pm\frac{\pi}{2}$ if $\mu - \tau$ symmetry is imposed. However, in light of Eq. 5.1 this diagonal phase matrix do not play any role in the present analysis. But they can play role in neutrinoless double β decay which will be discussed in Section 5.3. Following these conditions, one can obtain four different equalities among six mixing angles and three Dirac CP violating phases. To keep the present analysis simple, first we have assumed the sterile Dirac CP violating phases (δ_{14} and δ_{24}) to be zero. For this case, δ_{14} = δ_{24} = $0°$, from Eq. 5.1 these four correlations can be written as,

$$\cos\delta = \frac{(a_1^2+b_1^2)-(c_1^2+d_1^2)}{2(c_1d_1-a_1b_1)} \quad (\text{for } |\mathrm{U}_{\mu 1}| = |\mathrm{U}_{\tau 1}|) \tag{5.19}$$

$$\cos\delta = \frac{(a_2^2+b_2^2)-(c_2^2+d_2^2)}{2(a_2b_2-c_2d_2)} \quad (\text{for } |\mathrm{U}_{\mu 2}| = |\mathrm{U}_{\tau 2}|) \tag{5.20}$$

$$\cos\delta = \frac{(a_3^2+b_3^2)-(c_3^2+d_3^2)}{2(a_3b_3-c_3d_3)} \quad (\text{for } |\mathrm{U}_{\mu 3}| = |\mathrm{U}_{\tau 3}|) \tag{5.21}$$

$$\tan^2\theta_{24} = \sin^2\theta_{34} \quad (\text{for } |\mathrm{U}_{\mu 4}| = |\mathrm{U}_{\tau 4}|) \tag{5.22}$$

where

$$a_1 = (c_{12}s_{13}s_{23}s_{24}s_{34} - c_{12}c_{23}c_{34}s_{13}), b_1 = (c_{34}s_{12}s_{23} - c_{12}c_{13}c_{24}s_{14}s_{34} + c_{23}s_{12}s_{24}s_{34})$$

$$
\begin{aligned}
c_1 &= (c_{23}c_{24}s_{12} + c_{12}c_{13}s_{14}s_{24}), d_1 = (c_{12}c_{24}s_{13}s_{23}),\\
a_2 &= c_{12}(c_{34}s_{23} + c_{23}s_{24}s_{34}) + s_{12}c_{13}c_{24}s_{14}s_{34}\\
b_2 &= s_{12}(s_{13}s_{23}s_{24}s_{34} - c_{23}c_{34}s_{13}), c_2 = (c_{12}c_{23}c_{24} - s_{12}c_{13}s_{14}s_{24}), d_2 = s_{12}c_{24}s_{13}s_{23}\\
a_3 &= c_{13}(c_{23}c_{34} - s_{23}s_{24}s_{34}), b_3 = c_{24}s_{13}s_{14}s_{34}),\\
c_3 &= s_{13}s_{14}s_{24} \text{ and } d_3 = c_{13}c_{24}s_{23}. \qquad (5.23)
\end{aligned}
$$

Here, the first three equalities enable us to study the correlation among the mixing angles $\theta_{12}, \theta_{23}, \theta_{13}, \theta_{14}, \theta_{24}, \theta_{34}$ and Dirac CP phase δ whereas the fourth relation yields a crucial correlation between the two sterile mixing angles θ_{24} and θ_{34}. For δ_{14} & $\delta_{24} \neq 0°$, such compact expressions cannot be obtained. However, in our numerical analysis we have studied the effect of inclusion of these phases. When the sterile mixing angles $(\theta_{14}, \theta_{24}, \theta_{34})$ are taken to be zero, the correlations obtained in Eq. 5.19-5.23 reduces to the three neutrino mixing scenarios studied in [256, 234, 267, 268, 269] . Below we

Oscillation parameters	Best-fit	3σ range
θ_{13}	$8.6°$	$8.2° : 9.0°$
θ_{12}	$33.8°$	$31.6° : 36.3°$
θ_{23}	49.5	$40° : 52°$
Δm^2_{21} (eV^2)	7.4×10^{-5}	fixed
$\lvert\Delta m^2_{31}\rvert$ (eV^2)	2.5×10^{-3}	$(2.35 : 2.65) \times 10^{-3}$
δ	$0° : 360°$	$0° : 360°$
Oscillation parameters	Representative Value	3σ range
Δm^2_{41} (eV^2)	1	fixed
θ_{14}	$9°$	$4° : 10°$
θ_{24}	$9°$	$5° : 10°$
θ_{34}	$9°$	$0° : 11°$
δ_{14}	–	$0° : 360°$
δ_{24}	–	$0° : 360°$

Table 5.1: The best-fit values and 3σ ranges of the 3 neutrino oscillation parameters [3, 1] used in the present analysis and the representative ranges for 3+1 neutrino mixing [4].

study the various correlations between the parameters due to Eqs.5.19-5.22. We find that the phenomenologically interesting correlations are between $\theta_{23} - \delta$ and $\theta_{24} - \theta_{34}$. Since the other sterile mixing angles are already restricted to a narrow range, no other important correlations are obtained.

5.2.1 Total $\mu - \tau$ symmetry

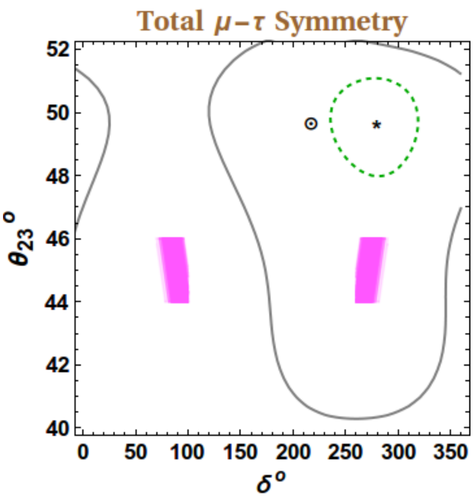

Figure 5.1: Allowed region for total $\mu - \tau$ symmetry for 3+1 neutrino scenario. Here the other mixing parameters are varied within 3σ range [3, 1, 4]. The $\odot$ and $\star$ represents the best-fit values for normal and inverted neutrino mass hierarchy respectively.

In this subsection we present the results assuming $\mu - \tau$ reflection symmetry to be valid for all the four columns simultaneously; we call this as the total $\mu - \tau$ reflection symmetry. The magenta shaded region in Fig. 5.1 represents the allowed region for total $\mu - \tau$ symmetry for 3+1 neutrino scenario in $\theta_{23} - \delta$ plane. The analysis is performed by varying the other mixing parameters in their 3σ range as in Tab. 6.1 and the sterile CP phases δ_{14} and δ_{24} between 0° to 360°[3]. The grey solid and green dashed contours denote the currently allowed parameter space for NH and IH respectively in this and the subsequent figures. The application of the total $\mu - \tau$ symmetry significantly restricts the parameters θ_{23} and δ. θ_{23} is primarily restricted around the maximal while δ falls in the close vicinity of 90° and 270°. Comparing the results with 3 neutrino scenario [218, 256] where θ_{23} is strictly restricted to be maximal and δ to 90° and 270° we conclude that the involvement of the sterile mixing angles and phases lead to slight deviations in θ_{23} and δ from their 3 generation predictions. However, the

[3]Here (and in the rest of the analysis, unless otherwise mentioned) we vary both δ_{14} and δ_{24} between 0° to 360°.

current global fit results from [3] suggests that the best fit for θ_{23} is 49.5° for both normal and inverted hierarchies. Thus, even with inclusion of sterile neutrinos, total $\mu - \tau$ reflection symmetry cannot explain the current best-fit. This motivates us to consider the partial $\mu - \tau$ reflection symmetry for the 3+1 scenario.

5.2.2 Partial $\mu - \tau$ reflection symmetry

In this section we discuss the implications partial $\mu - \tau$ reflection symmetry which implies that the condition $|U_{\mu i}| = |U_{\tau i}|$ is satisfied for individual columns.

5.2.2.1 $|U_{\mu 1}| = |U_{\tau 1}|$

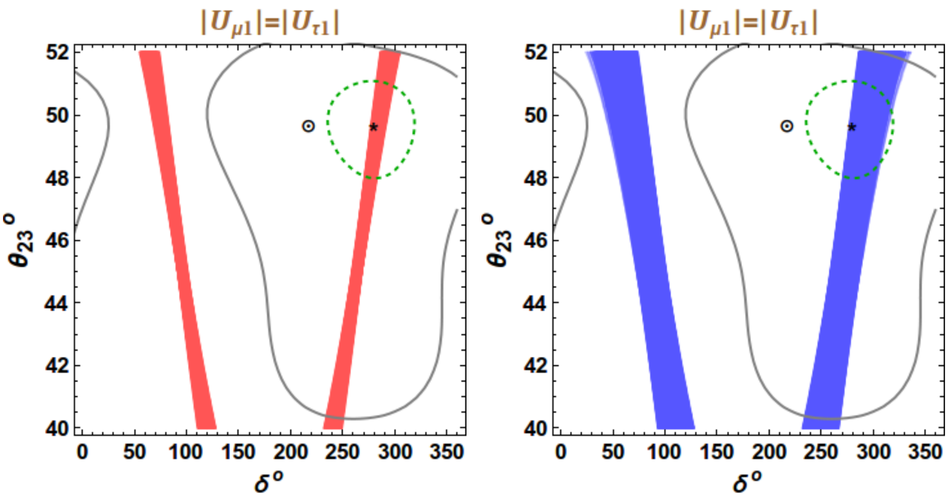

Figure 5.2: Correlation between θ_{23} and Dirac CP phase δ for $|U_{\mu 1}| = |U_{\tau 1}|$ with δ_{14}, $\delta_{24} = 0^\circ$ (left panel) and δ_{14}, $\delta_{24} \neq 0^\circ$ (right panel) respectively. Here all other mixing parameters are varied within their 3σ range as given in Tab. 6.1. The continuous and dashed contours represent 3σ allowed range in the $\theta_{23} - \delta$ plane and the $\odot$ and $\star$ represent the best-fit values for normal and inverted neutrino mass hierarchy respectively.

The correlation obtained from the equality $|U_{\mu 1}| = |U_{\tau 1}|$ has been plotted in the $\theta_{23} - \delta$ plane in Fig. 5.2. The left panel with red contours in Fig. 5.2 represents the case with sterile phases δ_{14} and δ_{24} taken to be zero while the right panel with blue contours denotes the case with δ_{14} and δ_{24} to be non-zero. In these panels, the grey continuous and green dashed contours represent 3σ allowed range in the $\theta_{23} - \delta$ plane and the $\odot$ and $\star$ represents the best-fit values for normal and inverted neutrino mass hierarchy respectively [4]. The interesting result obtained from these correlations are the range of δ allowed by the $\mu - \tau$ reflection symmetry. In this case the CP conserving values of δ are ruled out and preference is seen for maximal CP violation. This points towards an important consequence of $\mu - \tau$ reflection symmetry i.e. if $\mu - \tau$ reflection symmetry is true for the first column of lepton mixing matrix CP violation is implied. The recent global fit [3] result also point towards the maximal CP violation with with preference for $\delta \sim 270°$. From both these panels it is clear that under $\mu - \tau$ reflection symmetry in the first column of lepton mixing matrix, inverted hierarchy of neutrino mass is a more favored scenario given the current best-fit values, this is true with or without the involvement of sterile CP phases (δ_{14},δ_{24}). The inclusion of the sterile CP phases δ_{14},δ_{24} predicts slightly larger allowed range for δ.

5.2.2.2 $|U_{\mu 2}| = |U_{\tau 2}|$

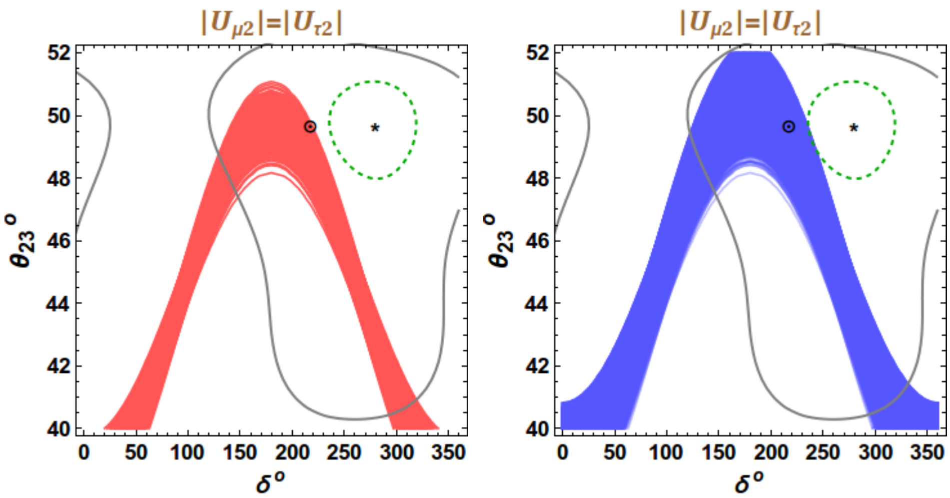

Figure 5.3: Correlation between θ_{23} and Dirac CP phase δ for $|U_{\mu 2}| = |U_{\tau 2}|$ with δ_{14},$\delta_{24} = 0°$ (left panel) and δ_{14}, $\delta_{24} \neq 0°$ (right panel) respectively. Here all other mixing parameters are varied within their 3σ range as given in Tab. 6.1. The continuous and dashed contours represent 3σ allowed range in the $\theta_{23} - \delta$ plane and the $\odot$ and $\star$ represents the best-fit values for normal and inverted neutrino mass hierarchy respectively.

$\mu - \tau$ reflection symmetry in the second column of lepton mixing matrix (given by

[4]Similar descriptions are also true for the subsequent figures for $|U_{\mu 2}| = |U_{\tau 2}|$ and $|U_{\mu 3}| = |U_{\tau 3}|$.

$|U_{\mu 2}| = |U_{\tau 2}|$) is plotted in Fig. 5.3. It is seen from the left panel of this figure that this symmetry disfavors $\delta = 0°$ while $\delta = 180°$ is allowed from the correlation for the current θ_{23} range when sterile CP phase are zero. The presence of the sterile CP phases δ_{14}, δ_{24} predicts slightly larger allowed range for both θ_{23} and δ, and in presence of these phases, both $\delta = 0°$ and $\delta = 180°$ become admissible unlike the previous case in Fig. 5.2. Interestingly the current 3σ global fit contours for inverted hierarchy do not overlap with the allowed region due to $\mu - \tau$ reflection symmetry in the second column of the lepton mixing matrix with sterile CP phases δ_{14} = δ_{24} = 0°. But, there is a slight overlap between the above specified regions once δ_{14} and δ_{24} are taken non-zero.

5.2.2.3 $|U_{\mu 3}| = |U_{\tau 3}|$

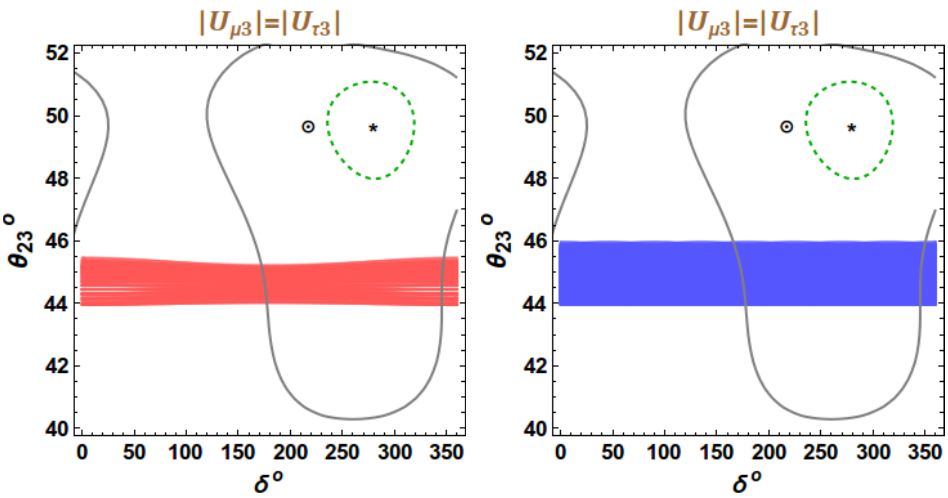

Figure 5.4: Correlation between θ_{23} and Dirac CP phase δ for $|U_{\mu 3}| = |U_{\tau 3}|$ with δ_{14},$\delta_{24} = 0°$ (left panel) and δ_{14}, $\delta_{24} \neq 0°$ (right panel) respectively. Here all other mixing parameters are varied within their 3σ range as given in Tab. 6.1. The continuous and dashed contours represent 3σ allowed range in the $\theta_{23} - \delta$ plane and the $\odot$ and $\star$ represents the best-fit values for normal and inverted neutrino mass hierarchy respectively.

In Fig. 5.4 we show the consequence of $|U_{\mu 3}| = |U_{\tau 3}|$, and it is seen that the allowed value of θ_{23} stays close to maximal with slight deviation within a very narrow range with a preference for the lower octant as given in the left panel of Fig. 5.4 with δ_{14},$\delta_{24} = 0°$. If we introduce the non-zero values for the sterile CP phases (δ_{14}, $\delta_{24} \neq 0°$), the variation of θ_{23} remains in the vicinity of $45°$ with equal deviations in both lower and higher octants as evident from the right panel of Fig. 5.4. However, the deviation is not enough to reach the best-fit θ_{23} from current data [3, 209, 270]. However, if future data from T2K or NOνA give a value closer to maximal θ_{23} (but not exactly maximal) then this scenario can be preferred over the three generation case. Since for the three flavor case, the condition $|U_{\mu 3}| = |U_{\tau 3}|$ leads to $\theta_{23} = 45°$. However, in presence of sterile neutrinos there is a spread around the maximal value and future measurements of θ_{23} can confirm or falsify if this condition can indeed be satisfied. In this context it is also worthwhile to discuss to what extent future high statistics experiments can determine the octant of θ_{23} close to maximal value. For instance, it was shown in [174] from a combined analysis of DUNE and T2HK that the octant of θ_{23} will remain unresolved for true values in the range $43° - 48.7°$. The maximum allowed range of θ_{23} for $|U_{\mu 3}| = |U_{\tau 3}|$ in presence of sterile mixing and phases being $44° - 46°$, the octant will remain undetermined in this situation even with the future high statistics experiments.

5.2.2.4 $|U_{\mu 4}| = |U_{\tau 4}|$

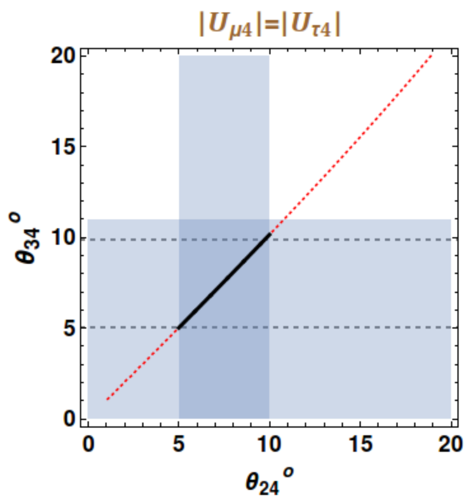

Figure 5.5: Constraints on θ_{34} obtained from $|U_{\mu 4}| = |U_{\tau 4}|$. Here the red dashed line (including the black line) represents this correlation. Shaded regions are current allowed range [4]. Here 3σ allowed range of θ_{24} [4] restricts θ_{34} within the range $4.9° - 9.8°$ (as given by the dark black line).

In this 3+1 neutrino framework, the fourth equality $|U_{\mu 4}| = |U_{\tau 4}|$ establishes a powerful correlation between the two sterile mixing angles θ_{24} and θ_{34}. Here we obtain a one-to-one correspondence between θ_{24} and θ_{34} as given in Eq. 5.22. Even with the involvement of sterile CP phase this relation remains same as evident from Eq. 5.11 and 6.12. This correlation yields a linear dependence between the two sterile mixing angles θ_{24} and θ_{34} as given in Fig. 5.5. Once we impose the constraints coming from the current allowed value of θ_{24} [4], the sterile mixing angle θ_{34} becomes restricted from below significantly. Note that so far there only exists a upper limit on θ_{34} [4]. In Fig. 5.5 we plot this correlation and find that θ_{34} lies within the range $4.9^\circ - 9.8^\circ$ corresponding to the 3σ allowed range of θ_{24} [4]. Therefore, the $\mu - \tau$ reflection symmetry presented here restricts the sterile mixing angle θ_{34} considerably. The allowed parameter space in the $\theta_{24} - \theta_{34}$ plane also gets restricted. This is one of the most crucial finding in this $\mu - \tau$ reflection symmetric framework for 3+1 neutrino scenario. It is to be noted that among the current constraints on sterile mixing angles, the bound on θ_{34} is much weaker, there being only an upper limit on this. The reactor neutrino experiments are sensitive to the mixing matrix element U_{e4}^2 or s_{14}^2 in our parametrization. The short baseline oscillation experiments using appearance channel are sensitive to the product $|U_{e4}|^2|U_{\mu4}^2|$ which contains the product $s_{14}^2 s_{24}^2$. Bounds on θ_{34} have been obtained from atmospheric neutrinos at SuperKamiokande [271], DeepCore detector at Icecube [272], and from Neutral Current data at MINOS [273], NOνA [274] and T2K [275] experiments. The constraints on θ_{34} from individual experiments are somewhat weaker (in the ballpark of $20^\circ - 30^\circ$) than what is obtained in the global analysis of [4]. In our analysis the later has been used. Neutral current events at the DUNE detector can also improve on the bound on θ_{34} coming from a single experiment [276]. The ν_τ appearance channel is also sensitive to θ_{34} and the potential of DUNE experiment to constrain this mixing angle has been studied in [277, 278, 279]. Thus it is expected that future data can test this correlation and the allowed parameter space.

These discussions lead us to the inference that partial $\mu - \tau$ reflection symmetry is more favorable scenario. However it is to be noted that in this scenario the case $|U_{\mu3}| = |U_{\tau3}|$ is disfavored because it fixes θ_{23} around the maximal value. Again, the simultaneous application of equalities $|U_{\mu1}| = |U_{\tau1}|$ and $|U_{\mu2}| = |U_{\tau2}|$ restricts

$\theta_{23} \sim 45^\circ$ hence both these equalities cannot be satisfied together. Such experimental constraints do not apply on $|U_{\mu 4}| = |U_{\tau 4}|$ therefore this equality may still hold. So, the favorable scenarios are:

- $|U_{\mu 1}| = |U_{\tau 1}|$ with $|U_{\mu 4}| = |U_{\tau 4}|$
- $|U_{\mu 2}| = |U_{\tau 2}|$ with $|U_{\mu 4}| = |U_{\tau 4}|$

5.3 Experimental consequences of μ-τ reflection symmetry

5.3.1 Consequences at Neutrino Oscillations Experiments

In this section we explore the consequences of partial $\mu - \tau$ reflection symmetry in the 3+1 scenario for the Deep Underground Neutrino Experiment (DUNE).

5.3.1.1 Experimental and Simulation details

The experimental simulation have been performed using the package General Long Baseline Experiment Simulator (GLoBES) [280, 281], and the sterile neutrino effects have been applied using the sterile neutrino engine as described in [282].

To test the correlations at DUNE we define χ^2 as

$$\chi^2_{\rm tot} = \min_{\xi,\omega}\{\chi^2_{\rm stat}(\omega,\xi) + \chi^2_{\rm pull}(\xi)\}. \tag{5.24}$$

where, the statistical χ^2 is $\chi^2_{\rm stat}$ while the systematic uncertainties are incorporated by χ^2_{pull}. The later is calculated by the method of pulls with pull variables given by ξ [244, 245, 246]. The oscillation parameters $\{\theta_{23}, \theta_{12}, \theta_{13}, \delta_{CP}, \Delta m^2_{21}, \Delta m^2_{31}, \Delta m^2_{41}, \theta_{14}, \theta_{24}, \theta_{34}, \delta_{14}\delta_{24}\}$ are represented by ω. The statistical χ^2_{stat} is calculated assuming Poisson distribution,

$$\chi^2_{stat} = \sum_i 2\left(N_i^{test} - N_i^{true} - N_i^{true}\log\frac{N_i^{test}}{N_i^{true}}\right). \tag{5.25}$$

Here, 'i' stands for the number of bins and N_i^{test}, N_i^{true} stands for total number of test and true events respectively. To include the effects of systematics in N_i^{test}, pull and "tilt" variables are incorporated as follows:

$$N_i^{\rm (k)test}(\omega,\xi) = \sum_{k=s,b} N_i^{(k)}(\omega)[1 + c_i^{(k)norm}\xi^{(k)norm} + c_i^{(k)tilt}\xi^{(k)tilt}\frac{E_i - \bar{E}}{E_{max} - E_{min}}] \tag{5.26}$$

where $k = s(b)$ represent the signal(background) events. The effect of the pull variable $\xi^{norm}(\xi^{tilt})$ on the number of events are denoted by $c_i^{norm}(c_i^{tilt})$. The bin by bin mean reconstructed energy is represented by E_i where i represents the bin. E_{min}, E_{max} and $\bar{E} = (E_{max} + E_{min})/2$ are the minimum energy, maximum energy and the mean energy over this range. The signal normalization uncertainties used are as follows: for $\nu_e/\bar{\nu}_e$ - 2% and $\nu_\mu/\bar{\nu}_\mu$ - 5%. While the background uncertainties vary from 5% to 20%.

5.3.1.2 μ-τ reflection symmetry at DUNE for 3+1 neutrino mixing

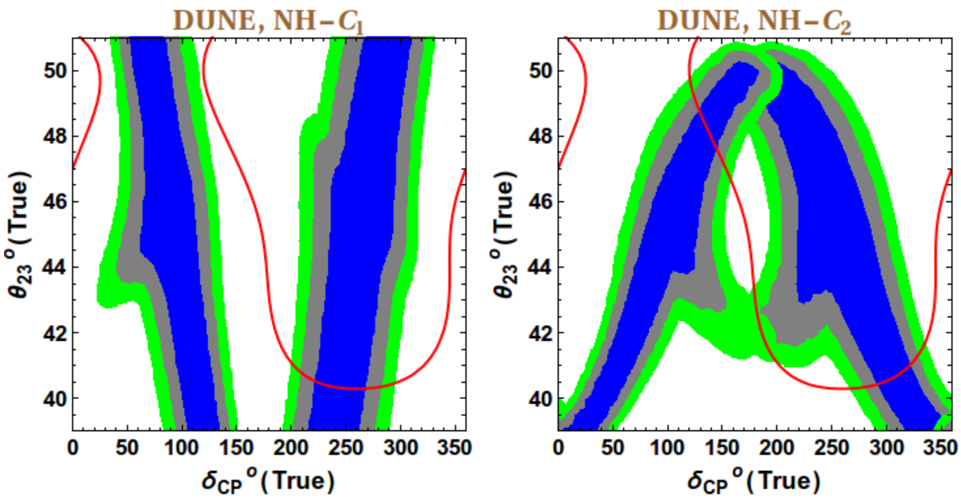

Figure 5.6: Experimental constraints on δ_{CP} from the correlations $|U_{\mu1}| = |U_{\tau1}|$ and $|U_{\mu2}| = |U_{\tau2}|$ for DUNE. The left(right) column indicate correlation $|U_{\mu1}| = |U_{\tau1}|(|U_{\mu2}| = |U_{\tau2}|)$. The blue, grey and green shaded regions depict 1σ, 2σ and 3σ confidence regions respectively. While the red contours represent the currently allowed 3σ region considering true Normal Hierarchy.

The consequences of the partial $\mu - \tau$ reflection symmetry at the experiment is observed by analyzing the confidence region in the θ_{23}(true) vs δ_{CP}(true) plane which remains allowed after the application of the symmetry relations in the test parameters. The approach taken for the numerical analysis can be summarized as follows:

- The simulated data for the experiment DUNE are generated for the representative true values of the oscillation parameters as given by the best-fit in Tab. 6.1 excepting for θ_{23} and δ. The true values of these parameters are varied over the range $39^\circ - 51^\circ$ and $0^\circ - 360^\circ$ respectively. The true values of δ_{14} & δ_{24} are taken as 0°.

- The test events are generated by marginalization of the parameters θ_{12}, θ_{13}, $|\Delta m^2_{31}|$, θ_{23}, θ_{14}, θ_{24}, θ_{34} over the range given in Tab. 6.1 subject to the condition embodied in Eq. 5.19 for the left panel and Eq. 5.20 for the right panel. The other parameters are held fixed at their true values for calculation of N_{test}. In this study we have assumed normal hierarchy as the true hierarchy. We have checked that marginalizing over test hierarchy do not have significant effect because the correlations are independent of hierarchy.

- For each true value of θ_{23} and δ the χ^2 is minimized and the allowed regions defined by $\chi^2 \le \chi^2_{min} + \Delta\chi^2$ are plotted corresponding to 1σ, 2σ and 3σ values of $\Delta\chi^2$.

The experimental consequences at DUNE are presented in Fig. 5.6. Here the first(second) column represents the correlation $|U_{\mu 1}| = |U_{\tau 1}|(|U_{\mu 2}| = |U_{\tau 2}|)$. The condition $|U_{\mu 4}| = |U_{\tau 4}|$ is also incorporated in both the plots. Each plot consists of 1σ, 2σ & 3σ confidence regions considering partial μ - τ reflection symmetry which are shaded as blue, grey and green respectively. The current 3σ permitted region from NuFIT[3, 1] data is drawn with red solid line. The plots show a similar nature as the correlation plots in Fig. 5.2 and 5.3, however, the allowed regions are wider which reflects the inclusion of the experimental errors. From the first column of the figure we observe that DUNE can reject the CP conserving values (0°, 180° & 360°) at 3σ. But when the correlation $|U_{\mu 2}| = |U_{\tau 2}|$ is considered as shown in the right column the CP conserving δ_{CP} values cannot be excluded at 3σ . Note that, some of the areas allowed by the current data are disfavored by applying the correlations. As the correlations predict a range of δ_{CP} given a set of oscillations parameters, the experiments can further constrain the range of δ_{CP} which are allowed by the present oscillation data.

5.3.2 Implications for Neutrino-less double β decay

Neutrinoless double β decay ($0\nu\beta\beta$) can test whether neutrinos are Majorana particles. This process takes place by emitting two electrons without the emission of the expected anti-neutrinos as observed in $2\nu\beta\beta$ decay. The half-life ($T_{1/2}$) for the $0\nu\beta\beta$ process is given as,

$$(T_{1/2})^{-1} = \frac{\Gamma_{0\nu\beta\beta}}{\ln 2} = G\left|\frac{M_\nu}{m_e}\right|^2 m_{\beta\beta}^2, \tag{5.27}$$

where G contains the lepton phase space integral, m_e is the mass of electron, M_ν is the nuclear matrix element (NME) which takes into consideration all the nuclear structure effects, $m_{\beta\beta}$ stands for the effective neutrino mass and can be expressed as

$$m_{\beta\beta} = |U_{ei}^2 m_i|. \tag{5.28}$$

Here m_i are the real positive neutrino mass eigenvalues with $i = 1, 2, 3$ for three generation and $i = 1, 2, 3, 4$ for $3 + 1$ neutrino mixing respectively.

Null results from several experiments have constrained the lifetimes of $0\nu\beta\beta$. KamLAND-Zen [283] have reported a lifetime of $T_{1/2}(^{136}Xe) > 10.7 \times 10^{25}$ years, GERDA [284] reported as $T_{1/2}(^{76}Ge) > 8 \times 10^{25}$ years, CURCINO and CUORE [285] combined results reported the lifetime as $T_{1/2}(^{130}Te) > 1.5 \times 10^{25}$ years at 90% confidence level. The lower bound on $T_{1/2}$ can be translated to the upper bound of effective neutrino mass ($m_{\beta\beta}$) [54, 286]. Using the parametrization of U in Eq. 5.18, $m_{\beta\beta}$ can be expressed as,

$$m_{\beta\beta} = |m_1\, c_{12}^2 c_{13}^2 c_{14}^2 + m_2\, s_{12}^2 c_{13}^2 c_{14}^2 e^{i2\alpha} + m_3\, s_{13}^2 c_{14}^2 e^{i2\beta} + m_4\, s_{14}^2 e^{i2\gamma}|. \tag{5.29}$$

For NH (IH) m_1 (m_3) is the lightest neutrino mass eigenstate. All other neutrino mass eigenvalues can be expressed in terms of the lightest neutrino mass and mass squared differences as follows :

- Normal Hierarchy (NH) : $m_1 < m_2 << m_3$ with

$$m_2 = \sqrt{m_1^2 + \Delta m_{sol}^2}\ ;\ m_3 = \sqrt{m_1^2 + \Delta m_{atm}^2}\ ; \tag{5.30}$$

$$m_4 = \sqrt{m_1^2 + \Delta m^2_{\rm LSND}},$$

- Inverted Hierarchy (IH) : $m_3 << m_1 \approx m_2$ with

$$\begin{aligned} m_1 &= \sqrt{m_3^2 + \Delta m^2_{atm}} \;\; ; \;\; m_2 = \sqrt{m_3^2 + \Delta m^2_{sol} + \Delta m^2_{atm}}; \\ m_4 &= \sqrt{m_3^2 + \Delta m^2_{atm} + \Delta m^2_{\rm LSND}}, \end{aligned} \tag{5.31}$$

where $\Delta m^2_{sol} = m_2^2 - m_1^2$, $\Delta m^2_{atm} = m_3^2 - m_1^2$ $(m_1^2 - m_3^2)$ for NH (IH) and $\Delta m^2_{\rm LSND} = m_4^2 - m_1^2$.

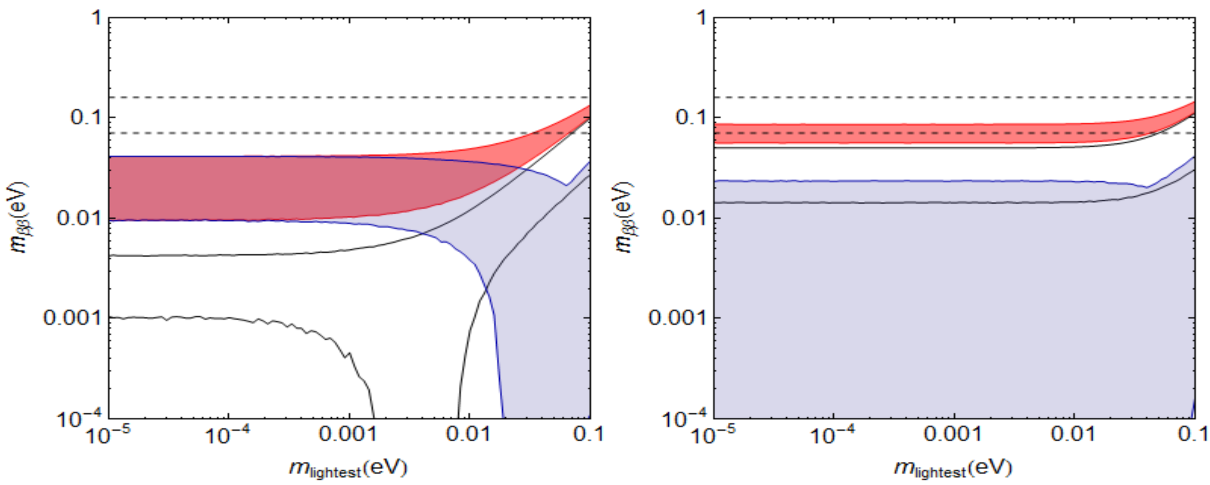

Figure 5.7: The effective neutrino mass $m_{\beta\beta}$ for $0\nu\beta\beta$ as a function of the lightest neutrino mass. The left panel shows the effective neutrino mass for NH while the right panel is for IH. The red region represents $m_{\beta\beta}$ in presence of $\mu-\tau$ reflection symmetry in 3+1 neutrino mixing where the Majorana phases are kept as zero whereas the blue region represents the scenario when all the Majorana phases are fixed at 90°. The areas inside the black solid lines are the 3 neutrino allowed regions. The pair of purple dashed lines at 0.071 eV & 0.161 eV represent the upper limit for $m_{\beta\beta}$ by combined analysis of GERDA and KamLAND-Zen experiments.

Predictions for $m_{\beta\beta}$ with respect to the lightest neutrino mass for 3+1 scheme along with the three neutrino case is presented in Fig. 5.7. The plot in the left panel shows the effective neutrino mass for NH while the right panel is for IH. In generating these plots we have varied the oscillations parameters within their 3σ range as given in Tab. 6.1 with $\Delta m^2_{\rm LSND} = 1.7$ eV^2 [4]. In both panels of Fig. 5.7, the red and blue shaded regions (corresponding to Majorana phases fixed at 0 and 90° respectively) represents $m_{\beta\beta}$ in presence of $\mu-\tau$ reflection symmetry in 3+1 neutrino mixing. In the plots (both left and right panel) the area between the black dashed lines at 0.071 eV & 0.161 eV represents the upper limit for $m_{\beta\beta}$ obtained from the combined analysis of GERDA and KamLAND-Zen experiments. The width in the upper limit of $m_{\beta\beta}$ is present because of the NME uncertainty. For purposes of comparison we also present the three neutrino allowed regions given by the black solid lines in the Fig. 5.7. Below we discuss from the analytic expression, the allowed regions for $m_{\beta\beta}$ for both hierarchies. The Majorana phases which are of interest to us from the point of view of $\mu-\tau$ reflection symmetry are 0 and 90°.

* **Inverted Hierarchy:**

  For inverted hierarchy, the red shaded region corresponds to the the case with $\alpha = \beta = \gamma = 0^\circ$. It is seen that $m_{\beta\beta}$ stays almost constant in the range $0.057 - 0.087$ eV till $m_{\text{lightest}} \sim 0.01$ eV, after which there is a slight increase in its value. The width of the band can be ascribed to the variation in the oscillation parameters in their 3σ range. The blue shaded region is obtained for $\alpha = \beta = \gamma = 90^\circ$. It is observed that complete cancellation can be obtained for these values of phases. Thus the two predictions of $\mu - \tau$ reflection symmetry give drastically different results. Also, the predictions of $m_{\beta\beta}$ for the sterile neutrino case with Majorana phases as 90° are markedly different from the three neutrino case for which there are no cancellation regions. Below we explain these features analytically in different limits of the lightest neutrino mass.

Case 1: When $m_3 << m_1 \approx m_2 \approx \sqrt{\Delta m^2_{atm}}$ and $m_4 \approx \sqrt{\Delta m^2_{\text{LSND}}}$ we find

$$\begin{aligned} m_{\beta\beta} &= |\sqrt{\Delta m^2_{atm}}\, c^2_{13} c^2_{14} (c^2_{12} + s^2_{12} e^{i2\alpha}) \\ &+ \sqrt{\Delta m^2_{\text{LSND}}}\, s^2_{14} e^{i2\gamma}|. \end{aligned} \tag{5.32}$$

Taking the approximations $c^2_{13} \sim c^2_{14} \sim 1$, $s^2_{12} \sim 0.33, c^2_{12} \sim 0.67$ and

$\sqrt{\Delta m^2_{atm}} \sim 0.05$ eV, $\sqrt{\Delta \mathrm{m}^2_{\mathrm{LSND}}} \sim 1$ eV we obtain

$$m_{\beta\beta} = 0.033 + 0.017 e^{i2\alpha} + s^2_{14} e^{i2\gamma}. \tag{5.33}$$

For $\alpha = \gamma = 0^\circ$ and s^2_{14} in the range 0.005-0.03 the above gives $m_{\beta\beta}$ in the range (0.057-0.087) eV which is consistent with the values observed in the figure 5.7. On the other hand for $\alpha \sim 90^\circ$ and $\gamma \sim 90^\circ$, one can get cancellations in $m_{\beta\beta}$ for $s^2_{14} \sim 0.016$. This explains the occurrence of the cancellation regions for this choice of phases.

Case 2: For $m_3 \approx \sqrt{\Delta m^2_{atm}}$, $m_1 \approx m_2 \approx \sqrt{2\Delta m^2_{atm}}$, $m_4 \approx \sqrt{\Delta m^2_{\mathrm{LSND}}}$ and we write

$$\begin{aligned} m_{\beta\beta} &= |\sqrt{2\Delta m^2_{atm}}\, c^2_{13} c^2_{14} (c^2_{12} + s^2_{12} e^{i2\alpha} + \frac{t^2_{13}}{\sqrt{2}} e^{i2\beta}) \\ &+ \sqrt{\Delta m^2_{\mathrm{LSND}}}\, s^2_{14} e^{i2\gamma}|. \end{aligned} \tag{5.34}$$

Again, utilizing the same values of parameters involved as in Case 1 along with $s^2_{13} \sim 0.024$ the effective mass can be obtained as

$$m_{\beta\beta} = 0.047 + 0.023 e^{i2\alpha} + 0.001 e^{i2\beta} + s^2_{14} e^{i2\gamma}. \tag{5.35}$$

Substituting $\alpha = \beta = \gamma = 0^\circ$ in eq. 5.34 one gets $m_{\beta\beta}$ in the range $0.075 - 0.106$ eV which can be seen from the figure for $m_{\mathrm{lightest}} \sim 0.05$ eV.

In this case also cancellations occur for $\alpha = \beta = \gamma \sim 90^\circ$ and $s^2_{14} \sim 0.023$.

Note that in both the limits the cancellations could only be achieved because of the large value of $\sqrt{\Delta m^2_{\mathrm{LSND}}}$. Cancellations in three generations is not possible because of absence of any term which can counter the large positive value of the first term. This leaves the effective neutrino mass bounded from below in the three generation case.

It is to be noted that in the red shaded region in the right panel of Fig. 5.7 the value of $m_{\beta\beta}$ is $> 0.06\text{eV}$, while, the current experimental bound is $m_{\beta\beta} < 0.07\text{eV}$. Therefore, a portion of $m_{\beta\beta}$ is already disfavored for certain parameter values from the current experimental bounds by GERDA and KamLAND-Zen experiments. This experimental bound can constrain the sterile parameter θ_{14} as

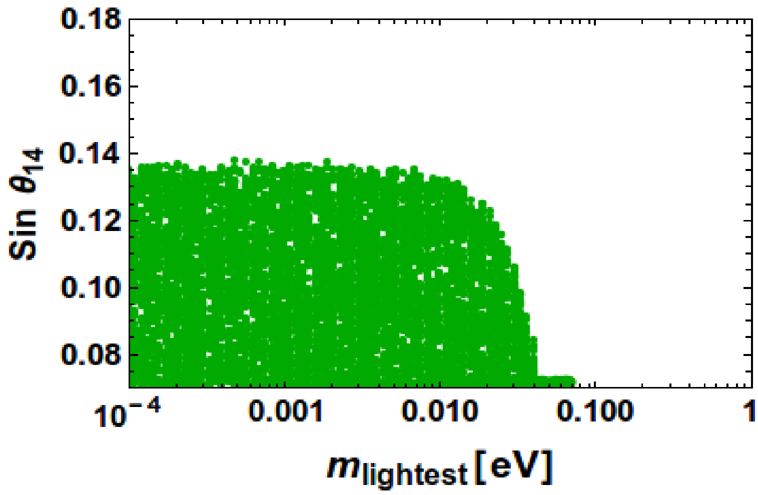

Figure 5.8: The effective neutrino mass $m_{\beta\beta}$ for $0\nu\beta\beta$ as a function of $\sin\theta_{14}$.

presented in Fig. 5.8. In this figure the green shaded zone represents the region allowed by GERDA and KamLAND-Zen in the m_{lightest} vs $\sin\theta_{14}$ plane for the case corresponding to zero Majorana phases of $\mu - \tau$ reflection symmetry for 3+1 neutrino mixing. We observe that $\sin\theta_{14} < 0.14$ is allowed upto $m_{\text{lightest}} = 0.02$ eV. As m_{lightest} increases further $\sin\theta_{14}$ sharply reduces because higher m_{lightest} is compensated by lower $\sin^2\theta_{14}$ in order to satisfy the upper limit of $m_{\beta\beta}$.

It is well known that near future $0\nu\beta\beta$ experiments like SNO+ Phase I[287], KamLAND-Zen 800[288], and LEGEND 200[289] can test the IH region in the context of the three generation scenario. These experiments will be able to test the predictions for $\alpha = \beta = \gamma = 0°$ further. However, in presence of an extra sterile neutrino, a null signal in these experiments cannot exclude IH because of the occurence of the cancellation regions.

* **Normal Hierarchy:**

From the first panel of Fig. 5.7 we observe that for $\alpha = \beta = \gamma = 0^\circ$, the red shaded region, $m_{\beta\beta}$ stays is in the range $\sim 0.01 - 0.05$ eV rising upto 0.1 eV for higher values of m_{lightest}. For both three neutrino case (region bounded by black lines) and 3+1 neutrino mixing (with $\alpha = \beta = \gamma = 90^\circ$, blue shaded region), complete cancellation in $m_{\beta\beta}$ is seen to occur for NH. The cancellations occur between 0.001 eV to 0.01 eV for three neutrino mixing while it occurs between 0.01 eV to 0.1 eV for 3+1 neutrino mixing. Thus, compared to the three neutrino case the cancellation region for 3+1 neutrino mixing shifts towards higher values of m_{lightest} due to involvement of $m_4 \sim 1\text{eV}$. To analytically understand the salient features of the predictions for $m_{\beta\beta}$ for NH we scrutinize the following limits:

Case 1: For $m_1 << \sqrt{\Delta m^2_{atm}}$ using Eq. 5.31 and Eq. 5.29 we obtain

$$m_{\beta\beta} = |\sqrt{\Delta m^2_{atm}} t^2_{13} e^{i2\beta} + \sqrt{\Delta m^2_{\text{LSND}}}\, s^2_{14} e^{i2\gamma}|. \tag{5.36}$$

In this case for $\alpha = \beta = \gamma = 0^\circ$, the value of $m_{\beta\beta}$ for $t^2_{13} \sim 0.024$, $s^2_{14} \sim 0.05$, $\sqrt{\Delta m^2_{atm}} \sim 0.05$ eV we get $m_{\beta\beta} \sim 0.03$ eV which is in the range obtained in the figure 5.7. Since $t^2_{13} \sim s^2_{14}$ and $\Delta m^2_{atm} << \Delta m^2_{\text{LSND}}$ cancellations are not possible for smaller values of m_1. For $\alpha = \beta = \gamma = 90^\circ$ gives similar results as the $\alpha = \beta = \gamma = 0^\circ$ case which is also corroborated from the figure.

Case 2: Now, when $m_1 \sim \sqrt{\Delta m^2_{atm}}$ then the expression for the effective mass reduces to

$$\begin{aligned} m_{\beta\beta} &= |\, c^2_{13} c^2_{14} \sqrt{\Delta m^2_{atm}} (c^2_{12} + s^2_{12} e^{i2\alpha} + \sqrt{2} t^2_{13} e^{i2\beta}) \qquad (5.37) \\ &\quad + \sqrt{\Delta m^2_{\text{LSND}}}\, s^2_{14} e^{i2\gamma}|, \\ &\approx 0.033 + 0.017 e^{i2\alpha} + 0.002 e^{i2\beta} + s^2_{14} e^{i2\gamma}. \qquad (5.38) \end{aligned}$$

		$m_{\beta\beta}$ for NH			$m_{\beta\beta}$ for IH		
		$m_1 = 0.001$ eV	$m_1 = 0.01$ eV	$m_1 = 0.052$ eV	$m_3 = 0.001$ eV	$m_3 = 0.01$ eV	$m_3 = 0.052$ eV
Sterile : Majorana Phases = 0	$m_{\beta\beta_{\rm min}} \times 10^{-3}$	10.28	17.01	57.70	56.43	57.19	77.28
	$m_{\beta\beta_{\rm max}} \times 10^{-3}$	42.15	48.40	89.27	86.47	87.37	108.58
Sterile : Majorana Phases = 90°	$m_{\beta\beta_{\rm min}} \times 10^{-3}$	8.92	3.82	0.03	0.01	0.02	0.01
	$m_{\beta\beta_{\rm max}} \times 10^{-3}$	40.94	36.76	20.40	23.68	23.15	24.54
3 Generation	$m_{\beta\beta_{\rm min}} \times 10^{-3}$	0.46	0.76	13.77	14.28	14.50	20.23
	$m_{\beta\beta_{\rm max}} \times 10^{-3}$	4.83	12.10	53.18	50.37	51.40	73.02

Table 5.2: Predictions for $m_{\beta\beta}$ for various cases for few benchmark points of the lightest neutrino mass (m_1 for NH and m_3 for IH). $m_{\beta\beta_{\rm min}}$ and $m_{\beta\beta_{\rm min}}$ stands for the respective minimum and maximum values of $m_{\beta\beta}$ for each benchmark point.

For zero values of the Majorana phases $m_{\beta\beta}$ can reach upto 0.08 eV for $s_{14}^2 = 0.03$. In this limit, cancellations can occur for $\alpha = \beta = \gamma = 90°$ and $s_{14}^2 \sim 0.015$.

Note that the predictions for $m_{\beta\beta}$ in the 3+1 picture for zero Majorana phases for higher values of $m_{\rm lightest}$ are already crossing the current experimental values and this can put bound on sterile parameters as in the previous case. Since the values of $m_{\beta\beta}$ upto $m_{\rm lightest} \sim 0.001$ eV is in the same ballpark as the IH values for three generation scenario, the near future experiments designed to test the 3 generation IH region can also probe this region. For representative purposes we have included the predictions for $m_{\beta\beta}$ for various cases for few benchmark points of the lightest neutrino mass (m_1 for NH and m_3 for IH) in Table 5.2.

In our analysis we have considered $\Delta m^2_{LSND} = 1.7$ eV^2 which gives the physical mass of sterile neutrino $m_4 = m^s_{ph} \sim 1.3$ eV. The Cosmic Microwave Background analysis in $\Lambda_{\rm CDM} + r_{0.05} + N_{\rm eff} + m^s_{\rm eff}$ model using the Planck 2015 data [290] gives the $N_{\rm eff} < 3.78$ and $m^s_{\rm eff} < 0.78$ eV [291]. The bounds including other datasets are more stringent than this. As the effective mass in terms of the $N_{\rm eff}$ and physical mass of sterile neutrino is given as $m^s_{\rm eff} = \Delta N^{3/4}_{\rm eff}\, m^s_{\rm ph}$, where, $\Delta N_{\rm eff} = N_{\rm eff} - 3.046$ one gets $m^s_{\rm ph} < 0.98$ eV at 95% CL.

5.4 Conclusion

To understand the observed pattern of lepton mixing, $\mu - \tau$ symmetry may play a crucial role as it can be originated from various discrete flavor symmetries. Along with three active neutrinos, presence of one sterile neutrino may have some interesting predictions on neutrino mixing angles and Dirac CP violating phases within the framework of such $\mu-\tau$ symmetries. Conventional $\mu-\tau$ permutation symmetry for 3+1 picture is not a phenomenologically viable scenario as it can not explain correct neutrino mixing (since it predicts $\theta_{13} = 0°$). Hence here we have analyzed a simple extension of it, known as $\mu - \tau$ reflection symmetry, in the context of 3+1 neutrino mixing. We formulate the mass matrix compatible with the lepton mixing matrix which can give rise to $\mu - \tau$ reflection symmetry, defined via $|U_{\mu i}| = |U_{\tau i}|$ where $i = 1, 2, 3, 4$. We obtain and plot the correlations connecting the mixing angle θ_{23} and the CP phase δ for the case when sterile phases are assumed to be zero, as well as present the correlation plots with the sterile phases varied in their full range. We find that if we consider total $\mu - \tau$ reflection symmetry i.e. $|U_{\mu i}| = |U_{\tau i}|$ is simultaneously satisfied for all the four columns then the mixing angle θ_{23} is confined in a narrow region around $\theta_{23} = 45°$ and δ is restricted around the maximal CP violating values. However, the deviation of θ_{23} from maximal value with the inclusion of the sterile mixing is not sufficient to account for the observed best fit value. This prompts us to consider partial $\mu - \tau$ reflection symmetry and study the consequences for each column individually.

The equalities $|U_{\mu 1}| = |U_{\tau 1}|$ and $|U_{\mu 2}| = |U_{\tau 2}|$ yield important correlations among the neutrino mixing angle θ_{23} and Dirac CP phase δ. Interestingly we find that the best-fit value for (θ_{23}, δ) shows a good agreement with inverted neutrino mass hierarchy for $|U_{\mu 1}| = |U_{\tau 1}|$ and normal mass hierarchy for $|U_{\mu 2}| = |U_{\tau 2}|$. With precise measurement of θ_{23} and δ in near future there is a clear possibility of verifying these correlations. The inclusion of the sterile CP phases widens the allowed regions. For the equality $|U_{\mu 3}| = |U_{\tau 3}|$ the mixing angle θ_{23} sightly deviates from its maximal value and falls mostly in the lower octant ($\theta_{23} < 45°$) including the effect of sterile mixing angle. This, however, is not supported by the global oscillation analysis [3, 1, 270]. The equality $|U_{\mu 4}| = |U_{\tau 4}|$ yields an one-to-one correspondence between the sterile mixing angles θ_{24} and θ_{34} making it one of the most significant finding in the present study. So far, there exists only an upper limit on θ_{34}. Interestingly, here we find that the correlation obtained from $|U_{\mu 4}| = |U_{\tau 4}|$ restricts θ_{34} within the range $4.9° - 9.8°$. The allowed region in the $\theta_{24} - \theta_{34}$ plane also gets severely restricted. Future experiments sensitive to these mixing angles can test the correlations discussed.

We also explore the possibility of testing the μ-τ reflection symmetry for 3+1 neutrino mixing at the future LBL experiment DUNE. The application of the correlations constrains a significant area of the parameter space yet unconstrained by the present global fit data. In particular the constraint is more stringent for the relation $|U_{\mu 1}| = |U_{\tau 1}|$ and all the CP conserving values $\delta = 0^\circ, 180^\circ, 360^\circ$ are excluded at 3σ. However, for $|U_{\mu 2}| = |U_{\tau 2}|$ CP conserving values of δ remain allowed.

Furthermore, we expound the implications of the μ-τ reflection symmetry for 3+1 neutrino mixing at neutrinoless double β experiments by calculating the effective neutrino mass ($m_{\beta\beta}$) for this scenario. The μ-τ reflection symmetry predicts the Majorana phases to be zero or 90°. For the former predicted effective neutrino mass is higher and can be explored at the future $0\nu\beta\beta$ experiments. In fact for higher values of the lightest neutrino mass the effective neutrino mass $m_{\beta\beta}$ can cross the current experimental bounds when Majorana phases are assumed to be zero. We have shown that, for IH, this constrains the sterile parameter θ_{14} under 8° using the bounds on the effective neutrino mass. For the Majorana phases as 90°, for IH there can be cancellation regions in stark contrast with the three generation predictions. For NH, the cancellation region for the 3+1 case occur for higher values of the lightest neutrino mass as compared to the three neutrino picture.

In conclusion, $\mu - \tau$ reflection symmetry for sterile neutrinos in a 3+1 picture gives some interesting predictions which can be tested in future neutrino oscillation and neutrinoless double beta experiments and the scenario can be confirmed or falsified.

Chapter 6

Neutral current events and new physics at nuSTORM

6.1 Introduction

Neutrinos from Stored Muons (nuSTORM)[5, 6] is a proposed facility for measurement of neutrino nucleus cross-sections with a percent-level precision owing to the possibility of the determination of neutrino flux with high accuracy. It has been shown in [5, 6] that nuSTORM has excellent capability to search for existence of light sterile neutrinos of the type postulated to explain the LSND and MiniBooNE results. This work considered only the charge current events. We study the sensitivity of nuSTORM to constrain the sterile neutrino parameters including the neutral current events. Along with exploring the presence of a sterile neutrino we also investigate the capability of nuSTORM to search for other new physics scenario like non-unitary neutrino mixing.

There are several new experiments planned to test the sterile neutrino hypothesis[292, 63, 293, 294, 295, 5, 6, 296]. It was realized recently that beam based long-baseline experiments can also probe parameter space for the sterile neutrinos and several studies have been carried out in this direction considering the currently running as well as future proposed experiments. Future experiments like DUNE[144] or T2HK[146] are high statistics experiments and therefore the systematics are expected to play a crucial role and one of the major sources of systematic uncertainty is the neutrino-nucleus interaction cross-sections.

The neutrino beam in nuSTORM facility originates from muon decay process: $\mu^+ \rightarrow e^+\nu_e\overline{\nu}_\mu$ with 50% ν_e and 50% $\overline{\nu}_\mu$ which can give e^- and μ^+ at the detectors in absence of oscillation or any other new physics. If however, there are flavour changing processes then one can get wrong sign leptons which can constitute smoking-gun signals of new physics. A detector with charge identification capability is therefore ideal.

The sterile neutrino analysis performed in [297] considered a magnetized iron-calorimeter detector with a superior efficiency to identify the charge of the muons. This gives the detector the ability to record the μ^- events originating from $P_{\nu_e\nu_\mu}$ oscillations along with the μ^+ coming from the $P_{\overline{\nu}_\mu\overline{\nu}_\mu}$ channel. In this analysis only the charged current events were considered. However, there are also a large number of neutral current (NC) events. In a three-flavour-mixing paradigm, given the flavour universality of the neutral current interactions and $P_{\mu e} + P_{\mu\mu} + P_{\mu\tau} = 1$, the NC events are not sensitive to the oscillation parameters. However, in the presence of new physics that may not be the case. For instance, for oscillations of muon neutrinos to sterile neutrinos the neutral current events will be multiplied by $(1 - P_{\mu s})$. The usefulness of the NC events for sterile neutrino searches in the context of beam experiments has been studied in [275, 274, 298, 276].

Along with the sterile neutrino other beyond the Standard Model (BSM) physics descriptions have become essential in describing the non-zero neutrino mass after the discovery of neutrino oscillations. The non-zero neutrino masses can be generated by the "see-saw" mechanism through an effective lepton number violating dimension-five operator of the form $LL\phi\phi$ which can be derived from physics beyond the Standard Model [40, 44, 299, 300, 301]. These BSM physics can also lead to non-unitarity of the neutrino mixing matrix[302, 300, 303, 304, 305, 306, 301, 307, 299]. The unitarity of the PMNS matrix can be tested in the accelerator based neutrino oscillations experiments. Several studies have been performed to understand the implications of non-unitarity in present and future long baseline experiments [308, 309, 277, 310]. In this context nuSTORM also holds promise to study the non-unitarity of the PMNS matrix and constrain the parameters which generates the non-unitarity in the PMNS sector.

The capabilities of Neutrinos from Stored Muons (nuSTORM) proposal to study sterile neutrino searches as well as the non-unitarity of the neutrino mixing matrix have been studied in this chapter. In the following section:6.2 we discuss the nuSTORM proposal and the simulation of the proposal in details. We discuss the results obtained in our study in section:6.3 where the subsection:6.3.1 focuses on the study of sterile neutrinos at nuSTORM while the results considering non-unitary neutrino mixing have been presented in the subsection:6.3.2. Eventually we discuss about the conclusions obtained in the final section:6.4.

6.2 Details of Simulation

We follow the configuration and detector simulations from [5, 6, 311]. The unoscillated flux was taken from [5]. The simulation has been performed unsing the General Long Baseline Experiment Simulator (GLoBES) packege[181, 182]. The flux is based on the decay $\mu^+ \to e^+ + \nu_e + \bar{\nu}_\mu$. The neutrino beam is generated with 50 GeV protons with 2×10^{21} protons on target over the duration of 10 years. Pions of 5 GeV are injected into the muon storage ring. Muons with energy of the order 3.8 GeV subsequently decay to give ν_e and $\bar{\nu}_\mu$. The ν_e flux peaks at 2.5 GeV whereas the $\bar{\nu}_\mu$ flux peaks at 3 GeV. nuSTORM is simulated as described in [5, 6] .

In our simulation we consider a far detector at a distance of 2 km from the source unless otherwise mentioned. A 1.3 kt magnetized iron-scintillator calorimeter has been selected as the detector for short-baseline oscillation physics at nuSTORM as it has excellent charge selection and detection characteristics for muons. Therefore, the important channels for this experiment are $\nu_e \to \nu_\mu$ appearance channel and $\bar{\nu}_\mu \to \bar{\nu}_\mu$ disappearance channel. The events in the i^{th} energy bin are calculated as

$$n^i_\alpha = \frac{N}{L^2} \int_{E_i - \frac{\Delta E_i}{2}}^{E_i + \frac{\Delta E_i}{2}} dE' \int_0^\infty \varepsilon(E)\phi_\beta(E)P_{\alpha\beta}(E)\sigma_\alpha(E)R^c(E,E')\varepsilon^c(E')dE \qquad (6.1)$$

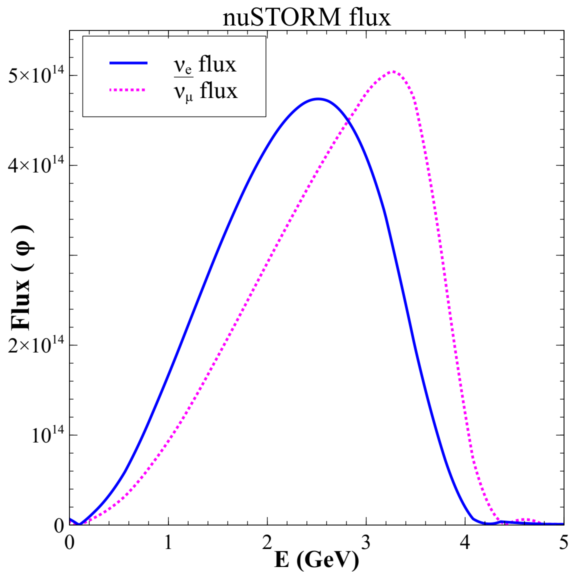

Figure 6.1: ν_e and $\bar{\nu}_\mu$ flux extracted from the storage ring.

where, E denotes the true neutrino energy and E' denotes the measured neutrino energy. $R^c(E, E')$ denotes the smearing matrix, which relates the true and the measured energy. This includes both kinematic smearing and the smearing due to energy reconstruction. This is often taken as a Gaussian. Migration matrices that give the probability for a neutrino generated in the i^{th} energy bin to be reconstructed in the j^{th} energy bin, if available from detector simulations, can also be used. $\varepsilon^c(E')$ denotes the post-smearing efficiency which contains for instance the information on energy cuts used. Whereas $\varepsilon(E)$ denotes the pre-smearing efficiency.

In our analysis we have taken the energy resolution as a Gaussian . With $R^c\,(E, E') = \dfrac{1}{\sigma(E)\sqrt{2\pi}} e^{-\frac{(E-E')^2}{2\sigma^2(E)}}$ and $\sigma(E) = 0.15E$. The energy cuts are incorporated as "post smearing efficiencies" as follows:

$$\epsilon^c\,(E') \;=\; 0 \;\;;\;\; 0 < E' < 1 \tag{6.2}$$

$$\epsilon^c\,(E') \;=\; 1 \;\;;\;\; E' > 1 \tag{6.3}$$

The event rates at the detector(multiplied by the efficiencies) and the corresponding pre-smearing efficiencies are given in table 6.1 and the unoscillated flux is given in fig.6.1.

Channel	N_{events}	Efficiency at the detector
$\nu_e \rightarrow \nu_\mu$ CC	61	0.18
$\nu_e \rightarrow \nu_e$ CC	39865	0.18
$\bar{\nu}_\mu \rightarrow \bar{\nu}_\mu$ NC	8630	0.18
$\bar{\nu}_\mu \rightarrow \bar{\nu}_\mu$ CC	114983	0.94
$\nu_e \rightarrow \nu_e$ NC	13605	0.18

Table 6.1: The events observed at the detector, this is equal to the expected number of events at the detector multiplied by their efficiencies according to [5, 6].

The impact of the neutral current events is evaluated using a χ^2 which is defined as

$$\chi^2_{\text{tot}} = \min_{\xi,\omega}\{\sum_r (\chi^2_{\text{stat}}(\omega,\xi) + \chi^2_{\text{pull}}(\xi))_r\}. \tag{6.4}$$

r denotes the "rules" and the statistical χ^2 is χ^2_{stat}, systematic uncertainties are incorporated by χ^2_{pull} calculated by the method of pulls with pull variables ξ. The significance over each rule is calculated separately and the total χ^2 is calculated by summation over all the various rules. Each "rule" signifies a different channel . The total χ^2 is marginalized over the oscillation parameters. The relevant oscillation parameters are represented by ω. The statistical χ^2_{stat} is calculated assuming Poisson distribution,

$$\chi^2_{stat} = \sum_i 2\left(N_i^{test} - N_i^{true} - N_i^{true}\log\frac{N_i^{test}}{N_i^{true}}\right). \tag{6.5}$$

Here, 'i' stands for the number of bins and N_i^{test}, N_i^{true} stands for total number of test and true events respectively. To include the effects of systematics in N_i^{test}, the normalization and energy calibration errors are parametrized using the"pull" and "tilt" variables respectively. These are incorporated as follows:

$$N_i^{(\text{k})\text{test}}(\omega,\xi) = \sum_{k=s,b} N_i^{(k)}(\omega)[1 + c_i^{(k)norm}\xi^{(k)norm} + c_i^{(k)tilt}\xi^{(k)tilt}\frac{E_i - \bar{E}}{E_{max} - E_{min}}] \tag{6.6}$$

where $k = s(b)$ represent the signal(background) events. The effect of the pull variable $\xi^{norm}(\xi^{tilt})$ on the number of events is denoted by $c_i^{norm}(c_i^{tilt})$. The bin-by-bin mean reconstructed energy is represented by E_i where i represents the bin. E_{min}, E_{max}

and $\bar{E} = (E_{max} + E_{min})/2$ are the minimum energy, maximum energy and the mean energy over this range.

The signal(background) normalization uncertainty for the appearance channel is taken as 1%(10%) [5, 6] while for $\nu_{\bar{\mu}}$ channel they are kept at 5%(10%). For NC the signal and background errors are taken to be 5% and 10% respectively. A background rejection factor of 10^{-3} is used for the disappearance channel while 10^{-5} is used for appearance channel [5, 6]. For NC events we use a background rejection factor of 10^{-4}. We have checked that the χ^2 does not depend significantly on the background rejection factor for the NC analysis. The unoscillated events observed at the detector have been shown in the fig.6.2.

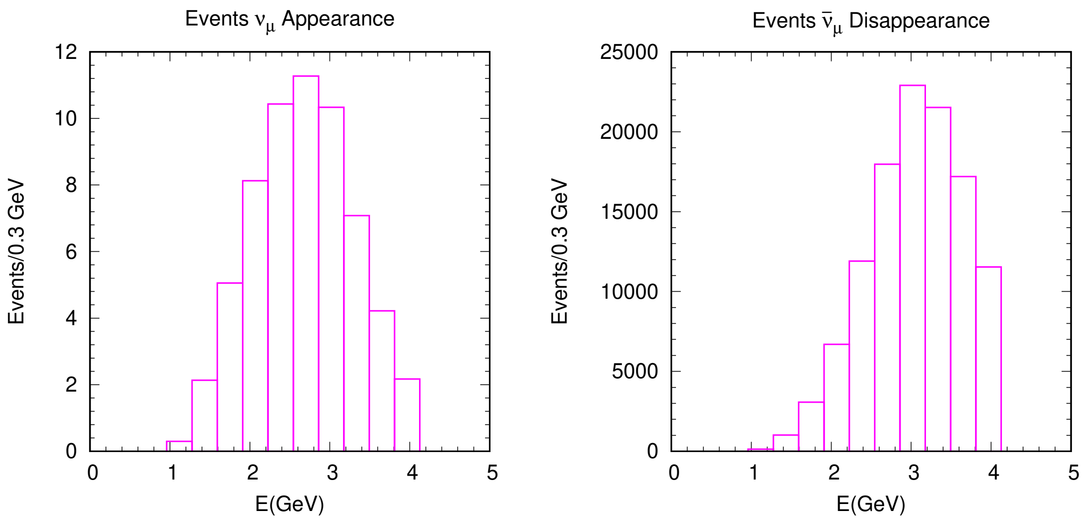

Figure 6.2: The figure shows the distribution of no oscillation events observed at the detector with bin width of 0.3 GeV. The left plot shows the appearance events while the right is for the disappearance events.

Data is generated assuming the standard three-neutrino oscillations scenario as the null hypothesis and the new physics scenario under study is used as the alternative hypothesis. Schematically the number of events in the different channels can be written as,

$$N_{\mu}^{CC} = \Phi(\nu_e) P_{e\mu} \sigma_{CC} \tag{6.7}$$

$$N_{\bar{\mu}}^{CC} = \Phi(\bar{\nu_{\mu}}) P_{\bar{\mu}\bar{\mu}} \sigma_{CC} \tag{6.8}$$

Oscillation parameters	Value considered to simulate nuSTORM
$\sin^2\theta_{13}$	0.01
$\sin^2\theta_{12}$	0.319
$\sin^2\theta_{23}$	0.462
Δm^2_{21} (eV^2)	7.59×10^{-5}
$\lvert\Delta m^2_{31}\rvert$ (eV^2)	2.46×10^{-3}
δ	0°
$\sin^2\theta_{14}$	0.025
$\sin^2\theta_{24}$	0.0.023
Δm^2_{41} (eV^2)	0.89

Table 6.2: The values of the 3 neutrino oscillation parameters [3, 1] and the representative values for 3+1 neutrino mixing [4] used in the present analysis.

$$N^{NC}_{total} \;=\; \Phi(\bar{\nu_\mu})(1 - P_{\mu s})\sigma_{NC} + \Phi(\nu_e)(1 - P_{es})\sigma_{NC}) \tag{6.9}$$

6.3 Results and Discussions

6.3.1 Sterile Neutrino

Since we are considering a distance of ∼2 km and $E \sim 3$ GeV there can be oscillations governed by a mass-squared difference of order eV^2. Other terms do not contribute since the oscillation wavelengths are much larger. Thus we have the “One Mass Scale Dominance” (OMSD) approximation in which the oscillation probabilities can be cast into an effective two flavor form. For the 3+1 picture, under the OMSD approximation, one has

$$P_{\alpha,\beta} = 4|U_{\alpha 4}|^2|U_{\beta 4}|^2 \sin^2\left(\frac{\Delta m^2_{41} L}{4E}\right) \tag{6.10}$$

and,

$$P_{\alpha\alpha} = 1 - 4|U_{\alpha 4}|^2(1 - |U_{\alpha 4}|^2)\sin^2\left(\frac{\Delta m^2_{41} L}{4E}\right) \tag{6.11}$$

Bounds on individual mixing angles are derived using the parametrization

$$U = R_{34}\tilde{R}_{24}\tilde{R}_{14}R_{23}\tilde{R}_{13}R_{12}. \tag{6.12}$$

Since we are in an effective two-generation approximation, the phases do not appear in the oscillation probabilities and ignoring them one has,

$$\begin{aligned}
U_{e4} &= \sin\theta_{14} \\
U_{\mu 4} &= \cos\theta_{14}\sin\theta_{24} \\
U_{\tau 4} &= \cos\theta_{14}\sin\theta_{34} \\
U_{s4} &= \cos\theta_{14}\cos\theta_{24}\cos\theta_{34}
\end{aligned} \tag{6.13}$$

The relevant oscillation probabilities are given as

$$P_{e\mu} = 4\cos^2\theta_{14}\sin^2\theta_{14}\sin^2\theta_{24}\sin^2\left(\frac{\Delta m^2_{41}L}{4E}\right) \tag{6.14}$$

$$P_{\mu\mu} = 1 - 4\sin^2\theta_{24}\cos^2\theta_{14}(1-\sin^2\theta_{24}\cos^2\theta_{14})\sin^2\left(\frac{\Delta m^2_{41}L}{4E}\right) \tag{6.15}$$

$$P_{\mu s} = 4\cos^4\theta_{14}\cos^2\theta_{24}\cos^2\theta_{34}\sin^2\theta_{24}\sin^2\left(\frac{\Delta m^2_{41}L}{4E}\right) \tag{6.16}$$

$$P_{es} = 4\cos^2\theta_{14}\sin^2\theta_{14}\cos^2\theta_{24}\cos^2\theta_{34}\sin^2\left(\frac{\Delta m^2_{41}L}{4E}\right) \tag{6.17}$$

$$\sin^2 2\theta_{\mu e} = 4|U_{e4}|^2|U_{\mu 4}|^2 = 4s^2_{14}c^2_{14}s^2_{24} \tag{6.18}$$

$$\sin^2 2\theta_{\mu\mu} = 4|U_{\mu 4}|^2(1-|U_{\mu 4}|^2) = 4c^2_{14}s^2_{24}(1-c^2_{14}s^2_{24}) \tag{6.19}$$

Figure 6.3 demonstrates the bounds on Δm^2_{41} with respect to the effective mixing angles $\theta_{\mu e}$ and $\theta_{\mu\mu}$ for baselines of 2 km and 3.5 km presented the first and the second row of the fig:6.3 respectively. The oscillation amplitudes satisfy: $P_{e\mu} \propto s^2_{14}s^2_{24}$; $P_{\mu\mu} \propto 1 - s^2_{24}$; and $P_{es} + P_{\mu s} \propto s^2_{14} + s^2_{24}$ (see eq.6.14 - 6.17). Therefore, in the case of the appearance channel, $P_{e\mu}$ can constrain the effective mixing angle $\sin^2 2\theta_{\mu e}$ which is a product of $s^2_{14}s^2_{24}$ while the neutral-current channel cannot constrain the product of $s^2_{14}s^2_{24}$ and hence cannot efficiently constrain $\sin^2 2\theta_{\mu e}$. The disappearance channel effectively probes the parameter $\theta_{\mu\mu}$ in terms of the parameter s^2_{24}, also the neutral current channel probes $s^2_{14} + s^2_{24}$ hence, the neutral current channel can significantly

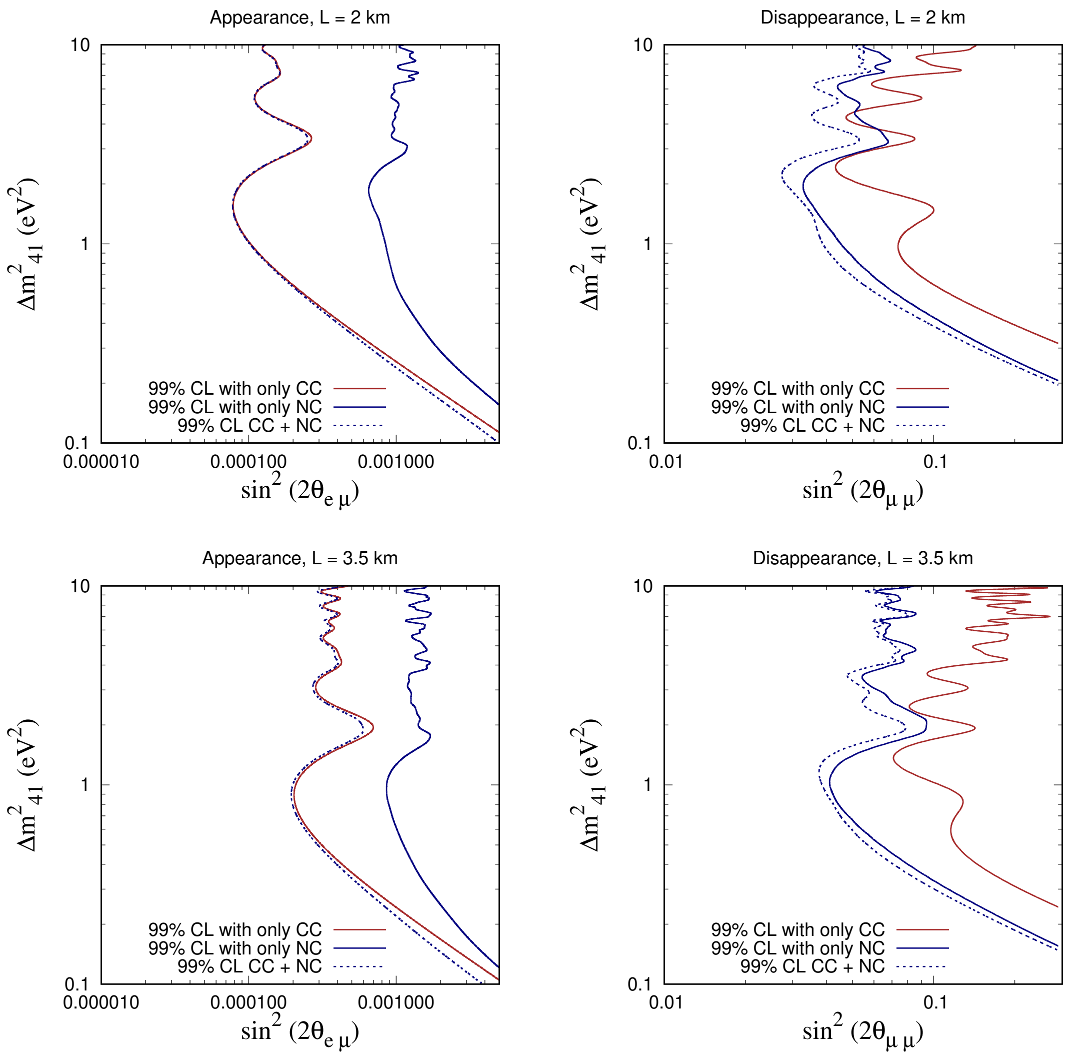

Figure 6.3: The testable regions for sterile neutrinos as predicted by nuSTORM in terms of Δm^2_{41} vs $\sin^2\theta_{\mu e}$ for the left plots and Δm^2_{41} vs $\sin^2\theta_{\mu\mu}$ for the right. The first row indicates the sensitivities or baseline of 2 km while the second row for 3.5 km. Each plot consists of 3 contours of 99% confidence level significance exclusion regions for various channels as labeled in the plots.

contribute to probe the parameter $\theta_{\mu\mu}$. This study was performed for two baselines of 2 km and 3.5 km. The choice of the 3.5 km baseline was motivated by the fact that this places the detector at oscillation maxima for $\Delta m^2_{41} \sim 1\text{eV}^2$. If we study the bottom panel of the fig.6.3 we observe that the best sensitivities for both $\theta_{\mu e}$ and $\theta_{\mu\mu}$ are observed around $\Delta m^2_{41} \sim 1\text{eV}^2$, which is expected. Proceeding to the top panel of the fig.6.3 we find that the most sensitive region has shifted to $\Delta m^2_{41} \sim 1.2\text{eV}^2$, this is expected because $\Delta m_{41}^2 L \approx 3.7\mathrm{eV}^2\mathrm{km}$. However, the overall sensitivity is better for the lower baseline of 2 km as the lower baseline has a lower statistical uncertainty because of a higher flux at the detector.

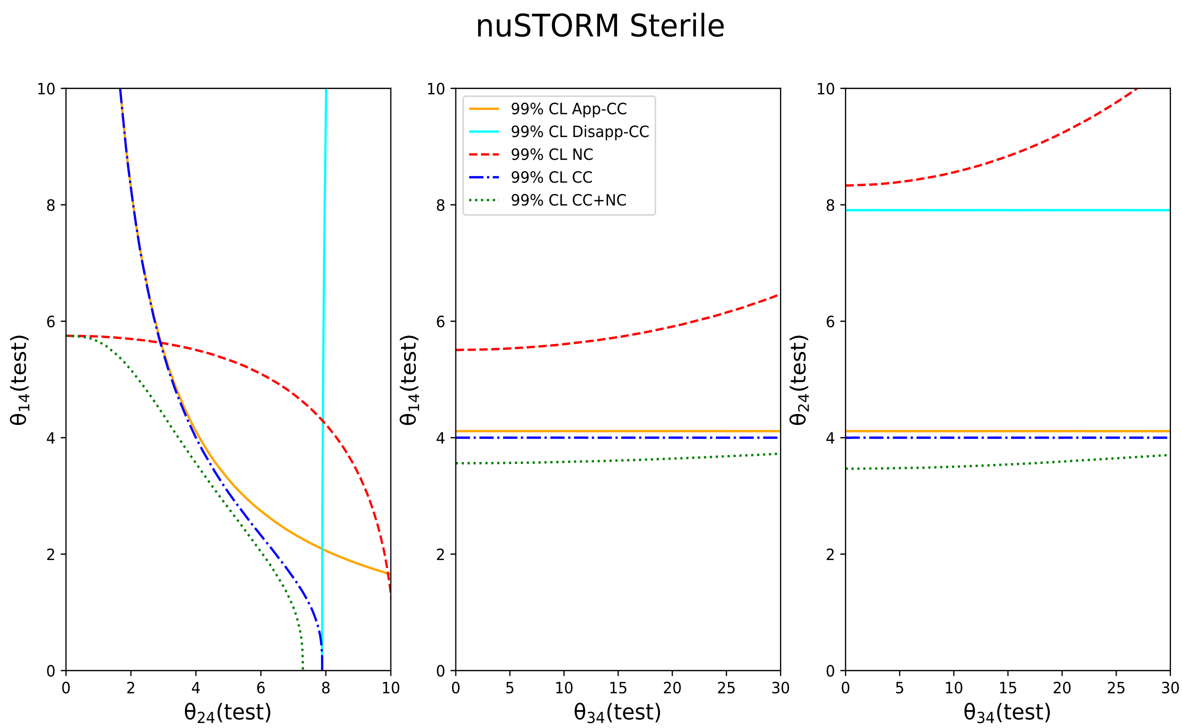

Figure 6.4: The testable regions for sterile neutrinos as predicted by nuSTORM for $\Delta m_{41}^2 = 1\mathrm{ev}^2$ and baseline of 2 km in terms of θ_{14}, θ_{24} and θ_{34} bounds. The first, second and third plots present the θ_{14}(test) vs θ_{24}(test), θ_{14}(test) vs θ_{34}(test) and θ_{24}(test) vs θ_{34}(test) contours respectively. Each plot consists of 5 contours of 99% confidence level significance exclusion regions for various channels as labeled in the plots.

Figure 6.4 presents the predicted θ_{14}, θ_{24} and θ_{34} bounds expected from nuSTORM. The first plot from fig.6.4 shows the θ_{14} versus θ_{24} exclusion region considering the data generated from 3 flavour oscillation with parameters as given in tab:6.1, but setting the fourth generation parameters to zero. The solid orange line shows the θ_{14} versus θ_{24} exclusion region predicted from the appearance channel, the relevant probability for this channel is $P_{e\mu}$ given by the expression in eq:6.14. As, the allowed regions for θ_{14}, θ_{24} are small hence the expression for $P_{e\mu}$ at constant energy and baseline is roughly $\propto \theta_{14}^2\theta_{24}^2$ which explains the hyperbolic nature of the charged current appearance plot. The disappearance probability $P_{\bar{\mu}\bar{\mu}}$ approximately reduces to $1-4\theta_{24}^2$, which is independent of θ_{14}, so θ_{14} remains unaffected by the disappearance channel. Another important channel which can be probed is the neutral-current channel. The total contribution to the neutral-current channel comes from $P_{\mu s} + P_{es}$ because neutral-current events from neutrino and antineutrino cannot be differentiated by the detector. The total neutral-current probability approximately reduces to $P_{\mu s} + P_{es} \propto \theta_{14}^2 + \theta_{24}^2$, which describes the approximate elliptical nature of the neutral current channel given by red dashed lines in the fig:6.4. The total CC event curve(blue dashed curve) is the total contribution of appearance CC and disappearance CC. While the green dotted curve presents the contribution of all the above channels i.e. the total CC and NC event samples. It is clear from the figure that the inclusion of NC events can put stringent bounds on both θ_{14} and θ_{24}. We can conclude from this study that nuSTORM will be capable to test θ_{14}, θ_{24} upto 6° and 7.5° respectively. Comparing the results obtained with expected sensitivity from DUNE [279] it was found that neutral current events from DUNE can resolve θ_{14} upto 10° and θ_{24} upto 15° with 5% systematics for $\Delta m_{41}^2 = 0.5\text{eV}^2$.

The second and third plots in the figure show the ability of nuSTORM to constrain θ_{14} and θ_{24} with respect to θ_{34}. Taking all the channels into account both θ_{14} and θ_{24} can be approximately constrained upto 4° at nuSTORM. In both the plots it is clear that the charged current interactions are independent of θ_{34} which is also understood from the expressions for $P_{e\mu}$ and $P_{\bar{\mu}\bar{\mu}}$. The only dependence on θ_{34} can come from the neutral current channel. However, $P_{e\mu} + P_{\bar{\mu}\bar{\mu}} \propto \cos^2\theta_{34}$, as a result of which there is weak dependence of θ_{34} onresolve the neutral current events hence θ_{34} cannot be constrained by neutral current events in nuSTORM.

The left plot in fig:6.5 shows the effect of varying the baseline of nuSTORM on the bounds in the θ_{14}, θ_{24} plane for $\Delta m_{41}^2 = 1\text{eV}^2$. The best sensitivity of an experiment is observed at the oscillation maxima. The first oscillation maximum is given by $1.27\Delta m_{41}^2 L/E = \pi/2$. As the mean energy of the experiment is ~ 3 GeV, $\Delta m_{41}^2 L \approx$

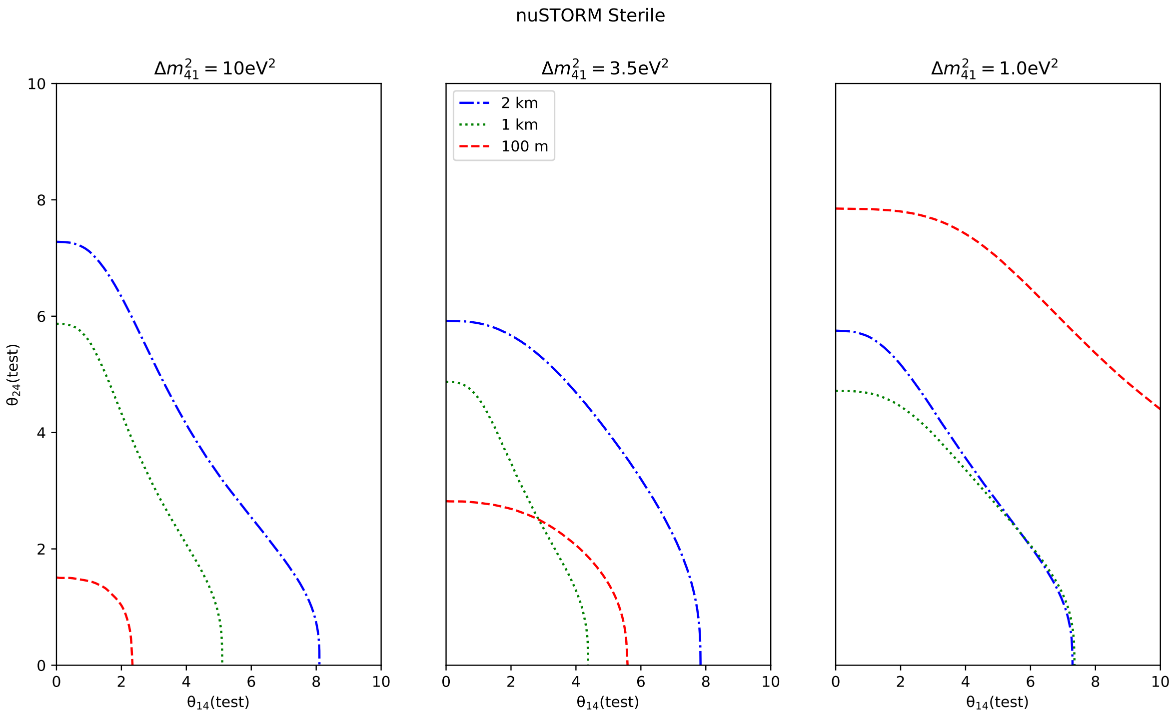

Figure 6.5: The testable regions for sterile neutrinos as predicted by nuSTORM in terms of θ_{14} vs θ_{24} bounds. The first plot presents the θ_{14}(test) vs θ_{24}(test) for $\Delta m^2_{41} = 1\text{eV}^2$,the second plot for $\Delta m^2_{41} = 3.5\text{eV}^2$ and the third plot for $\Delta m^2_{41} = 10\text{eV}^2$. Each plot consists of 3 contours of 99% confidence level significance exclusion regions for various baselines as labeled in the plots.

3.7eV^2 km. It is evident from the relation that probing a larger Δm^2_{41} requires a smaller baseline(L) and vice versa. Analyzing the red curves in the fig:6.5, which show result for a the baseline of 100 m, we observe that as Δm^2_{41} is increased the sensitivity also increases. Similarly, if we observe the green curves representing the 1 km baseline then we observe that the best sensitivity is observed for the case $\Delta m^2_{41} = 3.5$ eV^2 which is expected from the above relation. Deviation from $\Delta m^2_{41} = 3.5\text{eV}^2$, on either side compromises with the sensitivity. The blue curves demonstrate the sensitivities of the 2 km baseline for nuSTORM. The $\Delta m^2_{41} \approx 1.8\text{eV}^2$ km is expected to have the best sensitivity for the 2 km baseline. As we increase the Δm^2_{41} gradually the sensitivity decreases with increasing Δm^2_{41}. We observe that the 1 km baseline has good sensitivity for both θ_{14} and θ_{24} consistently over the range of Δm^2_{41}.

6.3.2 Non-Unitarity

In presence of non unitarity, the time evolution of the mass eigenstate in vacuum is:

$$i\frac{d \mid \nu_i >}{dt} = H \mid \nu_i >, \tag{6.20}$$

where H is the Hamiltonian in the mass basis. After time t(≡L), the flavour state can be written as

$$|\nu_\alpha(t) >= N^*_{\alpha i}|\nu_i(t) >= N^*_{\alpha i}(e^{-iHt})_{ij}|\nu_j(t=0) > . \tag{6.21}$$

In this framework the mixing matrix N can be parametrized as:

$$N = N^{NP}U = \begin{bmatrix} \alpha_{11} & 0 & 0 \\ \alpha_{21} & \alpha_{22} & 0 \\ \alpha_{31} & \alpha_{32} & \alpha_{33} \end{bmatrix} U; \tag{6.22}$$

where U is the PMNS matrix, N^{NP} is the left triangle matrix which portrays non unitarity. In the matrix N^{NP} the diagonal elements are real and the off diagonal elements can be complex.

The above discussions lead us to the transition probability as:

$$P(\nu_\alpha \to \nu_\beta) = | < \nu_\beta|\nu_\alpha(t) > |^2 = |N^*_{\alpha i} diag(e^{-i\Delta m^2_{i1}t/2E})_{ij} N_{\beta j}|^2 \tag{6.23}$$

Using the above parametrization the transition probabilities $P_{\mu e}$ and $P_{\mu\mu}$ can be written:

$$\begin{aligned} P_{e\mu} = \alpha_{11}^2|\alpha_{21}|^2 \; &- \; 4\sum_{j>i}^{3} Re\left[N^*_{\mu j}N_{ej}N_{\mu i}N^*_{ei}\right]\sin^2\left(\frac{\Delta m^2_{ji}L}{4E}\right) \\ &+ \; 2\sum_{j>i}^{3} Im\left[N^*_{\mu j}N_{ej}N_{\mu i}N^*_{ei}\right]\sin\left(\frac{\Delta m^2_{ji}L}{2E}\right). \end{aligned} \tag{6.24}$$

$$P_{\mu\mu} = (|\alpha_{21}|^2 + \alpha_{22}^2)^2 - 4\sum_{j>i}^{3}|N_{\mu j}|^2|N_{\mu i}|^2\sin^2\left(\frac{\Delta m^2_{ji}}{4E}L\right). \tag{6.25}$$

For nuSTORM, with a baseline of 2 km, the transition probabilities become independent of the baseline length because $\frac{\Delta m^2 L}{E} \ll 1$. Therefore, the relevant transition probabilities are:

$$P_{e\mu} = \alpha_{11}^2 |\alpha_{21}|^2, \tag{6.26}$$

$$P_{\mu\mu} = (|\alpha_{21}|^2 + \alpha_{22}^2)^2 \tag{6.27}$$

Along with the charged current events, neutral-current events can also be helpful in studying the non-unitarity of the mixing matrix. The important probabilities for the inclusion of the neutral current events are

$$P_{es} = 1 - (\alpha_{11}^2(\alpha_{11}^2 + |\alpha_{21}|^2 + |\alpha_{31}|^2)); \tag{6.28}$$

$$P_{\mu s} = 1 - (\alpha_{11}^2 |\alpha_{21}|^2 + \alpha_{22}^4 + 2\alpha_{22}^2 |\alpha_{21}|^2 + \alpha_{22}^2 |\alpha_{32}|^2) \tag{6.29}$$

The detector cannot distinguish the various kinds of neutral current events, so we can probe the total neutral current probability:

$$\begin{aligned} P_{es} + P_{\mu s} = 2 &- (\alpha_{11}^2(\alpha_{11}^2 + 2|\alpha_{21}|^2 + |\alpha_{31}|^2) \\ &+ \alpha_{22}^2(\alpha_{22}^2 + 2|\alpha_{21}|^2 + |\alpha_{32}|^2)). \end{aligned} \tag{6.30}$$

The capability of nuSTORM to probe the non unitarity parameters α_{11}, $|\alpha_{21}|$ and α_{22} are shown in the Fig.6.6. Each plot presents 3 cases for 3 different baselines: 100 m; 1 km; and 2 km, plotted with magenta, green and blue curves respectively. The first plot in fig.6.6 presents the sensitivity of nuSTORM to probe the parameter α_{11} keeping the diagonal parameters $\alpha_{22} = \alpha_{33} = 1.0$ and the off-diagonal parameters $|\alpha_{21}|$,$|\alpha_{31}|$ and $|\alpha_{32}|$ fixed at 0.01.Unitarity requires that the parameters be set to zero. However, the value of -.01 has been drawn so that a contribution from the $\nu_e \to \nu_\mu$ channel remains. Beginning with the first case, which shows the χ^2 as a function of α_{11}, under the condition that the parameters $|\alpha_{21}| = 0.1$ and $\alpha_{22} = 1.0$. The true data

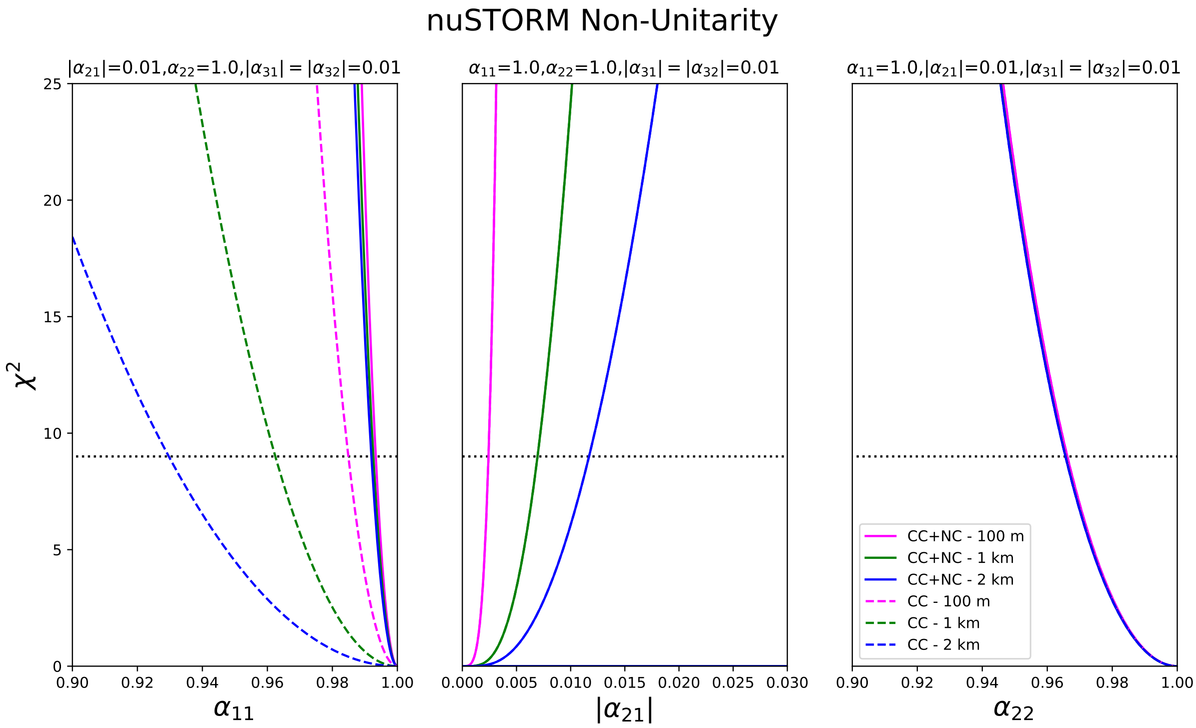

Figure 6.6: The figure denotes the sensitivity of nuSTORM for the non unitarity parameters α_{11}, $|\alpha_{21}|$ and α_{22}. The y-axis in the plots represent χ^2, while the x-axis denotes α_{11}, $|\alpha_{21}|$ and α_{22} for plots respectively. In each plot the dashed lines are for the contribution of only charge current interactions while the solid lines are for the combination of charge current and neutral current. The magenta, green and blue curves represent the sensitivities at the baseline of 100 m, 1 km and 2 km respectively.

have been generated keeping α_{11} fixed at unity while the test data have been generated by varying α_{11} between 0.9 and 1.0 while keeping all other parameters fixed. The relevant channel to study the α_{11} sensitivity is the $P_{e\mu}$ appearance channel because the probability $P_{\bar{\mu}\bar{\mu}}$ is independent of α_{11}. Under the above conditions $P_{e\mu} \sim 0.01\alpha_{11}^2$, therefore, the sensitivity plot has a quadratic dependence on α_{11}. From the expression it is clear that $P_{e\mu}$ is independent of the baseline so a change in sensitivity to α_{11} by varying the baseline is due to the change in the flux which occurs due to the change in the baseline. Hence, we observe that the sensitivity increases as the baseline is reduced. 3σ sensitivity for α_{11} is achieved for $\alpha_{11} = 0.93$ for a 2 km baseline, which increases to 0.96 for the 1 km baseline and the best result is achieved for the 100 m baseline where the same sensitivity is achieved for $\alpha_{11} = 0.99$. If neutral current events are also combined the charged current events a substantial improvement in the sensitivity is observed. 3σ sensitivity for $\alpha_{11} = 0.995$ when CC and NC both are taken into consideration. Similar studies have been performed at DUNE and T2HK [310] where the 3σ sensitivity for $\alpha_{11} \approx 0.94$ for DUNE and $\alpha_{11} \approx 0.96$ for T2HK. Therefore, we can see that nuSTORM with 2 km baseline has sensitivity similar to DUNE and with baseline 1 km has similar sensitivity to T2HK when the baseline is decreased further the sensitivity increases further exceeding the sensitivities attained by DUNE or T2HK.

The second plot in the Fig.6.6 shows the χ^2 vs $|\alpha_{21}|$ sensitivity with both the non-unitarity parameters α_{11} and α_{22} taken to be unity. Under such conditions $P_{e\mu}$ just reduces to $|\alpha_{21}|^2$ and $P_{\bar{\mu}\bar{\mu}}$ becomes $(1 + |\alpha_{21}|^2)^2$ which can be approximated to be $\sim\ 1 + 2|\alpha_{21}|^2$. Unlike the case discussed above, where only the appearance channel contributes, both the appearance and the disappearance channel contribute to the sensitivity to $|\alpha_{21}|$. Since both the channels depend on $|\alpha_{21}|^2$ we get a quadratic dependence of the χ^2 on $|\alpha_{21}|$. In this case the true data have been generated at $\alpha_{11} = \alpha_{22} = \alpha_{33} = 1.0$, $|\alpha_{21}| = |\alpha_{31}| = |\alpha_{32}| = 0$ and $\alpha_{22} = 1.0$, the test data have been generated with $|\alpha_{21}|$ varying in the range 0.0 to 0.01. In this case also we find that the sensitivity is dependent on the baseline for the same reason as discussed previously. The $|\alpha_{21}|$ sensitivity reaches 3σ for $|\alpha_{21}| = 0.011$ at the 2 km baseline, $|\alpha_{21}| = 0.006$ at the baseline 1 km, and $|\alpha_{21}| = 0.003$ at the baseline 100 m. Neutral current events do not contribute to the $|\alpha_{21}|$ sensitivity, this is because $P_{NC} \approx 2-(\alpha_{11}^2+\alpha_{22}^2)(\alpha_{11}^2+2|\alpha_{21}|^2+|\alpha_{31}|^2)$ where $(\alpha_{11}^2+2|\alpha_{21}|^2+|\alpha_{31}|^2) \approx 1$ as a result the NC channel cannot probe $|\alpha_{21}|$ independently. Comparing the sensitivities with DUNE and T2HK [310] we observe that nuSTORM can reach 3σ sensitivity for $|\alpha_{21}|$ for an order of magnitude smaller values of $|\alpha_{21}|$. nuSTORM has a significant advantage over DUNE and T2HK which can reach 3σ sensitivities for $|\alpha_{21}| = 0.08$ and 0.04 respectively.

The third figure presents the sensitivity to the parameter α_{22}. $P_{e\mu}$ is independent of α_{22} but $P_{\bar{\mu}\bar{\mu}}$ is sensitive to α_{22}. The true data has been generated by considering unitary evolution i.e. $\alpha_{11} = 1.0$, $|\alpha_{21}| = 0$ and $\alpha_{22} = 1.0$ which reduces $P_{\bar{\mu}\bar{\mu}}$ to α_{22}^4. The test data have been generated by taking $\alpha_{11} = 1.0$, $|\alpha_{21}| = 0$ and varying α_{22}

from 0.9 to 1.0. An interesting feature observed here is the independence of α_{22} on the baseline. This can be attributed to the fact that the sensitivity is solely dependent on the disappearance channel which already has enough statistics at 2 km, hence reducing the baseline does not help. The introduction of neutral current events is expected to increase the α_{22} sensitivity because of the dependence of P_{NC} on α_{22}^2. However, no improvement is observed because the introduction of the channel increases the statistics but it already had enough statistics from the disappearance channel itself. The 3σ sensitivity is reached at $\alpha_{22} = 0.97$ for all baselines. Again from [310], the 3σ sensitivities for DUNE and T2HK for α_{22} can be attained for $\alpha_{22} \approx 0.98$ for both the experiments.

6.4 Conclusions

In this chapter we have investigated the capabilities of nuSTORM to explore two new physics scenarios – (i) the existence of eV^2 scale oscillation, suggested as an explanation of LSND/MiniBOONE anomalies and (ii) non-unitarity of the neutrino mixing matrix. nuSTORM is proposed primarily to measure the $\nu_e\ N$ and $\nu_\mu\ N$ cross section. It was shown in [5, 6] that nuSTORM can also play in important role to study active-sterile oscillations governed by an eV^2 mass squared difference. We have studied the effect of including neutral current events and checked whether this can give improved sensitivity to sterile-neutrino searches. nuSTORM will have the capability to study two main channels, the conversion probability $P_{\mu e}$ and survival probability $P_{\bar{\mu}\bar{\mu}}$ with the proposed MIND detector. Whereas, for oscillations involving active neutrinos the NC events are not sensitive to oscillation parameters, for oscillations involving the sterile neutrinos, the neutral current events are also sensitive to the oscillation parameters through the probabilities involving conversion to sterile neutrinos $P_{\mu s}$ and P_{es}. Considering a 2 km baseline it is observed that taking only CC interactions can constrain the mixing angle $\theta_{24} \lesssim 7.5^{\circ}$, which is better than what can be achieved with CC interactions only. For non-zero values of θ_{24}, the constraint on θ_{14} also improves with inclusion of NC events. Since, nuSTORM is a proposed experiment, baseline optimization is important to maximize physics output. When we consider various baselines we find that the baseline of 1 km gives a good overall sensitivity for both θ_{14} and θ_{24} over a wide range of Δm^2_{41}.

For the other new-physics scenario – non-unitarity of the lepton mixing matrix studied, we find that nuSTORM can probe the non-unitarity parameters α_{11}, $|\alpha_{21}|$ and α_{22}. 3σ sensitivities for α_{11}, $|\alpha_{21}|$ and α_{22} are obtained at 0.995, 0.011 and 0.97 respectively for 2 km baselines combining both CC and NC events. The sensitivities for α_{11} and $|\alpha_{21}|$ significantly improves as the baseline is reduced.

In conclusion, we find that apart from measuring neutrino cross-sections with per mil precision, nuSTORM can also contribute significantly in probing new physics scenarios beyond Standard Model .

Chapter 7

Summary and Conclusions

In this thesis we explore the physics potential of current and future accelerator experiments in determining neutrino mass hierarchy, octant and δ_{CP} for model independent and model dependent scenarios. Additionally, we also study the new physics scenarios like sterile neutrino and non-unitarity in light of the future proposed accelerator based experiments.

We begin with the discussion regarding the history of neutrinos in chapter 1. Then we briefly discuss about neutrinos in the Standard Model followed by the natural and man-made sources of neutrinos. Next we describe neutrino oscillations and the open problems in this sector. Then we give a brief overview on neutrino mass generation. We end the chapter with a short discussion on neutrino oscillations beyond the three neutrino paradigm and outline the plan of the thesis.

The next chapter (ch. 2) contains the derivation of the neutrino oscillation probabilities for two and three generations in vacuum and in presence of matter. Next we review the experimental evidence of neutrino oscillation. Then we present the current status of neutrino oscillation parameters indicating the unknown parameters. Next we discuss in detail the parameter degeneracies which affect the unambiguous determination of the unknowns in the neutrino oscillations sector. In the final section of the chapter we describe the salient features of the present and future accelerator neutrino experiments T2K, NOνA , DUNE, T2HK/T2HKK and ESSνSB .

In chapter 3 we present a detailed analysis of sensitivities of the future accelerator based long baseline experiments DUNE, T2HK/T2HKK and ESSνSB for determination of the present unknowns in neutrino oscillation physics. We also compare the mass hierarchy sensitivity, octant sensitivity and CP violation discovery potential of these experiments. In our study we find that DUNE do not have any hierarchy degeneracy due to matter effect as a result of which DUNE will be able to determine the mass hierarchy with confidence level much greater than 5σ for all values of δ_{CP}. In the case of T2HK, hierarchy degeneracy is present the upper half plane ($0^\circ < \delta_{CP} < 180^\circ$) of δ_{CP} for NH and in the lower half plane ($-180^\circ < \delta_{CP} < 0^\circ$) of δ_{CP} for IH which compromises the hierarchy sensitivity in these regions. The hierarchy sensitivity gets a boost when the T2HKK proposal is considered instead, which is proposed to study both the first and the second oscillation maxima. Considering the second oscillations maxima the degeneracies which occurred in the unfavourable regions in the T2HK baseline is resolved which enhances the mass hierarchy sensitivities. The ESSνSB experiment suffers from hierarchy degeneracy for all values of δ_{CP} as a result of which it does not have significant mass hierarchy sensitivity. However, ESSνSB being an experiment at the second oscillation maxima has a very sharp dependence of the $P_{\mu e}$ over δ_{CP} which enables ESSνSB to differentiate the non-zero δ_{CP} values from the CP conserving values, this trend is also true for the third oscillation maxima where the flux at ESSνSB peaks. As, a result of which the CP violation sensitivity of ESSνSB is maximum among the experiments considered in our analysis. Along with ESSνSB , T2HKK proposal also explores the physics at the second oscillation maxima. So, the CP violation discovery sensitivity of T2HKK is also comparable to that of ESSνSB . DUNE and T2HK being experiments at the first oscillation maxima do not depend sharply on δ_{CP} as a result of which both suffer from degeneracies which affects their CP sensitivities. But, these being at the first oscillation maxima has better octant sensitivities. The probabilities at first oscillation maxima have wide octant bands which signifies greater variation in $P_{\mu e}$ with θ_{23}. But, ESSνSB and T2HKK being at the second oscillation maxima have very narrow octant band hence, high octant degeneracies. As, these experiments are very high statistics experiments we study the required exposure for these experiments standalone and in conjunction with T2K and NOνA to achieve 5σ mass hierarchy and octant sensitivities. DUNE with the proposed configuration is expected to determine the mass hierarchy in just 3.5 years while T2HKK in 4.5 years. We study the time for which 5σ CP violation discovery sensitivity for 60% fraction of δ_{CP} can be reached. T2HKK can reach the same 6 years(6.5 years) for T2HKK for true NH-LO(IH-HO). ESSνSB can reach the same in 9 years(10 years) for true NH-LO(IH-HO), which reduces to 7 years(8 years) adding T2K + NOνA . We also combine the experiments T2HK, DUNE, ESSνSB to explore the mass hierarchy sensitivity and observe that ESSνSB can also be very helpful in mass hierarchy sensitivity when combined with T2HK as the hierarchy degeneracies for T2HK and ESSνSB occur at different δ_{CP} values. T2HK can obtain an overall 5σ octant sensitivity with approximately 13.4 years of run time in IH-HO which can be reduced to 11 years approximately once data from T2K and NOνA are also added. These future experiments show immense promise in resolving the unknowns of the neutrino oscillations sector.

The above study was done without any assumptions on the model parameters. However, models predicting the observed neutrino mixing often give rise to some correlations among the parameters. In chapter 4 we study the partial $\mu - \tau$ reflection symmetry of the leptonic mixing matrix, U, which can arise from almost all the discrete subgroups of SU(3), except a few exceptional cases, having three dimensional irreducible representations. The application of the $\mu - \tau$ symmetry ($|U_{\mu i}| = |U_{\mu i}|, (i = 1, 2, 3)$) to the PMNS matrix for the third column of the PMNS matrix leads us the maximal value to θ_{23}, along with one of the two predictions of $\theta_{13} = 0$ or $\delta_{CP} = \pm\dfrac{\pi}{2}$. The reactor experiments have established $\theta_{13} \neq 0$ and the recent neutrino oscillations indicated toward a deviation from the maximal mixing of θ_{23}. These motivates one to look for partial $\mu - \tau$ symmetry, relaxing the constraint on the third column of PMNS matrix which leads to the maximal mixing in θ_{23}. Thus, one obtains two different predictions in terms of the mixing angles and δ_{CP} which are C_1(equality for the first column) and C_2(equality for the second column). From each scenario we obtain two values of δ_{CP} for a given θ_{23}, one in the range $0^\circ < \delta_{CP} < 180^\circ$ and the other belonging to $180^\circ > \delta_{CP} > 360^\circ$. The experiments DUNE, T2HK and T2HKK have potential to explore these correlations in terms of $\sin^2\theta_{23}(\text{true}) - \delta_{\text{CP}}(\text{true})$. These correlations when tested in DUNE, T2HK and T2HKK, can exclude certain combinations of the true θ_{23} and δ_{CP} values get excluded. Also, T2HK and T2HKK constrain the range of δ_{CP} better than that of DUNE because of its superior CP sensitivity.

In the next chapter (5) we consider $\mu - \tau$ symmetry in context of an additional light sterile neutrino. The motivation for sterile neutrinos first came from the LSND experiments which reported oscillations governed by eV^2 mass difference. The LSND anomaly is still unresolved and the recent MiniBooNE data also supporting the anomaly inspired us to investigate the implications of the $\mu - \tau$ symmetry in the presence of a light sterile neutrino. This leads us to four conditions $|U_{\mu i}| = |U_{\mu i}|, (i = 1, 2, 3, 4)$. When all the four conditions are simultaneously considered, θ_{23} is confined around the maximal mixing and δ_{CP} around maximal CP violating values. In the three generation scenario the $\mu - \tau$ symmetry on the PMNS matrix leads to the maximal value of θ_{23}. The application of $\mu - \tau$ symmetry in the presence of one light sterile neutrino relaxes the constraint the value of the atmospheric mixing angle with a deviation of $\pm 1^\circ$ to either side of $\theta_{23} = 45^\circ$. However, the deviation in the atmospheric mixing angle is not enough to explain the current best-fit observed from the neutrino oscillations data which led us to consider partial $\mu - \tau$ symmetry for $3 + 1$ neutrino mixing. We find that the equality of the first column of the mixing matrix reveals an important correlation among the neutrino mixing angle θ_{23} and Dirac CP phase δ_{CP}, where the best-fit value for (θ_{23}, δ_{CP}) shows a good agreement with inverted neutrino mass hierarchy. While the same equality when applied to the second column, the best-fit for (θ_{23}, δ_{CP}) prefers the normal mass hierarchy instead. The precise measurement of θ_{23} and δ_{CP} will be crucial in the verification of these correlations. The equality on the third column restricts the value of θ_{23} around $\frac{\pi}{4}$. The equality on the fourth column created the possibility of constraining the mixing angle θ_{34} which has no lower bound from experimental data as yet. This equality relates the mixing angles θ_{34} and θ_{24} in one-to-one correspondence with each other. So, θ_{34} can be directly restricted from the experimental data on θ_{24}. We examine the possibility of testing these correlations in future long baseline experiments like DUNE, T2HK/T2HKK. These correlations can limit a significant area of the current parameters space in the θ_{23} - δ_{CP} plane allowed by the current neutrino oscillations data. Moreover, the consequences of $\mu - \tau$ symmetry for $3+1$ neutrino mixing was also explored in neutrinoless double-β decay which is sensitive to the effective neutrino mass $m_{\beta\beta}$. It is to be noted that the $\mu - \tau$ symmetry predicts the Majorana phases to be either zero or $\frac{\pi}{2}$. When the Majorana phase is taken to be zero the effective neutrino mass assumes high values which can be tested in future neutrinoless double-β experiments. Additionally, for inverted hierarchy the mixing angle θ_{14} can be constrained with the help of the present bounds on the effective neutrino mass. $\mu - \tau$ symmetry in sterile sector can be tested in the future neutrino oscillation as well as neutrinoless double-β decay experiments if existence of this is confirmed in future experiments.

We also expound the model independent signatures of light sterile neutrino in neutrino oscillation experiments. In this regard, the nuSTORM proposal designed to measure the neutrino-nucleon cross section with remarkable precision was utilized to study involving sterile neutrino oscillations over a short baseline. nuSTORM with a baseline of about 2 km is ideal to study neutrino oscillations pertaining to the mass-squared difference $\sim 1\text{eV}^2$. Thus it is conductive to study oscillations to sterile neutrinos as suggested by LSND and MiniBooNE. nuSTORM proposes to study neutrinos from muon decay as opposed to accelerator experiments using ν_μ flux from pion decay. Thus, it gets flux of both $\bar{\nu_\mu}$ (ν_μ) and ν_e ($\bar{\nu_e}$) depending on if initial state is μ^+ (μ^-) and study both $\bar{\nu_\mu}$ (ν_μ) disappearance and ν_μ ($\bar{\nu_e}$) appearance. The μ^+ contains $\bar{\nu_\mu}$ and ν_e at source, hence the appearance channel will consist of ν_μ while $\bar{\nu_\mu}$ will constitute the disappearance channel. Since, an iron calorimeter detector with charge sensitivity can distinguish between the neutrino and antineutrino events the appearance and disappearance channels can be differentiated through charge current interactions at the detector. In the 6th chapter we study the impact of nuSTORM in constraining parameter space of sterile neutrinos considering both CC and NC interactions at the detector. Although, the neutral current interactions are not sensitive to neutrino oscillations for three generations, it can contribute significantly to explore new physics scenarios like sterile neutrinos through the probabilities P_{es} and $P_{\mu s}$. The ν_μ appearance the $\bar{\nu_\mu}$ disappearance channels can constrain the effective mixing angles $\sin^2\theta_{\mu e}$ and $\sin^2\theta_{\mu\mu}$ respectively. The neutral current channel has negligible effect on $\sin^2\theta_{\mu e}$ but has substantial influence on the restriction of parameter space on Δm^2_{41} vs $\sin^2\theta_{\mu\mu}$ plane. We also find that when CC and NC both channels are simultaneously considered the mixing angles θ_{14} can be tested up to the value of $6°$ while θ_{24} up to $7.5°$. Although, the proposed baseline for nuSTORM is 2 km, we find that the 1 km baseline has advantage if we consider the overall sensitivity for a wide range of Δm^2_{41}. Finally, we also investigate non-unitarity of neutrino mixing matrix at nuSTORM for three flavour neutrino mixing. Non-unitary neutrino mixing gives rise to conversions at source and for the short baseline involved the oscillations probabilities are independent of the baseline and the neutrino energy. We include both CC and NC events in our analysis. The charge current events can constrain α_{11}, $|\alpha_{21}|$ and α_{22} while the neutral current affects the sensitivity of α_{11} but do not have any effect on $|\alpha_{21}|$ or α_{22}.

In this thesis we have studied the determination of the undetermined neutrino oscillation parameters - sign of $|\Delta m^2_{31}|$, octant of θ_{23} and δ_{CP} in future accelerator based neutrino oscillation experiments including future projections of currently running experiments. We also considered correlations amongst parameters that can arise in models of partial $\mu - \tau$ symmetry and determine the potential of future proposed experiments in constraining the parameters in presence of such correlations in three neutrino framework and adding one light sterile neutrino. These scenarios can be tested by future experiments. Finally, we explored the potential of nuSTORM proposal in probing new physics scenarios like sterile neutrinos, non-unitarity of mixing matrix, emphasizing on the impact of including the neutral current events.

The study performed in this thesis can be confirmed or falsified by proposed experiments. Future direction includes continued exploration of physics beyond the Standard Model in neutrino oscillation experiments . We also aim to study such scenarios in proposed atmospheric neutrino experiments and explore synergy between different kind of experiments. Future plans also include the study of different new physics scenarios at nuSTORM.

Appendix A

Parametrization of the PMNS matrix

A.1 The Neutrino Mixing Matrix

The PMNS matrix is a unitary neutrino mixing matrix which establishes the relationship between the neutrino flavor and mass eigenstates. In this appendix we discuss the parametrization of the PMNS matrix.

A.1.1 Parameters in a general Unitary Matrix

Let us count the parameters of an $N \times N$ unitary matrix[312]. A general complex $N \times N$ matrix has $2N^2$ real independent parameters. Now, a unitary matrix is defined as $UU^\dagger = 1$ which leads to the equations:

$$u_{ik}u^\dagger_{kj} = \delta_{ij} \tag{A.1}$$

, where δ_{ij} is the Kronecker delta. The equation eq.A.1 can be divided into two sets:

- Case 1: $i = j$
  The diagonal elements follow the relation $u_{ik}u^\dagger_{ki} = 1$.
  This gives N different conditions for $i \in \{1, 2, ..., N\}$.

- Case 2: $i \neq j$, as Kronecker delta is symmetric in i and j so under the transformation $i \leftrightarrow j$ the equations are same. This set of equations will give ${}^nC_2$

conditions and since the elements are complex the total real independent conditions will be $2\,{}^nC_2 = N^2 - N$.

Therefore, the total independent constraints for a unitary matrix is N^2, which reduces the number of independent parameters in a unitary matrix to N^2. These, N^2 parameters can be further classified into $N(N-1)/2$ mixing angles and $N(N+1)/2$ phases.

General 2×2 unitary matrix

Equations (A.1) can be written out in terms of the elements of **U**,

$$|U_{11}|^2 + |U_{12}|^2 = 1 \tag{A.2}$$

$$U_{11}U_{21}^* + U_{12}U_{22}^* = 0 \tag{A.3}$$

$$U_{21}U_{11}^* + U_{22}U_{12}^* = 0 \tag{A.4}$$

$$|U_{21}|^2 + |U_{22}|^2 = 1 \tag{A.5}$$

$$|U_{11}|^2 + |U_{21}|^2 = 1 \tag{A.6}$$

$$U_{11}^*U_{12} + U_{21}^*U_{22} = 0 \tag{A.7}$$

$$U_{12}^*U_{11} + U_{22}^*U_{21} = 0 \tag{A.8}$$

$$|U_{12}|^2 + |U_{22}|^2 = 1 \tag{A.9}$$

Without loss of generality we can introduce an angle θ so that, $|U_{11}| = \cos\theta \equiv c$ and $|U_{12}| = \sin\theta \equiv s$. also $|U_{21}| = s$ and $|U_{22}| = c$.

$$\mathbf{U} = \begin{pmatrix} ce^{i\alpha_{11}} & se^{i\alpha_{12}} \\ se^{i\alpha_{21}} & ce^{i\alpha_{22}} \end{pmatrix} \tag{A.10}$$

and we have to determine the phases from the remaining equations. For example from (A.3)

$$cse^{i(\alpha_{11}-\alpha_{21})} + sce^{i(\alpha_{12}-\alpha_{22})} = 0 \tag{A.11}$$

From the above equation we can eliminate one phase, for example α_{21}, which leads to the arbitrary unitary matrix as:

$$\mathbf{U} = \begin{pmatrix} ce^{i\alpha_{11}} & se^{i\alpha_{12}} \\ -se^{i(\alpha_{11}-\alpha_{12}+\alpha_{22})} & ce^{i\alpha_{22}} \end{pmatrix} \tag{A.12}$$

$$= \begin{pmatrix} 1 & \\ & e^{i(\alpha_{22}-\alpha_{12})} \end{pmatrix} \begin{pmatrix} c & s \\ -s & c \end{pmatrix} \begin{pmatrix} e^{i\alpha_{11}} & \\ & e^{i\alpha_{12}} \end{pmatrix} \tag{A.13}$$

We obtain that an arbitrary 2×2 unitary matrix can be described by one angle and three phases. The phases could have been in any of the four diagonal positions in the left and right matrices, we can choose any three out of the four positions. Two of the three phases can be absorbed to redefine the charged lepton fields while the third phase is the Majorana phase which do not appear in neutrino oscillations.

General 3×3 unitary matrix

Similar exercise can also be done for a 3×3 unitary matrix. A 3×3 unitary matrix can be parametrized by 3 angles and 6 phases, but all the phases are not significant. The most general 3×3 unitary matrix $\mathbf{U}$ is given by,

$$\begin{aligned} \mathbf{U} &= \begin{pmatrix} 1 & & \\ & e^{i(\alpha_{23}-\alpha_{13})} & \\ & & e^{i(\alpha_{33}-\alpha_{13})} \end{pmatrix} \\ &\times \begin{pmatrix} c_{12}c_{13} & s_{12}c_{13} & s_{13}e^{-i\delta} \\ -s_{12}c_{23} - c_{12}s_{23}s_{13}e^{i\delta} & c_{12}c_{23} - s_{12}s_{23}s_{13}e^{i\delta} & s_{23}c_{13} \\ s_{12}s_{23} - c_{12}c_{23}s_{13}e^{i\delta} & -c_{12}s_{23} - s_{12}c_{23}s_{13}e^{i\delta} & c_{23}c_{13} \end{pmatrix} \\ &\times \begin{pmatrix} e^{i\alpha_{11}} & & \\ & e^{i\alpha_{12}} & \\ & & e^{i\alpha_{13}} \end{pmatrix} \end{aligned} \tag{A.14}$$

where, $s_{ij} = \sin\theta_{ij}$ and $c_{ij} = \cos\theta_{ij}$

Notice that $\mathbf{U}$ can be broken up into a product of matrices

$$\begin{aligned}
\mathbf{U} &= \begin{pmatrix} 1 & & \\ & e^{i(\alpha_{23}-\alpha_{13})} & \\ & & e^{i(\alpha_{33}-\alpha_{13})} \end{pmatrix} \\
&\times \begin{pmatrix} 1 & & \\ & c_{23} & s_{23} \\ & -s_{23} & c_{23} \end{pmatrix} \begin{pmatrix} e^{-i\delta} & & \\ & 1 & \\ & & 1 \end{pmatrix} \begin{pmatrix} c_{13} & & s_{13} \\ & 1 & \\ -s_{13} & & c_{13} \end{pmatrix} \\
&\times \begin{pmatrix} e^{i\delta} & & \\ & 1 & \\ & & 1 \end{pmatrix} \begin{pmatrix} c_{12} & s_{12} & \\ -s_{12} & c_{12} & \\ & & 1 \end{pmatrix} \\
&\times \begin{pmatrix} e^{i\alpha_{11}} & & \\ & e^{i\alpha_{12}} & \\ & & e^{i\alpha_{13}} \end{pmatrix}
\end{aligned} \tag{A.15}$$

All the phases do not appear in the PMNS matrix because 3 phases can be absorbed in the charged lepton fields which leaves with 1 Dirac and 2 Majorana phases.

Let us define the rotation matrices as $R_{ij}(\alpha)$ as,

$$R_{12} = \begin{pmatrix} c_{12} & s_{12} & \\ -s_{12} & c_{12} & \\ & & 1 \end{pmatrix}, \tag{A.16}$$

$$R_{13} = \begin{pmatrix} c_{13} & & s_{13} \\ & 1 & \\ -s_{13} & & c_{13} \end{pmatrix}, \tag{A.17}$$

$$R_{23} = \begin{pmatrix} 1 & & \\ & c_{23} & s_{23} \\ & -s_{23} & c_{23} \end{pmatrix}. \tag{A.18}$$

Suppose we take one of the angles to be zero in eq. A.15:

- Case 1: $\theta_{13} = 0$. In this case R_{13} will be identity hence $U_\delta U_\delta^\dagger$ will become $\mathbb{I}$ so δ_{CP} will be undetermined.
- Case 2: $\theta_{12} = 0$. In this case the phase in right $U_\delta^\dagger$ will be reabsorbed with α_{11} and the U_δ on the right will commute with R_{23} and can be redefined with the phase matrix on the left.δ_{CP} will be undetermined.
- Case 3: $\theta_{23} = 0$. This can be better understood by choosing $U_\delta = \{1, 1, e^{-i\delta}\}$. Under this choice U_δ on the left can be absorbed with $\alpha_{33} - \alpha_{13}$ whereas the $U_\delta^\dagger$ on the right can be absorbed with α_{13}.

Therefore, we can conclude that if any one of the three phases is zero the δ_{CP} will be undetermined.

The parametrization of PMNS matrix

We know that the PMNS matrix can be parametrized by 3 Euler angles and 1 phase. This can be done in 9 ways. They are:

$$\begin{gathered} R_{12}R_{23}(\delta)R_{12} \\ R_{23}R_{12}(\delta)R_{23} \\ R_{13}R_{12}(\delta)R_{13} \\ R_{12}R_{23}(\delta)R_{13} \\ R_{12}R_{13}(\delta)R_{23} \\ R_{23}R_{12}(\delta)R_{13} \\ R_{23}R_{13}(\delta)R_{12} \\ R_{13}R_{12}(\delta)R_{23} \\ R_{13}R_{23}(\delta)R_{12} \end{gathered} \tag{A.19}$$

We can choose a parametrization depending on the problem we are tackling. Let us take an example of how a smart parametrization can make make a problem easier.

First let us understand the effect, the ordering of the rotation matrices in the PMNS matrix in absence of the CP phase. We compare the parametrizations $R_{13}R_{12}R_{23}$ and $R_{23}R_{13}R_{12}$. The three generation neutrino mass spectrum is $\Delta m^2_{21} \ll \mid \Delta m^2_{31} \mid \approx \mid \Delta m^2_{32} \mid$. Calculating the survival probability P_{ee} with the parametrization $U = R_{23}R_{13}R_{12}$ we obtain,

$$P_{ee} = 1 - \sin 2\theta_{13} \sin^2(\frac{\Delta m^2_{31} L}{4E}) \tag{A.20}$$

Now let us calculate the same probability using other parametrization, $U = R_{13}R_{12}R_{23}$:

$$P_{ee} = 1 - 4(c_{13}s_{12}s_{23} + s_{13}c_{23})^2(c^2_{12}s^2_{13} + c_{13}s_{12}s_{23} - s_{13}s_{23})^2 \sin^2(\frac{\Delta m^2_{31} L}{4E}) \tag{A.21}$$

If we compare the P_{ee} expressions we observe that in the first case the expression is simple and is independent of θ_{12} but the second expression cannot be made independent of θ_{12}. So, a smart parametrization can simplify the analysis. Here we can arrive at a conclusion that the rotation matrix corresponding to the mixing of the degenerate mass eigenstates should not be at the center because the mixing angle corresponding to the degenerate mixing can only be removed if the rotation matrix is not at the center.

We can also perform a simple exercise to understand the effect of the positioning of δ_{CP} on the vacuum oscillation probabilities by calculating the Jarlskog invariant (J_{CP}). We keep the rotation ordering same but we vary the positioning of δ_{CP}. We take the following parametrizations:

$$U1 = R_{23}R_{13}(\delta)R_{12} \tag{A.22}$$

$$U2 = R_{23}(\delta)R_{13}R_{12} \tag{A.23}$$

$$U3 = R_{23}R_{13}R_{12}(\delta) \tag{A.24}$$

The Jarlskog invariant for the three parametrization are,

$$J_{CP}(U1) = \sin(\delta)\sin(\theta_{12})\cos(\theta_{12})\sin(\theta_{13})\cos^2(\theta_{13})\sin(\theta_{23})\cos(\theta_{23}) \quad (A.25)$$

$$J_{CP}(U2) = -\sin(\delta)\sin(\theta_{12})\cos(\theta_{12})\sin(\theta_{13})\cos^2(\theta_{13})\sin(\theta_{23})\cos(\theta_{23}) \quad (A.26)$$

$$J_{CP}(U3) = -\sin(\delta)\sin(\theta_{12})\cos(\theta_{12})\sin(\theta_{13})\cos^2(\theta_{13})\sin(\theta_{23})\cos(\theta_{23}) \quad (A.27)$$

We find that the sign of the Jarlskog invariant depends on the positioning of the CP phase.

Bibliography

[1] I. Esteban, M. Gonzalez-Garcia, A. Hernandez-Cabezudo, M. Maltoni, and T. Schwetz, "Global analysis of three-flavour neutrino oscillations: synergies and tensions in the determination of θ_{23}, δ_{CP}, and the mass ordering," *JHEP* **01** (2019) 106, arXiv:1811.05487 [hep-ph].

[2] NuFIT *NuFIT 4.1* (2019) , http://www.nu-fit.org/.

[3] NuFIT *NuFIT 3.2* (2018) , http://www.nu-fit.org/.

[4] S. Gariazzo, C. Giunti, M. Laveder, and Y. F. Li, "Updated Global 3+1 Analysis of Short-BaseLine Neutrino Oscillations," *JHEP* **06** (2017) 135, arXiv:1703.00860 [hep-ph].

[5] C. D. Tunnell, "Sterile Neutrino Sensitivity with Wrong-Sign Muon Appearance at nuSTORM," arXiv:1205.6338 [hep-ph].

[6] **nuSTORM** Collaboration, D. Adey *et al.*, "Light sterile neutrino sensitivity at the nuSTORM facility," *Phys. Rev.* **D89** no. 7, (2014) 071301, arXiv:1402.5250 [hep-ex].

[7] https://home.cern/science/physics/standard-model.

[8] C. Spiering, "Towards High-Energy Neutrino Astronomy. A Historical Review," *Eur. Phys. J. H* **37** (2012) 515–565, arXiv:1207.4952 [astro-ph.IM].

[9] "https://neutel11.wordpress.com/2011/03/16/neutrino-mass-models-by-steve-king/".

[10] M. Ahlers, K. Helbing, and C. Prez de los Heros, "Probing Particle Physics with IceCube," *Eur. Phys. J. C* **78** no. 11, (2018) 924, arXiv:1806.05696 [astro-ph.HE].

[11] I. Esteban, M. C. Gonzalez-Garcia, M. Maltoni, I. Martinez-Soler, and T. Schwetz, "Updated fit to three neutrino mixing: exploring the accelerator-reactor complementarity," *JHEP* **01** (2017) 087, arXiv:1611.01514 [hep-ph].

[12] F. Reines and C. L. Cowan, "The neutrino," *Nature* **178** (1956) 446–449.

[13] F. Reines, C. Cowan, F. Harrison, A. McGuire, and H. Kruse, "Detection of the free anti-neutrino," *Phys. Rev.* **117** (1960) 159–173.

[14] G. Danby, J. Gaillard, K. A. Goulianos, L. Lederman, N. B. Mistry, M. Schwartz, and J. Steinberger, "Observation of High-Energy Neutrino Reactions and the Existence of Two Kinds of Neutrinos," *Phys. Rev. Lett.* **9** (1962) 36–44.

[15] **DONUT** Collaboration, K. Kodama *et al.*, "Observation of tau neutrino interactions," *Phys. Lett. B* **504** (2001) 218–224, arXiv:hep-ex/0012035.

[16] S. Glashow, "Partial Symmetries of Weak Interactions," *Nucl. Phys.* **22** (1961) 579–588.

[17] S. Weinberg, "A Model of Leptons," *Phys. Rev. Lett.* **19** (1967) 1264–1266.

[18] A. Salam, "Weak and Electromagnetic Interactions," *Conf. Proc. C* **680519** (1968) 367–377.

[19] **ATLAS** Collaboration, G. Aad *et al.*, "Observation of a new particle in the search for the Standard Model Higgs boson with the ATLAS detector at the LHC," *Phys. Lett. B* **716** (2012) 1–29, arXiv:1207.7214 [hep-ex].

[20] **CMS** Collaboration, S. Chatrchyan *et al.*, "Observation of a New Boson at a Mass of 125 GeV with the CMS Experiment at the LHC," *Phys. Lett. B* **716** (2012) 30–61, arXiv:1207.7235 [hep-ex].

[21] T. Lee and C.-N. Yang, "Question of Parity Conservation in Weak Interactions," *Phys. Rev.* **104** (1956) 254–258.

[22] C. Wu, E. Ambler, R. Hayward, D. Hoppes, and R. Hudson, "Experimental Test of Parity Conservation in β Decay," *Phys. Rev.* **105** (1957) 1413–1414.

[23] M. Goldhaber, L. Grodzins, and A. Sunyar, "Helicity of Neutrinos," *Phys. Rev.* **109** (1958) 1015–1017.

[24] **ALEPH, DELPHI, L3, OPAL, SLD, LEP Electroweak Working Group, SLD Electroweak Group, SLD Heavy Flavour Group** Collaboration, S. Schael *et al.*, "Precision electroweak measurements on the Z resonance," *Phys. Rept.* **427** (2006) 257–454, `arXiv:hep-ex/0509008`.

[25] H. T. Janka, "Neutrino Emission from Supernovae," `arXiv:1702.08713 [astro-ph.HE]`.

[26] K. Hirata *et al.*, "Observation in the Kamiokande-II Detector of the Neutrino Burst from Supernova SN 1987a," *Phys. Rev. D* **38** (1988) 448–458.

[27] G. Raffelt, "Horizontal Branch Stars and the Neutrino Signal From SN1987A," *Phys. Rev. D* **38** (1988) 3811–3812.

[28] **KamLAND** Collaboration, A. Gando *et al.*, "Partial radiogenic heat model for Earth revealed by geoneutrino measurements," *Nature Geo.* **4** (2011) 647–651.

[29] **BOREXINO** Collaboration, R. Tartaglia, "BOREXINO: The technical description," *Nucl. Instrum. Meth. A* **461** (2001) 327–328.

[30] F. Stecker, C. Done, M. Salamon, and P. Sommers, "Neutrinos from hell," in *UCLA International Conference on Trends in Astroparticle Physics*, pp. 326–349. 11, 1990.

[31] E. Waxman and J. N. Bahcall, "High-energy neutrinos from cosmological gamma-ray burst fireballs," *Phys. Rev. Lett.* **78** (1997) 2292–2295, `arXiv:astro-ph/9701231`.

[32] K. Mannheim, "Neutrino signatures of the origins of cosmic rays," *Nucl. Phys. B Proc. Suppl.* **256-257** (2014) 264–266.

[33] **ANITA** Collaboration, C. Deaconu, "Recent Results from ANITA," in *13th Conference on the Intersections of Particle and Nuclear Physics*. 10, 2018. `arXiv:1810.00820 [astro-ph.HE]`.

[34] **ANTARES, KM3NeT** Collaboration, M. Sanguineti, "ANTARES and KM3NeT: The Latest Results of the Neutrino Telescopes in the Mediterranean," *Universe* **5** no. 2, (2019) 65.

[35] B. Pontecorvo, "Mesonium and anti-mesonium," *Sov. Phys. JETP* **6** (1957) 429.

[36] B. Pontecorvo, "Inverse beta processes and nonconservation of lepton charge," *Sov. Phys. JETP* **7** (1958) 172–173.

[37] Z. Maki, M. Nakagawa, and S. Sakata, "Remarks on the unified model of elementary particles," *Prog. Theor. Phys.* **28** (1962) 870–880.

[38] B. Pontecorvo, "Neutrino Experiments and the Problem of Conservation of Leptonic Charge," *Sov. Phys. JETP* **26** (1968) 984–988.

[39] **Planck** Collaboration, N. Aghanim *et al.*, "Planck 2018 results. VI. Cosmological parameters," *Astron. Astrophys.* **641** (2020) A6, `arXiv:1807.06209 [astro-ph.CO]`.

[40] S. Weinberg, "Baryon and Lepton Nonconserving Processes," *Phys. Rev. Lett.* **43** (1979) 1566–1570.

[41] P. Minkowski, "$\mu \to e\gamma$ at a Rate of One Out of 10^9 Muon Decays?," *Phys. Lett. B* **67** (1977) 421–428.

[42] M. Gell-Mann, P. Ramond, and R. Slansky, "Complex Spinors and Unified Theories," *Conf. Proc. C* **790927** (1979) 315–321, `arXiv:1306.4669 [hep-th]`.

[43] S. L. Glashow, "The future of elementary particle physics," in *Quarks and Leptons*, M. Lévy, J.-L. Basdevant, D. Speiser, J. Weyers, R. Gastmans, and M. Jacob, eds., pp. 687–713. Springer US, Boston, MA, 1980.

[44] R. N. Mohapatra and G. Senjanovic, "Neutrino Mass and Spontaneous Parity Nonconservation," *Phys. Rev. Lett.* **44** (1980) 912.

[45] M. Magg and C. Wetterich, "Neutrino Mass Problem and Gauge Hierarchy," *Phys. Lett. B* **94** (1980) 61–64.

[46] G. Lazarides, Q. Shafi, and C. Wetterich, "Proton Lifetime and Fermion Masses in an SO(10) Model," *Nucl. Phys. B* **181** (1981) 287–300.

[47] R. N. Mohapatra and G. Senjanovic, "Neutrino Masses and Mixings in Gauge Models with Spontaneous Parity Violation," *Phys. Rev. D* **23** (1981) 165.

[48] J. Schechter and J. Valle, "Neutrino Decay and Spontaneous Violation of Lepton Number," *Phys. Rev. D* **25** (1982) 774.

[49] R. Foot, H. Lew, X. He, and G. C. Joshi, "Seesaw Neutrino Masses Induced by a Triplet of Leptons," *Z. Phys. C* **44** (1989) 441.

[50] S. Weinberg, "Varieties of baryon and lepton nonconservation," *Phys. Rev. D* **22** (Oct, 1980) 1694–1700. `https://link.aps.org/doi/10.1103/PhysRevD.22.1694`.

[51] S. M. Bilenky, S. Pascoli, and S. Petcov, "Majorana neutrinos, neutrino mass spectrum, CP violation and neutrinoless double beta decay. 1. The Three neutrino mixing case," *Phys. Rev. D* **64** (2001) 053010, `arXiv:hep-ph/0102265`.

[52] W. Rodejohann, "Neutrino-less Double Beta Decay and Particle Physics," *Int. J. Mod. Phys. E* **20** (2011) 1833–1930, `arXiv:1106.1334 [hep-ph]`.

[53] J. Vergados, H. Ejiri, and F. Simkovic, "Theory of Neutrinoless Double Beta Decay," *Rept. Prog. Phys.* **75** (2012) 106301, `arXiv:1205.0649 [hep-ph]`.

[54] S. Dell'Oro, S. Marcocci, M. Viel, and F. Vissani, "Neutrinoless double beta decay: 2015 review," *Adv. High Energy Phys.* **2016** (2016) 2162659, arXiv:1601.07512 [hep-ph].

[55] J. Vergados, H. Ejiri, and F. ˇ Simkovic, "Neutrinoless double beta decay and neutrino mass," *Int. J. Mod. Phys. E* **25** no. 11, (2016) 1630007, arXiv:1612.02924 [hep-ph].

[56] S. Petcov, "The Nature of Massive Neutrinos," *Adv. High Energy Phys.* **2013** (2013) 852987, arXiv:1303.5819 [hep-ph].

[57] S. M. Bilenky and S. T. Petcov, "Massive neutrinos and neutrino oscillations," *Rev. Mod. Phys.* **59** (Jul, 1987) 671–754. https://link.aps.org/doi/10.1103/RevModPhys.59.671.

[58] **LSND** Collaboration, C. Athanassopoulos *et al.*, "Evidence for anti-muon-neutrino —¿ anti-electron-neutrino oscillations from the LSND experiment at LAMPF," *Phys. Rev. Lett.* **77** (1996) 3082–3085, arXiv:nucl-ex/9605003 [nucl-ex].

[59] **LSND** Collaboration, A. Aguilar-Arevalo *et al.*, "Evidence for neutrino oscillations from the observation of $\bar{\nu}_e$ appearance in a $\bar{\nu}_\mu$ beam," *Phys. Rev. D* **64** (2001) 112007, arXiv:hep-ex/0104049.

[60] **MiniBooNE** Collaboration, A. Aguilar-Arevalo *et al.*, "Improved Search for $\bar{\nu}_\mu \to \bar{\nu}_e$ Oscillations in the MiniBooNE Experiment," *Phys. Rev. Lett.* **110** (2013) 161801, arXiv:1303.2588 [hep-ex].

[61] **MiniBooNE** Collaboration, A. Aguilar-Arevalo *et al.*, "Significant Excess of ElectronLike Events in the MiniBooNE Short-Baseline Neutrino Experiment," *Phys. Rev. Lett.* **121** no. 22, (2018) 221801, arXiv:1805.12028 [hep-ex].

[62] **DANSS** Collaboration, N. Skrobova, "New results from the DANSS experiment," *Int. J. Mod. Phys. A* **35** no. 34n35, (2020) 2044015.

[63] **NEOS** Collaboration, Y. J. Ko *et al.*, "Sterile Neutrino Search at the NEOS Experiment," *Phys. Rev. Lett.* **118** no. 12, (2017) 121802, arXiv:1610.05134 [hep-ex].

[64] A. Diaz, C. A. Argüelles, G. H. Collin, J. M. Conrad, and M. H. Shaevitz, "Where Are We With Light Sterile Neutrinos?," *Phys. Rept.* **884** (2020) 1–59, arXiv:1906.00045 [hep-ex].

[65] **GALLEX** Collaboration, P. Anselmann *et al.*, "Solar neutrinos observed by GALLEX at Gran Sasso.," *Phys. Lett. B* **285** (1992) 376–389.

[66] **SAGE** Collaboration, J. Abdurashitov *et al.*, "Results from SAGE," *Phys. Lett. B* **328** (1994) 234–248.

[67] J. Abdurashitov *et al.*, "Measurement of the response of a Ga solar neutrino experiment to neutrinos from an Ar-37 source," *Phys. Rev. C* **73** (2006) 045805, arXiv:nucl-ex/0512041.

[68] M. A. Acero, C. Giunti, and M. Laveder, "Limits on nu(e) and anti-nu(e) disappearance from Gallium and reactor experiments," *Phys. Rev.* **D78** (2008) 073009, arXiv:0711.4222 [hep-ph].

[69] J. Kostensalo, J. Suhonen, C. Giunti, and P. C. Srivastava, "The gallium anomaly revisited," *Phys. Lett. B* **795** (2019) 542–547, arXiv:1906.10980 [nucl-th].

[70] G. Mention, M. Fechner, T. Lasserre, T. A. Mueller, D. Lhuillier, M. Cribier, and A. Letourneau, "The Reactor Antineutrino Anomaly," *Phys. Rev.* **D83** (2011) 073006, arXiv:1101.2755 [hep-ex].

[71] T. Mueller *et al.*, "Improved Predictions of Reactor Antineutrino Spectra," *Phys. Rev. C* **83** (2011) 054615, arXiv:1101.2663 [hep-ex].

[72] P. Huber, "On the determination of anti-neutrino spectra from nuclear reactors," *Phys. Rev.* **C84** (2011) 024617, arXiv:1106.0687 [hep-ph]. [Erratum: Phys. Rev.C85,029901(2012)].

[73] M. Maltoni, T. Schwetz, M. Tortola, and J. Valle, "Constraining neutrino oscillation parameters with current solar and atmospheric data," *Phys. Rev. D* **67** (2003) 013011, arXiv:hep-ph/0207227.

[74] S. Goswami, "Accelerator, reactor, solar and atmospheric neutrino oscillation: Beyond three generations," *Phys. Rev.* **D55** (1997) 2931–2949, arXiv:hep-ph/9507212 [hep-ph].

[75] X. Chu, B. Dasgupta, M. Dentler, J. Kopp, and N. Saviano, "Sterile neutrinos with secret interactionscosmological discord?," *JCAP* **1811** no. 11, (2018) 049, arXiv:1806.10629 [hep-ph].

[76] G. Gelmini, S. Palomares-Ruiz, and S. Pascoli, "Low reheating temperature and the visible sterile neutrino," *Phys. Rev. Lett.* **93** (2004) 081302, arXiv:astro-ph/0403323 [astro-ph].

[77] C. E. Yaguna, "Sterile neutrino production in models with low reheating temperatures," *JHEP* **06** (2007) 002, arXiv:0706.0178 [hep-ph].

[78] P. de Salas, M. Lattanzi, G. Mangano, G. Miele, S. Pastor, and O. Pisanti, "Bounds on very low reheating scenarios after Planck," *Phys. Rev. D* **92** no. 12, (2015) 123534, arXiv:1511.00672 [astro-ph.CO].

[79] M. Dentler, . Herndez-Cabezudo, J. Kopp, P. A. N. Machado, M. Maltoni, I. Martinez-Soler, and T. Schwetz, "Updated Global Analysis of Neutrino Oscillations in the Presence of eV-Scale Sterile Neutrinos," *JHEP* **08** (2018) 010, arXiv:1803.10661 [hep-ph].

[80] M. Maltoni, T. Schwetz, M. A. Tortola, and J. W. F. Valle, "Ruling out four neutrino oscillation interpretations of the LSND anomaly?," *Nucl. Phys. B* **643** (2002) 321–338, arXiv:hep-ph/0207157.

[81] C. Kim and A. Pevsner, *Neutrinos in physics and astrophysics*, vol. 8. 1993.

[82] S. Nussinov, "Solar Neutrinos and Neutrino Mixing," *Phys. Lett. B* **63** (1976) 201–203.

[83] P. B. Pal, "Particle physics confronts the solar neutrino problem," *Int. J. Mod. Phys. A* **7** (1992) 5387–5460.

[84] T.-K. Kuo and J. T. Pantaleone, "Neutrino Oscillations in Matter," *Rev. Mod. Phys.* **61** (1989) 937.

[85] L. Wolfenstein, "Neutrino Oscillations in Matter," *Phys. Rev.* **D17** (1978) 2369–2374.

[86] S. Mikheyev and A. Smirnov, "Resonance Amplification of Oscillations in Matter and Spectroscopy of Solar Neutrinos," *Sov. J. Nucl. Phys.* **42** (1985) 913–917.

[87] S. Choubey and P. Roy, "Testing maximality in muon neutrino flavor mixing," *Phys. Rev. Lett.* **93** (2004) 021803, `arXiv:hep-ph/0310316`.

[88] E. K. Akhmedov, R. Johansson, M. Lindner, T. Ohlsson, and T. Schwetz, "Series expansions for three flavor neutrino oscillation probabilities in matter," *JHEP* **04** (2004) 078, `arXiv:hep-ph/0402175`.

[89] **Kamiokande** Collaboration, Y. Fukuda *et al.*, "Solar neutrino data covering solar cycle 22," *Phys. Rev. Lett.* **77** (1996) 1683–1686.

[90] **GALLEX** Collaboration, W. Hampel *et al.*, "GALLEX solar neutrino observations: Results for GALLEX IV," *Phys. Lett. B* **447** (1999) 127–133.

[91] **GNO** Collaboration, M. Altmann *et al.*, "Complete results for five years of GNO solar neutrino observations," *Phys. Lett. B* **616** (2005) 174–190, `arXiv:hep-ex/0504037`.

[92] **Super-Kamiokande** Collaboration, J. Hosaka *et al.*, "Solar neutrino measurements in super-Kamiokande-I," *Phys. Rev. D* **73** (2006) 112001, `arXiv:hep-ex/0508053`.

[93] S. A. Bludman, N. Hata, and P. Langacker, "Astrophysical solutions are incompatible with the solar neutrino data," *Phys. Rev. D* **49** (1994) 3622–3625, `arXiv:hep-ph/9306212`.

[94] N. Hata and P. Langacker, "Model independent determination of the solar neutrino spectrum with and without MSW," *Phys. Rev. D* **52** (1995) 420–440, arXiv:hep-ph/9409372.

[95] N. Hata and P. Langacker, "Solutions to the solar neutrino anomaly," *Phys. Rev. D* **56** (1997) 6107–6116, arXiv:hep-ph/9705339.

[96] S. J. Parke, "Status of the solar neutrino puzzle," *Phys. Rev. Lett.* **74** (1995) 839–841, arXiv:hep-ph/9408397.

[97] K. M. Heeger and R. Robertson, "Probability of a solution to the solar neutrino problem within the minimal standard model," *Phys. Rev. Lett.* **77** (1996) 3720–3723, arXiv:nucl-th/9610030.

[98] A. Dar and G. Shaviv, "Standard solar neutrinos," *Astrophys. J.* **468** (1996) 933–946, arXiv:astro-ph/9604009.

[99] A. Cumming and W. Haxton, "He-3 transport in the sun and the solar neutrino problem," *Phys. Rev. Lett.* **77** (1996) 4286–4289, arXiv:nucl-th/9608045.

[100] J. N. Bahcall, S. Basu, and M. Pinsonneault, "How uncertain are solar neutrino predictions?," *Phys. Lett. B* **433** (1998) 1–8, arXiv:astro-ph/9805135.

[101] **SNO** Collaboration, Q. Ahmad *et al.*, "Direct evidence for neutrino flavor transformation from neutral current interactions in the Sudbury Neutrino Observatory," *Phys. Rev. Lett.* **89** (2002) 011301, arXiv:nucl-ex/0204008.

[102] **SNO** Collaboration, B. Aharmim *et al.*, "Electron energy spectra, fluxes, and day-night asymmetries of B-8 solar neutrinos from measurements with NaCl dissolved in the heavy-water detector at the Sudbury Neutrino Observatory," *Phys. Rev. C* **72** (2005) 055502, arXiv:nucl-ex/0502021.

[103] C. V. Achar *et al.*, "Detection of muons produced by cosmic ray neutrinos deep underground," *Phys. Lett.* **18** (1965) 196–199.

[104] R. Burns, K. A. Goulianos, E. Hyman, L. Lederman, W. Lee, N. Mistry, J. Rettberg, M. Schwartz, J. Sunderland, and G. Danby, "Search for Intermediate Bosons in High-Energy Neutrino Interactions," *Phys. Rev. Lett.* **15** (1965) 42–45.

[105] **Kamiokande-II** Collaboration, K. Hirata *et al.*, "Experimental Study of the Atmospheric Neutrino Flux,".

[106] D. Casper *et al.*, "Measurement of atmospheric neutrino composition with IMB-3," *Phys. Rev. Lett.* **66** (1991) 2561–2564.

[107] R. Becker-Szendy *et al.*, "The Electron-neutrino and muon-neutrino content of the atmospheric flux," *Phys. Rev. D* **46** (1992) 3720–3724.

[108] **Soudan-2** Collaboration, M. C. Goodman, "The Atmospheric neutrino anomaly in Soudan-2," *Nucl. Phys. B Proc. Suppl.* **38** (1995) 337–342.

[109] **Frejus** Collaboration, C. Berger *et al.*, "Study of Atmospheric Neutrino Interactions with the Frejus Detector," *Phys. Lett. B* **227** (1989) 489.

[110] **Frejus** Collaboration, C. Berger *et al.*, "A Study of atmospheric neutrino oscillations in the FREJUS experiment," *Phys. Lett. B* **245** (1990) 305–310.

[111] **NUSEX** Collaboration, M. Aglietta *et al.*, "Experimental study of atmospheric neutrino flux in the NUSEX experiment," *Europhys. Lett.* **8** (1989) 611–614.

[112] **Super-Kamiokande** Collaboration, T. Kajita, E. Kearns, and M. Shiozawa, "Establishing atmospheric neutrino oscillations with Super-Kamiokande," *Nucl. Phys. B* **908** (2016) 14–29.

[113] H. Kwon, F. Boehm, A. Hahn, H. Henrikson, J. Vuilleumier, J. Cavaignac, D. Koang, B. Vignon, F. Von Feilitzsch, and R. Mossbauer, "Search for Neutrino Oscillations at a Fission Reactor," *Phys. Rev. D* **24** (1981) 1097–1111.

[114] A. Kuvshinnikov, L. Mikaelyan, S. Nikolaev, M. Skorokhvatov, and A. Etenko, "Measuring the anti-electron-neutrino + p —¿ n + e+ cross-section and beta

decay axial constant in a new experiment at Rovno NPP reactor. (In Russian)," *JETP Lett.* **54** (1991) 253–257.

[115] Z. Greenwood *et al.*, "Results of a two position reactor neutrino oscillation experiment," *Phys. Rev. D* **53** (1996) 6054–6064.

[116] **Cal Tech-SIN-TUM** Collaboration, V. Zacek, G. Zacek, F. Boehm, F. von Feilitzsch, P. Fisher, K. Gabathuler, J. Gimlett, R. Mossbauer, L. Oberauer, and J. Vuilleumier, "Improved Limits on Oscillation Parameters From $\bar{\nu}_e$ Disappearance Measurements at the Gosgen Power Reactor," *Phys. Lett. B* **164** (1985) 193–198.

[117] G. Vidyakin *et al.*, "Limitations on the characteristics of neutrino oscillations," *JETP Lett.* **59** (1994) 390–393.

[118] Y. Declais *et al.*, "Search for neutrino oscillations at 15-meters, 40-meters, and 95-meters from a nuclear power reactor at Bugey," *Nucl. Phys. B* **434** (1995) 503–534.

[119] **CHOOZ** Collaboration, M. Apollonio *et al.*, "Initial results from the CHOOZ long baseline reactor neutrino oscillation experiment," *Phys. Lett. B* **420** (1998) 397–404, `arXiv:hep-ex/9711002`.

[120] **CHOOZ** Collaboration, M. Apollonio *et al.*, "Limits on neutrino oscillations from the CHOOZ experiment," *Phys. Lett. B* **466** (1999) 415–430, `arXiv:hep-ex/9907037`.

[121] F. Boehm *et al.*, "Search for neutrino oscillations at the Palo Verde nuclear reactors," *Phys. Rev. Lett.* **84** (2000) 3764–3767, `arXiv:hep-ex/9912050`.

[122] F. Boehm *et al.*, "Results from the Palo Verde neutrino oscillation experiment," *Phys. Rev. D* **62** (2000) 072002, `arXiv:hep-ex/0003022`.

[123] **KamLAND** Collaboration, K. Eguchi *et al.*, "First results from KamLAND: Evidence for reactor anti-neutrino disappearance," *Phys. Rev. Lett.* **90** (2003) 021802, `arXiv:hep-ex/0212021`.

[124] **Double Chooz** Collaboration, F. Ardellier *et al.*, "Double Chooz: A Search for the neutrino mixing angle theta(13)," arXiv:hep-ex/0606025.

[125] **RENO** Collaboration, S.-B. Kim, "RENO: Reactor experiment for neutrino oscillation at Yonggwang," *AIP Conf. Proc.* **981** no. 1, (2008) 205–207.

[126] **Daya Bay** Collaboration, X. Guo *et al.*, "A Precision measurement of the neutrino mixing angle θ_{13} using reactor antineutrinos at Daya-Bay," arXiv:hep-ex/0701029.

[127] **MINOS** Collaboration, P. Adamson *et al.*, "Improved search for muon-neutrino to electron-neutrino oscillations in MINOS," *Phys. Rev. Lett.* **107** (2011) 181802, arXiv:1108.0015 [hep-ex].

[128] **K2K** Collaboration, M. Ahn *et al.*, "Measurement of Neutrino Oscillation by the K2K Experiment," *Phys. Rev. D* **74** (2006) 072003, arXiv:hep-ex/0606032.

[129] **T2K** Collaboration, K. Abe *et al.*, "Measurements of neutrino oscillation in appearance and disappearance channels by the T2K experiment with 6.610^{20} protons on target," *Phys. Rev. D* **91** no. 7, (2015) 072010, arXiv:1502.01550 [hep-ex].

[130] **T2K** Collaboration, K. Abe *et al.*, "Measurement of neutrino and antineutrino oscillations by the T2K experiment including a new additional sample of ν_e interactions at the far detector," *Phys. Rev. D* **96** no. 9, (2017) 092006, arXiv:1707.01048 [hep-ex]. [Erratum: Phys.Rev.D 98, 019902 (2018)].

[131] **T2K** Collaboration, K. Abe *et al.*, "Combined Analysis of Neutrino and Antineutrino Oscillations at T2K," *Phys. Rev. Lett.* **118** no. 15, (2017) 151801, arXiv:1701.00432 [hep-ex].

[132] **NOvA** Collaboration, P. Adamson *et al.*, "First measurement of electron neutrino appearance in NOvA," *Phys. Rev. Lett.* **116** no. 15, (2016) 151806, arXiv:1601.05022 [hep-ex].

[133] **NOvA** Collaboration, M. Acero *et al.*, "New constraints on oscillation parameters from ν_e appearance and ν_μ disappearance in the NOvA experiment," *Phys. Rev. D* **98** (2018) 032012, arXiv:1806.00096 [hep-ex].

[134] **NOvA** Collaboration, M. Acero *et al.*, "First Measurement of Neutrino Oscillation Parameters using Neutrinos and Antineutrinos by NOvA," *Phys. Rev. Lett.* **123** no. 15, (2019) 151803, arXiv:1906.04907 [hep-ex].

[135] **MiniBooNE** Collaboration, A. Aguilar-Arevalo *et al.*, "Updated MiniBooNE Neutrino Oscillation Results with Increased Data and New Background Studies," arXiv:2006.16883 [hep-ex].

[136] **KamLAND** Collaboration, K. Eguchi *et al.*, "A high sensitivity search for anti-nu/e's from the sun and other sources at KamLAND," *Phys. Rev. Lett.* **92** (2004) 071301, arXiv:hep-ex/0310047. %%CITATION = HEP-EX/0310047;%%.

[137] **RENO collaboration** Collaboration, J. Ahn *et al.*, "Observation of Reactor Electron Antineutrino Disappearance in the RENO Experiment," *Phys.Rev.Lett.* **108** (2012) 191802, arXiv:1204.0626 [hep-ex].

[138] **MINOS** Collaboration, D. G. Michael *et al.*, "Observation of muon neutrino disappearance with the MINOS detectors and the NuMI neutrino beam," *Phys. Rev. Lett.* **97** (2006) 191801, arXiv:hep-ex/0607088. %%CITATION = HEP-EX/0607088;%%.

[139] **T2K** Collaboration, K. Abe *et al.*, "Indication of Electron Neutrino Appearance from an Accelerator-produced Off-axis Muon Neutrino Beam," *Phys. Rev. Lett.* **107** (2011) 041801, arXiv:1106.2822 [hep-ex]. %%CITATION = ARXIV:1106.2822;%%.

[140] **NOvA** Collaboration, P. Adamson *et al.*, "Constraints on Oscillation Parameters from ν_e Appearance and ν_μ Disappearance in NOvA," *Phys. Rev. Lett.* **118** no. 23, (2017) 231801, arXiv:1703.03328 [hep-ex].

[141] K. J. Kelly, P. A. N. Machado, S. J. Parke, Y. F. Perez-Gonzalez, and R. Z. Funchal, "Neutrino mass ordering in light of recent data," *Phys. Rev. D* **103** no. 1, (2021) 013004, arXiv:2007.08526 [hep-ph].

[142] **ICAL** Collaboration, S. Ahmed *et al.*, "Physics Potential of the ICAL detector at the India-based Neutrino Observatory (INO)," *Pramana* **88** no. 5, (2017) 79, arXiv:1505.07380 [physics.ins-det].

[143] **IceCube** Collaboration, M. Aartsen *et al.*, "PINGU: A Vision for Neutrino and Particle Physics at the South Pole," *J. Phys. G* **44** no. 5, (2017) 054006, arXiv:1607.02671 [hep-ex].

[144] **DUNE** Collaboration, R. Acciarri *et al.*, "Long-Baseline Neutrino Facility (LBNF) and Deep Underground Neutrino Experiment (DUNE): Conceptual Design Report, Volume 2: The Physics Program for DUNE at LBNF," arXiv:1512.06148 [physics.ins-det].

[145] **DUNE** Collaboration, B. Abi *et al.*, "The DUNE Far Detector Interim Design Report Volume 1: Physics, Technology and Strategies," arXiv:1807.10334 [physics.ins-det].

[146] **Hyper-Kamiokande** Collaboration, K. Abe *et al.*, "Physics potentials with the second Hyper-Kamiokande detector in Korea," *PTEP* **2018** no. 6, (2018) 063C01, arXiv:1611.06118 [hep-ex].

[147] **JUNO** Collaboration, F. An *et al.*, "Neutrino Physics with JUNO," *J. Phys. G* **43** no. 3, (2016) 030401, arXiv:1507.05613 [physics.ins-det].

[148] N. 3.2. www.nu-fit.org, 2018.

[149] **ESSnuSB** Collaboration, E. Baussan *et al.*, "A very intense neutrino super beam experiment for leptonic CP violation discovery based on the European

spallation source linac," *Nucl. Phys. B* **885** (2014) 127–149, arXiv:1309.7022 [hep-ex].

[150] J. Burguet-Castell, M. Gavela, J. Gomez-Cadenas, P. Hernandez, and O. Mena, "Superbeams plus neutrino factory: The Golden path to leptonic CP violation," *Nucl. Phys. B* **646** (2002) 301–320, arXiv:hep-ph/0207080.

[151] H. Minakata and H. Nunokawa, "Exploring neutrino mixing with low-energy superbeams," *JHEP* **10** (2001) 001, arXiv:hep-ph/0108085.

[152] G. L. Fogli and E. Lisi, "Tests of three flavor mixing in long baseline neutrino oscillation experiments," *Phys. Rev. D* **54** (1996) 3667–3670, arXiv:hep-ph/9604415.

[153] S. K. Raut, "Effect of non-zero theta(13) on the measurement of theta(23)," *Mod. Phys. Lett. A* **28** (2013) 1350093, arXiv:1209.5658 [hep-ph].

[154] H. Nunokawa, S. J. Parke, and R. Zukanovich Funchal, "Another possible way to determine the neutrino mass hierarchy," *Phys. Rev. D* **72** (2005) 013009, arXiv:hep-ph/0503283.

[155] A. Chatterjee, P. Ghoshal, S. Goswami, and S. K. Raut, "Octant sensitivity for large theta(13) in atmospheric and long baseline neutrino experiments," *JHEP* **06** (2013) 010, arXiv:1302.1370 [hep-ph].

[156] M. Ghosh, P. Ghoshal, S. Goswami, N. Nath, and S. K. Raut, "New look at the degeneracies in the neutrino oscillation parameters, and their resolution by T2K, NOνA and ICAL," *Phys. Rev.* **D93** no. 1, (2016) 013013, arXiv:1504.06283 [hep-ph].

[157] K. T. McDonald, "An Off-axis neutrino beam," arXiv:hep-ex/0111033.

[158] **T2K Collaboration** Collaboration, K. Abe *et al.*, "Measurement of Neutrino Oscillation Parameters from Muon Neutrino Disappearance with an Off-axis Beam," *Phys.Rev.Lett.* **111** no. 21, (2013) 211803, arXiv:1308.0465 [hep-ex].

[159] M. Dracos, "The European Spallation Source neutrino Super Beam," in *Prospects in Neutrino Physics*, pp. 33–41. 3, 2018. arXiv:1803.10948 [hep-ex].

[160] V. Santoro *et al.*, "Development of High Intensity Neutron Source at the European Spallation Source," in *23rd meeting of the International Collaboration on Advanced Neutron Sources (ICANS XXIII)*. 2, 2020. arXiv:2002.03883 [physics.ins-det].

[161] **MEMPHYS** Collaboration, L. Agostino, M. Buizza-Avanzini, M. Dracos, D. Duchesneau, M. Marafini, M. Mezzetto, L. Mosca, T. Patzak, A. Tonazzo, and N. Vassilopoulos, "Study of the performance of a large scale water-Cherenkov detector (MEMPHYS)," *JCAP* **01** (2013) 024, arXiv:1206.6665 [hep-ex].

[162] **Hyper-Kamiokande Working Group** Collaboration, K. Abe *et al.*, "A Long Baseline Neutrino Oscillation Experiment Using J-PARC Neutrino Beam and Hyper-Kamiokande," 2014. arXiv:1412.4673 [physics.ins-det]. https://inspirehep.net/record/1334360/files/arXiv:1412.4673.pdf.

[163] E. Baussan, M. Dracos, T. Ekelof, E. F. Martinez, H. Ohman, and N. Vassilopoulos, "The use the a high intensity neutrino beam from the ESS proton linac for measurement of neutrino CP violation and mass hierarchy," arXiv:1212.5048 [hep-ex].

[164] S. K. Raut, "Matter effects at the T2HK and T2HKK experiments," *Phys. Rev.* **D96** no. 7, (2017) 075029, arXiv:1703.07136 [hep-ph].

[165] S. K. Agarwalla, S. Prakash, and S. Uma Sankar, "Exploring the three flavor effects with future superbeams using liquid argon detectors," *JHEP* **03** (2014) 087, arXiv:1304.3251 [hep-ph].

[166] M. Ghosh, S. Goswami, and S. K. Raut, "Maximizing the DUNE early physics output with current experiments," *Eur. Phys. J.* **C76** no. 3, (2016) 114, arXiv:1412.1744 [hep-ph].

[167] K. Bora, D. Dutta, and P. Ghoshal, "Determining the octant of θ_{23} at LBNE in conjunction with reactor experiments," *Mod. Phys. Lett.* **A30** no. 14, (2015) 1550066, arXiv:1405.7482 [hep-ph].

[168] V. Barger, A. Bhattacharya, A. Chatterjee, R. Gandhi, D. Marfatia, and M. Masud, "Configuring the Long-Baseline Neutrino Experiment," *Phys. Rev.* **D89** no. 1, (2014) 011302, arXiv:1307.2519 [hep-ph].

[169] K. N. Deepthi, C. Soumya, and R. Mohanta, "Revisiting the sensitivity studies for leptonic CP-violation and mass hierarchy with T2K, NOnuA and LBNE experiments," *New J. Phys.* **17** no. 2, (2015) 023035, arXiv:1409.2343 [hep-ph].

[170] N. Nath, M. Ghosh, and S. Goswami, "The physics of antineutrinos in DUNE and determination of octant and δ_{CP}," *Nucl. Phys.* **B913** (2016) 381–404, arXiv:1511.07496 [hep-ph].

[171] C. Soumya, K. N. Deepthi, and R. Mohanta, "A comprehensive study of the discovery potential of NOvA, T2K and T2HK experiments," *Adv. High Energy Phys.* **2016** (2016) 9139402, arXiv:1408.6071 [hep-ph].

[172] P. Coloma, P. Huber, J. Kopp, and W. Winter, "Systematic uncertainties in long-baseline neutrino oscillations for large $_{13}$," *Phys. Rev.* **D87** no. 3, (2013) 033004, arXiv:1209.5973 [hep-ph].

[173] S. K. Agarwalla, S. Choubey, and S. Prakash, "Probing Neutrino Oscillation Parameters using High Power Superbeam from ESS," *JHEP* **12** (2014) 020, arXiv:1406.2219 [hep-ph].

[174] P. Ballett, S. F. King, S. Pascoli, N. W. Prouse, and T. Wang, "Sensitivities and synergies of DUNE and T2HK," *Phys. Rev.* **D96** no. 3, (2017) 033003, arXiv:1612.07275 [hep-ph].

[175] S. K. Agarwalla, M. Ghosh, and S. K. Raut, "A hybrid setup for fundamental unknowns in neutrino oscillations using T2HK (ν) and μ-DAR ($\bar{\nu}$)," *JHEP* **05** (2017) 115, arXiv:1704.06116 [hep-ph].

[176] M. Ghosh and O. Yasuda, "Effect of systematics in the T2HK, T2HKK, and DUNE experiments," *Phys. Rev.* **D96** no. 1, (2017) 013001, arXiv:1702.06482 [hep-ph].

[177] J. Evslin, S.-F. Ge, and K. Hagiwara, "The leptonic CP phase from T2(H)K and μ^+ decay at rest," *JHEP* **02** (2016) 137, arXiv:1506.05023 [hep-ph].

[178] S. K. Agarwalla, S. Choubey, and S. Prakash, "Probing Neutrino Oscillation Parameters using High Power Superbeam from ESS," arXiv:1406.2219 [hep-ph].

[179] K. Chakraborty, S. Goswami, C. Gupta, and T. Thakore, "Enhancing the hierarchy and octant sensitivity of ESSνSB in conjunction with T2K, NOνA and ICAL@INO," *JHEP* **05** (2019) 137, arXiv:1902.02963 [hep-ph].

[180] S. K. Agarwalla, S. Prakash, and S. U. Sankar, "Resolving the octant of theta23 with T2K and NOvA," *JHEP* **07** (2013) 131, arXiv:1301.2574 [hep-ph].

[181] P. Huber, M. Lindner, and W. Winter, "Simulation of long-baseline neutrino oscillation experiments with GLoBES," *Comput. Phys. Commun.* **167** (2005) 195, arXiv:hep-ph/0407333. %%CITATION = HEP-PH/0407333;%%.

[182] P. Huber, J. Kopp, M. Lindner, M. Rolinec, and W. Winter, "New features in the simulation of neutrino oscillation experiments with GLoBES 3.0" *Comput. Phys. Commun.* **177** (2007) 432–438, arXiv:hep-ph/0701187. %%CITATION = HEP-PH/0701187;%%.

[183] J.-E. Campagne, M. Maltoni, M. Mezzetto, and T. Schwetz, "Physics potential of the CERN-MEMPHYS neutrino oscillation project," *JHEP* **04** (2007) 003, arXiv:hep-ph/0603172 [hep-ph].

[184] S. K. Raut, "Effect of non-zero theta(13) on the measurement of theta(23)," *Mod.Phys.Lett.* **A28** (2013) 1350093, arXiv:1209.5658 [hep-ph].

[185] M. Ghosh, "Reason for T2K to run in dominant neutrino mode for detecting CP violation," *Phys. Rev.* **D93** no. 7, (2016) 073003, arXiv:1512.02226 [hep-ph].

[186] G. Altarelli and F. Feruglio, "Discrete Flavor Symmetries and Models of Neutrino Mixing," *Rev. Mod. Phys.* **82** (2010) 2701–2729, arXiv:1002.0211 [hep-ph].

[187] G. Altarelli, F. Feruglio, and L. Merlo, "Tri-Bimaximal Neutrino Mixing and Discrete Flavour Symmetries," *Fortsch. Phys.* **61** (2013) 507–534, arXiv:1205.5133 [hep-ph].

[188] A. Yu. Smirnov, "Discrete symmetries and models of flavor mixing," *J. Phys. Conf. Ser.* **335** (2011) 012006, arXiv:1103.3461 [hep-ph].

[189] H. Ishimori, T. Kobayashi, H. Ohki, Y. Shimizu, H. Okada, and M. Tanimoto, "Non-Abelian Discrete Symmetries in Particle Physics," *Prog. Theor. Phys. Suppl.* **183** (2010) 1–163, arXiv:1003.3552 [hep-th].

[190] S. F. King and C. Luhn, "Neutrino Mass and Mixing with Discrete Symmetry," *Rept. Prog. Phys.* **76** (2013) 056201, arXiv:1301.1340 [hep-ph].

[191] P. F. Harrison and W. G. Scott, "mu - tau reflection symmetry in lepton mixing and neutrino oscillations," *Phys. Lett.* **B547** (2002) 219–228, arXiv:hep-ph/0210197 [hep-ph].

[192] W. Grimus and L. Lavoura, "A Nonstandard CP transformation leading to maximal atmospheric neutrino mixing," *Phys. Lett.* **B579** (2004) 113–122, arXiv:hep-ph/0305309 [hep-ph].

[193] P. M. Ferreira, W. Grimus, L. Lavoura, and P. O. Ludl, "Maximal CP Violation in Lepton Mixing from a Model with Delta(27) flavour Symmetry," *JHEP* **09** (2012) 128, arXiv:1206.7072 [hep-ph].

[194] W. Grimus and L. Lavoura, "mu-tau Interchange symmetry and lepton mixing," *Fortsch. Phys.* **61** (2013) 535–545, arXiv:1207.1678 [hep-ph].

[195] R. N. Mohapatra and C. C. Nishi, "S_4 Flavored CP Symmetry for Neutrinos," *Phys. Rev.* **D86** (2012) 073007, arXiv:1208.2875 [hep-ph].

[196] E. Ma, A. Natale, and O. Popov, "Neutrino Mixing and CP Phase Correlations," *Phys. Lett.* **B746** (2015) 114–116, arXiv:1502.08023 [hep-ph].

[197] A. S. Joshipura and K. M. Patel, "Generalized μ-τ symmetry and discrete subgroups of O(3)," *Phys. Lett.* **B749** (2015) 159–166, arXiv:1507.01235 [hep-ph].

[198] A. S. Joshipura, "Neutrino masses and mixing from flavour antisymmetry," *JHEP* **11** (2015) 186, arXiv:1506.00455 [hep-ph].

[199] A. S. Joshipura and N. Nath, "Neutrino masses and mixing in A_5 with flavor antisymmetry," *Phys. Rev.* **D94** no. 3, (2016) 036008, arXiv:1606.01697 [hep-ph].

[200] C. C. Nishi and B. L. Snchez-Vega, "Mu-tau reflection symmetry with a texture-zero," *JHEP* **01** (2017) 068, arXiv:1611.08282 [hep-ph].

[201] Z.-h. Zhao, "Breakings of the neutrino $\mu - \tau$ reflection symmetry," *JHEP* **09** (2017) 023, arXiv:1703.04984 [hep-ph].

[202] Z.-C. Liu, C.-X. Yue, and Z.-h. Zhao, "Neutrino $\mu - \tau$ reflection symmetry and its breaking in the minimal seesaw," *JHEP* **10** (2017) 102, arXiv:1707.05535 [hep-ph].

[203] Z.-z. Xing, D. Zhang, and J.-y. Zhu, "The $\mu - \tau$ reflection symmetry of Dirac neutrinos and its breaking effect via quantum corrections," arXiv:1708.09144 [hep-ph].

[204] Z.-z. Xing and J.-y. Zhu, “Neutrino mass ordering and $\mu - \tau$ reflection symmetry breaking,” arXiv:1707.03676 [hep-ph].

[205] A. S. Joshipura, “Perturbed flavour symmetries and predictions of CP violating phase δ,” arXiv:1801.02843 [hep-ph].

[206] N. Nath, Z.-z. Xing, and J. Zhang, “$\mu - \tau$ Reflection Symmetry Embedded in Minimal Seesaw,” arXiv:1801.09931 [hep-ph].

[207] Z.-h. Zhao, “Modifications to the neutrino mixing given by the mu-tau reflection symmetry,” arXiv:1803.04603 [hep-ph].

[208] **Particle Data Group** Collaboration, C. Patrignani *et al.*, “Review of Particle Physics,” *Chin. Phys.* **C40** no. 10, (2016) 100001.

[209] P. F. de Salas, D. V. Forero, C. A. Ternes, M. Tortola, and J. W. F. Valle, “Status of neutrino oscillations 2018: 3σ hint for normal mass ordering and improved CP sensitivity,” *Phys. Lett.* **B782** (2018) 633–640, arXiv:1708.01186 [hep-ph].

[210] F. Capozzi, E. Lisi, A. Marrone, D. Montanino, and A. Palazzo, “Neutrino masses and mixings: Status of known and unknown 3ν parameters,” *Nucl. Phys.* **B908** (2016) 218–234, arXiv:1601.07777 [hep-ph].

[211] T. Fukuyama and H. Nishiura, “Mass matrix of Majorana neutrinos,” arXiv:hep-ph/9702253 [hep-ph].

[212] E. Ma and M. Raidal, “Neutrino mass, muon anomalous magnetic moment, and lepton flavor nonconservation,” *Phys. Rev. Lett.* **87** (2001) 011802, arXiv:hep-ph/0102255 [hep-ph]. [Erratum: Phys. Rev. Lett.87,159901(2001)].

[213] C. S. Lam, “A 2-3 symmetry in neutrino oscillations,” *Phys. Lett.* **B507** (2001) 214–218, arXiv:hep-ph/0104116 [hep-ph].

[214] K. R. S. Balaji, W. Grimus, and T. Schwetz, "The Solar LMA neutrino oscillation solution in the Zee model," *Phys. Lett.* **B508** (2001) 301–310, arXiv:hep-ph/0104035 [hep-ph].

[215] W. Grimus, A. S. Joshipura, S. Kaneko, L. Lavoura, H. Sawanaka, and M. Tanimoto, "Non-vanishing U(e3) and cos 2 theta(23) from a broken Z(2) symmetry," *Nucl. Phys.* **B713** (2005) 151–172, arXiv:hep-ph/0408123 [hep-ph].

[216] A. S. Joshipura, "Universal 2-3 symmetry," *Eur. Phys. J.* **C53** (2008) 77–85, arXiv:hep-ph/0512252 [hep-ph].

[217] Z.-z. Xing and Z.-h. Zhao, "A review of - flavor symmetry in neutrino physics," *Rept. Prog. Phys.* **79** no. 7, (2016) 076201, arXiv:1512.04207 [hep-ph].

[218] Z.-z. Xing and S. Zhou, "A partial symmetry and its prediction for leptonic CP violation," *Phys. Lett.* **B737** (2014) 196–200, arXiv:1404.7021 [hep-ph].

[219] S.-F. Ge, D. A. Dicus, and W. W. Repko, "Z_2 Symmetry Prediction for the Leptonic Dirac CP Phase," *Phys. Lett.* **B702** (2011) 220–223, arXiv:1104.0602 [hep-ph].

[220] S.-F. Ge, D. A. Dicus, and W. W. Repko, "Residual Symmetries for Neutrino Mixing with a Large θ_{13} and Nearly Maximal δ_D," *Phys. Rev. Lett.* **108** (2012) 041801, arXiv:1108.0964 [hep-ph].

[221] S. T. Petcov, "Discrete Flavour Symmetries, Neutrino Mixing and Leptonic CP Violation," arXiv:1711.10806 [hep-ph].

[222] R. de Adelhart Toorop, F. Feruglio, and C. Hagedorn, "Discrete Flavour Symmetries in Light of T2K," *Phys. Lett.* **B703** (2011) 447–451, arXiv:1107.3486 [hep-ph].

[223] A. D. Hanlon, S.-F. Ge, and W. W. Repko, "Phenomenological consequences of residual $\mathbb{Z}_2^s$ and $\overline{\mathbb{Z}}_2^s$ symmetries," *Phys. Lett.* **B729** (2014) 185–191, arXiv:1308.6522 [hep-ph].

[224] A. D. Hanlon, W. W. Repko, and D. A. Dicus, "Residual Symmetries Applied to Neutrino Oscillations at NOvA and T2K," *Adv. High Energy Phys.* **2014** (2014) 469572, arXiv:1403.7552 [hep-ph].

[225] V. Barger, A. Bhattacharya, A. Chatterjee, R. Gandhi, D. Marfatia, *et al.*, "Configuring the Long-Baseline Neutrino Experiment," *Phys.Rev.* **D89** no. 1, (2014) 011302, arXiv:1307.2519 [hep-ph].

[226] S. K. Agarwalla, S. Prakash, and S. Uma Sankar, "Exploring the three flavor effects with future superbeams using liquid argon detectors," *JHEP* **1403** (2014) 087, arXiv:1304.3251 [hep-ph].

[227] V. Barger, A. Bhattacharya, A. Chatterjee, R. Gandhi, D. Marfatia, and M. Masud, "Optimal configurations of the Deep Underground Neutrino Experiment," *Int. J. Mod. Phys.* **A31** no. 07, (2016) 1650020, arXiv:1405.1054 [hep-ph].

[228] D. Dutta and k. Bora, "Probing CP violation at LBNE with reactor experiments," *Mod. Phys. Lett.* **A30** no. 07, (2015) 1550017, arXiv:1409.8248 [hep-ph].

[229] R. Srivastava, C. A. Ternes, M. Trtola, and J. W. F. Valle, "Zooming in on neutrino oscillations with DUNE," arXiv:1803.10247 [hep-ph].

[230] P. Pasquini, "Review: Long-baseline oscillation experiments as a tool to probe High Energy Models," arXiv:1802.00821 [hep-ph].

[231] R. Srivastava, C. A. Ternes, M. Trtola, and J. W. F. Valle, "Testing a lepton quarticity flavor theory of neutrino oscillations with the DUNE experiment," *Phys. Lett.* **B778** (2018) 459–463, arXiv:1711.10318 [hep-ph].

[232] S. K. Agarwalla, S. S. Chatterjee, S. T. Petcov, and A. V. Titov, "Addressing Neutrino Mixing Schemes with DUNE and T2HK," arXiv:1711.02107 [hep-ph].

[233] S. S. Chatterjee, M. Masud, P. Pasquini, and J. W. F. Valle, "Cornering the revamped BMV model with neutrino oscillation data," *Phys. Lett.* **B774** (2017) 179–182, arXiv:1708.03290 [hep-ph].

[234] S. T. Petcov and A. V. Titov, "Assessing the Viability of A_4, S_4 and A_5 Flavour Symmetries for Description of Neutrino Mixing," arXiv:1804.00182 [hep-ph].

[235] P. Ballett, S. F. King, S. Pascoli, N. W. Prouse, and T. Wang, "Precision neutrino experiments vs the Littlest Seesaw," *JHEP* **03** (2017) 110, arXiv:1612.01999 [hep-ph].

[236] P. Ballett, S. Pascoli, and J. Turner, "Mixing angle and phase correlations from A5 with generalized CP and their prospects for discovery," *Phys. Rev.* **D92** no. 9, (2015) 093008, arXiv:1503.07543 [hep-ph].

[237] P. Ballett, S. F. King, C. Luhn, S. Pascoli, and M. A. Schmidt, "Testing solar lepton mixing sum rules in neutrino oscillation experiments," *JHEP* **12** (2014) 122, arXiv:1410.7573 [hep-ph].

[238] J. T. Penedo, S. T. Petcov, and T. Yanagida, "Low-Scale Seesaw and the CP Violation in Neutrino Oscillations," *Nucl. Phys.* **B929** (2018) 377–396, arXiv:1712.09922 [hep-ph].

[239] S. F. King and T. Neder, "Lepton mixing predictions including Majorana phases from $(6n^2)$ flavour symmetry and generalised CP," *Phys. Lett.* **B736** (2014) 308–316, arXiv:1403.1758 [hep-ph].

[240] A. S. Joshipura and K. M. Patel, "Residual Z_2 symmetries and leptonic mixing patterns from finite discrete subgroups of $U(3)$," *JHEP* **01** (2017) 134, arXiv:1610.07903 [hep-ph].

[241] W. Grimus and P. O. Ludl, "On the characterization of the SU(3)-subgroups of type C and D," *J. Phys.* **A47** no. 7, (2014) 075202, arXiv:1310.3746 [math-ph].

[242] M. D. Messier, "Evidence for neutrino mass from observations of atmospheric neutrinos with Super-Kamiokande,". Ph.D. Thesis (Advisor: James L. Stone). %%CITATION = UMI-99-23965 ETC.;%%.

[243] E. Paschos and J. Yu, "Neutrino interactions in oscillation experiments," *Phys.Rev.* **D65** (2002) 033002, arXiv:hep-ph/0107261 [hep-ph]. %%CITATION = HEP-PH/0107261;%%.

[244] M. C. Gonzalez-Garcia and M. Maltoni, "Atmospheric neutrino oscillations and new physics," *Phys. Rev.* **D70** (2004) 033010, arXiv:hep-ph/0404085. %%CITATION = HEP-PH/0404085;%%.

[245] G. Fogli, E. Lisi, A. Marrone, D. Montanino, and A. Palazzo, "Getting the most from the statistical analysis of solar neutrino oscillations," *Phys.Rev.* **D66** (2002) 053010, arXiv:hep-ph/0206162 [hep-ph].

[246] R. Gandhi *et al.*, "Mass Hierarchy Determination via future Atmospheric Neutrino Detectors," *Phys. Rev.* **D76** (2007) 073012, arXiv:0707.1723 [hep-ph]. %%CITATION = ARXIV:0707.1723;%%.

[247] **JUNO** Collaboration, Y.-F. Li, "Jiangmen Underground Neutrino Observatory: Status and Prospectives," in *Proceedings, 17th Lomonosov Conference on Elementary Particle Physics: Moscow, Russia, August 20-26, 2015*, pp. 27–33. 2017. arXiv:1606.04743 [physics.ins-det]. https://inspirehep.net/record/1469449/files/arXiv:1606.04743.pdf.

[248] J. Barry, W. Rodejohann, and H. Zhang, "Light Sterile Neutrinos: Models and Phenomenology," *JHEP* **07** (2011) 091, arXiv:1105.3911 [hep-ph].

[249] J. Barry, W. Rodejohann, and H. Zhang, "Sterile Neutrinos for Warm Dark Matter and the Reactor Anomaly in Flavor Symmetry Models," *JCAP* **1201** (2012) 052, arXiv:1110.6382 [hep-ph].

[250] D. C. Rivera-Agudelo and A. Prez-Lorenzana, "Generating $_{13}$ from sterile neutrinos in - symmetric models," *Phys. Rev.* **D92** no. 7, (2015) 073009, arXiv:1507.07030 [hep-ph].

[251] A. Merle, S. Morisi, and W. Winter, "Common origin of reactor and sterile neutrino mixing," *JHEP* **07** (2014) 039, arXiv:1402.6332 [hep-ph].

[252] D. Borah, "Non-zero θ_{13} with Unbroken $\mu - \tau$ Symmetry of the Active Neutrino Mass Matrix in the Presence of a Light Sterile Neutrino," *Phys. Rev.* **D95** no. 3, (2017) 035016, arXiv:1607.05556 [hep-ph].

[253] N. Sarma, K. Bora, and D. Borah, "Compatibility of A_4 Flavour Symmetric Minimal Extended Seesaw with $(3 + 1)$ Neutrino Data," *Eur. Phys. J.* **C79** no. 2, (2019) 129, arXiv:1810.05826 [hep-ph].

[254] C. C. Nishi, "New and trivial CP symmetry for extended A_4 flavor," *Phys. Rev.* **D93** no. 9, (2016) 093009, arXiv:1601.00977 [hep-ph].

[255] N. Nath, "Consequences of $\mu - \tau$ Reflection Symmetry at DUNE," *Phys. Rev.* **D98** no. 7, (2018) 075015, arXiv:1805.05823 [hep-ph].

[256] K. Chakraborty, K. Deepthi, S. Goswami, A. S. Joshipura, and N. Nath, "Exploring partial μ-τ reflection symmetry at DUNE and Hyper-Kamiokande," *Phys. Rev. D* **98** no. 7, (2018) 075031, arXiv:1804.02022 [hep-ph].

[257] N. Nath, "$\mu - \tau$ Reflection Symmetry and Its Explicit Breaking for Leptogenesis in a Minimal Seesaw Model," arXiv:1808.05062 [hep-ph].

[258] C. C. Nishi, B. L. Snchez-Vega, and G. Souza Silva, "$\mu\tau$ reflection symmetry with a high scale texture-zero," *JHEP* **09** (2018) 042, arXiv:1806.07412 [hep-ph].

[259] W. Rodejohann and X.-J. Xu, "Trimaximal μ-τ reflection symmetry," *Phys. Rev.* **D96** no. 5, (2017) 055039, arXiv:1705.02027 [hep-ph].

[260] P. Chen, G.-J. Ding, F. Gonzalez-Canales, and J. W. F. Valle, "Generalized $\mu - \tau$ reflection symmetry and leptonic CP violation," *Phys. Lett.* **B753** (2016) 644–652, arXiv:1512.01551 [hep-ph].

[261] Y.-L. Zhou, "μ-τ reflection symmetry and radiative corrections," arXiv:1409.8600 [hep-ph].

[262] H.-J. He, W. Rodejohann, and X.-J. Xu, "Origin of Constrained Maximal CP Violation in Flavor Symmetry," *Phys. Lett.* **B751** (2015) 586–594, arXiv:1507.03541 [hep-ph].

[263] H.-J. He and X.-J. Xu, "Octahedral Symmetry with Geometrical Breaking: New Prediction for Neutrino Mixing Angle θ_{13} and CP Violation," *Phys. Rev.* **D86** (2012) 111301, arXiv:1203.2908 [hep-ph].

[264] S.-F. Ge, H.-J. He, and F.-R. Yin, "Common Origin of Soft mu-tau and CP Breaking in Neutrino Seesaw and the Origin of Matter," *JCAP* **1005** (2010) 017, arXiv:1001.0940 [hep-ph].

[265] H.-J. He and F.-R. Yin, "Common Origin of $\mu - \tau$ and CP Breaking in Neutrino Seesaw, Baryon Asymmetry, and Hidden Flavor Symmetry," *Phys. Rev.* **D84** (2011) 033009, arXiv:1104.2654 [hep-ph].

[266] N. Nath, "Impact of RGE-induced $\mu - \tau$ reflection symmetry breaking on the effective Majorana neutrino mass in $0\nu\beta\beta$ decay," *Phys. Rev.* **D99** no. 3, (2019) 035026, arXiv:1810.07938 [hep-ph].

[267] C. H. Albright and W. Rodejohann, "Comparing Trimaximal Mixing and Its Variants with Deviations from Tri-bimaximal Mixing," *Eur. Phys. J.* **C62** (2009) 599–608, arXiv:0812.0436 [hep-ph].

[268] W. Grimus and L. Lavoura, "A Model for trimaximal lepton mixing," *JHEP* **09** (2008) 106, arXiv:0809.0226 [hep-ph].

[269] I. Girardi, S. T. Petcov, and A. V. Titov, "Predictions for the Majorana CP Violation Phases in the Neutrino Mixing Matrix and Neutrinoless Double Beta Decay," *Nucl. Phys.* **B911** (2016) 754–804, arXiv:1605.04172 [hep-ph].

[270] F. Capozzi, E. Lisi, A. Marrone, and A. Palazzo, "Current unknowns in the three neutrino framework," arXiv:1804.09678 [hep-ph].

[271] **Super-Kamiokande** Collaboration, K. Abe *et al.*, "Limits on sterile neutrino mixing using atmospheric neutrinos in Super-Kamiokande," *Phys. Rev.* **D91** (2015) 052019, arXiv:1410.2008 [hep-ex].

[272] **IceCube** Collaboration, M. G. Aartsen *et al.*, "Search for sterile neutrino mixing using three years of IceCube DeepCore data," *Phys. Rev.* **D95** no. 11, (2017) 112002, arXiv:1702.05160 [hep-ex].

[273] **MINOS** Collaboration, P. Adamson *et al.*, "Search for Sterile Neutrinos Mixing with Muon Neutrinos in MINOS," *Phys. Rev. Lett.* **117** no. 15, (2016) 151803, arXiv:1607.01176 [hep-ex].

[274] **NOvA** Collaboration, P. Adamson *et al.*, "Search for active-sterile neutrino mixing using neutral-current interactions in NOvA," *Phys. Rev.* **D96** no. 7, (2017) 072006, arXiv:1706.04592 [hep-ex].

[275] **T2K** Collaboration, K. Abe *et al.*, "Search for light sterile neutrinos with the T2K far detector Super-Kamiokande at a baseline of 295 km," *Phys. Rev.* **D99** no. 7, (2019) 071103, arXiv:1902.06529 [hep-ex].

[276] R. Gandhi, B. Kayser, S. Prakash, and S. Roy, "What measurements of neutrino neutral current events can reveal," *JHEP* **11** (2017) 202, arXiv:1708.01816 [hep-ph].

[277] A. De Gouvła, K. J. Kelly, G. V. Stenico, and P. Pasquini, "Physics with Beam Tau-Neutrino Appearance at DUNE," *Phys. Rev.* **D100** no. 1, (2019) 016004, arXiv:1904.07265 [hep-ph].

[278] A. Ghoshal, A. Giarnetti, and D. Meloni, "On the Role of the ν_τ Appearance in DUNE in Constraining Standard Neutrino Physics and Beyond," arXiv:1906.06212 [hep-ph].

[279] P. Coloma, D. V. Forero, and S. J. Parke, "DUNE Sensitivities to the Mixing between Sterile and Tau Neutrinos," *JHEP* **07** (2018) 079, arXiv:1707.05348 [hep-ph].

[280] P. Huber, M. Lindner, and W. Winter, "Simulation of long-baseline neutrino oscillation experiments with GLoBES (General Long Baseline Experiment Simulator)," *Comput. Phys. Commun.* **167** (2005) 195, arXiv:hep-ph/0407333 [hep-ph].

[281] P. Huber, J. Kopp, M. Lindner, M. Rolinec, and W. Winter, "New features in the simulation of neutrino oscillation experiments with GLoBES 3.0: General Long Baseline Experiment Simulator," *Comput. Phys. Commun.* **177** (2007) 432–438, arXiv:hep-ph/0701187 [hep-ph].

[282] J. Kopp, M. Lindner, and T. Ota, "Discovery reach for non-standard interactions in a neutrino factory," *Phys. Rev.* **D76** (2007) 013001, arXiv:hep-ph/0702269 [HEP-PH].

[283] **KamLAND-Zen** Collaboration, A. Gando *et al.*, "Search for Majorana Neutrinos near the Inverted Mass Hierarchy Region with KamLAND-Zen," *Phys. Rev. Lett.* **117** no. 8, (2016) 082503, arXiv:1605.02889 [hep-ex]. [Addendum: Phys. Rev. Lett.117,no.10,109903(2016)].

[284] **GERDA** Collaboration, M. Agostini *et al.*, "Improved Limit on Neutrinoless Double-β Decay of ^{76}Ge from GERDA Phase II," *Phys. Rev. Lett.* **120** no. 13, (2018) 132503, arXiv:1803.11100 [nucl-ex].

[285] **CUORE** Collaboration, C. Alduino *et al.*, "First Results from CUORE: A Search for Lepton Number Violation via $0\nu\beta\beta$ Decay of ^{130}Te," *Phys. Rev. Lett.* **120** no. 13, (2018) 132501, arXiv:1710.07988 [nucl-ex].

[286] V. K. N., S. Choubey, and S. Goswami, "A New Sensitivity Goal for Neutrino-less Double Beta Decay Experiments," arXiv:1901.04313 [hep-ph].

[287] V. Lozza, "Magellan workshop, hamburg, germany, 2016 (magellan workshop,hamburg, germany, 2016), pp. 8794.".

[288] J. Shirai. http://neutrino2016.iopconfs.org/IOP/media/uploaded/EVIOP/event_948/09.45__5__Shirai.pdf, 2016.

[289] **LEGEND** Collaboration, J. Myslik, "LEGEND: The Large Enriched Germanium Experiment for Neutrinoless Double-Beta Decay," in *13th Conference on the Intersections of Particle and Nuclear Physics (CIPANP 2018) Palm Springs, California, USA, May 29-June 3, 2018*. 2018. arXiv:1810.00849 [physics.ins-det].

[290] **Planck** Collaboration, P. A. R. Ade *et al.*, "Planck 2015 results. XIII. Cosmological parameters," *Astron. Astrophys.* **594** (2016) A13, arXiv:1502.01589 [astro-ph.CO].

[291] S. Roy Choudhury and S. Choubey, "Constraining light sterile neutrino mass with the BICEP2/Keck Array 2014 B-mode polarization data," arXiv:1807.10294 [astro-ph.CO].

[292] **JSNS^2** Collaboration, C. Rott, "Status and Prospects of the JSNS^2 Experiment," *PoS* **ICHEP2018** (2019) 185, arXiv:1811.03321 [physics.ins-det].

[293] **NEUTRINO-4** Collaboration, A. P. Serebrov *et al.*, "First Observation of the Oscillation Effect in the Neutrino-4 Experiment on the Search for the Sterile Neutrino," *Pisma Zh. Eksp. Teor. Fiz.* **109** no. 4, (2019) 209–218, arXiv:1809.10561 [hep-ex]. [JETP Lett.109,no.4,213(2019)].

[294] A. Haghighat, P. Huber, S. Li, J. M. Link, C. Mariani, J. Park, and T. Subedi, "Observation of Reactor Antineutrinos with a Rapidly-Deployable Surface-Level Detector," arXiv:1812.02163 [physics.ins-det].

[295] **DANSS** Collaboration, I. Alekseev *et al.*, "Search for sterile neutrinos at the DANSS experiment," *Phys. Lett.* **B787** (2018) 56–63, arXiv:1804.04046 [hep-ex].

[296] **STEREO** Collaboration, N. Allemandou *et al.*, "The STEREO Experiment," *JINST* **13** no. 07, (2018) P07009, arXiv:1804.09052 [physics.ins-det].

[297] S. P. Behera, A. Ghosh, S. Choubey, V. M. Datar, D. K. Mishra, and A. K. Mohanty, "Search for the sterile neutrino mixing with the ICAL detector at INO," *Eur. Phys. J.* **C77** no. 5, (2017) 307, arXiv:1605.08607 [hep-ph].

[298] **MINOS** Collaboration, P. Adamson *et al.*, "Active to sterile neutrino mixing limits from neutral-current interactions in MINOS," *Phys. Rev. Lett.* **107** (2011) 011802, arXiv:1104.3922 [hep-ex].

[299] F. J. Escrihuela, D. V. Forero, O. G. Miranda, M. Tortola, and J. W. F. Valle, "On the description of nonunitary neutrino mixing," *Phys. Rev.* **D92** no. 5, (2015) 053009, arXiv:1503.08879 [hep-ph]. [Erratum: Phys. Rev.D93,no.11,119905(2016)].

[300] W. Rodejohann, "Non-Unitary Lepton Mixing Matrix, Leptogenesis and Low Energy CP Violation," *EPL* **88** no. 5, (2009) 51001, arXiv:0903.4590 [hep-ph].

[301] M. Blennow, P. Coloma, E. Fernandez-Martinez, J. Hernandez-Garcia, and J. Lopez-Pavon, "Non-Unitarity, sterile neutrinos, and Non-Standard neutrino Interactions," *JHEP* **04** (2017) 153, arXiv:1609.08637 [hep-ph].

[302] S. Goswami and T. Ota, "Testing non-unitarity of neutrino mixing matrices at neutrino factories," *Phys. Rev.* **D78** (2008) 033012, arXiv:0802.1434 [hep-ph].

[303] M. Malinsky, T. Ohlsson, and H. Zhang, "Non-unitarity effects in a realistic low-scale seesaw model," *Phys. Rev.* **D79** (2009) 073009, arXiv:0903.1961 [hep-ph].

[304] S. Antusch, C. Biggio, E. Fernandez-Martinez, M. B. Gavela, and J. Lopez-Pavon, "Unitarity of the Leptonic Mixing Matrix," *JHEP* **10** (2006) 084, arXiv:hep-ph/0607020 [hep-ph].

[305] S. Antusch, M. Blennow, E. Fernandez-Martinez, and J. Lopez-Pavon, "Probing non-unitary mixing and CP-violation at a Neutrino Factory," *Phys. Rev.* **D80** (2009) 033002, arXiv:0903.3986 [hep-ph].

[306] M. Malinsky, T. Ohlsson, Z.-z. Xing, and H. Zhang, "Non-unitary neutrino mixing and CP violation in the minimal inverse seesaw model," *Phys. Lett.* **B679** (2009) 242–248, arXiv:0905.2889 [hep-ph].

[307] S. Antusch and O. Fischer, "Non-unitarity of the leptonic mixing matrix: Present bounds and future sensitivities," *JHEP* **10** (2014) 094, arXiv:1407.6607 [hep-ph].

[308] D. Dutta and P. Ghoshal, "Probing CP violation with T2K, NOνA and DUNE in the presence of non-unitarity," *JHEP* **09** (2016) 110, arXiv:1607.02500 [hep-ph].

[309] L. S. Miranda, P. Pasquini, U. Rahaman, and S. Razzaque, "Searching for non-unitary neutrino oscillations in the present T2K and NOνA data," arXiv:1911.09398 [hep-ph].

[310] D. Dutta and S. Roy, "Non Unitarity at DUNE and T2HK with Charged and Neutral Current Measurements," arXiv:1901.11298 [hep-ph].

[311] **MINOS** Collaboration, J. Evans, "The MINOS Experiment: Results and Prospects," *Adv. High Energy Phys.* **2013** (2013) 182537, `arXiv:1307.0721 [hep-ex]`.

[312] A. Rasin, "Diagonalization of quark mass matrices and the Cabibbo-Kobayashi-Maskawa matrix," `arXiv:hep-ph/9708216`.

List of Publications

Thesis Related Publications

1. **Kaustav Chakraborty**, K. Deepthi, and S. Goswami, *Spotlighting the sensitivities of Hyper-Kamiokande, DUNE and ESS ν SB,* Nucl. Phys. B **937**, 303–332 (2018).

2. **Kaustav Chakraborty**, K. Deepthi, S. Goswami, A. S. Joshipura, and N. Nath, *Exploring partial μ-τ reflection symmetry at DUNE and Hyper-Kamiokande,* Phys. Rev. D **98**, 075031 (2018).

3. **Kaustav Chakraborty**, S. Goswami, and B. Karmakar, *Consequences of μ-τ reflection symmetry for $3+1$ neutrino mixing,* Phys. Rev. D **100**, 035017 (2019).

4. **Kaustav Chakraborty**, S. Goswami, and K. Long, *New Physics at nuSTORM,* arxiv:2007.03321.

Publication(s) not part of the thesis

Kaustav Chakraborty, S. Goswami, C. Gupta, and T. Thakore, *Enhancing the hierarchy and octant sensitivity of ESSνSB in conjunction with T2K, NOνA and ICAL@INO,* JHEP **05**, 137 (2019).